ACTIVE VIBRATION CONTROL OF SMART MULTISCALE COMPOSITE BEAMS, PLATES, AND SHELLS

Ph.D. Thesis

by

MADHUR GUPTA

(Roll No. 1901103005)

DEPARTMENT OF MECHANICAL ENGINEERING

INDIAN INSTITUTE OF TECHNOLOGY INDORE

NOVEMBER 2022

ACTIVE VIBRATION CONTROL OF SMART MULTISCALE COMPOSITE BEAMS, PLATES AND SHELLS

A THESIS

Submitted in partial fulfillment of the requirements for the award of the degree

of

DOCTOR OF PHILOSOPHY

by

MADHUR GUPTA

(Roll No. 1901103005)

DEPARTMENT OF MECHANICAL ENGINEERING

INDIAN INSTITUTE OF TECHNOLOGY INDORE

NOVEMBER 2022

INDIAN INSTITUTE OF TECHNOLOGY INDORE

CANDIDATE'S DECLARATION

I hereby certify that the work which is being presented in the thesis entitled **ACTIVE VIBRATION CONTROL OF SMART MULTISCALE COMPOSITE BEAMS, PLATES AND SHELLS** in the partial fulfillment of the requirements for the award of the degree of **DOCTOR OF PHILOSOPHY** and submitted in the **DEPARTMENT OF MECHNIACL ENGINEERING, Indian Institute of Technology Indore**, is an authentic record of my own work carried out during the time period from June 2019 to November 2022 under the supervision of **Dr. Shailesh I. Kundalwal**, **Associate Professor, and Indian Institute of Technology, Indore and Dr. Nagesh D. Patil, Assistant Professor, and Indian Institute of Technology Bhilai.**

The matter presented in this thesis has not been submitted by me for the award of any other degree of this or any other institute.

11 November 2022

Signature of the student with date

(MADHUR GUPTA)

This is to certify that the above statement made by the candidate is correct to the best of my/our knowledge.

Nov 18, 2022

Signature of Thesis Supervisor #1 with date

(Dr. Shailesh Ishwarlal Kundalwal)

Nov 18, 2022

Signature of Thesis Supervisor #2 with date

(Dr. Nagesh Devidas Patil)

Madhur Gupta has successfully given his/her Ph.D. Oral Examination held on **November 10, 2022**.

Nov 18, 2022

Signature of Thesis Supervisor #1 with date

(Dr. Shailesh Ishwarlal Kundalwal)

Nov 18, 2022

Signature of Thesis Supervisor #2 with date

(Dr. Nagesh Devidas Patil)

Acknowledgements

It is a great pleasure for me to acknowledge all the people who have helped and supported me to complete this thesis. First and foremost, I express my deep and heartfelt gratitude to my supervisors, **Dr. Shailesh Ishwarlal Kundalwal** and **Dr. Nagesh Devidas Patil.** I have had the privilege of being associated with them throughout this entire period of doctoral studies. I have been fortunate to have **Dr. Shailesh Ishwarlal Kundalwal** as my supervisor, who cared so much about my work, and who always responded to my questions and queries so promptly. He has always inspired me with his hardworking and passionate approach toward research and his urge to achieve high-quality work. I have also received continuous academic support, inspiration, and encouragement from my co-supervisor, **Dr. Nagesh Devidas Patil**. Their support not only enriched me academically but also nourished my inner self and changed my perspective and attitude a lot. Through this association with them, I have been able to acquire, develop and sharpen the skills and the scientific methodologies which are invaluable for good independent research. Their immense knowledge, guidance, observations, and comments helped me a lot to establish the overall direction of the research and to move forward with the investigation in depth. For all this, I will remain indebted and grateful to them for my entire life.

I gratefully extend my gratitude towards my PSPC members **Prof. Bhupesh Kumar Lad,** Department of Mechanical Engineering, **Dr. Srimanta Pakhira,** Department of Physics, Indian Institute of Technology Indore, for their valuable suggestions and comments to improve my work. I am grateful to the **Head**, **DPGC Convener,** all the faculty members, and staff of the Department of Mechanical Engineering, **IIT Indore** for providing an encouraging environment to carry out research effectively.

I would like to acknowledge **Prof. Suhas S. Joshi, Director, IIT Indore** for providing a conducive environment for research and opportunity to explore my research capabilities at IIT Indore. I am also thankful to **The Dean of Academic Affairs, The Dean of Research and Development, and The Dean of Student Affairs, IIT Indore**.

I am lucky to have good friends who have been constantly encouraging, motivating, and cheering me in all situations. I extend my thanks to **Mr. Mayank Shukla**, **Mrs. Kayla Breann Dockery**, **Mrs. Mahima Sonakiya Dubey**, **Ms. Namrta Patidar, Mr. Rahul Prajapati** and each and every one of my friends. There have been so many of you – it is impossible to name all of you.

I am indebted to my seniors, lab mates and colleague researchers especially **Dr. Kishore Shingare, Mr. Subhash Nevhal, Mr. Nitin Luhadiya, Mr. Rajnish Prakesh Modanwal, Mr. Saurabh Mishra, Mr. Anas Ullah Khan, Ms. Nilima Sinha and Mr. Vaibhav Nemane** for their cooperation and stay so as to make my Ph.D. journey joyful and with whom I have spent so much time discussing both technical and non-technical stuff.

This acknowledgment would not be complete without mentioning the pain staking efforts and patience of my family. No words are adequate to express my indebtedness to my father **Mr. Mahesh Kumar Gupta** and my mother **Mrs. Mrinalini Gupta** for their support, blessings, and good wishes. Thank you to my sweet younger sister, **Ms. Meha Gupta**, for always being there for me and for always cheering me up. I owe this thesis to my grandparents, my parents, my sister and other family members who always stood by me and provided strength in pursuing this work. This achievement of my life would not be possible without their support and cooperation throughout this study. Finally, I am thankful to all who directly or indirectly contributed, helped and supported me.

Lastly, I express my hearty thanks to those whom I might have missed to mention by name, who helped directly or indirectly and cooperated me a lot in completion of this Ph.D. research work.

-Madhur Gupta

Indian Institute of Technology Indore

Date: November 10, 2022

Dedicated To

My Beloved Family

Mother, Father and Sister for their love, care, and blessings

SYNOPSIS

1 Introduction

The laminated composite materials have been extensively used in almost all engineering applications such as space structures, robotic manipulators, aerospace structures due to their remarkable mechanical properties, light-weight, and high performance. These multilayered structures consist of relatively thin layers of different material compositions which may influence the different degrees of axial compliance. As a result, the axial displacement of anisotropic structures varies nonlinearly along the thickness of the structure. In a general layer-wise formulation, the axial displacement field could be modeled as a piecewise continuous function, that is, a collection of linear functions defined for each layer of the thin structure. The responses of the laminated composite structures have been accurately studied by many researchers by the use of different theories like the first-order shear deformation theory **(FSDT)** and higher-order shear deformation theory **(HSDT)**, and mixed variational theories (Reddy and Phan, 1985; Narita et al., 1993; Eisenberger et al., 1995). The low values of transverse to in-plane modulus result in higher transverse shear resulting in the zig-zag effect, which needs to be accounted for. The zig-zag effect considerations lead to many advantages like the degrees of freedom **(DOF)** becoming layer independent resulting in the use of fewer numbers of variables and hence reduction in the overall computation time. In addition, the zig-zag function vanishes at the top and bottom surfaces of the plate, thus the full shear-stress continuity across the depth of the multilayered plate is not required. To overcome these drawbacks the early efforts of Di Sciuva (1985) and Murakami (1986) employed zig-zag-like displacement fields that satisfy a priori the transverse shear stress and displacement continuity conditions at the layer interfaces while keeping the number of kinematic variables independent of the number of layers.

The low damping nature of the laminated composite structures poses a threat of vibration-induced failures and hence to address this issue a concept called laminated smart structure has been developed. These types of structures usually comprise a laminated substrate member (either beam, plate, or shell) embedded with smartness adding material like the piezoelectric material. When this smart material is supplied with a control voltage, the enhancement in damping of the entire structure is observed which makes the overall structure safe during operation (Bailey and Ubbard, 1985; Ray et al., 1993). The fiber form of piezoelectric material reinforced in the conventional epoxy form a new material class called the piezoelectric composite **(PZC)** and piezoelectric fiber-reinforced composite **(PFRC)**. **1–3 PZC** material, which is commercially available is a type of **PFRC** that has profound use in investigating the damping characteristics of structures. To enhance their performance, it is observed that when this material is used in unison with the viscoelastic material, the host structures exhibit the active (voltage $\neq$ 0) and passive (voltage = 0) behavior. The unison of such materials resulted in a new concept material system developed by Baz called the active constraining layer damping **(ACLD)** (Baz and Ro, 1995b). Ray and Pradhan (2006) studied the active damping performance of the smart piezoelectric structures integrated with the **ACLD** treatment, observing that a **1–3 PZC** layer effectively attenuates the vibrations of composite structures. Kundalwal and Ray (2016) developed a finite element **(FE)** model to investigate the damping behavior of a smart fuzzy fiber-reinforced composite **(FFRC)** integrated with **ACLD** treatment layer constraining **1–3 PZC** material employing **FSDT**.

Carbon nanotubes **(CNTs)** have attracted the great attention of researchers to predict their thermo-mechanical properties since their discovery in 1991 by Iijima (1991). Treacy et al. (1996) experimentally found that the **CNT** possesses extraordinarily high Young's modulus in the range of tera-pascal **(TPa)** range which led to the theoretical/numerical investigations of unique thermo-mechanical and other properties of different types of **CNTs** (Shen and Li, 2004; Gupta et al., 2010). Owing to their extraordinary thermo-mechanical and physical properties, nanoscale **CNTs** can be utilized as nano-fillers in the conventional composite to modify its overall behavior. Such multiscale composite can be termed as hybrid composite comprised of primary microscale fibers and secondary nanoscale **CNTs** embedded in the matrix. In recent advances, the research activities in the field of composites have shown that the **CNT**-based hybrid composite can be fabricated easily in view of matured fabrication techniques and commercially available cheaper **CNTs**. On this basis, some attempts were made to investigate the dynamic/damping performance of **CNT**-based hybrid composite structures. Deepak et al. (2012) investigated the free vibrations and wave propagation of the **CNT** reinforced polymer composite rotating beam and observed that incorporation of **CNTs** in the polymer matrix improves the performance of the composite beam. Kundalwal and Ray (2016) studied the active damping characteristics of fuzzy-fiber reinforced composite **(FFRC)** plates attached with **ACLD** patches. They found that the waviness of the **CNTs** significantly influences the damping performance and natural frequency of the **FFRC** plate. Kumar et al. (2017) investigated the non-linear vibrations of the sandwich shell with facing compostед of **FFRC** using a **FE** model based on the Golla-Hughes−McTavish **(GHM)** method. Sciuva and Sorrenti (2019) developed a **FE** model using a refined zig-zag theory to investigate the static and dynamic analysis of **FG-CNTR** sandwich plates. Mallek et al. (2021) carried out a non-linear dynamic analysis of piezo-laminated functionally graded carbon nanotube-reinforced **(FG-CNTR)** composite shell using an improved **FSDT**.

From the reviewed literature, it can be observed that the dynamic analysis and active control of **CNT**-based hybrid carbon fiber reinforced composite structures have been reported in some of the studies. To the best of current authors' knowledge, the dynamic analysis and active control of **CNT**-based hybrid carbon fiber reinforced composites structures (beams, plates, and shells) based on the refined **FSDT** by incorporating the Murakami Zig-Zag theory is not yet explored. A laminated composite structure is an important building block element and hence, the present research is directed to study the active damping performance of laminated multiscale hybrid fiber-reinforced composites **(HFRC)** structures such as beam, plate, and shell. For this, the damping performance of smart laminated **HFRC** substrate structures is investigated via the **FE** approach using piece-wise modified **FSDT** incorporating zig-zag function. The multiscale substrate structure is embedded with **ACLD** treatment patches at the top surface. A closed-loop model to supply control voltage to the **ACLD** treatment patch is also presented based on simple velocity feedback control law. The comparison of the frequency response of the laminated **HFRC** with base composite plates is analyzed considering three cases: symmetric and anti-symmetric cross-ply, and anti-symmetric angle-ply.

2 Summary of the Present Work

This Section summarizes the research work carried out for the Thesis. The problem statements and the salient results of the problems are presented below.

2.1 Micromechanical Analysis of a Multiscale Hybrid Fiber Reinforced Composite

In this section, the effective elastic properties of the multiscale **HFRC** lamina are estimated by using the two- and three-phase micromechanical model based on the **MOM** and **MT** approach. A novel **HFRC** is composed of **CNTs** embedded in the matrix phase of a conventional epoxy/carbon fiber reinforced composite by considering the rectangular representative volume elements **(RVEs)** incorporated with cylindrical fibers. In this micromechanical analysis, we restricted ourselves to a single **RVE**. Figure 1(a) represents the schematic of **HFRC** lamina reinforced with carbon fiber in **1-**axis and epoxy matrix mixed with **CNT** to improve damping and material properties of the matrix. The axial and transverse cross-sections of the **HFRC RVE** are illustrated in Fig. 1(b), respectively. The analytical model based on the **MOM** and **MT** approach for predicting the effective elastic properties of **HFRC** is now briefly discussed here, and the two-phase analytical models and analytical model for predicting the influence of waviness on the effective elastic properties of **HFRC** are not presented here for the sake of brevity and are presented in the Thesis.

2.1.1 Three-Phase MOM Approach

The problem coordinate and principal material coordinate systems are represented by **1-2-3** and **x-y-z**, respectively. For the three-phase composite material which is also known as a hybrid composite material, the constitutive relation for the individual phases of **HFRC** can be expressed as:

$$\{\boldsymbol{\sigma}^r\} = [\boldsymbol{C}^r]\{\boldsymbol{\varepsilon}^r\};\ \boldsymbol{r} = \boldsymbol{CF}, \boldsymbol{CNT}\ \boldsymbol{and}\ \boldsymbol{Exy} \tag{1}$$

where the superscripts **CF**, **CNT**, and **Exy** denote carbon fiber, **CNT** nanofiller, and epoxy matrix, respectively. To satisfy no slippage condition between all individual phases, the assumption of iso-field and **ROM** can be expressed as:

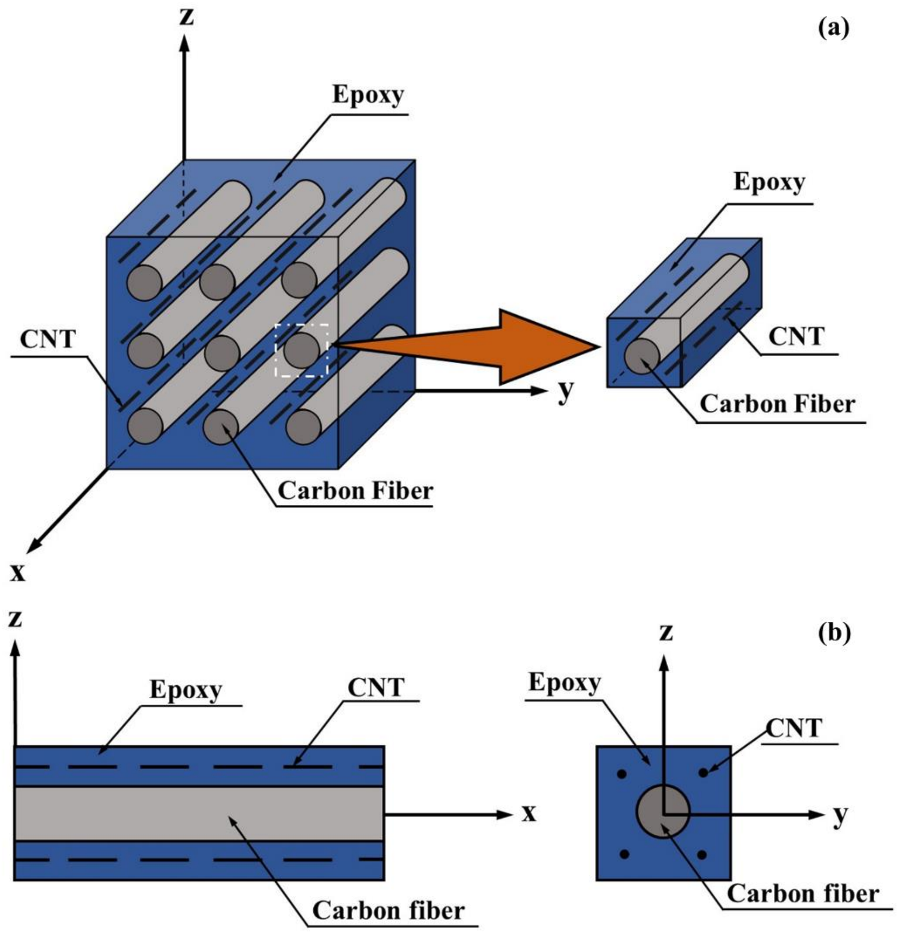

Figure 1. (a) Schematic of **RVE** of **HFRC**; (b) axial and transverse cross-sections of three-phase **RVE**.

In the case of iso-field condition:

$$\begin{Bmatrix} \varepsilon_{11}^{CF} \\ \sigma_{22}^{CF} \\ \sigma_{33}^{CF} \\ \sigma_{23}^{CF} \\ \sigma_{13}^{CF} \\ \sigma_{12}^{CF} \end{Bmatrix} = \begin{Bmatrix} \varepsilon_{11}^{CNT} \\ \sigma_{22}^{CNT} \\ \sigma_{33}^{CNT} \\ \sigma_{23}^{CNT} \\ \sigma_{13}^{CNT} \\ \sigma_{12}^{CNT} \end{Bmatrix} = \begin{Bmatrix} \varepsilon_{11}^{Exy} \\ \sigma_{22}^{Exy} \\ \sigma_{33}^{Exy} \\ \sigma_{23}^{Exy} \\ \sigma_{13}^{Exy} \\ \sigma_{12}^{Exy} \end{Bmatrix} = \begin{Bmatrix} \varepsilon_{11} \\ \sigma_{22} \\ \sigma_{33} \\ \sigma_{23} \\ \sigma_{13} \\ \sigma_{12} \end{Bmatrix} \tag{2}$$

and in case of **ROM** condition:

$$v_{CF}\begin{Bmatrix}\sigma_{11}^{CF}\\ \varepsilon_{22}^{CF}\\ \varepsilon_{33}^{CF}\\ \varepsilon_{23}^{CF}\\ \varepsilon_{13}^{CF}\\ \varepsilon_{12}^{CF}\end{Bmatrix}+v_{CNT}\begin{Bmatrix}\sigma_{11}^{CNT}\\ \varepsilon_{22}^{CNT}\\ \varepsilon_{33}^{CNT}\\ \varepsilon_{23}^{CNT}\\ \varepsilon_{13}^{CNT}\\ \varepsilon_{12}^{CNT}\end{Bmatrix}+v_{Exy}\begin{Bmatrix}\sigma_{11}^{Exy}\\ \varepsilon_{22}^{Exy}\\ \varepsilon_{33}^{Exy}\\ \varepsilon_{23}^{Exy}\\ \varepsilon_{13}^{Exy}\\ \varepsilon_{12}^{Exy}\end{Bmatrix}=\begin{Bmatrix}\sigma_{11}\\ \varepsilon_{22}\\ \varepsilon_{33}\\ \varepsilon_{23}\\ \varepsilon_{13}\\ \varepsilon_{12}\end{Bmatrix} \tag{3}$$

where v_{CNT} denotes the volume fraction of the **CNT**.

Finally, the effective elastic properties of **HFRC** can be expressed as:

$$[C]=[C_1][V_5]^{-1}+[C_7][V_6]^{-1} \tag{4}$$

2.1.2 Three-Phase MT Approach

The effective elastic properties of such multiscale **HFRC** can be determined using the three-phase **MT** model, as follows:

$$[C]=\left[v_m[C^m][I]+v_f[C^f][A_f]+v_i[C^i][A_i]\right]\left[v_m[I]+v_f[A_f]+v_i[A_i]\right]^{-1} \tag{5}$$

in which v_m, v_i and v_f denote the volume fractions of the epoxy matrix, **CNT** nanofiller, and carbon fiber, respectively. The terms $[A_{CF}]$ and $[A_{CNT}]$ appearing in Eq. (5) represent the concentration factors, as follows:

$$[A_f]=\left[[I]+[S_f]\{([C^m])^{-1}([C^f]-[C^m])\}\right]^{-1}$$

$$[A_i]=\left[[I]+[S_i]\{([C^m])^{-1}([C^i]-[C^m])\}\right]^{-1} \tag{6}$$

where $[S_f]$ and $[S_i]$ are the Esheby tensors for the **CF** and **CNT** phases, respectively (Qiu and Weng, 1990); and $[I]$ is an identity matrix. For the sake of simplicity, the **CNT** is assumed as an equivalent solid cylinder fiber (Kundalwal, 2017).

Figure 2 demonstrates the comparison of the values of effective longitudinal and transverse elastic constants (C_{11} and C_{33}) against the carbon fiber volume fraction (v_{CF}) of the **HFRC** incorporating 0.1 volume fraction of **CNT** (v_{CNT}). It can be observed from Figs. 2(a–b) that due to the incorporation of **CNTs**, the effective elastic properties of the

HFRC lamina show substantial improvement as compared to the base composite. It can also be observed that both **MOM** and **MT** models show good agreement. Figure 2(c) illustrates the variation of longitudinal elastic coefficient C_{11} of different cases: **HFRC** with straight (n = 0) and wavy **CNTs** in **1–2** and **1–3** planes. It can be observed that the C_{11} linearly varies with v_{CF} because the carbon fibers are oriented along the x-axis of **HFRC**. This is attributed to the iso-strain condition imposed on constituents and, thus, the strain induced in the x-direction of **HFRC** composite is equal to that of matrix and fibers. Figure 2(c) also depicts that the magnitude of C_{11} for wavy **CNT** case is lower compared to the straight **CNT** case. This is attributed to the fact the load-bearing capacity of the **CNT** reduces due to waviness.

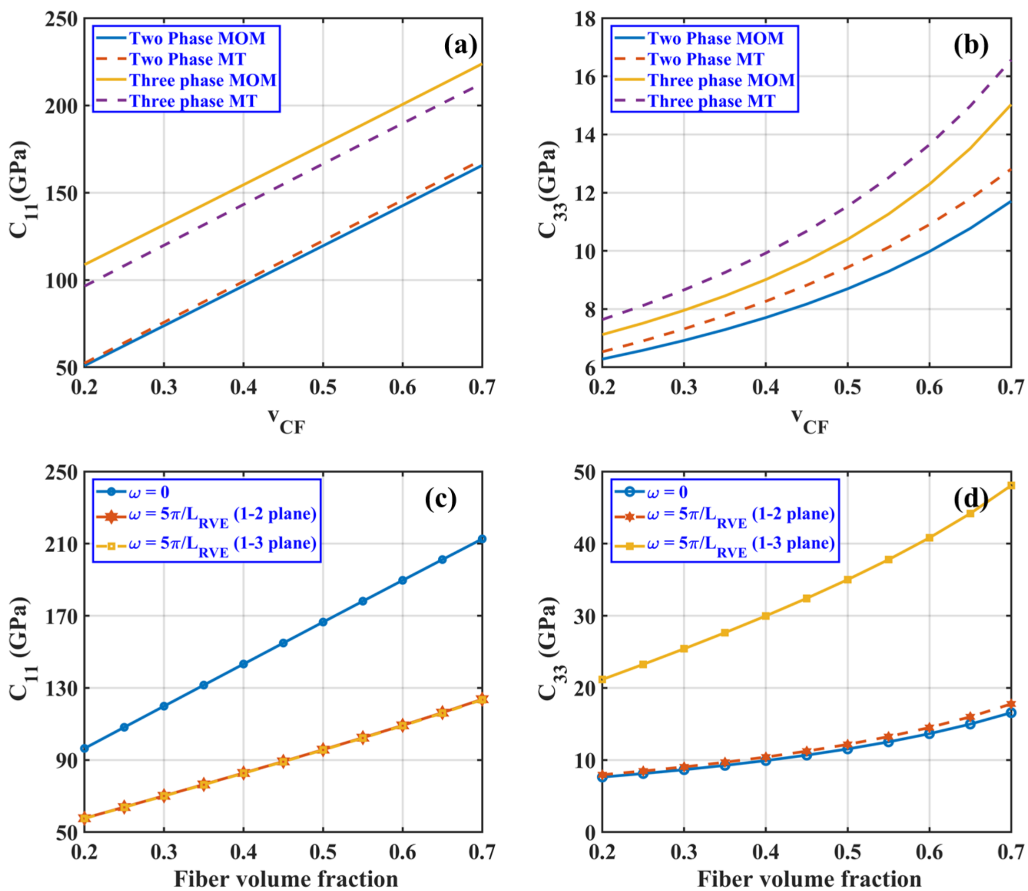

Figure 2. Variation of the effective longitudinal elastic constant (C_{11}) and transverse elastic constant (C_{33}) with respect to the volume fraction of carbon fiber.

Figure 2(d) demonstrates the variation of transverse elastic coefficient $\boldsymbol{C_{33}}$ for different cases, which demonstrates the substantial improvement in the value of $\boldsymbol{C_{33}^{MSC}}$ when **CNT** waves are coplanar with the **1–3** plane. This is due to the fact that the transformed value of $\boldsymbol{C_{33}^{MSC}}$ improves with the amplitude of **CNT** waves coplanar with the **1–3** plane. Next, the obtained effective properties of **HFRC** are used for studying the active damping characteristics of the smart beam, plate, and shell with multiscale **HFRC** as a host structure.

2.2 Active Vibration Damping of Smart Multiscale Hybrid Fiber Reinforced Composite Beams Using 1–3 Piezoelectric Composites

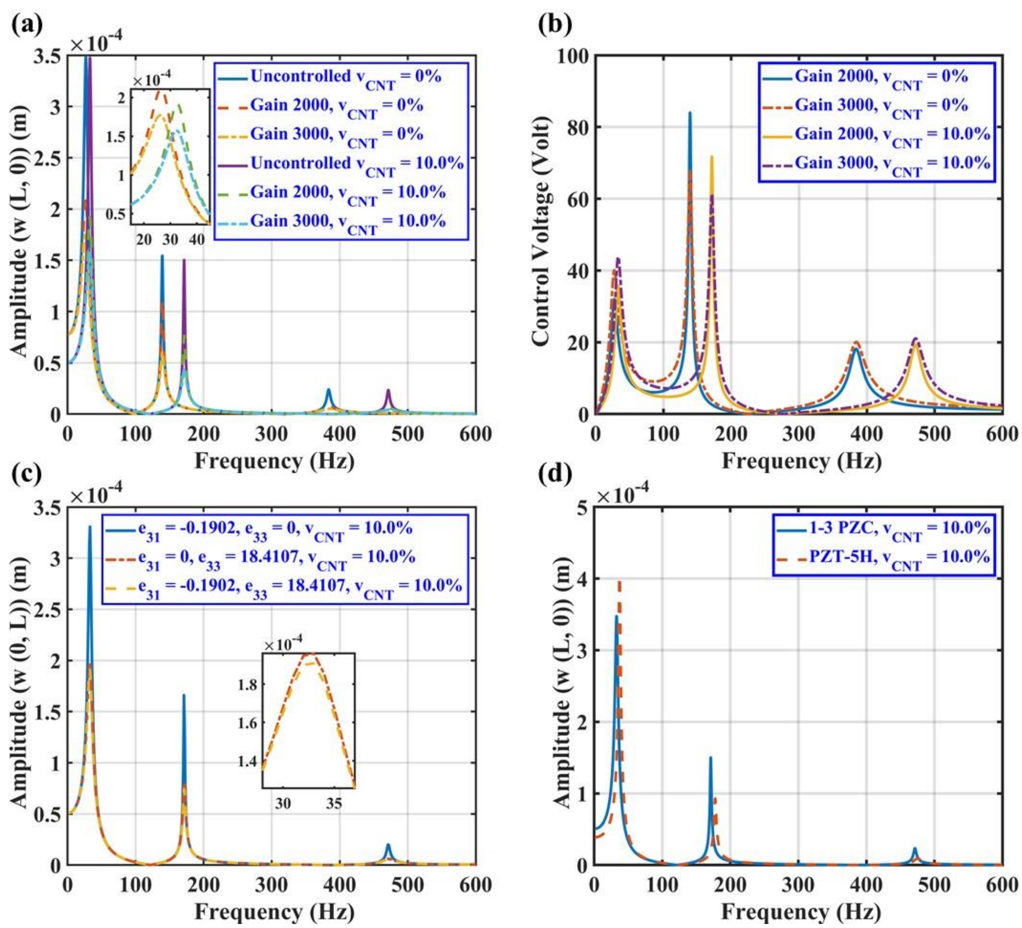

Figure 3. Variation of (a) amplitude of deflection, (b) control voltage, (c) piezoelectric coefficient, and (d) **1–3 PZC** of 0°/90°/0° multiscale **HFRC** substrate beam with frequency response.

In this study, an attempt has been made to investigate the active damping performance of multiscale **HFRC** substrate beam constraining the layer of an **ACLD** treatment using an in-house **FE** model based on **FSDT**. The **ACLD** treatment layer is installed at the top surface of the host structure covering its 3/5 surface area from the fixed end. The effect of in-plane and transverse-plane actuation of the integrated **ACLD** treatment layer on the damping characteristics of the novel smart cantilever **HFRC** beam is considered. The parameters affecting the damping characteristics of the **HFRC** substrate beam such as the volume fraction of both **CNTs** and carbon fiber, and the aspect ratio are also studied. Figure 3(a-b) demonstrates the vibrational amplitudes and control voltage of the base composite and **HFRC**. It can be observed that the **HFRC** shows better damping performance and required less control voltage compared to the base composite.

Figure 3(c) illustrates that the piezoelectric coefficient significantly influences the control authority of the **ACLD** patches. It can be concluded that the constraining layer of **ACLD** is mainly responsible for the attenuation of vertical shear deformation. This also means that the out-of-plane actuation has a much higher contribution in vibration attenuation than the in-plane actuation of the laminated smart beam. Whereas it can be observed from Fig. 3(d) that the performance of tailor-made **1–3 PZC** shows better transverse vibration attenuation compared to the conventional monolithic piezoelectric material.

2.3 Active Vibration Damping of a Simply Supported Smart Multiscale Hybrid Fiber Reinforced Composite Plates Using 1–3 Piezoelectric Composites

A **FE** model is developed based on the **FSDT** considering the zig-zag theory which acts as a natural extension to **FSDT** to investigate the active damping performance of the laminated multiscale **HFRC** substrate with two **ACLD** treatment layers attached at the top surface host structure. The multiscale **HFRC** plate is subjected to the simply-supported **(SS)** boundary conditions. Figure 4(a-b) demonstrates the active damping performance of **SS** symmetric cross-ply base composite and **HFRC** square plates and the required control voltage to achieve the corresponding vibration attenuation.

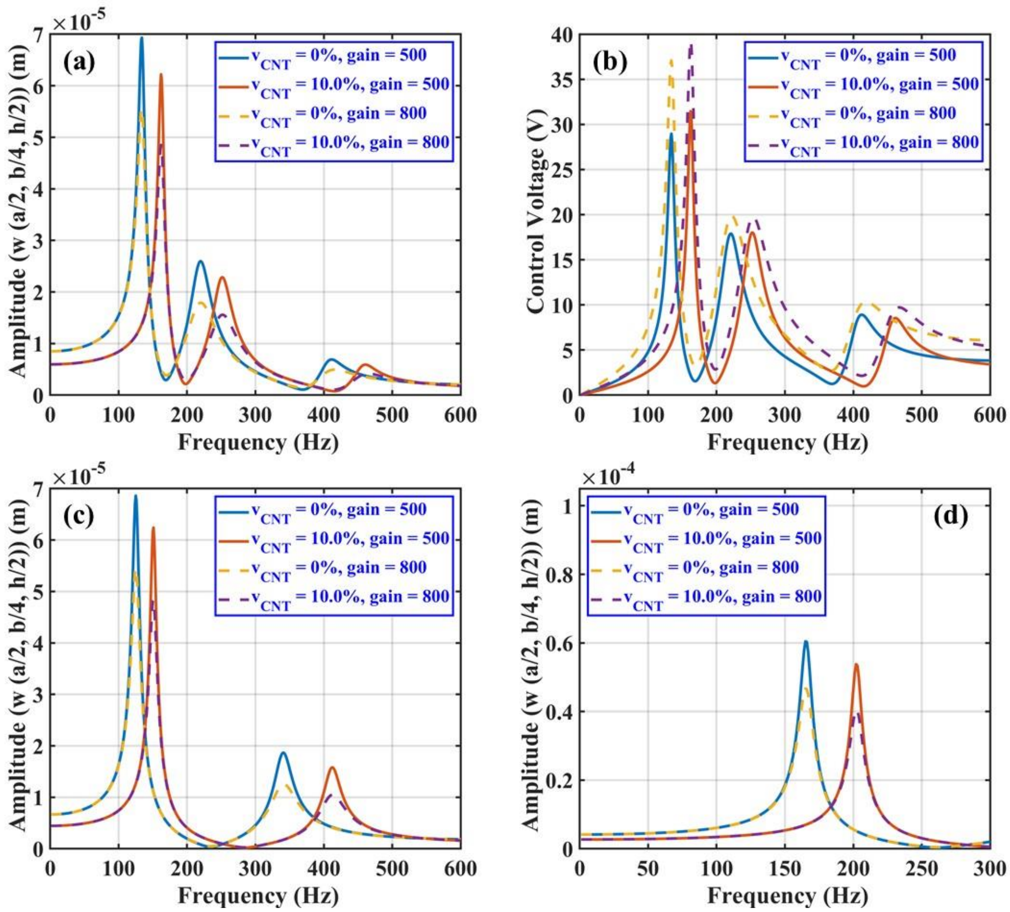

Figure 4. Variation of the amplitude of deflection and control voltage vs frequency response of **SS** laminated **HFRC** plates: (a, b) $0°/90°/0°$, (c) $0°/90°/0°/90°$, and (d) $-45/45°/-45°/45°$.

It can be observed from Fig. 4(a) that the multiscale **HFRC** shows higher vibration attenuation compared to the base composite for all the values of gain ($\boldsymbol{k_d} = 500 \text{ and } 800$). To achieve the following vibration attenuation the required control voltage is shown in Fig. 4(b). Here, we can observe that the maximum required control voltage is $\sim 37\ \boldsymbol{V}$, which is in the practical range and could be easily achievable. Similar to Fig 4(a), the variation of frequency response with the amplitudes of vibration for anti-symmetric cross-ply and anti-symmetric angle-play is shown in Fig. 4(c-d), respectively. These figures display that both anti-symmetric cross-ply and anti-symmetric angle-ply laminated **HFRC** plate shows better damping characteristics due to the incorporation of **CNTs** in terms of attenuation of amplitudes and enhancement in the first mode natural frequencies.

2.4 Active Vibration Damping of a Clamped-Clamped Smart Multiscale Hybrid Fiber Reinforced Composite Plates Using 1–3 Piezoelectric Composites

Based on a piece-wise continuum **FSDT** incorporating the zig-zag function the **FE** model is developed to investigate the effect of **CNT** waviness on the damping performance of the laminated multiscale **HFRC** smart plate. In addition, the effect of piezoelectric fiber orientation of **1–3 PZC** on the control authority of the **ACLD** treatment layer is also examined. For this, the **MOM** model is derived to evaluate the effective elastic properties of **1–3 PZC** for various fiber orientations. For the sake of brevity, the **FE** and **MOM** models are not shown here. It can be seen from Fig. 5(a) that the symmetric cross-ply laminated **HFRC** plate with **CNT** waves coplanar with the **1–3** plane significantly attenuates the amplitudes of vibration compared to the other cases of laminated plates (with or without **CNTs**). This is attributed to the enhanced transverse stiffness of the multiscale **HFRC** substrate due to the waviness of **CNT** in the **1–3** plane. Thus, the energy dissipation capability of the multiscale **HFRC** plate is high, and it significantly attenuates the transverse vibrations. Further analysis is carried out for anti-symmetric cross-ply plates, and Fig 5(b) shows that the multiscale **HFRC** plates with **CNT** waves coplanar with the **1–3** plane have better vibration attenuating capability compared to the other cases.

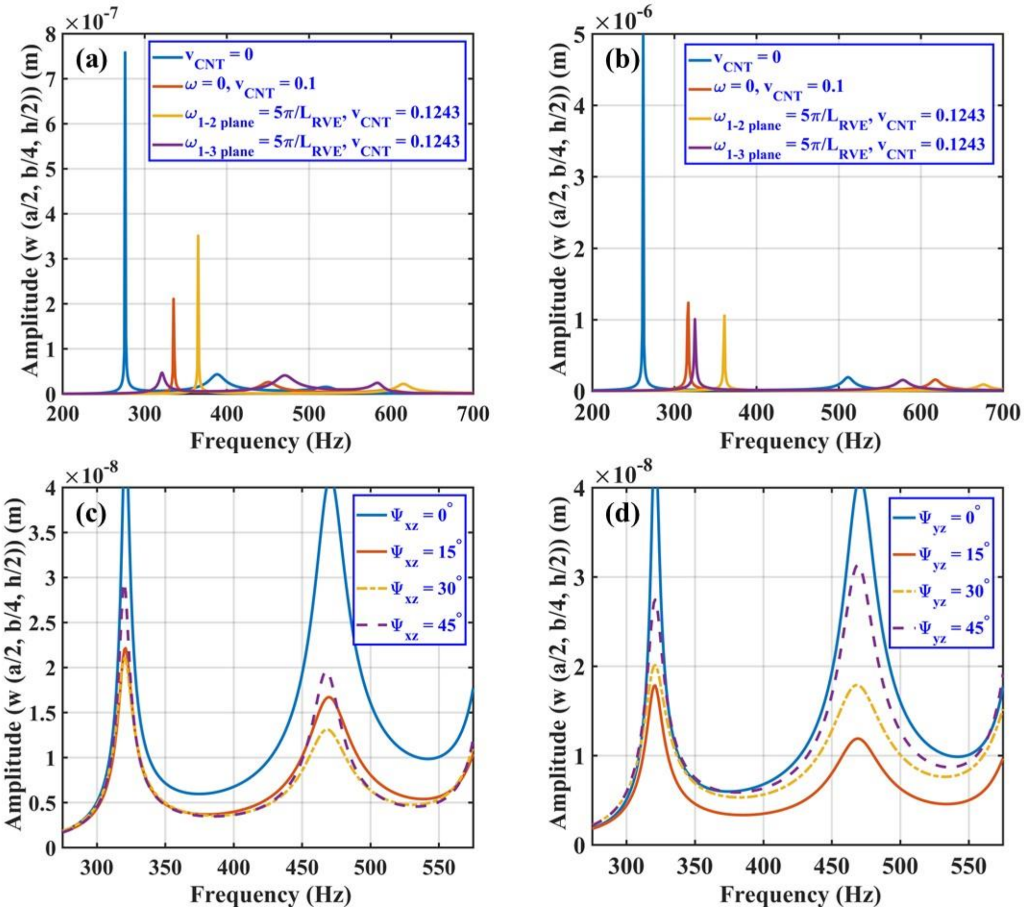

Figure 5. Frequency response of (a) $0°/90°/0°$, (b) $0°/90°/0°/90°$ and effect of piezo-fiber orientation ($\boldsymbol{\Psi}$) in the ***xz***- and ***yz***-planes on the frequency response of (c–d) $0°/90°/0°$ **HFRC** plates when $\boldsymbol{k_d}$ = 600.

2.5 Active Vibration Damping of a Clamped-Free Smart Multiscale Hybrid Fiber Reinforced Composite Shells Using 1–3 Piezoelectric Composites

In this study, a **FE** model is developed based on the sinusoidal shear deformation theory accounting for the Murakami zig-zag function to investigate the influence of **CNT** waviness on the damping performance of the laminated multiscale **HFRC** smart shell. The proposed theory is the modified form of **FSDT** which considers a sinus function to avoid the shear locking phenomenon. Whereas the Murakami zig-zag function accounts for the higher transverse shear resulting in the zig-zag effects. The zig-zag function also vanishes at the top and bottom surfaces of the structure, and thus, the full shear-stress continuity across the depth of the multilayered plate is not required.

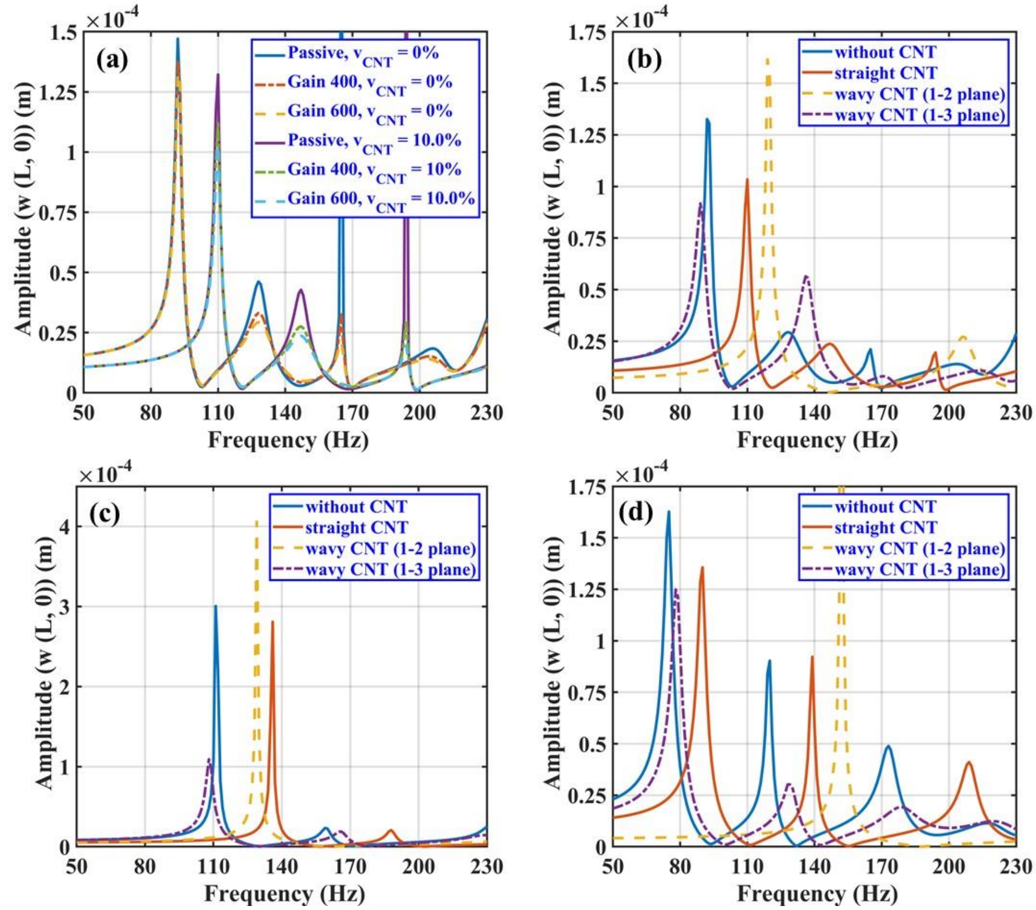

Figure 6. Variation of the amplitude of deflection with the frequency response of laminated **HFRC** smart shell (a, b) $0°/90°/0°$, (c) $0°/90°/0°/90°$, and (d) $-45/45°/-45°/45°$.

Figure 6(a) illustrates the comparison of amplitudes of the defection of symmetric cross-ply base composite and multiscale **HFRC** smart shells for the passive (uncontrolled, $\boldsymbol{k_d} = 0$) and active damping. It can be observed that the active damping significantly attenuates the amplitudes of vibration with multiscale **HFRC** shell showing better performance. Figure 6(b) demonstrates the influence of **CNT** waviness of the damping characteristics of the symmetric cross-ply multiscale **HFRC** shell. The figure depicts that **CNT** waviness shows significant effects on the damping performance of multiscale **HFRC** shell and the maximum attenuation is observed when the **CNT** waviness is coplanar with **1–3** plane. This is attributed to the fact that the transverse stiffness coefficient is enhanced substantially when **CNT** waviness is coplanar with **1–3** plane. Similar results are observed in the case of anti-symmetric cross-ply and anti-symmetric angle-ply. Among all the cases symmetric cross-ply multiscale **HFRC** shell with **CNT** waviness coplanar with **1–3** plane shows better results than the anti-symmetric cross-ply and anti-symmetric angle-ply. The effect of piezoelectric fiber orientation in ***xz*** and ***yz*** direction of **1–3 PZC** is also studied but for the sake of brevity, the results are not here and are presented in the Thesis.

TABLE OF CONTENTS

LIST OF FIGURES

LIST OF TABLES

List of Abbreviations and Symbols

ACLD	Active Constrained Layered Damping
ADF	Anelastic Displacement Fields
AFM	Atomic Force Microscopy
CC	Clamped-Clamped
CLT	Classical Laminate Theory
CNT	Carbon Nanotube
CVD	Chemical Vapor Deposition
DCEF	Damping Characteristic Enhancement Factor
DOF	Degrees of Freedom
ECM	Equivalent-Continuum Modeling
FE	Finite Element
FFRC	Fuzzy-Fiber Reinforced Composites
FRF	Frequency Response Function
FSDT	First-Order Shear Deformation Theory
GHM	Golla-Hughes-McTavish
GSD	Graphitic Structures by Design
HFRC	Hybrid Fiber-Reinforced Composites
HSDT	Higher-Order Shear Deformation Theory
LMS	Least Mean Square
MEE	Magneto Electro-Elastic
MOM	Mechanics of Material

MT	Mori-Tanaka
MWCNT	Multi-Walled Carbon Nanotube
MZZF	Murakami's Zig-Zag Function
PCLD	Passive Constrained Layer Damping
PECVD	Plasma Enhanced Chemical Vapor Deposition
PZCs	Piezoelectric Composites
RMT	Reissner Multilayered Theory
ROM	Rules of Mixture
RVE	Representative Volume Element
SEM	Scanning Electron Microscope
SFEM	Spectral Finite-Element Model
SinusZZ	Sinusoidal Shear Deformation Theory Incorporating the Murakami's Zig-Zag Function
SMEE	Skew Magneto-Electro-Elastic
SS	Simply Supported
SWCNT	Single-Walled Carbon Nanotube
TEM	Transmission Electron Microscopy
VE	Viscoelastic
ZZ	Zig-Zag
ZZTs	Zig-Zag Theories

1-2-3	Problem coordinate
3D	Three dimensional
$\boldsymbol{a_e}, \boldsymbol{b_e}$	Elemental length and width

$\boldsymbol{A}$	Surface area (m^2) of the substrate
$[\boldsymbol{A_1}]$, $[\boldsymbol{A_f}]$, $[\boldsymbol{A_i}]$	Concentration factor
$\boldsymbol{b}$	Width (m) of the substrate
$[\boldsymbol{B_{tb}}]$, $[\boldsymbol{B_{rb}}]$, $[\boldsymbol{B_{ts}}]$, $[\boldsymbol{B_{rs}}]$	Nodal strain-displacement matrices
$\boldsymbol{C_h}$	Chiral vector
$\boldsymbol{C_{ij}^{MSC}}$	Effective elastic coefficients of multiscale **HFRC**
$[\boldsymbol{C}]$	Stiffness matrix
$[\boldsymbol{\bar{C}_{ij}^{MSC}}]$	Average effective elastic coefficient matrix
$\boldsymbol{\bar{C}_{ij}^{k}}$	Transformed elastic stiffness constants
$\boldsymbol{d_n}$	Diameter of a **CNT** (nm)
$\{\boldsymbol{d_r}\}$	Rotational displacements (m)
$\{\boldsymbol{d_t}\}$	Translational displacements (m)
$\boldsymbol{D_z}$	Electric displacement ($\mathrm{C/m^2}$)
$[\boldsymbol{D_{tb}}]$, $[\boldsymbol{D_{trb}}]$, $[\boldsymbol{D_{rrb}}]$	Rigidity matrices associated with in-plane bending deformations
$[\boldsymbol{D_{ts}}]$, $[\boldsymbol{D_{trs}}]$, $[\boldsymbol{D_{rrs}}]$	Rigidity matrices associated with transverse shear deformations
$\boldsymbol{E}$	Young's moduli (GPa)
$\boldsymbol{E_z}$	Electric field (V/m)
$\{\boldsymbol{F}\}$	Global nodal force vector
$\{\boldsymbol{F^e}\}$	Elemental load vector
$\{\boldsymbol{F_{tp}}\}$, $\{\boldsymbol{F_{rp}}\}$	Global electro-elastic coupling matrices
$\{\boldsymbol{F_{tp}^e}\}$, $\{\boldsymbol{F_{rp}^e}\}$	Elemental electroelastic coupling vectors
$\boldsymbol{G}$	Shear moduli (GPa)

$\boldsymbol{G'}$	Storage modulus ($\mathrm{MNm^{-2}}$)
$\boldsymbol{h}$	Thickness (m) of the substrate beam
$\boldsymbol{h_p}$	Thickness (μm) of piezoelectric layer
$\boldsymbol{h_v}$	Thickness (μm) of **ACLD** treatment layer
$[\boldsymbol{I}]$	Identity matrix
$\boldsymbol{k_d}$	Control gain
$[\boldsymbol{K_{tt}}]$, $[\boldsymbol{K_{tr}}]$, $[\boldsymbol{K_{rt}}]$, $[\boldsymbol{K_{rr}}]$	Global stiffness matrices
$[\boldsymbol{K^e_{tt}}]$, $[\boldsymbol{K^e_{tr}}]$, $[\boldsymbol{K^e_{rt}}]$, $[\boldsymbol{K^e_{rr}}]$	Elemental stiffness matrices
$\boldsymbol{L}$	Length (m) of the substrate beam
$\boldsymbol{L_a}$	Length (m) of **ACLD** treatment layer
$\boldsymbol{L_{RVE}}$	Linear distance (nm) between the two ends of **CNT**
$\boldsymbol{L_{nr}}$	Running length (nm) of the **CNT**
$\boldsymbol{\bar{m}}$	Mass parameter
$[\boldsymbol{M}]$	Global mass matrix
$[\boldsymbol{M^e}]$	Elemental mass matrix
$\boldsymbol{n}$	Number of waves of the **CNT**
$[\boldsymbol{S}]$, $[\boldsymbol{S_f}]$, $[\boldsymbol{S_i}]$	Eshelby tensor
$\boldsymbol{u_0}, \boldsymbol{v_0}, \boldsymbol{w_0}$	Generalized translational displacement (m) at any point on the reference plane in x, y and z directions
$[\boldsymbol{U^j_t}]$, $[\boldsymbol{U^j_r}]$	Unit vectors for the transverse velocity
x-y-z	Principal material coordinate

$\{\boldsymbol{X_r}\}, \{\boldsymbol{X}\}$	Global nodal rotational
$\boldsymbol{\nu}$	Poisson's ratio
$\boldsymbol{v_{Exy}}$	Volume fraction of epoxy matrix
$\boldsymbol{v_{CF}}$	Volume fraction of carbon fiber
$\boldsymbol{v_{CNT}}, \boldsymbol{v_i}$	Volume fraction of **CNT**
$\boldsymbol{\rho^k}$	Mass density $(\mathrm{kg/m^3})$
$\boldsymbol{\Omega}$	Volume of the substrate, **ACLD** treatment layer and 1–3 **PZC**
$\boldsymbol{\eta}$	Loss factor
$\boldsymbol{\theta_x}, \boldsymbol{\phi_x}, \boldsymbol{\gamma_x}$	Generalized rotations (rad) of the normals to the mid planes of the **HFRC** substrate, the **ACLD** layer, and the **1–3 PZC** layer, respectively about y-axis
$\boldsymbol{\theta_y}, \boldsymbol{\phi_y}, \boldsymbol{\gamma_y}$	Generalized rotations (rad) of the normals to the mid planes of the **HFRC** substrate, the **ACLD** layer, and the **1–3 PZC** layer, respectively about x-axis
$\boldsymbol{\theta_z}, \boldsymbol{\phi_z}, \boldsymbol{\gamma_z}$	Gradients (rad) of the transverse deformations of the **HFRC** substrate, the **ACLD** layer, and the **1–3 PZC** layer, respectively about z-axis
$\{\boldsymbol{\sigma}\}$	Stress vector
$\boldsymbol{\sigma_x}, \boldsymbol{\sigma_y}, \boldsymbol{\sigma_z}$	Normal stresses (GPa)
$\boldsymbol{\sigma_{xy}}, \boldsymbol{\sigma_{xz}}, \boldsymbol{\sigma_{yz}}$	In-plane and out-of-plane shear stresses (GPa)
$\{\boldsymbol{\varepsilon}\}$	Strain vector
$\boldsymbol{\epsilon_x}, \boldsymbol{\epsilon_y}, \boldsymbol{\epsilon_z}$	In-plane normal strains
$\boldsymbol{\epsilon_{xy}}, \boldsymbol{\epsilon_{xz}}, \boldsymbol{\epsilon_{yz}}$	In-plane and out-of-plane shear strains
$\{\boldsymbol{\epsilon_b}\}_p, \{\boldsymbol{\epsilon_b}\}_v, \{\boldsymbol{\epsilon_b}\}_c$ $\{\boldsymbol{\epsilon_s}\}_p, \{\boldsymbol{\epsilon_s}\}_v, \{\boldsymbol{\epsilon_s}\}_c$	Elemental strains vectors expressed in terms of nodal displacement vectors

$\boldsymbol{\Psi}$	Piezoelectric fibers orientation angle (rad)
$\boldsymbol{\omega}$	Wave frequency (Hz)

Abstract

Owing to their unique structure, carbon nanotubes (**CNTs**) exhibit unprecedented physical and mechanical properties, **CNTs** emerged as promising reinforcement with potential benefits in the engineering applications such as nano/micro-electromechanical systems **NEMS/MEMS**, and structural health monitoring (**SHM**) systems. An overview of the literature revealed that **CNTs** can be incorporated to improve the structural damping of composite structures as **CNT** reinforcement improves the strength and stiffness of the composite structures. With the advancement in nanotechnology, nanofibers like **CNTs** can be utilized along with conventional fibers for the development of advanced hybrid composite materials. Such composites are known as multiscale composites that are reinforced with nanoscale materials along with macroscale fibers. These multiscale composites have potential applications in almost every field due to their remarkable features like extraordinary mechanical properties, uniformity, flexibility, and stability of the fibers. In this context, we proposed a **CNT**-based hybrid fiber-reinforced composite (**HFRC**) material. The **HFRC** is composed of **CNT** nanofillers and carbon fibers uniformly distributed along the longitudinal direction in the polymer matrix phase. The effective elastic properties of multiscale **HFRC** are required prior and therefore, these properties were evaluated as the literature does not provide the same. For this, analytical micromechanical models are developed for predicting the effective elastic properties of **HFRC** which can be utilized for the active damping analysis of laminated **HFRC** smart structures. The objective of the present work is to develop a finite element (**FE**) model to investigate the active vibrational damping of multiscale **HFRC** smart structures such as beams, plates, and shells by utilizing the layerwise shear deformation theory considering the zig-zag (**ZZ**) effects.

In this dissertation, two- and three-phase micromechanical models based on the mechanics of materials (**MOM**) and Mori-Tanaka (**MT**) approaches are developed to predict the effective elastic properties of the base composite (without **CNTs**) and the **HFRC** with straight and wavy **CNTs**. The distinctive feature of novel **HFRC** is that the

wavy/straight **CNTs** are distributed uniformly in the matrix phase of hybrid carbon fiber-reinforced composites, and the waviness of **CNTs** is considered to be coplanar with two mutually orthogonal planes. The predictions by both the models are found to be in good agreement and we observed that due to the incorporation of **CNTs** the effective elastic properties of **HFRC** lamina show significant enhancement compared to base composite. The effects of waviness of **CNTs** on the effective elastic properties of the **HFRC** is also investigated when the wavy **CNTs** are coplanar with either of the two mutually orthogonal planes. It is found that the transverse effective elastic properties of **HFRC** containing wavy **CNTs** are significantly improved while the longitudinal elastic properties of the **HFRC** are decreased compared to that of the composite with and without the straight **CNTs**. It is also revealed that increasing the **CNT** waves results in drastic improvement in the transverse effective elastic properties of **HFRC**.

Finally, laminated multiscale **HFRC** beams, plates, and shells are considered for the analysis of the active constrained layer damping (**ACLD**) of vibrational amplitudes of deformation. The constraining layer of the **ACLD** treatment is considered to be composed of the vertically/obliquely reinforced **1–3** piezoelectric composite (**PZC)** material. Based on the layerwise displacement theories and incorporating the **ZZ** effects, three-dimensional (**3D**) electro-mechanical **FE** models of the overall beams, plates, and shells integrated with the patches of the **ACLD** treatment have been developed. A closed-loop model to supply control voltage to the **ACLD** treatment patch based on simple velocity feedback control law to activate the **ACLD** treatment patches is also presented. Frequency response function **(FRF)** curves are derived to determine the level of the amplitude of the uncontrolled response. The analyses reveal that the **ACLD** treatment in which the constraining layer is made of the obliquely reinforced **1-3 PZC** maximizes the damping characteristics of the laminated **HFRC** smart plates while the constraining layer composed of the vertically reinforced **1–3 PZC** maximizes the controllability of the **ACLD** treatment for causing active vibrational damping of the doubly curved laminated **HFRC** smart shells. The investigation also reveals that for the laminated **HFRC** beams, plates, and shells with straight or wavy **CNT**s, the performance of the **ACLD** treatment increases as compared to that without **CNT**s. More importantly, it is found that the performance of the **ACLD** treatment is better in the case of controlling the vibrational amplitudes of the **HFRC** plates and shells with wavy **CNT**s than that in the case of controlling the same with straight **CNT**s. Thus, it is suggested that the wavy **CNT**s can be properly exploited to gain structural benefits from the exceptional properties of **CNT**s and develop high-performance smart structures superior to the existing ones.

Keywords: *Carbon nanotubes; Multiscale composite;* ***ACLD*** *patches; Smart structures; Finite element model; Active damping;* ***1-3*** *piezoelectric composite; Vertically/obliquely piezoelectric fibers.*

Chapter 1

Introduction and Literature Review

*In this Chapter a brief introduction to the carbon nanotube **(CNT)** and the concept of estimations of **CNT** properties and **CNT**-reinforced composite materials, multiscale composites, smart structures, active constrained layered damping (**ACLD**) treatment, piezoelectric composites (**PZCs**) along with the review of literature have been discussed. Based on the review of literature, the scope for this dissertation has been identified and the objectives of the Thesis have been outlined. The organization of the Chapters has been delineated at the end of this Chapter.*

1.1 Carbon Nanotubes (CNTs)

The research on the synthesis of molecular carbon structure by an arc-discharge method for evaporation of carbon led to the discovery of an extremely thin needle-like graphitic carbon molecule knows as carbon nanotubes or **CNTs** in short (Iijima, 1991).

While examining under an electron microscope at the level of atomic resolution, Iijima (1991) observed that such needle-like carbon materials are seamless coaxial tubes made of carbon atom sheets. The thickness of the carbon atom sheet is less than a nanometer while the separation between the walls of the tubes is found to be 0.34 nm. The outer diameter of such needle-like material is in the range of few nanometers. Iijima (1991) named such needle-like carbon materials as multi-walled carbon nanotube (**MWCNT**).

Within a couple of years, Iijima and Ichihashi (1993) discovered the synthesis of single-walled carbon nanotube (**SWCNT**). The other manufacturing processes such as laser ablation, chemical vapor deposition (**CVD**) and plasma enhanced **CVD** (**PECVD**) are being employed to synthesize the **CNTs** in large scale (Pan *et al.*, 1999; Bower *et al.*, 2001; Thostenson *et al.*, 2002; Zhu *et al.*, 2003; Ci *et al.*, 2005; Chen *et al.*, 2006; Agnihotri *et al.*, 2011).

The length of a carbon nanotube produced by common production methods is often not reported but is typically much larger than its diameter. Thus, for many purposes, end effects are neglected, and the length of carbon nanotubes is assumed infinite.

Carbon nanotubes can exhibit remarkable electrical conductivity (Mintmire *et al.*, 1992; Tans *et al.*, 1997), while others are semiconductors (Hamada *et al*., 1992; Wildöer *et al.*, 1998). They also have exceptional tensile strength (Yu *et al.*, 2000) and thermal conductivity (Kim *et al.*, 2001; Sadri *et al.*, 2014) because of their nanostructure and strength of the bonds between carbon atoms. In addition, they can be chemically modified (Karousis *et al*., 2010). These properties are expected to be valuable in many areas of technology, such as electronics, optics, composite materials (replacing or complementing carbon fibers), nanotechnology, and other applications of materials science.

Rolling up a hexagonal lattice along different directions to form different infinitely long single-wall carbon nanotubes shows that all of these tubes not only have helical but also translational symmetry along the tube axis and many also have nontrivial rotational symmetry about this axis. In addition, most are chiral, meaning the tube and its mirror image cannot be superimposed. This construction also allows single-wall carbon nanotubes to be labeled by a pair of integers (Hamada *et al*., 1992).

1.1.1 Structure of CNT

A **CNT** is a cylindrical molecule composed of hexagonal array of carbon atoms. The constructional feature of the **CNT** structure corresponds to a hexagon pattern that repeats itself periodically in space. As a result of the periodicity, each carbon atom is bonded to three neighboring carbon atoms. The resulting structure is mainly due to the process of sp^2 hybridization forming three in-plane $\boldsymbol{\sigma}$ bonds with an out-of-plane $\boldsymbol{\pi}$ bond. The in-plane $\boldsymbol{\sigma}$ bond is a strong covalent bond that plays an important role in the impressive mechanical properties of **CNTs**. This $\boldsymbol{\sigma}$ bond is 0.14 nm long and 420 kcal/mol strong in sp^2 orbital. On the other hand, an out-of-plane $\boldsymbol{\pi}$ bond is relatively weak and contributes to the interactions between the layers in **MWCNTs** and in between **SWCNTs** in

SWCNT bundles while making **CNTs** more thermally and electrically conductive.

A **CNT** can be viewed as a hollow seamless cylinder formed by rolling a graphene sheet. A widely used approach to identify the types of **SWCNT** is due to the rolling direction of the rolled graphene sheet. The key geometric parameter associated with this process is the roll-up or the chiral vector $\boldsymbol{C_h}$, which can be expressed as the linear combination of the lattice bases ($\boldsymbol{a_1}$ and $\boldsymbol{a_2}$). Mathematically, the tube chirality can be defined in terms of the roll-up vector as follows:

$$\boldsymbol{C_h = ma_1 + na_2} \tag{1.1}$$

where the integers ***(m, n)*** are the number of steps along the zig-zig carbon bonds of the hexagonal lattice and $\boldsymbol{a}_1$ and $\boldsymbol{a}_2$ are unit basis vectors as shown in Fig. 1.1. The roll-up vector determines the direction of rolling a graphene sheet such that a lattice point (m, n) which is the terminus of the vector $\boldsymbol{C_h}$ is superimposed with the origin (0, 0) of the vector. Therefore, the diameter of a **CNT** can be expressed as

$$\boldsymbol{d_n = \frac{a\sqrt{m^2 + mn + n^2}}{\pi}} \tag{1.2}$$

where $\boldsymbol{a} = 1.42 \times \sqrt{3} \times 10^{-10}$ m corresponds to the lattice constant in the graphene sheet. Note that the distance between two covalently bonded carbon atoms (**C-C** distance) is 1.42×10^{-10} m for sp^2-hybridized carbon.

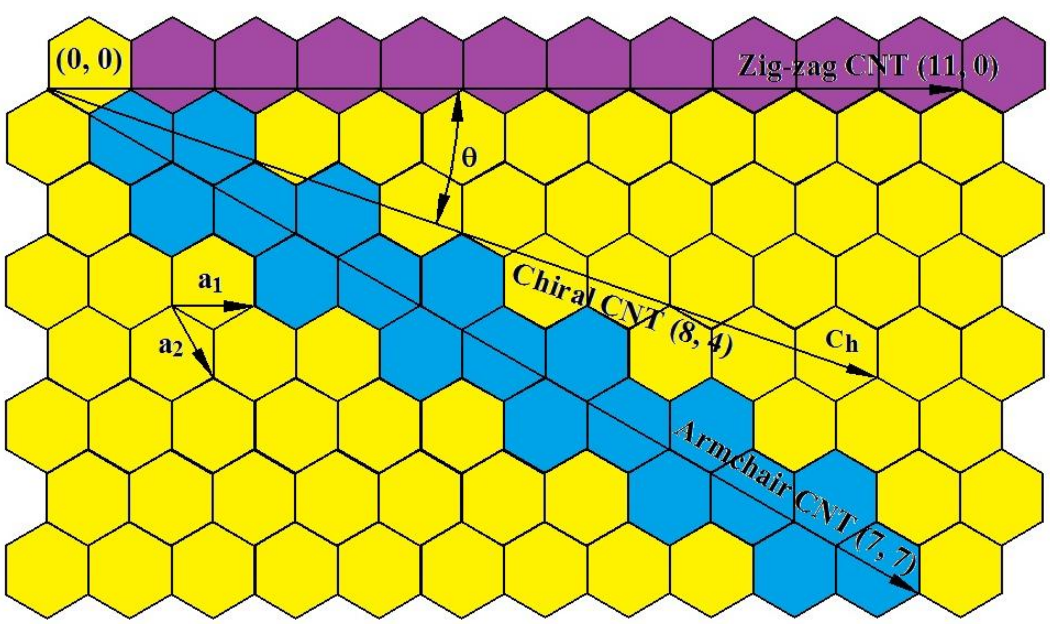

Figure 1.1: Schematic diagram of a hexagonal graphene sheet

The angle $\boldsymbol{\theta}$ between the chiral vector and the lattice base vector $\boldsymbol{a}_1$ is called as the chiral angle and is given by

$$\boldsymbol{\theta} = \boldsymbol{arctan}\left(\frac{\sqrt{3}\boldsymbol{n}}{2\boldsymbol{m}+\boldsymbol{n}}\right) \tag{1.3}$$

The zig-zag axis of the graphene sheet corresponds to $\boldsymbol{\theta} = 0^{o}$ and if the rolling chiral vector is along this axis, a zig-zag (m, 0) **CNT** is generated. On the other hand, the armchair axis of the sheet is specified by $\boldsymbol{\theta} = 30^{o}$ and if this is the direction of the rolling chiral vector, an armchair (m, m) **CNT** is formed. The **SWCNT** generated for other values of $\boldsymbol{\theta}$ (i.e., $0 < \boldsymbol{\theta} < 30^{o}$) is referred as the chiral **CNT**. Figure 1.2 illustrates the schematic representations of these three types of **CNTs**. The chirality of the **CNTs** has significant implications on the material properties. In particular, the **CNT** chirality significantly affects the electronic properties of **CNTs**. Graphite is considered to be a semi-metal but it has been reported that **CNTs** can be either metallic or semi-conducting depending on the **CNT** chirality (Dresselhaus et al., 1996)**.**

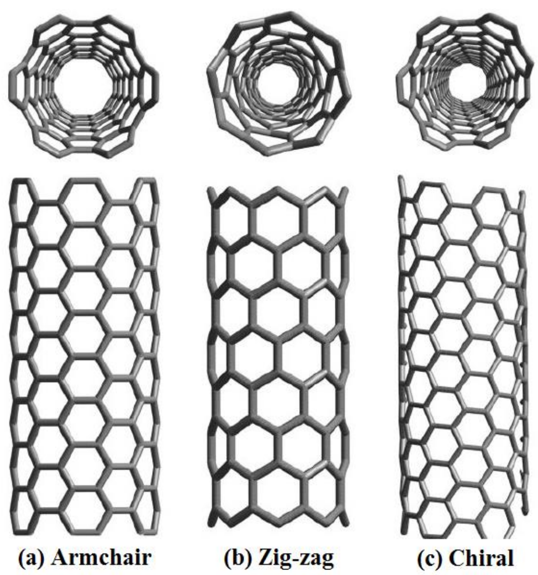

Figure 1.2: Molecular models of **SWCNTs** (Courtesy by (Terrones, 2003))

1.1.2 Properties of CNT

Researchers probably thought that **CNTs** may be useful as nanoscale fibers for developing novel nanocomposites and this conjecture motivated them to accurately predict the properties of **CNTs**. Hence, since the discovery of **CNTs**, researchers have been carrying out extensive research to estimate the physical properties (mechanical, thermal and electrical properties) of **CNTs** as reviewed in the following Sections.

1.1.2.1 Mechanical Properties of CNT

The in-plane $\boldsymbol{\sigma}$ bond is the strongest in nature and thus a **CNT** that is structured with all $\boldsymbol{\sigma}$ bonds is considered as the ultimate fiber with the strength in its axial direction. Both experimental measurements and theoretical calculations agree that a **CNT** is as stiff as or stiffer than diamond with the highest Young's modulus and tensile strength. In general, various types of **CNTs** are stronger than graphite. This is mainly because of the fact that the axial component of the $\boldsymbol{\sigma}$ bond is greatly increased when the graphite sheet is rolled over to form a seamless cylindrical structure of a **CNT**. The practical application of **CNTs** requires the study of their elastic response, inelastic behavior and buckling, yield strength and fracture. A great number of experimental studies have been carried out to estimate the mechanical properties of **CNTs**. Experimental methods for measuring the mechanical properties of **CNTs** are mainly based on transmission electron microscopy (**TEM**) and atomic force microscopy (**AFM**).

For example, based on the experimental analysis, Treacy *et al.* (1996) found the extraordinarily high Young's modulus of **CNTs** ranging in tera-pascal ***(TPa)***. They computed the Young's modulus of **CNTs** by measuring the amplitude of their intrinsic thermal vibrations in the **TEM**.

A similar experimental study on **SWCNT** was performed by Krishnan *et al*. (1998) and reported an average Young's modulus of $1.3 - 0.4/{+0.6}$ ***TPa*** by measuring amplitudes of 27 **SWCNTs**. Using the same form of structural model, Poncharal *et al*. (1999) measured the resonance frequency of **MWCNTs** by driving the resonance with a counter electrode and radio frequency excitation. They obtained the Young's modulus of **MWCNT** with radius smaller than 12 nm as ~1 ***TPa***. A similar type of experiment has also been carried out by Dikin *et al*. (2003) inside a scanning electron microscope (**SEM**). The elastic response of a **CNT** to deformation is also very remarkable. Most hard materials fail with a strain of 1% or less due to propagation of dislocations and defects. Both theory and experiment show that **CNTs** can sustain up to 15% tensile strain before fracture (Lu and Han, 1998).

Tombler *et al*. (2000) reported the Young's modulus of 1.2 ***TPa*** for **SWCNT** by 3-point bending using **AFM**. The first experimental value of the shear moduli of **SWCNT** bundle with **CNT** diameters of about 1.4 nm was reported by Salvetat *et al*. (1999). They obtained the value of shear modulus in the range of 0.7–6.5 ***GPa***.

In addition to experimental endeavors, theoretical evaluations of the mechanical properties of **CNTs** have also been extensively carried out. The computational approaches can be classified into two categories, namely, the 'bottom up' approach (Yakobson *et al*., 1996; Lu, 1997), based on quantum/molecular mechanics including the classical molecular dynamics and the ab initio methods, and the 'top down' approach (Ru, 2000; Odegard *et al*., 2002) based on continuum mechanics.

Generally, ab initio methods give more accurate results than molecular dynamics, but it is computationally expensive and only effective for small systems containing a few hundreds of carbon atoms. Molecular dynamics can be used in a larger systems, but it is still limited to simulating up to millions of atoms on a too-short time scale (less than $10^{-6} - 10^{-9}$ ***s***), since the frequency of molecular thermal vibration is so high (Klein and Shinoda, 2008). Continuum mechanics modeling (top down approach), in contrast, is practical for the analysis of **CNTs** for large-scale systems.

Equivalent-continuum modeling (**ECM**) approach is one of the major developments of continuum method. It has been regarded as a very efficient method, especially for nanostructures with large scale. Molecular mechanics method in conjunction with the finite element (**FE**) method is the essence of the **ECM** approach. Over the past years, many **ECM** models were presented in the open literature.

The **ECM** approaches mainly involve continuum shell modeling, continuum truss modeling and continuum beam modeling. For example, Yakobson *et al*. (1996) fitted the results from the molecular dynamics simulations to the continuum shell model. The Young's modulus can also be estimated by evaluating the energy in the **CNT** system. Based on the relation that the strain energy of the **CNT** is proportional to $1/\boldsymbol{R}^2$ (where ***R*** is the radius of the **CNT**), Robertson *et al*. (1992) and Gao *et al*. (1998) reported the values of the Young's modulus of **SWCNTs** ranging from 640.30 ***GPa*** to 673.49 ***GPa*** by computing the second derivative of the potential energy. Lu (1997) estimated the elastic properties of **CNTs** and nanoropes using an empirical force constant relation and estimated the Young's modulus and the shear modulus of **SWCNT** as 1 ***TPa*** and 0.5

TPa, respectively. By employing different potential models, Li and Chou (2003) linked structural and molecular mechanics approaches to compute the elastic properties of **CNTs** and found that the Young's moduli of armchair and zig-zag **CNTs** lie between 0.995 ***TPa*** and 1.033 ***TPa***, showing good agreement with known graphene Young's modulus. Shen and Li (2004) reported that **CNTs** can be modeled as transversely isotropic materials with the axis of transverse isotropy coincident with the centroidal axis of the **CNT** and developed variational models to determine the values of the five elastic constants of **CNTs**. They reported the values of the axial Young's modulus, the transverse Young's modulus, the bulk modulus, the axial shear modulus and the transverse shear modulus of the armchair (5, 5) **CNT** as 2080 ***GPa***, 421 ***GPa***, 536 ***GPa***, 791 ***GPa*** and 132 ***GPa***, respectively. Also, Shen and Li (2005) studied five independent effective elastic moduli of a transversely isotropic **MWCNT**. They reported the values of the axial Young's modulus, the bulk modulus, the axial shear modulus and the transverse shear modulus of the **MWCNT** as 1580 ***GPa***, 298 ***GPa***, 493 ***GPa*** and 10.57 ***GPa***, respectively.

Xiao *et al*. (2005) developed an analytical model based on the molecular structural mechanics approach for estimating the mechanical properties of **CNTs**. Liu *et al*. (2005) studied the bulk properties of **SWCNT** bundles by employing hybrid atomic/continuum model and predicted the values of the axial Young's modulus, the transverse Young's modulus, the bulk modulus, the axial shear modulus and the transverse shear modulus of the transversely isotropic **SWCNT** bundles as 621.9 ***GPa***, 2.7 ***GPa***, 40 ***GPa***, 1.22 ***GPa*** and 0.68 ***GPa***, respectively. Their predictions agree well with the experimental observations.

Three-dimensional **FE** models for armchair, zig-zag and chiral **SWCNTs** have been derived by Tserpes and Papanikos (2005) to investigate the effects of the **CNT** wall thickness, the **CNT** diameter and the chirality on the elastic moduli of **SWCNTs**. They varied the diameter of armchair (8, 8) **CNT** between 0.066–0.34 ***nm*** and obtained Young's modulus in the range of 5.296–1.028 ***TPa***. Batra and Sears (2007) proposed that the axis of transverse isotropy of a **CNT** is a radial line rather than the centroidal axis of the **CNT** and found that the Young's modulus in the radial direction equals about ¼ of that in the axial direction.

Al-Ostaz *et al*. (2008) performed molecular dynamics simulations to estimate the elastic properties of **SWCNTs** under various types of loading conditions. Results obtained from various types of loading applied to **SWCNT** reveal that **SWCNTs** are transversely isotropic and the values of the elastic constants of **SWCNT** under various loadings are same.

Batra and Gupta (2008) determined the wall thickness and the material moduli of a **CNT** based on the frequencies of axial, torsional, and radial breathing modes. An atomistic-based continuum model has been developed by Cheng *et al*. (2009) for the estimation of the mechanical properties of **SWCNTs**.

1.2 CNT-Reinforced Composites

The review of literature presented in Section 1.1 theoretically and experimentally confirms that **CNTs** possess exceptionally high mechanical properties such as stiffness and strength. The quest for utilizing such exceptional mechanical properties of **CNTs** and their high aspect ratio and low density led to the opening of an emerging area of research on the development of **CNT**-reinforced nanocomposites. It was observed that the performance of the composite materials enhances significantly by adding a small number of **CNTs**. For example, Thostenson and Chou (2003) have estimated the elastic moduli of **CNT**-reinforced composite through micromechanical analysis considering **CNTs** as continuous fiber reinforcements. Using the approach of continuum mechanics, Odegard *et al*. (2003) predicted the effective elastic moduli of **CNT**-reinforced composite using **ECM** method. In their study, the **CNT**, the local polymer near the **CNT**, and the **CNT**/polymer interface have been modeled as an effective continuum fiber. Liu and Chen (2003) have determined the effective mechanical properties of **CNT**-based composites by employing the continuum mechanics approach and the **FE** method. In their study, 33% enhancement in the axial stiffness of the composite was observed with the addition of long **CNTs** in a polymer matrix at a volume fraction of 3.6%.

Gao and Li (2005) derived a shear lag model of discontinuous **CNT**-reinforced polymer composites by considering the **CNT** as an equivalent solid fiber. It is accepted by many researchers that **CNT**-reinforced composites can be considered as fiber-reinforced composites so that their elastic properties can be predicted by using the available micromechanics methods (Valavala and Odegard, 2005).

Seidel and Lagoudas (2006) estimated the effective elastic properties of **CNT**-

reinforced composites employing the self-consistent and the Mori-Tanaka methods. Song and Youn (2006) numerically estimated the effective elastic properties of **CNT**-reinforced polymer based composites by using the homogenization technique. The control volume finite element method is adopted in their study to implement the homogenization method with the assumption that the **CNT**/epoxy nanocomposites have geometrical periodicity with respect to a microscopic scale.

Ashrafi and Hubert (2006) carried out **FE** analysis to predict the elastic properties of **CNT** arrays and their composites. Zhang and He (2008) theoretically investigated the viscoelastic behavior of **CNT**-reinforced composites by developing a three-phase shear lag model. Jiang *et al*. (2009) determined the maximum volume fraction of **CNTs** in the **CNT**-reinforced composite and investigated its effect on the effective elastic properties of the composite using molecular dynamics simulations. Esteva and Spanos (2009) studied the effect of weakened interfaces between **CNTs** and polymer matrix on the effective properties of **CNT**-reinforced polymer matrix composite. They reported that the imperfect bonding does not affect the effective longitudinal Young's modulus of the **CNT**-reinforced polymer matrix composite and marginally affects the transverse properties of the composite for high volume fraction (> 0.8) of **CNTs**.

Meguid *et al*. (2010) developed a model of an atomistic-based representative volume element (**RVE**) which consists of the **CNT**, the surrounding epoxy matrix, and the interface between **CNT** and epoxy to estimate the effective properties of **CNT**-reinforced epoxies. Their results reveal that **CNT** length, volume fraction, orientation and aspect ratio of the representative **CNT** fiber have significant effects on the effective properties of the **CNT**-reinforced composites.

Tsai *et al*. (2010) characterized the elastic properties of **CNT**-reinforced polymer nanocomposites considering an effective interphase between a **CNT** and the polymer matrix.Wernik and Meguid (2011) presented a nonlinear atomistic-based continuum model for predicting the effective mechanical properties of **CNT**-reinforced polymer composite. Ayatollahi *et al*. (2011) presented a multiscale analysis for investigating the mechanical behavior of **CNT**-reinforced composite under tensile, bending, and torsional loading conditions.

Using the ball milling technique, Esawi *et al.* (2010) showed the enhancement of tensile strength by 50% and stiffness by 23% due to the addition of 5 wt.% of **CNT** in the aluminum matrix. Through an experimental investigation such as open-hole tension, shear beam test, and flatwise tension tests, Tarfaoui *et al.* (2016) found a significant control in crack propagation by adding **CNT** up to 2% volume fraction in the polymer matrix, which improved the overall thermo-elastic properties of the composites. Similar results were observed by Park *et al.* (2003) and they observed the highest Young's modulus and mechanical properties at 2% volume fraction of **CNT** in the epoxy matrix.

From the above literature, researchers observed that **CNTs** tend to agglomerate when reinforced with matrix phase and hence weaken the junction, which in result limits the use of **CNTs** as a nanofiller in the composite materials up to a certain wt.%. Further research was carried out to increase the wt.% of **CNT** in the matrix phase by developing the new techniques (Wernik and Meguid, 2010; Meguid, Wernik and Al Jahwari, 2013; Peddavarapu and Jayendra Bharathi, 2018).

1.3 CNT–Reinforced Hybrid Composites or Multiscale Composites

Traditional fiber-reinforced composites have excellent in-plane properties but have poor out-of-plane properties. The failure of traditional composites may occur due to the fiber bending and the fiber breaking because of the lack of support by the matrix. The bonding between the reinforcement and the matrix is thus a crucial parameter for controlling the load transfer between the composite constituents. The hybridization of the conventional fibers with **CNTs** is a new way of improving the load transfer capabilities of conventional composites, such hybrid composites are termed '*multiscale composites*'. Most recently, the multiscale composite with nanoscale **CNTs** and microscale conventional fibers have captivated a great interest in the development of lightweight, low density, and high-performance composite structures (Thostenson *et al.*, 2002; Kim *et al.*, 2009). To some extent, these multiscale composites can solve the problem of agglomeration. Some studies on the multiscale composite reveal that incorporating **CNTs** along with conventional fibers show excellent thermo-mechanical properties (Mathur *et al.*, 2008). Enormous efforts have been made to improve the matrix-dominant properties by incorporating the **CNTs** in the bulk matrix. High-energy sonication, calendaring, and ultrasonic duel mixing (Gojny *et al.*, 2005; Iwahori *et al.*, 2005) are widely used techniques for dispersing **CNTs** in the matrix phase. Later, the **CNT**-based matrix solution can be used to fabricate multiscale composite in which primary reinforcements are microscale fibers. Liu *et al.* (2006) investigated the damping performance of **CNT**-based polymer composites by considering the interfacial slip effect using an analytical model. They observed that Young's modulus and loss factor of the hybrid composite was influenced by the interfacial slip effect. Grimmer and Dharan (2008) studied the fatigue analysis of glass fiber-reinforced **CNT**/polymer composites, noticing that the poor fatigue performance of glass-fiber composites was improved by the addition of **CNTs** in the matrix phase. The electron microscopy showed that the high density of **CNTs** prevented larger cracks in the matrix that were attributed to the enhanced fatigue strength.

By using the novel shear pressing method, several researchers reported that the high-volume fraction **CNT**-based hybrid composites are possible when the conventional micro-fibers were used. Bradford *et al.* (2010) confirmed 27% volume fraction of the long aligned **CNTs** (in order of mm) in the composite materials with suitable microfibers. Huang *et al.* (2012) reported 20% **MWCNTs** along with 20% graphene nanoplatelet in an epoxy matrix hybrid composite through a well-designed fabrication method. The damping of the hybrid composite structures with graphitic structures by design (**GSD)**-grown **CNTs** improved by 56%. Ultra-high wt. percent of **MWCNT** (68 wt.%) was reported by Mecklenburg *et al.* (2015) in the epoxy-based composite using the novel hot-press infiltration manufacturing process through a semi-permeable membrane with long aligned **MWCNTs** (in order of mm) grown using **CVD** process.

Tehrani *et al.* (2013) analyzed the damping performance of hybrid **CNT**-based composite structures with **CNTs** grown over the carbon fibers using **GSD**. Kundalwal and Ray (2013) developed micromechanical models based on mechanics of material (**MOM**) and Mori-Tanaka (**MT**) approach to investigate the influence of **CNT** waviness on effective elastic properties of fuzzy-fiber reinforced composites (**FFRC**). The advanced fiber augmented with **CNTs** on its circumferential surface is known as fuzzy fiber. They observed that the axial effective elastic properties of the **FFRC** containing wavy **CNTs** can be improved over those of the **FFRC** with straight **CNTs**. Kundalwal *et al.* (2014) investigated the stress transfer characteristics of a novel hybrid hierarchical nanocomposite in which the regularly staggered short fuzzy fibers are interlaced in the polymer matrix. Their study revealed that the existence of the non-negligible shear tractions along the length of the **RVE** of the staggered **FFRC** plays a significant role in the stress transfer characteristics. They also observed that the reductions in the maximum values of the axial stress in the carbon fiber and the interfacial shear stress along its length become more pronounced in the presence of the externally applied radial loads on the **RVE**.

Ma *et al.* (2015) evaluated the electromechanical properties of a multiscale **CNT**/fiber/polymer composite using the micromechanical model, finding considerable enhancement in the electrical conductivity of the composite by incorporating 2% volume fraction of **CNTs**. Gholami *et al.* (2018) investigated the nonlinear dynamics of hybrid **CNT**-reinforced composite plates using a FE model based on Mindlin plate theory and the von Kármán hypotheses. Hasanzadeh *et al.* (2019) evaluated the piezo-mechanical properties of **CNT**/polymer hybrid composites using a three-phase micromechanical model. They observed a significant enhancement in the electrical as well as mechanical properties by adding **CNTs**.

Recently, Ebrahimi along with his coauthors (Ebrahimi and Dabbagh, 2020, 2021; Ebrahimi *et al.* 2021) studied the multiscale nanocomposites utilizing the potential benefits of **CNTs**. Their findings show that the static and dynamic response of multiscale composites improved due to the reinforcement of **CNTs** nanofillers. Ebrahami and Dabbagh (2020) investigate the vibrational behavior of agglomerated multiscale nanocomposite shells using the well-known first-order shear deformation theory **(FSDT)** employing the principle of virtual work to obtain the Euler-Lagrange equations. Ebrahami and Dabbagh (2021) studied the stability of multiscale nanocomposite plates considering the buckling problem. For this, they used an energy-based Hamiltonian approach and derived the equation of motion using classical plates theories. Also, Ebrahami *et al.* (2021) studied the effects of **CNT** waviness of the vibrational behavior of multiscale nanocomposite plates employing the higher-order shear deformation theory (**HSDT**) of plates. Their findings indicate that the vibration suppression in the nanocomposite structures can be delayed by considering the higher characteristic relaxation time of the polymer.

1.4 Smart Structures

Lightweight flexible structures have attained the growing demand for the design of space structures, robotic manipulators and aerospace structures. The multilayer composites possess low structural damping, thus, the large dynamic excitation may lead to large deformation and geometric failure. Accordingly, '*smart structures*' (Crawley *et al.*, 1988) are developed to address this issue and are schematically illustrated in Fig. 1.3. The smart structures have the capabilities of self-monitoring and self-controlling. These capabilities were achieved by exploiting the direct and converse effects of piezoelectric material installed or mounted at the surface of the host structure. The damping characteristics of the overall structure improve when the electric potential is applied to the smart structures known as active control damping, making the structure safe against vibrational-induced failures.

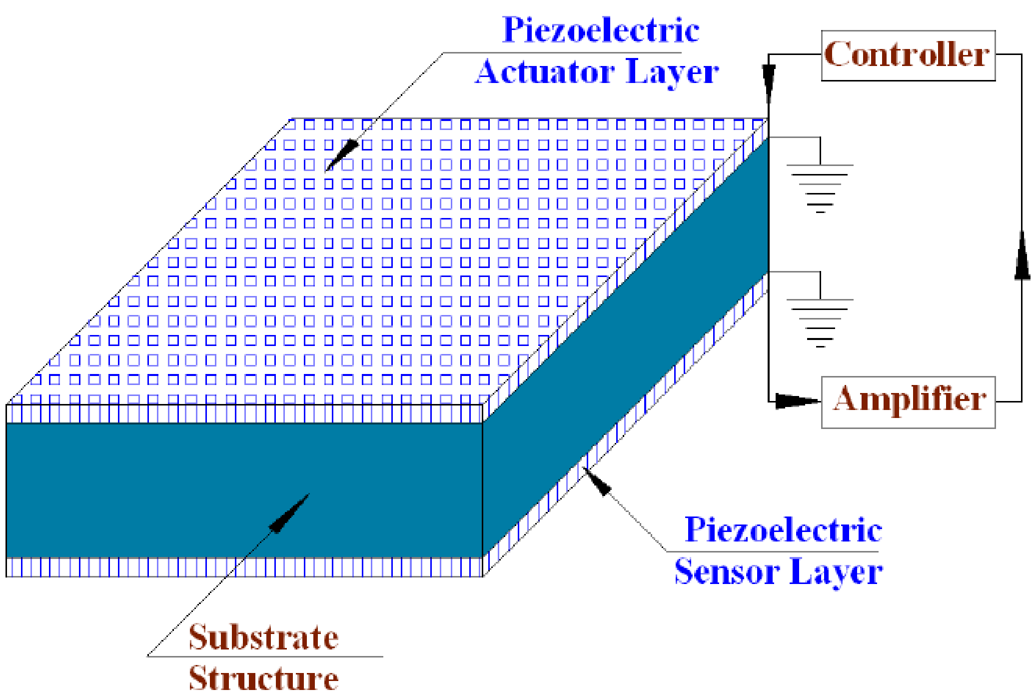

Figure 1.3: Schematic representation of the smart structure

The passive material part of a smart structure is the load-bearing part i.e. the host structure and the active material parts of the same are the layers/patches of piezoelectric materials which perform the operations of sensing and actuation. Piezoelectric materials can easily be integrated with the load-bearing structures by surface bonding or embedding into them and do not significantly alter the passive stiffness characteristics of the host structures. The load-bearing part or passive part of the smart structure is generally called as a substrate which can be a beam, plate, or shell. A great deal of research on smart structures has already been reported on the exact solutions (Batra *et al.*, 1996; Ray, 1998), analytical solutions (Tzou and Cadre, 1989; Dimitriadis *et al.*, 1991), **FE** analysis (Ha *et al.*, 1992; Robbins and Reddy, 1996) and active control analysis (Baz and Poh, 1990; Tzou and Gadre, 1990; Baz *et al.*, 1992; Ray, 1998, 2003; Balamurugan and Narayanan, 2001b). The concept of smart structures has also been implemented for the active control of vibrating structures. Sze and Yao (2000) developed numerous **FE** models for the vibration control of smart structures with segmented piezoelectric sensing and actuating patches. Furthermore, this concept has been used for structural health monitoring as a nondestructive evaluation technique (Lin and Chang, 2002; Mook *et al.*, 2003; Sastry *et al.*, 2004). Later, using the Kalman filter identification (**OKID**) technique, Dong *et al.* (2006) studied the active vibration control of smart structures, numerically and experimentally..

Ray and Pradhan (2006) investigated the piezoelectric smart composite beams using first-order shear deformation theory. Bendary *et al.* (2010) developed a **FE** beam model using isoperimetric Hermit cubic shape functions and the Lagrange interpolation functions to analyze the smart beams with distributed piezoelectric actuators. Kucuk *et al.* (2011) studied the active vibration control of Euler-Bernoulli beam with piezoelectric actuators bonded on the top and the bottom faces of the beam.

Wang *et al.* (2001) investigated the vibration control of smart plates by developing a **FE** model based on **FSDT**. They analyzed the effect of the stretching–bending coupling of the piezoelectric sensor/actuator pairs on the system stability of smart composite plates. Robaldo *et al.* (2006) developed a unified formulation for the finite element analysis of adaptive plates integrated with piezoelectric layers using the principle of virtual displacement approach. Qiu *et al.* (2007) presented the theoretical and experimental analysis for optimal placement and active vibration control for piezoelectric smart flexible cantilever plates. They observed that free vibrations can be effectively suppressed by changing the location of the piezoelectric patches. Larbi *et al.* (2012) carried out finite element analysis of smart composite plate coupled with acoustic fluid.

1.5 Active Constrained Layer Damping

The main drawback of the existing monolithic piezoelectric materials is that the magnitudes of their piezoelectric coefficients are very small. Thus, the distributed actuators made of monolithic piezoelectric materials possess very low control authority and require large control voltage for achieving appreciable results. Further investigation on the efficient use of these monolithic piezoelectric materials for active control of flexible structures led to the development of **ACLD** treatment (Azvine *et al.*, 1995; Baz and Ro, 1995a). The **ACLD** treatment consists of a layer of viscoelastic material constrained between the host structure and an active constraining layer made of piezoelectric material. When the host structure undergoes vibrations, the active constraining layer not only restrains the constrained soft viscoelastic layer to undergo transverse shear deformations but also controls its transverse shear deformations to cause improved damping characteristics of the overall structure over the passive damping. If the constraining layer is not subjected to the applied voltage, the treatment turns out to be the conventional passive constrained layer damping (**PCLD**) treatment. Thus, the **ACLD** treatment provides the attributes of both active and passive damping (Baz and Ro, 1996; Baz, 1997; Shin, 1997; Varadan *et al.*, 1997; Ro and Baz, 2002). Further, optimization of energy dissipation characteristics of beams, plates, and shells integrated with the **ACLD** treatment has been studied by many researchers.

For example, Huang *et al.* (1996) studied the vibration suppurating in the smart beams by the means of **ACLD** treatment patches. They observed that the active constrained layer damping treatment provides better vibration suppression than passive damping treatments, and it even out-performs pure active control for low-gain applications. Baz (1997) developed a variational mathematical model using Hamilton's principle to describe the dynamics of beams fully-treated with **ACLD** treatments. Their outcomes demonstrated the high damping characteristics of the boundary controller, particularly over broad frequency bands. Trindade *et al.* (2000) studied the frequency response function (**FRF**) of smart beam integrated with **ACLD** treatment patches by developing and comparing two **FE** models so-called Golla-Hughes-McTavish (**GHM**) and Anelastic Displacement Fields (**ADF**) models.

Baz and Ro (2001) developed a **FE** model for the vibration control of rotating beams with the **ACLD** treatment layer. The **ACLD** treatment consisted of a viscoelastic damping layer which was sandwiched between two piezoelectric layers. Lim *et al.* (2002) developed a three-dimensional **FE** closed-loop model to predict the effects of active-passive damping on a vibrating structure. The **GHM** method was employed to capture the viscoelastic material behavior in a time-domain analysis. Sun and Tong (2003) presented a model for a smart beam with a partially debonded **ACLD**, and the effects of the debonding of the **ACLD** patch on both passive and hybrid control are investigated. Ray and Reddy (2004a) derived a finite element model to investigate the dynamics of the composite beams integrated with a patch of **ACLD** treatment and a patch of piezoelectric film acting as a distributed sensor with and without the presence of delamination at different locations. They observed that the **ACLD** treatment improves the active damping characteristics of the beams, even in the presence of delamination, and that the responses of the beams are sensitive to the variation of the location of delamination. Making use of Hamilton's principle, Fung and Yau (2004) developed a **FE** model to investigate the vibration behavior and control of a clamped–free rotating flexible cantilever arm with fully covered.

Ray and Pradhan (2006) investigated the performance of **1–3 PZC** smart beams embedded with **ACLD** patches using the **FE** model based on **FSDT**. Li *et al.* (2008) proposed an analytical model for the active vibration control of the smart beams with **ACLD** treatments. Vasques and Dias Rodrigues (2008) performed a numerical analysis of feedback, adaptive feedforward, and hybrid (combined feedback/feedforward) control systems on the active control of vibrations of beams with **ACLD** treatments. Sarangi and Ray (2010) studied the geometrically nonlinear vibrations of laminated composite beams installed with **ACLD** patches. Kumar (2012) studied the active vibration control of beams by combining precompressed layer damping and **ACLD** treatment. For this $\boldsymbol{H}_{\infty}$ loop shaping controller was designed and implemented experimentally on a smart flexible beam. Li *et al.* (2017) investigated the dynamics of a rotating flexible beam with fully covered **ACLD** treatment by using the method of assumed modes to describe the deformations of the three sub-layer beams. Sahoo and Ray (2018) derived a **FE** model for the analysis of smart damping of laminated composite beams embedded with **ACLD** treatment patches using the meshfree method.

Baz and Ro (1996) analyzed the bending vibration control of flat plates using patches of **ACLD** treatments. Each **ACLD** patch consisted of a visco-elastic damping layer which was sandwiched between two piezoelectric layers. The first layer was directly bonded to the plate to sense its vibration and the second layer acted as an actuator to actively control the shear deformation of the viscoelastic damping layer according to the plate response. Varadan *et al*. (1996) presented a closed-loop **FE** model of active/passive damping in structural vibration control using **ACLD** treatment. Optimization of energy dissipation characteristics of plates integrated with the **ACLD** treatment has been studied by Ray and Baz (1997). Azzouz and Ro (2002) studied the control of sound radiation of the **ACLD** plate/cavity system using the structural intensity approach. They determined the optimum placement of **ACLD** patches by the structural intensity of **ACLD** treated plates. Ray and Batra (2007b) investigated the active damping of functionally graded plates with **1–3 PZC** being the constraining layer of **ACLD** treatment. They observed that the controlling ability of **ACLD** improves significantly because of the **1–3 PZC** layer. Lui *et al.* (2007) studied the dynamic characteristics and vibration control of a rotating cantilever plate installed with the **ACLD** treatment layer. Using the second kind of Lagrange formulation they derived a **FE** model based on Kirchhoff's classical laminated theory. Providakis *et al.* (2007) developed a **FE** model of electromechanical impedance for the analysis of smart damping of composite plates with **ACLD** treatments. Ray *et al.* (2009) theoretically and experimentally investigated the active structural–acoustic control of a thin plate using a vertically reinforced **1–3 PZC** as constraining layer of **ACLD** treatment patches.

Kattamani and Ray (2014) studied the smart damping of geometrically nonlinear vibrations of large amplitudes of magneto-electro-elastic plates integrated with **ACLD** treatment patches using the **GHM** method in the time domain. Sarangi and Basa (2014) developed a three-dimensional (**3D**) **FE** model based on Von Kármán type nonlinear strain–displacement relations and **FSDT** individually for each layer of the sandwich plate integrated with **ACLD** treatments. Dutta and Ray (2016) presented a **3D** fractional derivative model of smart constrained layer damping treatment for composite plates integrated with **ACLD** patches. Kundalwal and Ray (2016) investigated the effects of **CNTs** waviness on the active damping performance of **FFRC** composite plates integrated with two **ACLD** treatment patches at the top surface of the host structure using **FSDT**. They observed that the **CNT** waviness significantly influences the damping characteristics of the **FFRC** smart plate with maximum vibration attenuation observed when **CNT** waviness was coplanar with **1–3** plane. Vinayas (2020) studied the interphase effect on the controlled frequency response of three-phase smart magneto-electro-elastic plates embedded with **ACLD** treatments. Khan and Kumar (2021b) studied the vibration control of laminated plates by the **ACLD** treatment using the **FE** model based on **FSDT**, incorporating Murakami's zig-zag function (**MZZF**) while deriving the displacement fields.

Using the adaptive least mean square (**LMS**) algorithm, Poh *et al.* (1996) performed an experimental investigation for the adaptive control of sound radiation from a panel into an acoustic cavity using the **ACLD** layer. Baz and Chen (2000) derived a **FE** model utilizing Hamilton's principle to control the axisymmetric vibrations of cylindrical shells integrated with the **ACLD** treatment layer. Baz (2000) developed a spectral finite-element model (**SFEM**) to describe the propagation of longitudinal waves in rods treated with **ACLD** treatments. The model was formulated in the frequency domain using dynamic shape functions that capture the exact displacement distributions of the different **ACLD** layers. Ray *et al.* (2001) performed an experimental investigation to determine the effectiveness of the **ACLD** treatments in enhancing the damping characteristics of thin cylindrical shells. Ray and Reddy (2004b) derived a **FE** model based on classical shell theory for the optimal control of thin circular cylindrical laminated composite shells using **ACLD** treatment. Ray and Batra (2008) studied the effect of piezoelectric fiber orientation on the control authority of the **ACLD** treatment layer of functionally graded smart shells using a **FE** model. Yuan *et al.* (Yuan *et al.*, 2010) presented a semi-analytical method using the integrated first-order differential equation and the circumferential dominant modal control of circular cylindrical shells with **ACLD** treatment. Utilizing the modal strain energy method, Kumar and Singh (Kumar and Singh, 2012) performed an experimental investigation for the vibration control of curved panels treated with optimally placed **PCLD**/**ACLD** patches. Saranji and Ray (Sarangi and Ray, 2013) derived a **FE** model based on the **GHM** method for the smart control of nonlinear vibrations of doubly curved functionally graded laminated composite shells under a thermal environment using **1–3 PZC**. Ni *et al.* (2013) developed a semi-analytical method using the integrated first-order differential matrix equation of a shell of revolution partially treated with ring **ACLD** blocks for dynamics analysis of shells of revolution. Kundalwal and Meguid (2015) developed a **FE** model based on **FSDT** to investigate the effect of carbon nanotube waviness on active damping of laminated hybrid **FFRC** composite shells installed with the two **ACLD** treatment patches. Kumar *et al.* (2017) derived a **FE** model based on the **GHM** approach for the control of nonlinear large-amplitude vibrations of doubly curved sandwich shells composed of **FFRC** facings integrated with **ACLD** treatment patches. Sahoo and Ray (2019a) developed a mesh-free **FE** model based on **FSDT** to investigate the active control of doubly curved laminated composite shells using elliptical **ACLD** treatment. Accounting for the inherent zig-zag (**ZZ**) effects developed in the laminated composite structures Khan and Kumar (2021a) derived the **FE** model employing the **FSDT** incorporating the **MZZF** for the active vibration control of smart laminated shell embedded with the **ACLD** treatment patches.

1.6 Piezoelectric Composite

It is known that brittle fibers are efficiently exploited to form polymer matrix composites with improved properties suitable for structural applications. Probably, this motivated the researchers to develop the **PZCs** with brittle piezoceramic fibers. **PZCs** are usually composed of an epoxy matrix reinforced with fibers of monolithic piezoceramic materials such as **PZT**, **PZT5H**, etc. They provide a wide range of effective material properties not offered by the existing monolithic piezoelectric materials and are characterized by good conformability and strength. Being a composite material, the **PZCs** have the ability to cause orthotropic actuation.

Various micromechanics models were proposed to predict the effective properties of these **PZCs** from the properties of their constituents. For example, Chan and Unsworth (1989) derived a simple micromechanics model for the analysis of piezoelectric ceramic/polymer **1–3** composites. Smith and Auld (1991) predicted the effective properties of vertically reinforced **1–3 PZC** materials using the strength of material approach of micromechanics. These materials have improved mechanical performance and electro-mechanical coupling, and are useful for studying the thickness mode oscillations of structures.

Mallik and Ray (2003) proposed the concept of a new horizontally reinforced **1–3 PZC** material and predicted the effective mechanical and piezoelectric properties of these composites. The constructional feature of the lamina made of the vertically/obliquely reinforced **1–3 PZC** (Smith and Auld, 1991; Ray and Pradhan, 2007) is schematically illustrated in Fig. 1.4. As shown in Fig. 1.4 (a), the piezoelectric fibers are uniformly distributed and vertically aligned across the thickness of the lamina. Figure 1.4 (b) shows that the piezoelectric fibers are coplanar with the vertical ***xz***-plane while the fibers are oriented at an angle ($\boldsymbol{\Psi}$) with the transverse direction and Fig. 1.4 (c) represents the same when the fibers are coplanar with the vertical ***yz*** -plane. The top and the bottom surfaces of the lamina are coated with surface electrodes and the fibers are poled along their length with their ends being in contact with the surface electrodes. In case of the vertically reinforced **1–3 PZC**, the orientation angle ($\boldsymbol{\Psi}$) is zero while it is nonzero for the obliquely reinforced **1–3 PZC**.

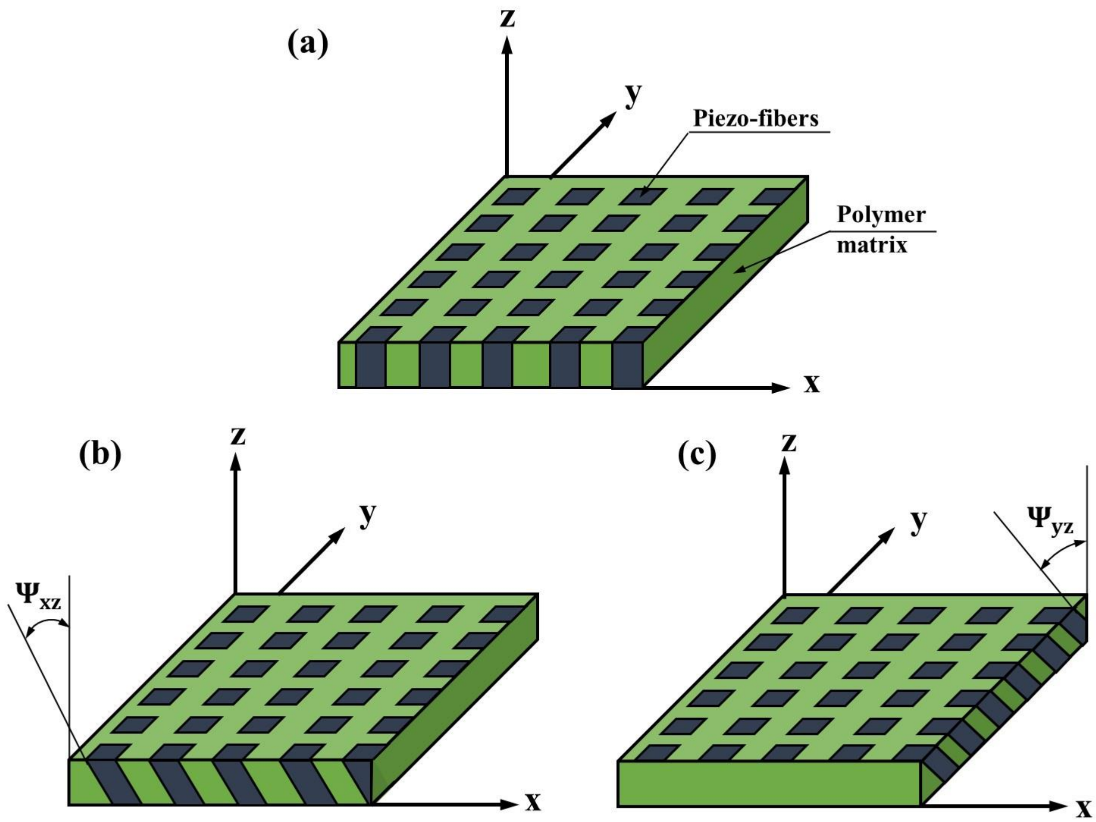

Figure 1.4. Schematic representation of **1–3 PZC** lamina with (a) vertically aligned piezo-fibers, (b) piezo-fibers coplanar in the ***xz***–plane, and (c) piezo-fibers coplanar in the ***yz***–plane.

Extensive research has been carried out to demonstrate the performance of these **PZC** materials as the materials of the distributed actuators or constraining layer of the **ACLD** treatment for active control of linear deformations and vibrations of laminated structures (Ray and Mallik, 2005; Ray and Reddy, 2005; Ray and Pradhan, 2006, 2007; Ray and Balaji, 2007; Kumar and Singh, 2009; Gupta *et al.*, 2022a). Balamurugan and Narayanan (2001a) investigated the active vibration control of smart shells using a shear-flexible nine-noded shell element derived from the field consistency approach. Ray and Pradhan (2006) investigated the vibrations response of laminated composite beams using **FSDT**. Ray and Pradhan (2010) investigated the use of vertically/obliquely reinforced **1–3 PZCs** for active damping of linear vibrations of thin laminated composite cylindrical shells. Kundalwal *et al.* (2013) developed a **3D FE** model to investigate the frequency response of multilayered composite shells integrated with **ACLD** patches constraining layer of **1–3 PZC**. Kattimani (2017) studied the layer-wise shear deformation theory using **1–3 PZC** for active damping of the magneto-electro-elastic (**MEE**) smart composite plates. Vinyas (2019) studied the effect of the **ACLD** treatment layer on the frequency response of the skew magneto-electro-elastic (**SMEE**) plate, observing that the skew angle significantly influences the frequency response of the **SMEE** smart plate. Making use of **FSDT**, Sahoo and Ray (2019a) investigated the smart doubly curved laminated shell integrated with rectangular and elliptical **ACLD** patches.

1.7 Scope and Objectives of the Dissertation

The review of literature reveals that the exceptionally attractive properties of **CNTs** can be exploited to develop two-phase **CNT**-reinforced polymer matrix composites and three-phase hybrid **CNT**-reinforced composites, where **CNTs** are used as fiber reinforcements. For structural applications, the manufacturing of two-phase unidirectional continuous **CNT**-reinforced composites on a large scale has to encounter some challenging difficulties. Typical among these are the agglomeration of **CNTs**, the misalignment, and the difficulty in manufacturing long **CNTs**. In case of three-phase hybrid **CNT**-reinforced composite or multiscale composites, **CNTs** are used as nanofillers in combination with the conventional micro-fibers. It seems that using the **CNTs** as nanofiller along with the advanced fibers for achieving uniform distribution of **CNTs** throughout a composite is practically more feasible and advantageous in comparison to the manufacturing of long **CNTs** and the dispersion of long **CNTs** in the polymer matrix (Bradford *et al.*, 2010), as it provides a mean to tailor the multifunctional properties of the existing advanced fiber-reinforced composites. The literature, reviewed in Section 1.3, authenticate that the multiscale composites with nanoscale **CNTs** and microscale carbon fibers result in the enhancement of the mechanical, thermal, and electrical properties of existing fiber-reinforced composites. Such multiscale composites are termed hybrid fiber-reinforced composites (**HFRC**). The current status of progress in research on **CNT**-reinforced composites brings to light that the three-phase hybrid **CNT**-reinforced composite can be the promising candidate material for achieving structural benefits from the exceptionally attractive properties of **CNTs**.

The lightweight and high-performance smart structures with a high stiffness-to-weight ratio are the need of the hour. This can be achieved by making the substrate of the smart structure very thin conventional laminated composite structures to meet the above criteria of higher strength and stiffness-to-weight ratios. Such laminated composites are also termed as multilayered structures. These multilayered structures consist of relatively thin layers of different material compositions which may influence the different degrees of axial compliance. As a result, the axial displacement of anisotropic structures varies nonlinearly along the thickness of the structure, which causes discontinuous derivatives between the interface of two individual layers. This change in slope between two adjacent layers is known as the **ZZ** effect. The low values of transverse to in-plane modulus result in higher transverse shear resulting in the **ZZ** effect, which needs to be accounted for. Also, the multilayer composites possess low structural damping, thus, the large dynamic excitation may lead to large deformation and geometric failure. Accordingly, '*smart structures'* are developed to address this issue. The smart structures have the capabilities of self-monitoring and self-controlling. These capabilities were achieved by exploiting the direct and converse effects of piezoelectric material installed or mounted at the surface of the host structure in combination with the viscoelastic layer. Such, combination of the viscoelastic material and piezoelectric material is known as the **ACLD** treatment layer. The **ACLD** treatment over the last decade has been accredited as a very effective means for achieving the active vibration control of multilayered structures. The damping characteristics of the overall structure improve when the electric potential is applied to the smart structures known as active control damping, making the structure safe against vibrational-induced failures (Sun *et al.*, 2001; Ray, 2003). The literature review on piezoelectric materials indicates that **1–3 PZC** materials provide a wide range of material properties which monolithic piezoelectric materials cannot. Hence in order to attain the efficient damping characteristics of the host structures, commercially available **PZC** materials like vertically/obliquely reinforced **1–3 PZCs** may be used as the materials of the constraining layer of the **ACLD** treatment. The review of the literature presented in Sections 1.5 and 1.6 indicates that the **ACLD** of large amplitude vibrations of conventional laminated composite structures has been studied in detail. However, the research on the **ACLD** of vibrations of laminated multiscale **HFRC** beams, plates, shells using the vertically/obliquely reinforced **1–3 PZC** incorporating the **ZZ** effects is still not available in the open literature. The dynamic characteristics of the multiscale **HFRC** beams, plates and shells undergoing **ACLD** are different from that of the conventional thin composite beams, plates and shells and also it is not known yet whether the vertical actuation by the **1–3 PZC** constraining layer of the **ACLD** treatment can cause the active control of the vibrations of multiscale structures with straight and wavy **CNTs**. This lack of knowledge provides ample scope for further research.

Considering the above-mentioned aspects into account, the main objective of the present research is directed to investigate the performance of the novel laminated multiscale **HFRC** substrate structure installed with the vertically/obliquely reinforced **1–3 PZCs** as the candidate materials of the constraining layer of the **ACLD** treatment for controlling the vibrations of the laminated structures like beams, plates, and shells. To fulfill the objective the following theoretical analyzes have been carried out:

- To predict the effective elastic properties of the unidirectional continuous **HFRC** utilizing the micromechanical model. (Gupta *et al.*, 2021)
- To investigate the effect of **CNTs** waviness on the effective elastic properties of the continuous **HFRC**. (Gupta *et al.*, 2022b)
- To develop a **FE** model to investigate the performance of laminated multiscale **HFRC** smart beam. (Gupta *et al.*, 2021)
- To investigate the damping performance of laminated multiscale **HFRC** smart plate using a **FE** method. (Gupta *et al.*, 2022c)
- To investigate the effect of piezoelectric fiber orientation of **1–3 PZC** and **CNTs** waviness on the damping performance of the multiscale **HFRC** smart plate. (Gupta *et al.*, 2022b)

- To investigate the damping performance of laminated multiscale **HFRC** smart shell using a **FE** method based on the sinusoidal shear deformation (**Sinus**) theory incorporating the **MZZF** (Gupta *et al.*, 2022d).

1.8 Contributions from the Present Thesis

The following contributions in the field of smart structures with advanced **CNT**-reinforced hybrid composites have been made towards the preparation of the dissertation:

1. A novel unidirectional continuous multiscale **HFRC** has been analyzed in which the reinforcement materials (**CNT** nanofiller and carbon fibers) are uniformly aligned along the longitudinal direction. Analytical micromechanics models have been developed to estimate all the effective elastic properties of this novel multiscale **HFRC** lamina.
2. The effect of the **CNTs** waviness on the effective elastic properties of the multiscale **HFRC** has been investigated when the wavy **CNTs** are coplanar with either of the two mutually orthogonal planes.
3. FE models are developed to study the **ACLD** of vibrations of smart multiscale **HFRC** beams, plates, and shells. The constraining layer of the **ACLD** treatment is considered to be composed of vertically/obliquely reinforced **1–3 PZC** materials.
4. The **FSDT** and **Sinus** theories are implemented accounting for the inherent effects of **ZZ** to model the constrained viscoelastic layer of the **ACLD** treatment for the active vibration control of the smart **HFRC** beams, plates, and shells.
5. To exploit the transverse attenuation by the active constraining **1–3 PZC** layer of the **ACLD** treatment, transverse normal deformations in all the layers of the overall **HFRC** structures are considered. Emphasis has been placed on investigating the effects of variation of the piezoelectric fiber orientation angle on the performance of the patches of the **ACLD** treatment.
6. Investigation of the effect of waviness of **CNTs** on the performance of the **ACLD** patches for **ACLD** of vibrations of **HFRC** beams, plates, and shells is an important contribution. Such investigation confirms that the wavy **CNTs** can also be exploited to develop a high-performance multiscale **HFRC** structure.

7. Also, the **FRF** of the laminated multiscale **HFRC** beams, plates, and shells have been computed which could serve as future reference results for other researchers.

1.9 Organization of the Thesis

The remaining part of the Thesis is organized as follows:

- Chapter 2 deals with the micromechanical analyses of the multiscale **HFRC** and **1–3 PZC** for estimating the effective elastic coefficients of the **HFRC** with or without considering the waviness of **CNTs** and effective piezo-elastic coefficients of **1–3 PZC**. In this context, various micromechanical models are derived based on the **MOM** approach and the **MT** approach.
- Chapter 3 is concerned with the active damping of a cantilever type smart laminated multiscale **HFRC** beam integrated with the **ACLD** treatment layer utilizing a **FE** model based on **FSDT**.
- In Chapter 4, damping characteristics of multiscale **HFRC** smart plate subjected to simply-supported boundary conditions is investigated using a **FE** model accounting for the **ZZ** effects.
- Chapter 5 is devoted to study the effect of **CNTs** waviness and piezo-fiber orientation on active damping of multiscale **HFRC** smart plate subjected to clamped-clamped boundary conditions. The **HFRC** plate is integrated with two **ACLD** treatment patches at its top surface.
- In Chapter 6, a **FE** model is presented based on the Sinus theory incorporating the **MZZF** to investigate the damping performance of the multiscale **HFRC** substrate shell embedded with two **ACLD** treatment patches at the upper circumference of the cylindrical shell.

Chapter 2

Micromechanical Analysis of a Multiscale Hybrid Fiber Reinforced Composite

*This Chapter presents the micromechanical modeling of the unidirectionally multiscale hybrid fiber reinforced composite (**HFRC**)* (Gupta *et al.*, 2021, 2022b). *Two-phase and three-phase micromechanical models based on the mechanics of materials (**MOM**) approach and the Mori-Tanaka (**MT**) method are derived to estimate the effective elastic coefficients of base composite and multiscale **HFRC**. The effective elastic properties of the **HFRC** are estimated by considering the straight and wavy **CNTs**. Also, effect of **CNT** waviness on the effective elastic coefficients of **HFRC** is studied when the wavy **CNTs** are coplanar with either of the two mutually orthogonal planes. Effects of the carbon fiber volume fractions on the effective elastic properties of the **HFRC** are also investigated.*

2.1 Introduction

In this Chapter, the two- and three-phase analytical micromechanics models based on the **MOM** approach and the **MT** method derived to study the effect of **CNT** reinforcement on the effective elastic properties of proposed multiscale **HFRC**. The distinctive feature of novel multiscale **HFRC** is that the wavy/straight **CNTs** are distributed uniformly in the matrix phase of **HFRC** along the fiber direction i.e., $\boldsymbol{x}$–axis, and the waviness of **CNTs** is considered to be coplanar with two mutually orthogonal planes.

It has been experimentally observed that **CNTs** are curved cylindrical tubes with a relatively high aspect ratio (Shaffer and Windle, 1999; Qian *et al.*, 2000; Vigolo *et al.*, 2000; Ning *et al.*, 2003; Chen *et al.*, 2011; Tsai *et al.*, 2011). It is hypothesized that their affinity to become curved is due to their high aspect ratio and the associated low bending stiffness. Fisher *et al*. (2002) first determined the effective modulus of **CNT**-reinforced composite incorporating curvature of the **CNTs**. They predicted that the **CNT** curvature significantly reduces the effective modulus of the **CNT**-reinforced composite by using a combined finite element and micromechanics approach. In their study, the waviness of a **CNT** was described by a sinusoidal shape. Berhan *et al*. (2004) studied the effect of the waviness of **CNTs** on the mechanical properties of nanotube sheets by using a micromechanics approach. Shi *et al*. (2004) analyzed the influence of the **CNT** waviness and agglomeration on the elastic properties of **CNT**-reinforced composites by employing a micromechanics model. Anumandla and Gibson (2006) estimated the elastic modulus of **CNT**-reinforced composites incorporating **CNT** curvature by deriving a closed-form micromechanics model. In their study, the closed-form analytical micromechanics model is seen to provide reasonable estimates of the effective elastic properties when compared with the experimental results and the predictions by the **FE** models. The effect of the **CNT** curvature on the polymer matrix nanocomposite stiffness has been investigated by Pantano and Cappello (2008). They concluded that in the presence of weak bonding, the enhancement of nanocomposite stiffness can be achieved through the bending energy of **CNTs** rather than through the axial stiffness of **CNTs**. Li and Chou (2009) studied the failure of **CNT**/polymer matrix composites by using the micromechanics model and conducting **FE** simulations. Their results indicate that the **CNT** waviness tends to reduce the elastic modulus and the tensile strength but enhances the ultimate strain of the nanocomposite. Shao *et al*. (2009) derived an analytical model to investigate the influence of the waviness of **CNTs** on the elastic moduli and found that the waviness significantly reduces the stiffening effect of **CNTs**. Shady and Gowayed (2010) investigated the effect of **CNT** curvature on the elastic properties of the nanocomposites utilizing the modified fiber model and the **MT** method. Their results indicate that for a low weight fraction of **CNTs** the effect of curvature is small and as the weight fraction of **CNTs** increases, the effect of **CNT** curvature becomes critical. Tsai *et al*. (2011) studied the effects of **CNT** waviness and its distribution on the effective nanocomposite stiffness. In their study, elastic moduli were over estimated when the **CNT** aspect or the **CNT** waviness followed a symmetric distribution.

Hence, in this Chapter (Gupta *et al.*, 2021, 2022b), two analytical micromechanics models have been presented for estimating the effective elastic properties of the base composite and novel multiscale **HFRC**. In addition, the effect of **CNT** waviness on the effective elastic properties of multiscale **HFRC** is investigated.

2.2 Effective Elastic Properties of HFRC Utilizing MOM Approach

In this Section, the effective elastic properties of the **HFRC** composite were estimated by using the two- and three-phase micromechanical model based on the **MOM** approach. A novel **HFRC** was composed of **CNT**, carbon fiber, and epoxy matrix by considering the rectangular **RVEs** incorporated with cylindrical fibers. In this micromechanical analysis, we restricted ourselves to a single **RVE**. Figure 1(a) represents the schematic of **HFRC** lamina reinforced with carbon fiber in ***x***-axis and epoxy matrix mixed with **CNT** to improve damping and material properties of the matrix. The axial and transverse cross-sections of base composite and **HFRC RVE** is illustrated in Fig. 1(b and c), respectively.

The principal material coordinate (***x-y-z***) or problem coordinate (**1-2-3**) system was followed for deriving the **MOM** model as both coordinate systems exactly matched with each other. The stresses and strains developed in the **HFRC** were illustrated based on this coordinate system, where **1**-axis is known as the fiber axis while the other two axes (i.e., **2**- and **3**-axis) are known as the matrix axis. According to Hooke's law, the constitutive relation for the individual phases of **HFRC** can be expressed as follows,

$$\{\boldsymbol{\sigma}^r\} = [\boldsymbol{C}^r]\{\boldsymbol{\varepsilon}^r\};\ \boldsymbol{r} = \boldsymbol{CF}\ \textbf{and}\ \boldsymbol{Exy} \tag{2.1}$$

$$\{\boldsymbol{\sigma}^r\} = \begin{Bmatrix} \boldsymbol{\sigma}_1 \\ \boldsymbol{\sigma}_2 \\ \boldsymbol{\sigma}_3 \\ \boldsymbol{\sigma}_{23} \\ \boldsymbol{\sigma}_{13} \\ \boldsymbol{\sigma}_{12} \end{Bmatrix}, \quad \{\boldsymbol{\varepsilon}^r\} = \begin{Bmatrix} \boldsymbol{\varepsilon}_1 \\ \boldsymbol{\varepsilon}_2 \\ \boldsymbol{\varepsilon}_3 \\ \boldsymbol{\varepsilon}_{23} \\ \boldsymbol{\varepsilon}_{13} \\ \boldsymbol{\varepsilon}_{12} \end{Bmatrix}$$

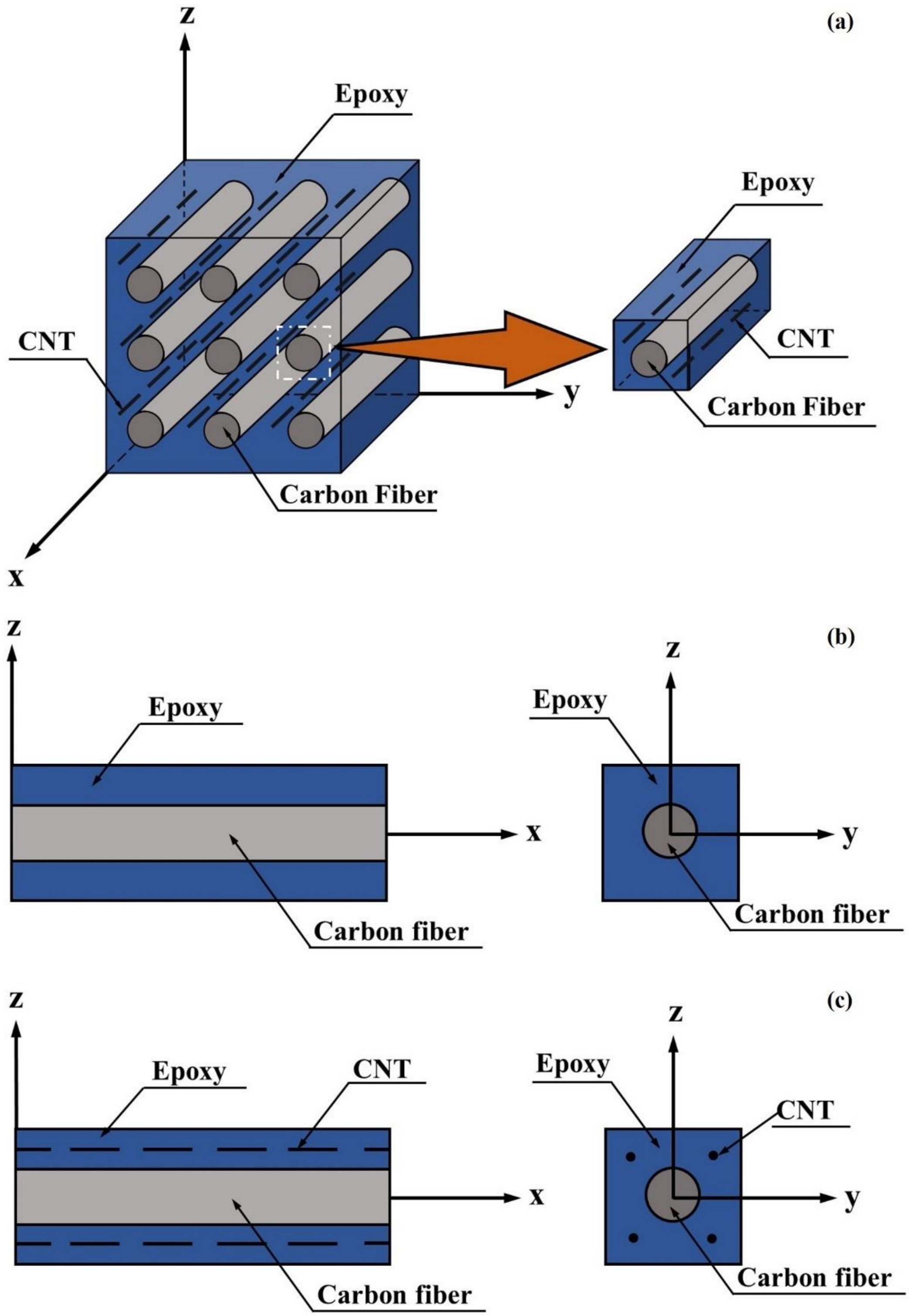

Figure 2.1. (a) Schematic diagram of **HFRC** lamina; axial and transverse cross-sections of **HFRC RVE** considering: (b) two-phase and (c) three-phase.

$$[\boldsymbol{C}^r] = \begin{bmatrix} \boldsymbol{C}_{11} & \boldsymbol{C}_{12} & \boldsymbol{C}_{13} & 0 & 0 & 0 \\ \boldsymbol{C}_{12} & \boldsymbol{C}_{22} & \boldsymbol{C}_{23} & 0 & 0 & 0 \\ \boldsymbol{C}_{13} & \boldsymbol{C}_{23} & \boldsymbol{C}_{33} & 0 & 0 & 0 \\ 0 & 0 & 0 & \boldsymbol{C}_{44} & 0 & 0 \\ 0 & 0 & 0 & 0 & \boldsymbol{C}_{55} & 0 \\ 0 & 0 & 0 & 0 & 0 & \boldsymbol{C}_{66} \end{bmatrix} \tag{2.2}$$

where the stress-strain vector and stiffness matrix are represented by $\{\boldsymbol{\sigma}\}$, $\{\boldsymbol{\varepsilon}\}$ and $[\boldsymbol{C}]$ for ***r***th phase, respectively. The superscript **CF** and ***Exy*** denote carbon fiber and epoxy matrix, respectively, while no superscript is used for composite lamina. In Eq. (2.2), $\boldsymbol{\sigma_1}$, $\boldsymbol{\sigma_2}$ and $\boldsymbol{\sigma_3}$ represent the normal stresses; $\boldsymbol{\varepsilon_1}$, $\boldsymbol{\varepsilon_2}$ and $\boldsymbol{\varepsilon_3}$ represent the normal strains in the respective **1**, **2**, and **3**–directions; $\boldsymbol{\sigma_{12}}$, $\boldsymbol{\sigma_{13}}$ and $\boldsymbol{\sigma_{23}}$ represent shear stresses; $\boldsymbol{\varepsilon_{12}}$, $\boldsymbol{\varepsilon_{13}}$ and $\boldsymbol{\varepsilon_{23}}$ represent shear strains and $\boldsymbol{C_{ij}}$ indicates the elastic stiffness coefficients. Using iso-field (iso-stress and iso-strain) and rules-of-mixture (**ROM**) conditions (Smith and Auld, 1991; Benveniste and Dvorak, 1992; Ray, 2006), the assumptions are mentioned below:

- The analysis is linearly elastic.
- The composite is homogeneous throughout.
- Fibers and nanofillers are aligned in **1**-axis i.e. axial direction.
- Fibers and nanofillers are parallel and continuous.
- Fiber, nanofiller, and matrix are equally long.
- No slippage between fiber, nanofiller, and matrix.

2.2.1 Two-Phase MOM Approach

The two-phase **MOM** model developed by earlier researcher Kundalwal and Ray (2011) is implemented in the present work to evaluate the elastic properties. The model determines the transversely isotropic effective elastic properties of a base composite constituting two phases such as carbon fiber and epoxy matrix. To satisfy no slippage condition between fiber and matrix, the assumption of iso-field and **ROM** can be expressed as follows, In the case of iso-field condition:

$$\begin{Bmatrix} \boldsymbol{\varepsilon_{11}^{CF}} \\ \boldsymbol{\sigma_{22}^{CF}} \\ \boldsymbol{\sigma_{33}^{CF}} \\ \boldsymbol{\sigma_{23}^{CF}} \\ \boldsymbol{\sigma_{13}^{CF}} \\ \boldsymbol{\sigma_{12}^{CF}} \end{Bmatrix} = \begin{Bmatrix} \boldsymbol{\varepsilon_{11}^{Exy}} \\ \boldsymbol{\sigma_{22}^{Exy}} \\ \boldsymbol{\sigma_{33}^{Exy}} \\ \boldsymbol{\sigma_{23}^{Exy}} \\ \boldsymbol{\sigma_{13}^{Exy}} \\ \boldsymbol{\sigma_{12}^{Exy}} \end{Bmatrix} = \begin{Bmatrix} \boldsymbol{\varepsilon_{11}} \\ \boldsymbol{\sigma_{22}} \\ \boldsymbol{\sigma_{33}} \\ \boldsymbol{\sigma_{23}} \\ \boldsymbol{\sigma_{13}} \\ \boldsymbol{\sigma_{12}} \end{Bmatrix} \tag{2.3}$$

and in case of **ROM** condition:

$$\boldsymbol{v_{CF}} \begin{Bmatrix} \boldsymbol{\sigma_{11}^{CF}} \\ \boldsymbol{\varepsilon_{22}^{CF}} \\ \boldsymbol{\varepsilon_{33}^{CF}} \\ \boldsymbol{\varepsilon_{23}^{CF}} \\ \boldsymbol{\varepsilon_{13}^{CF}} \\ \boldsymbol{\varepsilon_{12}^{CF}} \end{Bmatrix} + \boldsymbol{v_{Exy}} \begin{Bmatrix} \boldsymbol{\sigma_{11}^{Exy}} \\ \boldsymbol{\varepsilon_{22}^{Exy}} \\ \boldsymbol{\varepsilon_{33}^{Exy}} \\ \boldsymbol{\varepsilon_{23}^{Exy}} \\ \boldsymbol{\varepsilon_{13}^{Exy}} \\ \boldsymbol{\varepsilon_{12}^{Exy}} \end{Bmatrix} = \begin{Bmatrix} \boldsymbol{\sigma_{11}} \\ \boldsymbol{\varepsilon_{22}} \\ \boldsymbol{\varepsilon_{33}} \\ \boldsymbol{\varepsilon_{23}} \\ \boldsymbol{\varepsilon_{13}} \\ \boldsymbol{\varepsilon_{12}} \end{Bmatrix} \tag{2.4}$$

where $\boldsymbol{v_{CF}}$ and $\boldsymbol{v_{Exy}}$ denote the volume fraction of carbon fiber and epoxy matrix and $\boldsymbol{v_{Exy}} = 1 - \boldsymbol{v_{CF}}$. By using the Eqs. (2.1), (2.3)-(2.4), the stress and strain vector in the base composite can be written with respect to their constituent phases can be written as:

$$\{\boldsymbol{\sigma}\} = [\boldsymbol{C_1}]\{\boldsymbol{\varepsilon^{CF}}\} + [\boldsymbol{C_2}]\{\boldsymbol{\varepsilon^{Exy}}\} \tag{2.5}$$

$$\{\boldsymbol{\varepsilon}\} = [\boldsymbol{V_1}]\{\boldsymbol{\varepsilon^{CF}}\} + [\boldsymbol{V_2}]\{\boldsymbol{\varepsilon^{Exy}}\} \tag{2.6}$$

The relation between stresses and strains in Eqs. (2.1) and (2.3) of fiber and matrix is given by:

$$[\boldsymbol{C_3}]\{\boldsymbol{\varepsilon^{CF}}\} - [\boldsymbol{C_4}]\{\boldsymbol{\varepsilon^{Exy}}\} = 0 \tag{2.7}$$

The matrices used in Eqs. (2.5)-(2.7) are expressed as:

$$[\boldsymbol{C_1}] = \boldsymbol{v_{CF}} \begin{bmatrix} \boldsymbol{C_{11}^{CF}} & \boldsymbol{C_{12}^{CF}} & \boldsymbol{C_{13}^{CF}} & 0 & 0 & 0 \\ 0 & 0 & 0 & 0 & 0 & 0 \\ 0 & 0 & 0 & 0 & 0 & 0 \\ 0 & 0 & 0 & 0 & 0 & 0 \\ 0 & 0 & 0 & 0 & 0 & 0 \\ 0 & 0 & 0 & 0 & 0 & 0 \end{bmatrix},$$

$$[\boldsymbol{C_2}] = \begin{bmatrix} \boldsymbol{v_{Exy}C_{11}^{Exy}} & \boldsymbol{v_{Exy}C_{12}^{Exy}} & \boldsymbol{v_{Exy}C_{13}^{Exy}} & 0 & 0 & 0 \\ \boldsymbol{C_{12}^{Exy}} & \boldsymbol{C_{22}^{Exy}} & \boldsymbol{C_{23}^{Exy}} & 0 & 0 & 0 \\ \boldsymbol{C_{13}^{Exy}} & \boldsymbol{C_{23}^{Exy}} & \boldsymbol{C_{33}^{Exy}} & 0 & 0 & 0 \\ 0 & 0 & 0 & \boldsymbol{C_{44}^{Exy}} & 0 & 0 \\ 0 & 0 & 0 & 0 & \boldsymbol{C_{55}^{Exy}} & 0 \\ 0 & 0 & 0 & 0 & 0 & \boldsymbol{C_{66}^{Exy}} \end{bmatrix},$$

$$[\boldsymbol{C_3}] = \begin{bmatrix} 1 & 0 & 0 & 0 & 0 & 0 \\ \boldsymbol{C_{12}^{CF}} & \boldsymbol{C_{22}^{CF}} & \boldsymbol{C_{23}^{CF}} & 0 & 0 & 0 \\ \boldsymbol{C_{13}^{CF}} & \boldsymbol{C_{23}^{CF}} & \boldsymbol{C_{33}^{CF}} & 0 & 0 & 0 \\ 0 & 0 & 0 & \boldsymbol{C_{44}^{CF}} & 0 & 0 \\ 0 & 0 & 0 & 0 & \boldsymbol{C_{55}^{CF}} & 0 \\ 0 & 0 & 0 & 0 & 0 & \boldsymbol{C_{66}^{CF}} \end{bmatrix},$$

$$[\boldsymbol{C_4}] = \begin{bmatrix} 1 & 0 & 0 & 0 & 0 & 0 \\ \boldsymbol{C_{12}^{Exy}} & \boldsymbol{C_{22}^{Exy}} & \boldsymbol{C_{23}^{Exy}} & 0 & 0 & 0 \\ \boldsymbol{C_{13}^{Exy}} & \boldsymbol{C_{23}^{Exy}} & \boldsymbol{C_{33}^{Exy}} & 0 & 0 & 0 \\ 0 & 0 & 0 & \boldsymbol{C_{44}^{Exy}} & 0 & 0 \\ 0 & 0 & 0 & 0 & \boldsymbol{C_{55}^{Exy}} & 0 \\ 0 & 0 & 0 & 0 & 0 & \boldsymbol{C_{66}^{Exy}} \end{bmatrix},$$

$$[\boldsymbol{V_1}] = \begin{bmatrix} 0 & 0 & 0 & 0 & 0 & 0 \\ 0 & \boldsymbol{v_{CF}} & 0 & 0 & 0 & 0 \\ 0 & 0 & \boldsymbol{v_{CF}} & 0 & 0 & 0 \\ 0 & 0 & 0 & \boldsymbol{v_{CF}} & 0 & 0 \\ 0 & 0 & 0 & 0 & \boldsymbol{v_{CF}} & 0 \\ 0 & 0 & 0 & 0 & 0 & \boldsymbol{v_{CF}} \end{bmatrix},$$

$$[\boldsymbol{V_2}] = \begin{bmatrix} 0 & 0 & 0 & 0 & 0 & 0 \\ 0 & \boldsymbol{v_{Exy}} & 0 & 0 & 0 & 0 \\ 0 & 0 & \boldsymbol{v_{Exy}} & 0 & 0 & 0 \\ 0 & 0 & 0 & \boldsymbol{v_{Exy}} & 0 & 0 \\ 0 & 0 & 0 & 0 & \boldsymbol{v_{Exy}} & 0 \\ 0 & 0 & 0 & 0 & 0 & \boldsymbol{v_{Exy}} \end{bmatrix}$$

Substituting the Eqs. (2.6) and (2.7) in Eq. (2.5), the subsequent constitutive equation for the two-phase composite is obtained as:

$$\{\boldsymbol{\sigma}\} = [\boldsymbol{C}]\{\boldsymbol{\varepsilon}\} \tag{2.8}$$

Finally, the effective elastic properties of the two-phase **MOM** model can be expressed as:

$$[\boldsymbol{C}] = [\boldsymbol{C_1}][\boldsymbol{V_3}]^{-\mathbf{1}} + [\boldsymbol{C_2}][\boldsymbol{V_4}]^{-\mathbf{1}} \tag{2.9}$$

$$[\boldsymbol{V_3}] = [\boldsymbol{V_1}] + [\boldsymbol{V_2}][\boldsymbol{C_4}]^{-\mathbf{1}}[\boldsymbol{C_3}] \text{ and } [\boldsymbol{V_4}] = [\boldsymbol{V_2}] + [\boldsymbol{V_1}][\boldsymbol{C_3}]^{-\mathbf{1}}[\boldsymbol{C_4}] \tag{2.10}$$

2.2.2 Three-Phase MOM Approach

To enhance the optimal performance of a composite there should be an interaction between fiber and matrix. This could be done by surface treating the fiber or matrix or both before using them. The surface treatment of fiber is the most commonly used technique called sizing. Such treatment on the matrix to improve its adhesive property due to the addition of nanofillers is promising and received a lot of attention from the researchers (Yu *et al.*, 2014; Rathi and Kundalwal, 2020). In this study, we are treating the epoxy matrix before impregnating carbon fiber into it, as shown in Fig. 1(c). For the three-phase composite material which is also known as a hybrid composite material, the constitutive relation for the individual phases of **HFRC** can be expressed as:

$$\{\boldsymbol{\sigma}^{r}\} = [\boldsymbol{C}^{r}]\{\boldsymbol{\varepsilon}^{r}\}; \; \boldsymbol{r} = \boldsymbol{CF}, \boldsymbol{CNT} \text{ and } \boldsymbol{Exy} \tag{2.11}$$

where the superscripts **CF**, **CNT**, and ***Exy*** denote carbon fiber, **CNT** nanofiller, and epoxy matrix, respectively. To satisfy no slippage condition between all individual phases, the assumption of iso-field and **ROM** can be expressed as:

In the case of iso-field condition:

$$\begin{Bmatrix} \varepsilon_{11}^{CF} \\ \sigma_{22}^{CF} \\ \sigma_{33}^{CF} \\ \sigma_{23}^{CF} \\ \sigma_{13}^{CF} \\ \sigma_{12}^{CF} \end{Bmatrix} = \begin{Bmatrix} \varepsilon_{11}^{CNT} \\ \sigma_{22}^{CNT} \\ \sigma_{33}^{CNT} \\ \sigma_{23}^{CNT} \\ \sigma_{13}^{CNT} \\ \sigma_{12}^{CNT} \end{Bmatrix} = \begin{Bmatrix} \varepsilon_{11}^{Exy} \\ \sigma_{22}^{Exy} \\ \sigma_{33}^{Exy} \\ \sigma_{23}^{Exy} \\ \sigma_{13}^{Exy} \\ \sigma_{12}^{Exy} \end{Bmatrix} = \begin{Bmatrix} \varepsilon_{11} \\ \sigma_{22} \\ \sigma_{33} \\ \sigma_{23} \\ \sigma_{13} \\ \sigma_{12} \end{Bmatrix} \tag{2.12}$$

and in case of **ROM** condition:

$$v_{CF}\begin{Bmatrix} \sigma_{11}^{CF} \\ \varepsilon_{22}^{CF} \\ \varepsilon_{33}^{CF} \\ \varepsilon_{23}^{CF} \\ \varepsilon_{13}^{CF} \\ \varepsilon_{12}^{CF} \end{Bmatrix} + v_{CNT}\begin{Bmatrix} \sigma_{11}^{CNT} \\ \varepsilon_{22}^{CNT} \\ \varepsilon_{33}^{CNT} \\ \varepsilon_{23}^{CNT} \\ \varepsilon_{13}^{CNT} \\ \varepsilon_{12}^{CNT} \end{Bmatrix} + v_{Exy}\begin{Bmatrix} \sigma_{11}^{Exy} \\ \varepsilon_{22}^{Exy} \\ \varepsilon_{33}^{Exy} \\ \varepsilon_{23}^{Exy} \\ \varepsilon_{13}^{Exy} \\ \varepsilon_{12}^{Exy} \end{Bmatrix} = \begin{Bmatrix} \sigma_{11} \\ \varepsilon_{22} \\ \varepsilon_{33} \\ \varepsilon_{23} \\ \varepsilon_{13} \\ \varepsilon_{12} \end{Bmatrix} \tag{2.13}$$

where v_{CNT} denotes the volume fraction of the **CNT**. The stress and strain vector on the carbon fiber and its neighboring phases of **HFRC** can be written with respect to their constituent phases as follows:

$$\{\sigma\} = [C_1]\{\varepsilon^{CF}\} + [C_2]\{\varepsilon^{CNT}\} + [C_3]\{\varepsilon^{Exy}\} \tag{2.14}$$

$$\{\varepsilon\} = [V_1]\{\varepsilon^{CF}\} + [V_2]\{\varepsilon^{CNT}\} + [V_3]\{\varepsilon^{Exy}\} \tag{2.15}$$

$$[C_4]\{\varepsilon^{CF}\} - [C_5]\{\varepsilon^{CNT}\} = 0 \tag{2.16}$$

$$[C_5]\{\varepsilon^{CNT}\} - [C_6]\{\varepsilon^{Exy}\} = 0 \tag{2.17}$$

The following matrices are used in Eqs. (2.14)-(2.17),

$$[C_1] = \begin{bmatrix} v_{CF}C_{11}^{CF} & v_{CF}C_{12}^{CF} & v_{CF}C_{13}^{CF} & 0 & 0 & 0 \\ C_{12}^{CF} & C_{22}^{CF} & C_{23}^{CF} & 0 & 0 & 0 \\ C_{13}^{CF} & C_{23}^{CF} & C_{33}^{CF} & 0 & 0 & 0 \\ 0 & 0 & 0 & C_{44}^{CF} & 0 & 0 \\ 0 & 0 & 0 & 0 & C_{55}^{CF} & 0 \\ 0 & 0 & 0 & 0 & 0 & C_{66}^{CF} \end{bmatrix},$$

$$[\boldsymbol{C}_2] = \boldsymbol{v}_{\boldsymbol{CNT}} \begin{bmatrix} \boldsymbol{C}_{11}^{CNT} & \boldsymbol{C}_{12}^{CNT} & \boldsymbol{C}_{13}^{CNT} & 0 & 0 & 0 \\ 0 & 0 & 0 & 0 & 0 & 0 \\ 0 & 0 & 0 & 0 & 0 & 0 \\ 0 & 0 & 0 & 0 & 0 & 0 \\ 0 & 0 & 0 & 0 & 0 & 0 \\ 0 & 0 & 0 & 0 & 0 & 0 \end{bmatrix},$$

$$[\boldsymbol{C}_3] = \boldsymbol{v}_{\boldsymbol{Exy}} \begin{bmatrix} \boldsymbol{C}_{11}^{Exy} & \boldsymbol{C}_{12}^{Exy} & \boldsymbol{C}_{13}^{Exy} & 0 & 0 & 0 \\ 0 & 0 & 0 & 0 & 0 & 0 \\ 0 & 0 & 0 & 0 & 0 & 0 \\ 0 & 0 & 0 & 0 & 0 & 0 \\ 0 & 0 & 0 & 0 & 0 & 0 \\ 0 & 0 & 0 & 0 & 0 & 0 \end{bmatrix},$$

$$[\boldsymbol{C}_4] = \begin{bmatrix} 1 & 0 & 0 & 0 & 0 & 0 \\ \boldsymbol{C}_{12}^{CF} & \boldsymbol{C}_{22}^{CF} & \boldsymbol{C}_{23}^{CF} & 0 & 0 & 0 \\ \boldsymbol{C}_{13}^{CF} & \boldsymbol{C}_{23}^{CF} & \boldsymbol{C}_{33}^{CF} & 0 & 0 & 0 \\ 0 & 0 & 0 & \boldsymbol{C}_{44}^{CF} & 0 & 0 \\ 0 & 0 & 0 & 0 & \boldsymbol{C}_{55}^{CF} & 0 \\ 0 & 0 & 0 & 0 & 0 & \boldsymbol{C}_{66}^{CF} \end{bmatrix},$$

$$[\boldsymbol{C}_5] = \begin{bmatrix} 1 & 0 & 0 & 0 & 0 & 0 \\ \boldsymbol{C}_{12}^{CNT} & \boldsymbol{C}_{22}^{CNT} & \boldsymbol{C}_{23}^{CNT} & 0 & 0 & 0 \\ \boldsymbol{C}_{13}^{CNT} & \boldsymbol{C}_{23}^{CNT} & \boldsymbol{C}_{33}^{CNT} & 0 & 0 & 0 \\ 0 & 0 & 0 & \boldsymbol{C}_{44}^{CNT} & 0 & 0 \\ 0 & 0 & 0 & 0 & \boldsymbol{C}_{55}^{CNT} & 0 \\ 0 & 0 & 0 & 0 & 0 & \boldsymbol{C}_{66}^{CNT} \end{bmatrix},$$

$$[\boldsymbol{C}_6] = \begin{bmatrix} 1 & 0 & 0 & 0 & 0 & 0 \\ \boldsymbol{C}_{12}^{Exy} & \boldsymbol{C}_{22}^{Exy} & \boldsymbol{C}_{23}^{Exy} & 0 & 0 & 0 \\ \boldsymbol{C}_{13}^{Exy} & \boldsymbol{C}_{23}^{Exy} & \boldsymbol{C}_{33}^{Exy} & 0 & 0 & 0 \\ 0 & 0 & 0 & \boldsymbol{C}_{44}^{Exy} & 0 & 0 \\ 0 & 0 & 0 & 0 & \boldsymbol{C}_{55}^{Exy} & 0 \\ 0 & 0 & 0 & 0 & 0 & \boldsymbol{C}_{66}^{Exy} \end{bmatrix},$$

$$[\boldsymbol{V}_1] = \begin{bmatrix} 0 & 0 & 0 & 0 & 0 & 0 \\ 0 & \boldsymbol{v}_{\boldsymbol{CF}} & 0 & 0 & 0 & 0 \\ 0 & 0 & \boldsymbol{v}_{\boldsymbol{CF}} & 0 & 0 & 0 \\ 0 & 0 & 0 & \boldsymbol{v}_{\boldsymbol{CF}} & 0 & 0 \\ 0 & 0 & 0 & 0 & \boldsymbol{v}_{\boldsymbol{CF}} & 0 \\ 0 & 0 & 0 & 0 & 0 & \boldsymbol{v}_{\boldsymbol{CF}} \end{bmatrix},$$

$$[\boldsymbol{V_2}] = \begin{bmatrix} 0 & 0 & 0 & 0 & 0 & 0 \\ 0 & \boldsymbol{v_{CNT}} & 0 & 0 & 0 & 0 \\ 0 & 0 & \boldsymbol{v_{CNT}} & 0 & 0 & 0 \\ 0 & 0 & 0 & \boldsymbol{v_{CNT}} & 0 & 0 \\ 0 & 0 & 0 & 0 & \boldsymbol{v_{CNT}} & 0 \\ 0 & 0 & 0 & 0 & 0 & \boldsymbol{v_{CNT}} \end{bmatrix}, \text{ and}$$

$$[\boldsymbol{V_3}] = \begin{bmatrix} 0 & 0 & 0 & 0 & 0 & 0 \\ 0 & \boldsymbol{v_{Exy}} & 0 & 0 & 0 & 0 \\ 0 & 0 & \boldsymbol{v_{Exy}} & 0 & 0 & 0 \\ 0 & 0 & 0 & \boldsymbol{v_{Exy}} & 0 & 0 \\ 0 & 0 & 0 & 0 & \boldsymbol{v_{Exy}} & 0 \\ 0 & 0 & 0 & 0 & 0 & \boldsymbol{v_{Exy}} \end{bmatrix} \tag{2.18}$$

Using Eqs. (2.15)-(2.17), the local strain vectors can be expressed in terms of the composite strain and subsequently, using them in Eq. (2.14), the following effective elastic coefficient matrix of the composite can be obtained.

Finally, the effective elastic properties of **HFRC** can be expressed as:

$$[\boldsymbol{C}] = [\boldsymbol{C_1}][\boldsymbol{V_5}]^{-1} + [\boldsymbol{C_7}][\boldsymbol{V_6}]^{-1} \tag{2.19}$$

where

$$[\boldsymbol{C_7}] = [\boldsymbol{C_3}] + [\boldsymbol{C_2}][\boldsymbol{C_5}]^{-1}[\boldsymbol{C_6}],$$

$$[\boldsymbol{V_4}] = [\boldsymbol{V_3}] + [\boldsymbol{V_2}][\boldsymbol{C_5}]^{-1}[\boldsymbol{C_6}],$$

$$[\boldsymbol{V_5}] = [\boldsymbol{V_1}] + [\boldsymbol{V_4}][\boldsymbol{C_6}]^{-1}[\boldsymbol{C_4}], \quad \text{and}$$

$$[\boldsymbol{V_6}] = [\boldsymbol{V_4}] + [\boldsymbol{V_1}][\boldsymbol{C_4}]^{-1}[\boldsymbol{C_6}] \tag{2.20}$$

2.3 Effective Elastic Properties of HFRC Using MT Approach

In this Section, we derived two- and three-phase micromechanical models based on the **MT** method to evaluate the effective elastic properties of base composite and **HFRC**. A novel **HFRC** comprises carbon fibers and epoxy matrix incorporated with **CNTs**. The **RVEs** of **HFRC** considering cylindrical carbon fiber and **CNTs** are shown in Fig. 2.2. For the present investigation, we restricted ourselves to a single **RVE**. Figure 2.2(a) shows the schematic of **HFRC** reinforced with carbon fiber along the ***x***-axis and epoxy matrix mixed with **CNTs** to improve damping and material properties of the resulting

HFRC. The longitudinal and transverse cross-sections of base composite and **HFRC RVEs** are illustrated in Fig. 2.2(b) and 2.2(c), respectively.

2.3.1 Two-Phase MT Approach

The **MT** model is an efficient micromechanical model that accounts for the Eshelby tensor for interaction between fibers and matrix. Therefore, in this study, the **MT** model is used to predict the effective elastic properties of the base composite and **HFRC**. According to Benveniste (1987), the effective elastic properties of two-phase composite using **MT** model can be predicted as follows:

$$[\boldsymbol{C}] = [\boldsymbol{C}^{\boldsymbol{m}}] + \boldsymbol{v}_{\boldsymbol{f}}\left([\boldsymbol{C}^{\boldsymbol{f}}] - [\boldsymbol{C}^{\boldsymbol{m}}]\right)[\boldsymbol{A}_{\mathbf{1}}] \tag{2.21}$$

in which the subscripts $\boldsymbol{m}$ and $\boldsymbol{f}$ are used for the matrix and carbon fiber phases, respectively. The concentration factor $[\boldsymbol{A}_{\mathbf{1}}]$ is given by:

$$[\boldsymbol{A}_{\mathbf{1}}] = [\widetilde{\boldsymbol{A}}_{\mathbf{1}}]\left[\boldsymbol{v}_{\boldsymbol{m}}[\boldsymbol{I}] + \boldsymbol{v}_{\boldsymbol{f}}[\widetilde{\boldsymbol{A}}_{\mathbf{1}}]\right]^{-\mathbf{1}} \qquad \text{and}$$

$$[\widetilde{\boldsymbol{A}}_{\mathbf{1}}] = \left[[\boldsymbol{I}] + [\boldsymbol{S}]([\boldsymbol{C}^{\boldsymbol{m}}])^{-\mathbf{1}}\left([\boldsymbol{C}^{\boldsymbol{f}}] - [\boldsymbol{C}^{\boldsymbol{m}}]\right)\right]^{-\mathbf{1}} \tag{2.22}$$

in which $\boldsymbol{v}_{\boldsymbol{m}}$, and $\boldsymbol{v}_{\boldsymbol{f}}$ denote the volume fractions of epoxy matrix and carbon fiber, respectively. In Eq. (2.22), $[\boldsymbol{S}]$ represents the Eshelby tensor and for the cylindrical carbon fiber, the Eshelby tensor is given by:

$$[\boldsymbol{S}] = \begin{bmatrix} \boldsymbol{S}_{11} & \boldsymbol{S}_{12} & \boldsymbol{S}_{13} & 0 & 0 & 0 \\ \boldsymbol{S}_{21} & \boldsymbol{S}_{22} & \boldsymbol{S}_{23} & 0 & 0 & 0 \\ \boldsymbol{S}_{31} & \boldsymbol{S}_{32} & \boldsymbol{S}_{33} & 0 & 0 & 0 \\ 0 & 0 & 0 & \boldsymbol{S}_{44} & 0 & 0 \\ 0 & 0 & 0 & 0 & \boldsymbol{S}_{55} & 0 \\ 0 & 0 & 0 & 0 & 0 & \boldsymbol{S}_{66} \end{bmatrix}$$

where

$$\boldsymbol{S}_{11} = 0, \qquad \boldsymbol{S}_{22} = \boldsymbol{S}_{33} = \frac{5 - 4\boldsymbol{v}^{\boldsymbol{m}}}{8(1 - \boldsymbol{v}^{\boldsymbol{m}})}\ , \qquad \boldsymbol{S}_{21} = \boldsymbol{S}_{31} = \frac{\boldsymbol{v}^{\boldsymbol{m}}}{2(1 - \boldsymbol{v}^{\boldsymbol{m}})}\ ,$$

$$\boldsymbol{S}_{23} = \boldsymbol{S}_{32} = \frac{4\boldsymbol{v}^{\boldsymbol{m}} - 1}{8(1 - \boldsymbol{v}^{\boldsymbol{m}})}, \qquad \boldsymbol{S}_{12} = \boldsymbol{S}_{13} = 0, \qquad \boldsymbol{S}_{55} = \boldsymbol{S}_{66} = \frac{1}{4},$$

$$\text{and } \boldsymbol{S_{44}} = \frac{3 - 4\boldsymbol{v^m}}{8(1 - \boldsymbol{v^m})}$$

where $\boldsymbol{v^m}$ denote the Poisson's ratio of the polymer matrix.

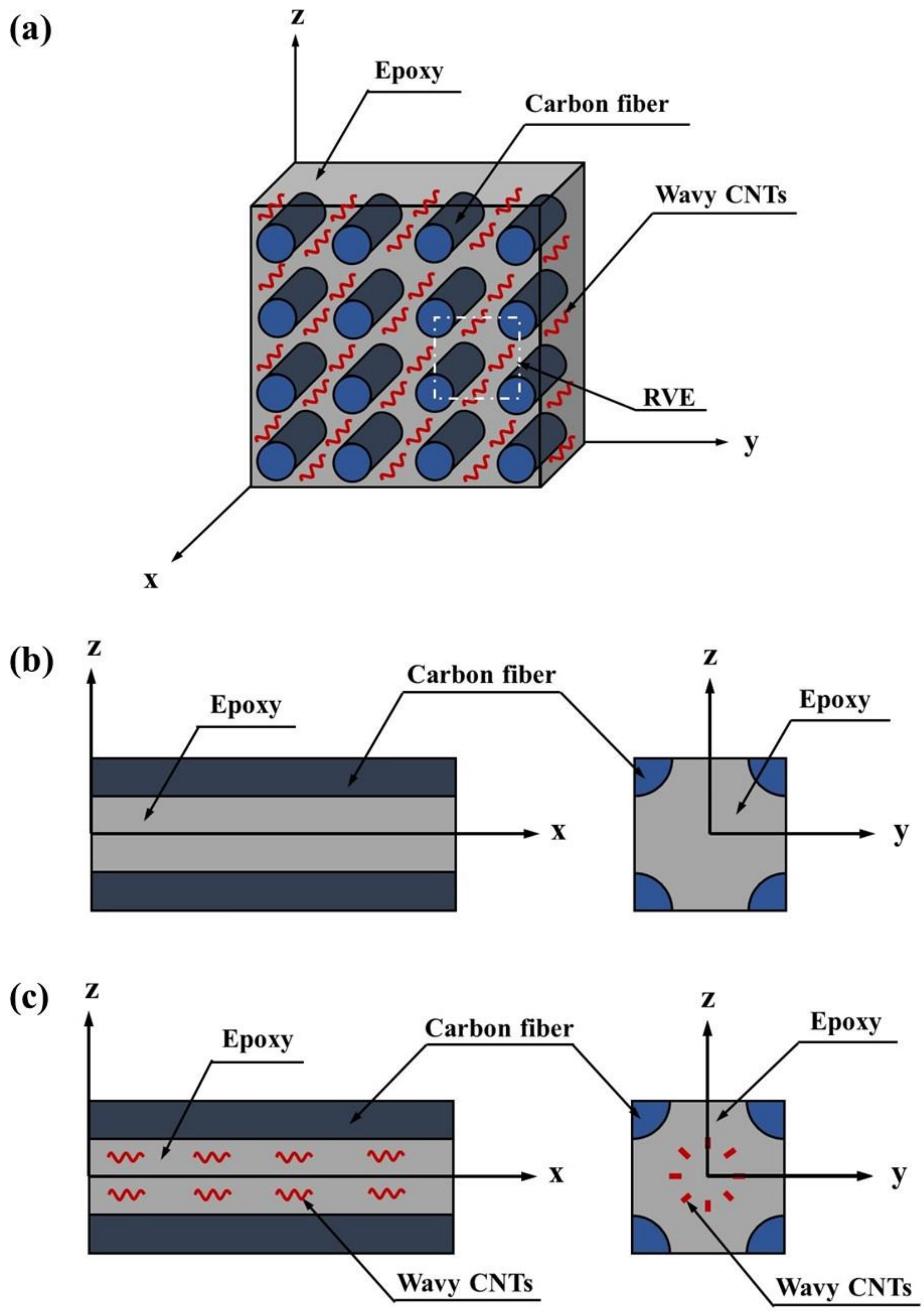

Figure 2.2. (a) Schematic of **RVEs** of base composite/**HFRC** with wavy CNTs; axial and transverse cross-sections of (b) two-phase and (c) three-phase **RVEs**.

2.3.2 Three-Phase MT Approach

In the present study, a multiscale **HFRC** is also considered, which comprises three phases: microscale carbon fibers, nanoscale **CNTs**, and epoxy matrix. The schematic representation of multiscale composite with **CNTs** is shown in Fig. 2.2(a) and the cross-section of the same is shown in Fig. 2.2(c). The effective elastic properties of such multiscale **HFRC** can be determined using the three-phase **MT** model, as follows,

$$[\boldsymbol{C}] = \left[v_m[\boldsymbol{C}^m][\boldsymbol{I}] + v_f[\boldsymbol{C}^f][\boldsymbol{A}_f] + v_i[\boldsymbol{C}^i][\boldsymbol{A}_i]\right]\left[v_m[\boldsymbol{I}] + v_f[\boldsymbol{A}_f] + v_i[\boldsymbol{A}_i]\right]^{-1} \quad (2.23)$$

where $\boldsymbol{v_i}$ is the volume fractions of **CNT** nanofiller and $[\boldsymbol{A}_f]$ and $[\boldsymbol{A}_i]$ appearing in Eq. (2.23) represent the concentration factors, as follows,

$$[\boldsymbol{A}_f] = \left[[\boldsymbol{I}] + [\boldsymbol{S}_f]\{([\boldsymbol{C}^m])^{-1}([\boldsymbol{C}^f] - [\boldsymbol{C}^m])\}\right]^{-1}$$

$$[\boldsymbol{A}_i] = \left[[\boldsymbol{I}] + [\boldsymbol{S}_i]\{([\boldsymbol{C}^m])^{-1}([\boldsymbol{C}^i] - [\boldsymbol{C}^m])\}\right]^{-1} \quad (2.24)$$

where $[\boldsymbol{S}_f]$ and $[\boldsymbol{S}_i]$ are the Esheby tensors for the **CF** and **CNT** phases, respectively; and $[\boldsymbol{I}]$ is an identity matrix. For the sake of simplicity, the **CNT** is assumed as an equivalent solid cylinder fiber (Kundalwal, 2018). Thus, the Eshelby tensor for the cylindrical inclusion of carbon fiber and **CNT** in the polymer matrix can be explicitly written as (Qiu and Weng, 1990):

$$[\mathrm{S_f}] = \begin{bmatrix} \boldsymbol{S}_{11}^f & \boldsymbol{S}_{12}^f & \boldsymbol{S}_{13}^f & 0 & 0 & 0 \\ \boldsymbol{S}_{21}^f & \boldsymbol{S}_{22}^f & \boldsymbol{S}_{23}^f & 0 & 0 & 0 \\ \boldsymbol{S}_{31}^f & \boldsymbol{S}_{32}^f & \boldsymbol{S}_{33}^f & 0 & 0 & 0 \\ 0 & 0 & 0 & \boldsymbol{S}_{44}^f & 0 & 0 \\ 0 & 0 & 0 & 0 & \boldsymbol{S}_{55}^f & 0 \\ 0 & 0 & 0 & 0 & 0 & \boldsymbol{S}_{66}^f \end{bmatrix} \quad \text{and}$$

$$[\boldsymbol{S_i}] = \begin{bmatrix} \boldsymbol{S^i_{11}} & \boldsymbol{S^i_{12}} & \boldsymbol{S^i_{13}} & 0 & 0 & 0 \\ \boldsymbol{S^i_{21}} & \boldsymbol{S^i_{22}} & \boldsymbol{S^i_{23}} & 0 & 0 & 0 \\ \boldsymbol{S^i_{31}} & \boldsymbol{S^i_{32}} & \boldsymbol{S^i_{33}} & 0 & 0 & 0 \\ 0 & 0 & 0 & \boldsymbol{S^i_{44}} & 0 & 0 \\ 0 & 0 & 0 & 0 & \boldsymbol{S^i_{55}} & 0 \\ 0 & 0 & 0 & 0 & 0 & \boldsymbol{S^i_{66}} \end{bmatrix} \tag{2.25}$$

where

$$\boldsymbol{S^f_{11}} = 0, \qquad \boldsymbol{S^f_{22}} = \boldsymbol{S^f_{33}} = \frac{5 - 4\boldsymbol{v^m}}{8(1 - \boldsymbol{v^m})}, \qquad \boldsymbol{S^f_{21}} = \boldsymbol{S^f_{31}} = \frac{\boldsymbol{v^m}}{2(1 - \boldsymbol{v^m})},$$

$$\boldsymbol{S^f_{23}} = \boldsymbol{S^f_{32}} = \frac{4\boldsymbol{v^i} - 1}{8(1 - \boldsymbol{v^i})}, \qquad \boldsymbol{S^f_{12}} = \boldsymbol{S^f_{13}} = 0, \qquad \boldsymbol{S^f_{55}} = \boldsymbol{S^f_{66}} = \frac{1}{4},$$

$$\text{and} \quad \boldsymbol{S^f_{44}} = \frac{3 - 4\boldsymbol{v^m}}{8(1 - \boldsymbol{v^m})}$$

$$\boldsymbol{S^i_{11}} = 0, \qquad \boldsymbol{S^i_{22}} = \boldsymbol{S^i_{33}} = \frac{5 - 4\boldsymbol{v^m}}{8(1 - \boldsymbol{v^m})}, \qquad \boldsymbol{S^i_{21}} = \boldsymbol{S^i_{31}} = \frac{\boldsymbol{v^m}}{2(1 - \boldsymbol{v^m})},$$

$$\boldsymbol{S^i_{23}} = \boldsymbol{S^i_{32}} = \frac{4\boldsymbol{v^m} - 1}{8(1 - \boldsymbol{v^m})}, \qquad \boldsymbol{S^i_{12}} = \boldsymbol{S^i_{13}} = 0, \qquad \boldsymbol{S^i_{55}} = \boldsymbol{S^i_{66}} = \frac{1}{4},$$

$$\text{and} \quad \boldsymbol{S^i_{44}} = \frac{3 - 4\boldsymbol{v^m}}{8(1 - \boldsymbol{v^m})}$$

2.4 HFRC with Wavy CNTs

The schematic representation of wavy **CNT** embedded in the epoxy matrix is illustrated in Fig. 2.3. Since the carbon fiber and **CNT** are oriented along the $\boldsymbol{x}$-axis, Fig. 2.3(a-b) shows the transmission electron microscopes **(TEM)** image of wavy **CNT** which depicts the sinusoidal waviness of **CNT**. Thus, in the current work, we modeled the wavy **CNT** as a sinusoidal solid **CNT** nanofiller. Figure 2.3(c) represents the **RVE** of epoxy matrix incorporated with wavy **CNT** nanofillers. The wavy **CNTs** are considered to be coplanar with **1–2** or **1–3** plane, attributing to the constructional feature of **HFRC**. The **RVE** is distributed into infinitesimally thin slices of thickness $\boldsymbol{dx}$. Then, the homogenized effective elastic properties of the **HFRC** can be predicted by averaging the effective elastic properties of these slices over the length $\boldsymbol{L_{RVE}}$, and such wavy **CNT** can be categorized as:

$$\boldsymbol{y = A\sin(\omega x)} \text{ or}$$

$$\boldsymbol{z = A\sin(\omega x)};\ \ \boldsymbol{\omega = \frac{n\pi}{L_{RVE}}} \tag{2.26}$$

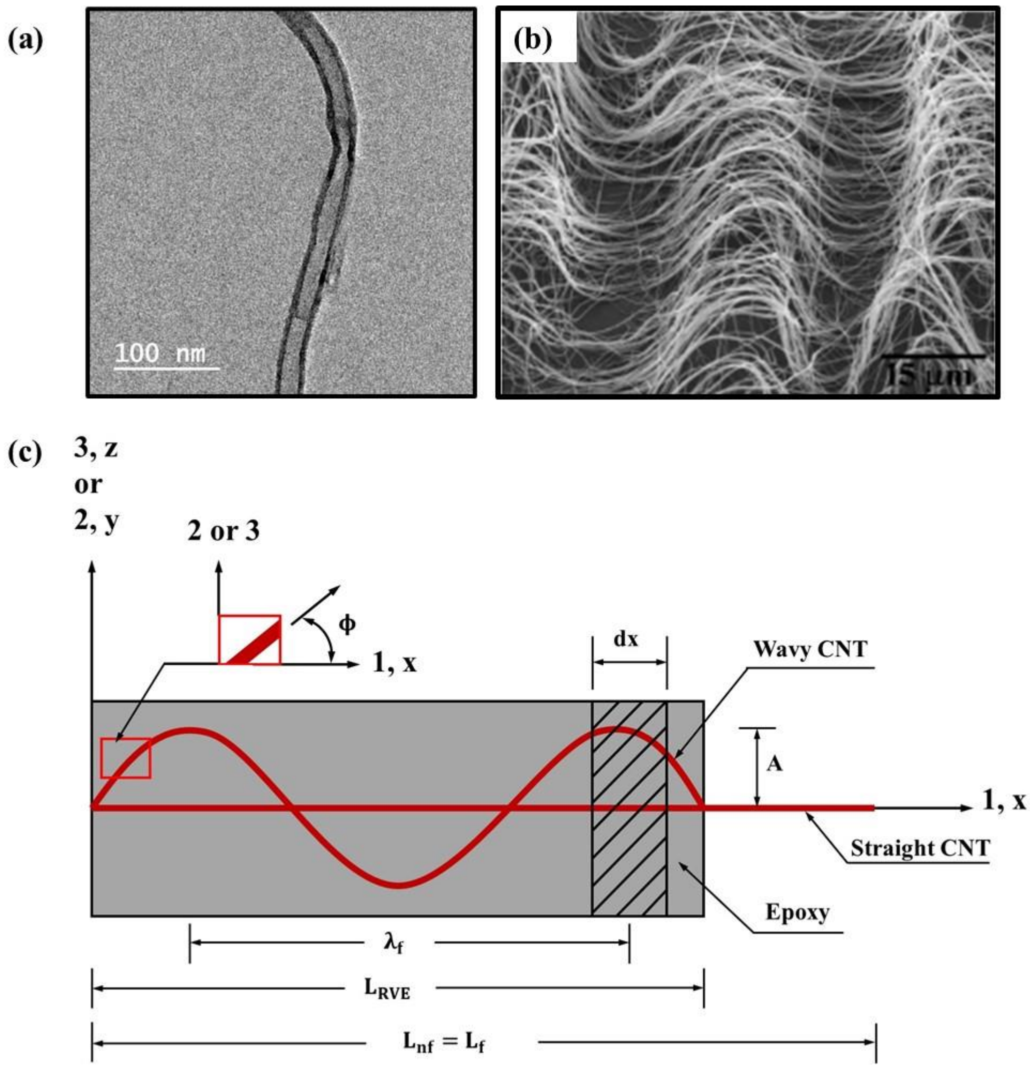

Figure 2.3. (a) **TEM** image of wavy **CNT** (Rathi *et al*., 2021), (b) **TEM** image of a periodic array of wavy **CNTs** (Xu *et al*., 2012), and (c) **RVE** of epoxy matrix incorporated with wavy **CNT** coplanar with **1–2** or **1–3** plane.

in which the wavy **CNT** waviness is coplanar with **1–2** or **1–3** plane. In Eq. (2.26), '$\boldsymbol{A}$' represents the amplitude of **CNT** wave, $\boldsymbol{L_{RVE}}$ is the linear distance between the two ends of **CNT**, and $\boldsymbol{n}$ denotes the number of waves of the **CNT**, such that, when $\boldsymbol{n} = 0$, we can have straight **CNT**. The running length of the **CNT** can be given by:

$$\boldsymbol{L_{nr}} = \int_{0}^{L_n} \sqrt{1 + \boldsymbol{A^2\omega^2\cos^2(\omega x)}}\boldsymbol{dx} \tag{2.27}$$

The angle $\boldsymbol{\phi}$ shown in Fig. 2.3(b) is given by:

$$\boldsymbol{\tan\phi} = \frac{\boldsymbol{dz}}{\boldsymbol{dx}} = \boldsymbol{A\omega\cos(\omega y)} \tag{2.27}$$

in which the waviness of **CNT** is coplanar with **1–2** or **1–3** plane. It should be noted that, for a particular value of $\boldsymbol{\omega}$, the value of $\boldsymbol{\phi}$ varies with the amplitude of the **CNT** wave.

The effective elastic coefficients of multiscale **HFRC** $\left(\boldsymbol{C_{ij}^{MSC}}\right)$ incorporated with wavy **CNT** having an angle $\boldsymbol{\phi}$ with the longitudinal axis can be determined by considering the suitable transformation. Thus, when the **CNT** waviness is coplanar with **1–2** plane, the $\boldsymbol{C_{ij}^{MSC}}$ at any point in the **HFRC** lamina can be expressed as:

$$[\boldsymbol{C^{MSC}}] = [\boldsymbol{T_1}]^{-\boldsymbol{T}}[\boldsymbol{C}][\boldsymbol{T_1}]^{-\boldsymbol{1}} \tag{2.28}$$

where

$$[\boldsymbol{T_1}] = \begin{bmatrix} \boldsymbol{k^2} & \boldsymbol{l^2} & 0 & 0 & 0 & \boldsymbol{kl} \\ \boldsymbol{l^2} & \boldsymbol{k^2} & 0 & 0 & 0 & -\boldsymbol{kl} \\ 0 & 0 & 1 & 0 & 0 & 0 \\ 0 & 0 & 0 & \boldsymbol{k} & -l & 0 \\ 0 & 0 & 0 & l & \boldsymbol{k} & 0 \\ -2\boldsymbol{kl} & 2\boldsymbol{kl} & 0 & 0 & 0 & \boldsymbol{k^2 - l^2} \end{bmatrix}$$

with

$$\boldsymbol{k} = \boldsymbol{\cos\phi} = [1 + \{\boldsymbol{n\pi A/L_{RVE}cos(n\pi x/L_{RVE})}\}^2]^{-\boldsymbol{1/2}} \quad \text{and}$$

$$\boldsymbol{l} = \boldsymbol{n\pi A/L_{RVE}cos(n\pi x/L_{RVE})}[1 + \{\boldsymbol{n\pi A/L_{RVE}cos(n\pi x/L_{RVE})}\}^2]^{-\boldsymbol{1/2}}$$

The following relation can be obtained by solving Eq (2.28):

$$\boldsymbol{C_{11}^{MSC}} = \boldsymbol{C_{11}k^4} + \boldsymbol{C_{22}l^4} + 2(\boldsymbol{C_{12}} + 2\boldsymbol{C_{66}})\boldsymbol{k^2l^2},$$

$$\boldsymbol{C_{12}^{MSC}} = (\boldsymbol{C_{11}} + \boldsymbol{C_{22}} - 4\boldsymbol{C_{66}})\boldsymbol{k^2 l^2} + \boldsymbol{C_{12}}(\boldsymbol{k^4} + \boldsymbol{l^4}), \qquad \boldsymbol{C_{13}^{MSC}} = \boldsymbol{C_{13} k^2} + \boldsymbol{C_{23} l^2},$$

$$\boldsymbol{C_{22}^{MSC}} = \boldsymbol{C_{11} l^4} + \boldsymbol{C_{22} k^4} + 2(\boldsymbol{C_{12}} + 2\boldsymbol{C_{66}})\boldsymbol{k^2 l^2}, \qquad \boldsymbol{C_{23}^{MSC}} = \boldsymbol{C_{13} l^2} + \boldsymbol{C_{23} k^2},$$

$$\boldsymbol{C_{33}^{MSC}} = \boldsymbol{C_{33}},\ \boldsymbol{C_{44}^{MSC}} = \boldsymbol{C_{44} k^2} + \boldsymbol{C_{55} l^2},\ \boldsymbol{C_{55}^{MSC}} = \boldsymbol{C_{44} l^2} + \boldsymbol{C_{55} k^2}, \qquad \text{and}$$

$$\boldsymbol{C_{66}^{MSC}} = (\boldsymbol{C_{11}} + \boldsymbol{C_{22}} - 2\boldsymbol{C_{12}} - 2\boldsymbol{C_{66}})\boldsymbol{k^2 l^2} + \boldsymbol{C_{66}}(\boldsymbol{k^4} + \boldsymbol{l^4}) \tag{2.29}$$

Similarly, when the **CNT** waviness is coplanar with **1–3** plane, the $\boldsymbol{C_{ij}^{MSC}}$ at any point in the **HFRC** lamina can be expressed using the following transformations:

$$[\boldsymbol{C^{MSC}}] = [\boldsymbol{T_2}]^{-\boldsymbol{T}}[\boldsymbol{C}][\boldsymbol{T_2}]^{-\boldsymbol{1}} \tag{2.30}$$

where

$$[\boldsymbol{T_2}] = \begin{bmatrix} \boldsymbol{k^2} & 0 & \boldsymbol{l^2} & 0 & \boldsymbol{kl} & 0 \\ 0 & 1 & 0 & 0 & 0 & 0 \\ \boldsymbol{l^2} & 0 & \boldsymbol{k^2} & 0 & -\boldsymbol{kl} & 0 \\ 0 & 0 & 0 & \boldsymbol{k} & 0 & -\boldsymbol{l} \\ -2\boldsymbol{kl} & 0 & 2\boldsymbol{kl} & 0 & \boldsymbol{k^2} - \boldsymbol{l^2} & 0 \\ 0 & 0 & 0 & \boldsymbol{l} & 0 & \boldsymbol{k} \end{bmatrix}$$

The following relation can be obtained by solving Eq. (2.30):

$$\boldsymbol{C_{11}^{MSC}} = \boldsymbol{C_{11} k^4} + \boldsymbol{C_{33} l^4} + 2(\boldsymbol{C_{13}} + 2\boldsymbol{C_{55}})\boldsymbol{k^2 l^2}, \qquad \boldsymbol{C_{12}^{MSC}} = \boldsymbol{C_{12} k^2} + \boldsymbol{C_{23} l^2},$$

$$\boldsymbol{C_{13}^{MSC}} = (\boldsymbol{C_{11}} + \boldsymbol{C_{33}} - 4\boldsymbol{C_{55}})\boldsymbol{k^2 l^2} + \boldsymbol{C_{13}}(\boldsymbol{k^4} + \boldsymbol{l^4}), \qquad \boldsymbol{C_{22}^{MSC}} = \boldsymbol{C_{22}},$$

$$\boldsymbol{C_{23}^{MSC}} = \boldsymbol{C_{12} l^2} + \boldsymbol{C_{23} k^2}, \qquad \boldsymbol{C_{33}^{MSC}} = \boldsymbol{C_{11} l^4} + \boldsymbol{C_{33} k^4} + 2(\boldsymbol{C_{13}} + 2\boldsymbol{C_{55}})\boldsymbol{k^2 l^2},$$

$$\boldsymbol{C_{44}^{MSC}} = \boldsymbol{C_{44} k^2} + \boldsymbol{C_{66} l^2},\ \boldsymbol{C_{66}^{MSC}} = \boldsymbol{C_{44} l^2} + \boldsymbol{C_{66} k^2}, \qquad \text{and}$$

$$\boldsymbol{C_{55}^{MSC}} = (\boldsymbol{C_{11}} + \boldsymbol{C_{33}} - 2\boldsymbol{C_{13}} - 2\boldsymbol{C_{55}})\boldsymbol{k^2 l^2} + \boldsymbol{C_{55}}(\boldsymbol{k^4} + \boldsymbol{l^4}) \tag{2.31}$$

Since the value of $\boldsymbol{\phi}$ varies along the length of the wavy **CNT**, the effective elastic coefficients $\left(\boldsymbol{C_{ij}^{MSC}}\right)$ also varies with the length of **CNT** waviness. The average effective elastic coefficient matrix $\left[\boldsymbol{\overline{C}_{ij}^{MSC}}\right]$ of such multiscale **HFRC** can be obtained by averaging the transformed elastic coefficients $\left(C_{ij}^{MSC}\right)$ over the linear distance between the **CNT** ends, using the following relation:

$$[\bar{C}_{ij}^{MSC}] = \frac{1}{L_{RVE}} \int_{0}^{L_n} [C_{ij}^{MSC}] dx \tag{2.32}$$

2.5 Results and Discussion

In this section, the numerical outcomes are presented for the effective elastic properties of **HFRC** determined using the two- and three-phase analytical **MOM** and **MT** models as presented in previous Sections 2.2 and 2.3, respectively. We also evaluated the effects of **CNTs** waviness on the effective elastic properties of **HFRC**, considering the **CNT** waves are coplanar with two mutually orthogonal planes.

2.5.1 Effective Elastic Properties of HFRC

To determine the effective elastic properties of the base composite (without **CNTs**) and the **HFRC,** epoxy and carbon fiber are used as the matrix and fiber material, respectively. While we mixed an adequate amount of **CNT** with epoxy to improve the mechanical and damping property of the composite and its structures, such three-phase composites result in **HFRC**. The mechanical properties of the epoxy, carbon fiber, and **CNT** nanofiller are enlisted in **Table 2.1**. The epoxy used in the present work is the Epoxy phenol novolac resin Araldite LY5052and amine-based hardener Aradur 5052CH at a weight ratio of 100:38.

For the development of lightweight and high-performance composite, the v_{CNT} in the epoxy matrix can vary practically up to 27% when used with different conventional fibers via one of the novel fabrication methods such as shear pressing (Bradford *et al.*, 2010; Huang *et al.*, 2012; Bradbury *et al.*, 2014). The v_{CF} in the composite can varies from 0.2 to 0.7. Unless otherwise mentioned, **CNT** (5, 5) is used to evaluate the mechanical properties of the multiscale **HFRC** using the **MOM** and **MT** models, and the estimated results are shown in Figs. 2.4–2.9. In the current study, we estimated the results for 0 and 10% of v_{CNT} in the multiscale **HFRC**. It should be noted that to predict the mechanical properties of the base composite, the two-phase **MOM** and **MT** model is used for which $\boldsymbol{v_{CNT}} = 0$ and for the multiscale **HFRC**, three-phase **MOM** and **MT** models is used when **CNT** ($\boldsymbol{v_{CNT}} = 10$ %) is added to the composite.

Table 2.1. Properties of the nanofiller, fiber, and matrix.

Material	Ref.	C_{11} (GPa)	C_{12} (GPa)	C_{13} (GPa)	C_{23} (GPa)	C_{33} (GPa)	C_{44} (GPa)	ρ $(\mathrm{kg/m^3})$
CNT (5,5)	(Ray and Batra, 2009)	668	404	184	184	2153	791	1400
CNT (10,10)	(Ray and Batra, 2007a)	288	254	87.8	87.8	1088	442	1400
CNT (10,0)	(Kundalwal and Ray, 2011)	709.9	172.4	240	240	1513.1	1120	1400
CNT (14,0)	(Kundalwal and Ray, 2011)	557.5	137.5	187.7	187.7	1082.8	779.2	1400
Carbon Fiber	(Kundalwal and Ray, 2011)	236.4	10.6	10.6	10.7	24.8	7	1700
Epoxy	(Ray and Batra, 2007a)	5.3	3.1	3.1	3.1	5.3	0.64	1250

Figure 2.4 shows the comparison of the effective longitudinal elastic constant ($\boldsymbol{C_{11}}$) with respect to $\boldsymbol{v_{CF}}$ of multiscale **HFRC** and base composite. We obtained almost a linear curve as $\boldsymbol{C_{11}}$ varies with $\boldsymbol{v_{CF}}$, this is mainly because the iso-strain condition was considered with the axis of symmetry for the prediction of effective longitudinal elastic constant ($\boldsymbol{C_{11}}$), a similar trend was obtained by Kundalwal and Ray (2011). As the value of $\boldsymbol{v_{CNT}}$ increases from 0 to 10% a significant improvement in the elastic constant $\boldsymbol{C_{11}}$ of the **HFRC** can be observed due to the incorporation of **CNT** nanofiller in the pure matrix as shown in Fig. 2.4. It is also be observed that for base composite the results predicted from both the models almost coincide with each other. Whereas for **HFRC**, the **MT** approach underestimates the outcomes as compared with the **MOM** approach. This is attributed to the consideration of different modeling assumptions

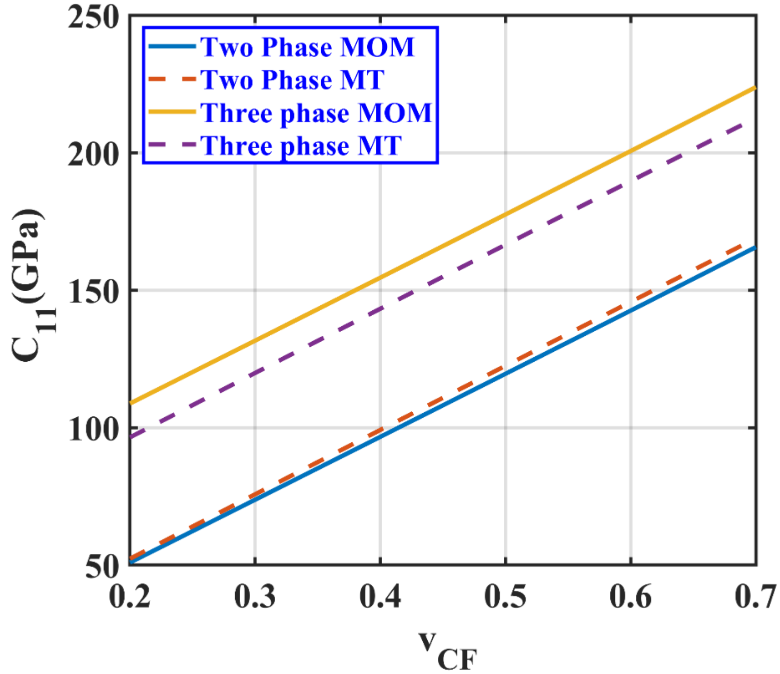

Figure 2.4. Comparison of $\boldsymbol{C_{11}}$ with respect to $\boldsymbol{v_{CF}}$ for **HFRC** and base composite.

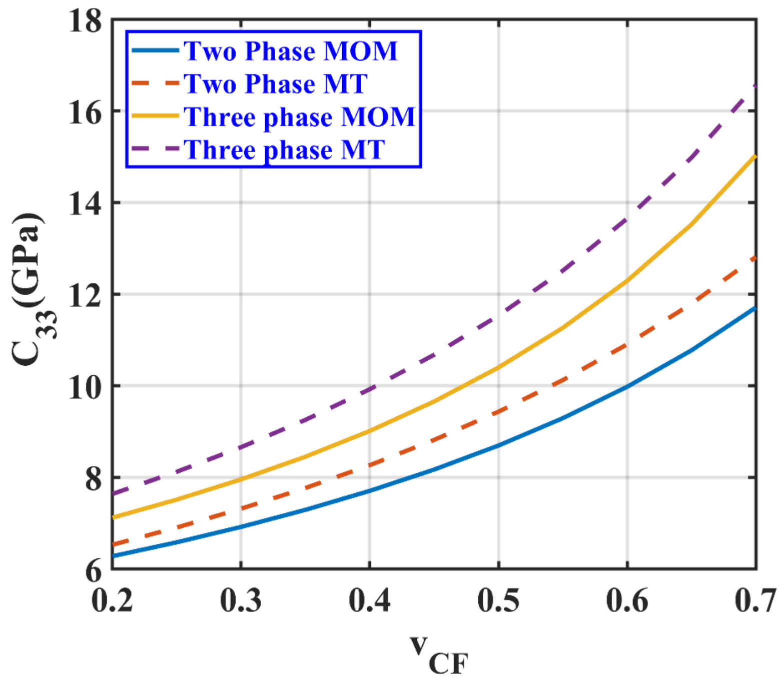

Figure 2.5. Comparison of $\boldsymbol{C_{33}}$ with respect to $\boldsymbol{v_{CF}}$ for **HFRC** and base composite.

for deriving the two models. **MOM** model considers **ROM** approach while **MT** model considers the Eshelby tensor for the interaction of the fiber and matrix phase. Thus, for three-phase or **HFRC**, the **MT** approach takes the interaction of carbon fiber/matrix phase and interaction of **CNT** nanofillers/matrix phase into consideration. Hence, for the three-phase composite, we observed some discrepancies between the two models. Although, outcomes of both the models show good agreement, hence validating the assumptions made for the development of both **MOM** and **MT** models.

Next, the comparison of the effective transverse elastic constant ($\boldsymbol{C_{33}}$) with $\boldsymbol{v_{CF}}$ of the **HFRC** and base composite are illustrated in Fig. 2.5. For the variation of **CNT** from 0 to 10%, at the lower value of $\boldsymbol{v_{CF}}$ less improvement in $\boldsymbol{C_{33}}$ is observed. Whereas comparatively high enhancement may be seen in $\boldsymbol{C_{33}}$ as the value of $\boldsymbol{v_{CF}}$ increases. Similar results were observed for $\boldsymbol{C_{22}}$, however, for the sake of brevity, the results are not present here. Since the material is considered as transversely isotropic along the longitudinal direction, therefore, due to the constructional feature of both **HFRC** and base composite the two results ($\boldsymbol{C_{33}}$) and ($\boldsymbol{C_{22}}$) are similar. In this case, the **MOM** model slightly underestimates the values of $\boldsymbol{C_{33}}$ as compared to the **MT** approach. From Figs. 2.4 and 2.5, it may be observed that for the given $\boldsymbol{v_{CF}}$ the values of $\boldsymbol{C_{11}}$ is much higher as compared to the values of $\boldsymbol{C_{33}}$ in magnitude. This is because these transverse elastic constants $\boldsymbol{C_{33}}$ are matrix-dependent. Since the **CNTs** and carbon fibers are aligned in the longitudinal axis the longitudinal stiffness of the **HFRC** lamina is improved. Similarly, the effective elastic constant ($\boldsymbol{C_{12}}$) and ($\boldsymbol{C_{13}}$) are computed using similar predictions as shown in Figs. 2.6 and 2.7. Here also we observed that the **MT** model overestimates the values of $\boldsymbol{C_{12}}$ and $\boldsymbol{C_{13}}$ as compared to the **MOM** model.

Figure 2.8 illustrates the comparison of the effective elastic constant ($\boldsymbol{C_{23}}$) with respect to $\boldsymbol{v_{CF}}$. For the lower value of $\boldsymbol{v_{CF}}$, there is a slight increment in the results obtained for the **HFRC** as compared to the base composite. Whereas for the higher value of $\boldsymbol{v_{CF}}$, a significant enhancement may be observed. The trend of results for $\boldsymbol{C_{23}}$ and $\boldsymbol{C_{13}}$ are found to be almost similar. Although for predicting the $\boldsymbol{C_{23}}$ the normal strain ($\boldsymbol{\varepsilon_{33}}$) and normal stress ($\boldsymbol{\sigma_{22}}$) are under the extension-extension coupling as the loading condition was considered along the longitudinal direction. Figure 2.9 depicts the comparison of the effective shear elastic constant ($\boldsymbol{C_{44}}$) with $\boldsymbol{v_{CF}}$ of the **HFRC** and base composite. It may be noted that the $\boldsymbol{C_{44}}$ follow the same trend as $\boldsymbol{C_{33}}$ and $\boldsymbol{C_{23}}$, mainly, due to the dependency of $\boldsymbol{C_{44}}$ on the values of effective elastic constants $\boldsymbol{C_{33}}$ and $\boldsymbol{C_{23}}$. It may be noted that the earlier researcher (Pettermann and Suresh, 2000) reported similar outcomes for predicting effective elastic constant (C_{44}). In their study, they found that the longitudinal shear modulus C_{44} of the laminated composite computed with the analytical model can be changed considerably compared to the experimental values.

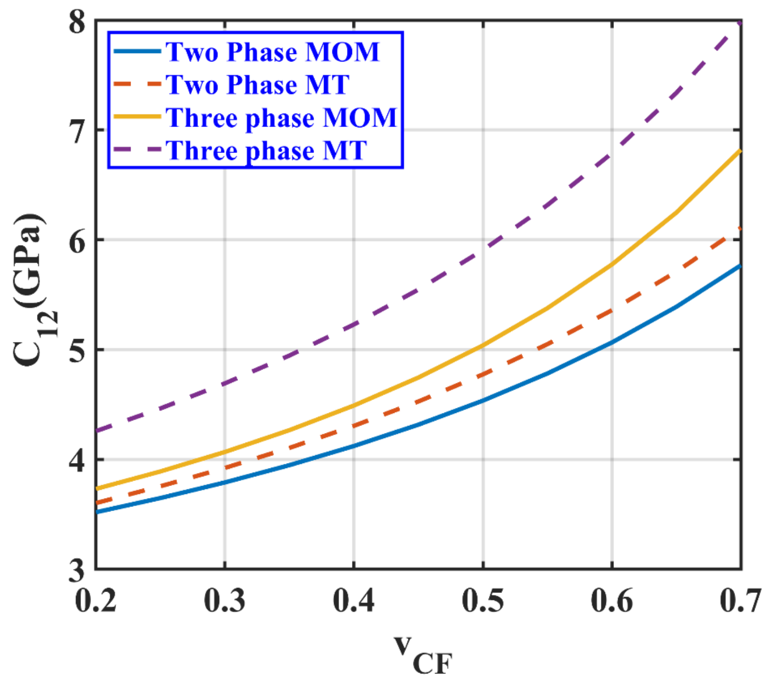

Figure 2.6. Comparison of C_{12} with respect to v_{CF} for **HFRC** and base composite.

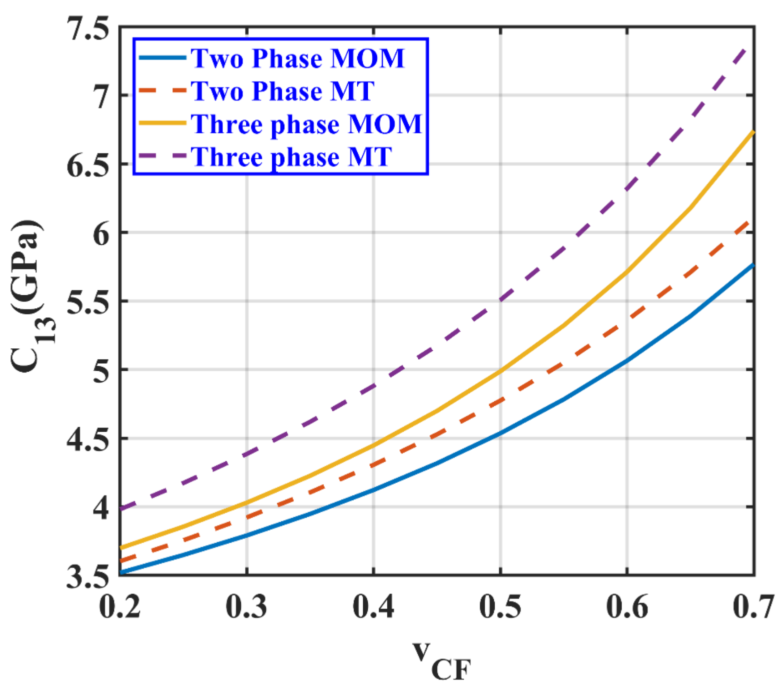

Figure 2.7. Comparison of C_{13} with respect to v_{CF} for **HFRC** and base composite.

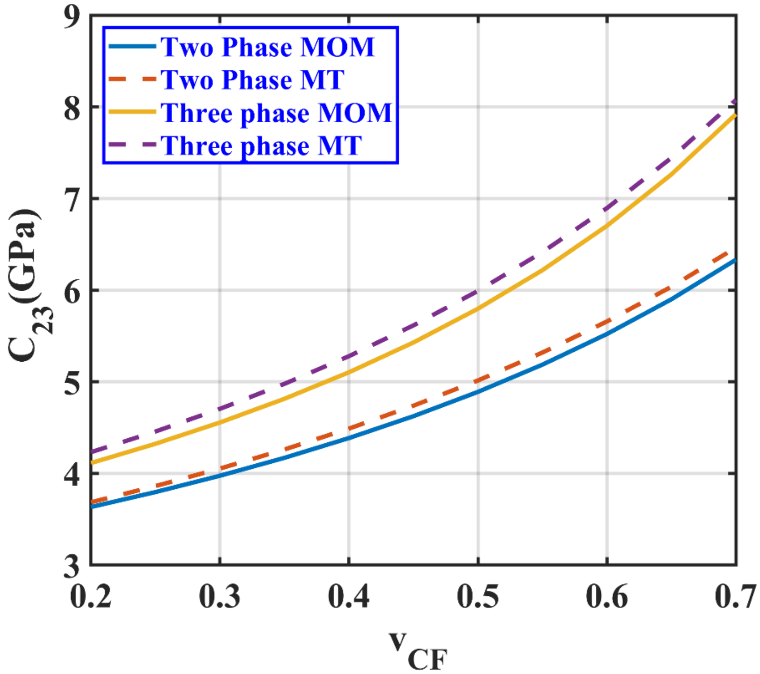

Figure 2.8. Comparison of C_{23} with respect to v_{CF} for **HFRC** and base composite.

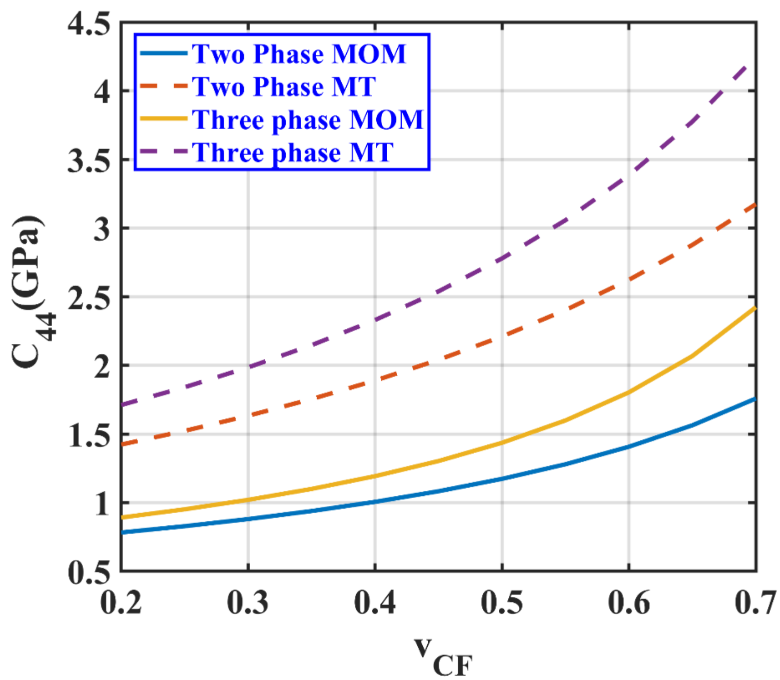

Figure 2.9. Comparison of C_{44} with respect to v_{CF} for **HFRC** and base composite.

From Figs. 2.4–2.9, it may be concluded that the effective axial, transverse, and shear elastic properties of the **HFRC** are improved by incorporation of **CNTs** into the epoxy matrix, due to the high elastic properties of **CNTs** and the non-bonded interaction formed between **CNTs** and the epoxy phase. We also observed that for most of the part **MOM** model overestimates the value of effective elastic properties when compared with the **MT** approach. Although, the outcomes of both **MOM** and **MT** approaches are found to be in excellent agreement. Thus in the next section, we will discuss the effects of **CNTs** waviness of the effective elastic properties of multiscale **HFRC** using the **MT** approach.

2.5.2 Effective Elastic Properties of HFRC with Wavy CNTs

Unless otherwise mentioned, **CNT** (5, 5) is used for predicting the elastic properties of multiscale **HFRC** with straight and wavy **CNTs**. The $\boldsymbol{v_{CNT}}$ of uniformly distributed straight **CNT** in the **HFRC** is taken as 0.1. The maximum amplitude of the **CNT** (5, 5) is considered as $\boldsymbol{A} = 100\ \boldsymbol{d_n}$, with a diameter of **CNT** $\boldsymbol{d_n} = 0.78\ \mathbf{nm}$, and waviness factor $(\boldsymbol{A}/\boldsymbol{L_{RVE}}) = 0.17$. The amplitude variation of **CNT** waviness in the **1–2** and **1–3** planes is estimated by considering the constant value of wave frequency, $\boldsymbol{\omega} = 5\boldsymbol{\pi}/\boldsymbol{L_{RVE}}$. The estimated effective elastic properties of **HFRC** with straight or wavy **CNTs** are demonstrated in Figs. 2.10 to 2.15.

Figure 2.10 illustrates the variation of longitudinal elastic coefficient $\boldsymbol{C_{11}^{MSC}}$ of different cases: **HFRC** with straight (***n*** = 0) and wavy **CNTs** in **1–2** and **1–3** planes. We observed that the $\boldsymbol{C_{11}^{MSC}}$ linearly varies with $\boldsymbol{v_{CF}}$ because the carbon fibers are oriented along the ***x***–axis of **HFRC**. This is attributed to the iso-strain condition imposed on constituents. Thus the strain induced in the ***x***–direction of **HFRC** composite is equal to that of matrix and fibers. Figure 2.10 also depicts that the magnitude of $\boldsymbol{C_{11}^{MSC}}$ for wavy **CNT** case is lower compared to the straight **CNT** case. This is attributed to the fact the load-bearing capacity of the **CNT** reduces due to waviness.

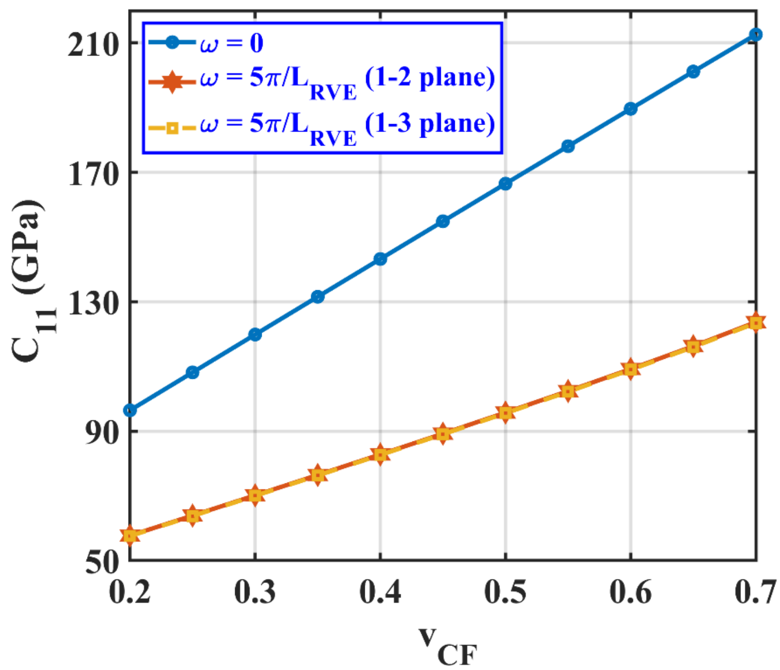

Figure 2.10. Variation of effective elastic coefficient $\boldsymbol{C_{11}^{MSC}}$ with $\boldsymbol{v_{CF}}$ of **HFRC**.

Figure 2.11 demonstrates the variation of transverse elastic coefficient $\boldsymbol{C_{33}^{MSC}}$ for different cases, which demonstrates the substantial improvement in the value of $\boldsymbol{C_{33}^{MSC}}$ when **CNT** waves are coplanar with the **1–3** plane. This is because the transformed value of $\boldsymbol{C_{33}^{MSC}}$ improves with the amplitude of **CNT** waves coplanar with the **1–3** plane. Likewise, the values of $\boldsymbol{C_{22}^{MSC}}$ improve when the **CNT** waves are coplanar with **1–2** plane (see Eq. 2.29). Note that the values of $\boldsymbol{C_{22}^{MSC}}$ are identical to those of $\boldsymbol{C_{33}^{MSC}}$ and for the sake of brevity, the results of $\boldsymbol{C_{22}^{MSC}}$ are not presented here. Similar behavior is also observed by Yanase *et al.* (2013) and Alian *et al.* (2016).

Figures 2.12–2.13 demonstrate the effect of **CNT** waviness on the effective elastic coefficients $\boldsymbol{C_{12}^{MSC}}$ and $\boldsymbol{C_{13}^{MSC}}$. It can be observed that, when the **CNT** waves are coplanar with **1–2** plane, the values of $\boldsymbol{C_{12}^{MSC}}$ are significantly enhanced.Whereas the values of $\boldsymbol{C_{12}^{MSC}}$ remain similar to the value of straight **CNT** case when the **CNT** waves are coplanar to **1–3** plane. We observed a similar trend for $\boldsymbol{C_{13}^{MSC}}$ as well, because the **HFRC** demonstrated transversely isotropic behavior. The variation of values of $\boldsymbol{C_{23}^{MSC}}$ with the $\boldsymbol{v_{CF}}$ of **HFRC** is shown in Fig. 2.14. It can be noted that the effect of **CNT** waviness is not pronounced when the **CNT** waves are coplanar with **1–2** and **1–3** planes. It can be observed from the transformation relations (Eqs. 2.29 and 2.31) that the waviness of **CNT** has a major impact on $\boldsymbol{C_{12}^{MSC}}$ and $\boldsymbol{C_{13}^{MSC}}$ but on the $\boldsymbol{C_{23}^{MSC}}$.

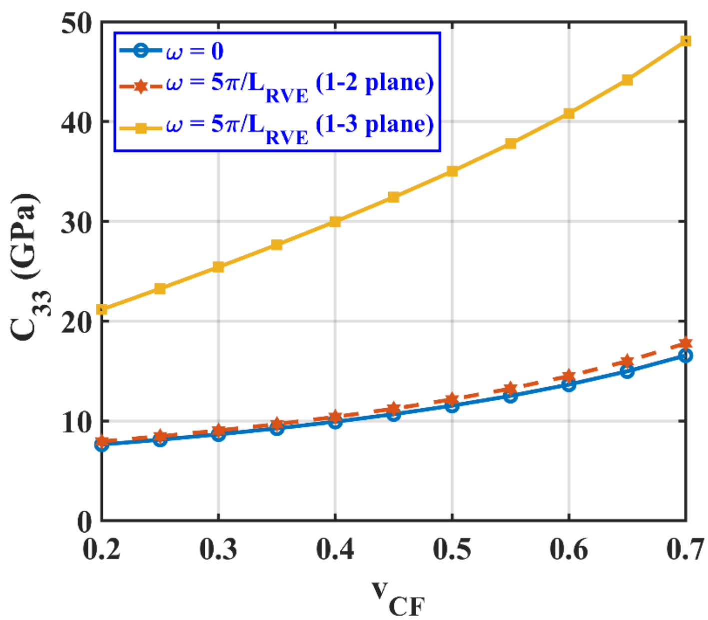

Figure 2.11. Variation of effective elastic coefficient $\boldsymbol{C_{33}^{MSC}}$ with $\boldsymbol{v_{CF}}$ of **HFRC**.

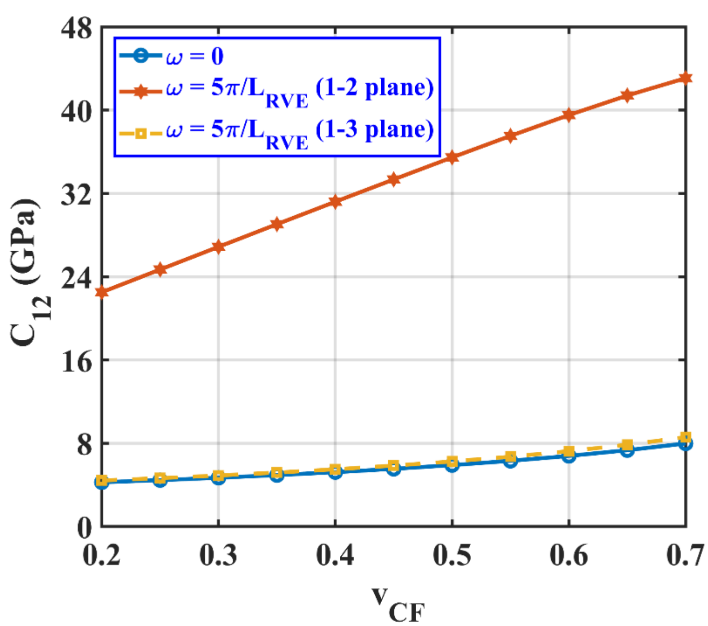

Figure 2.12. Variation of effective elastic coefficient $\boldsymbol{C_{12}^{MSC}}$ with $\boldsymbol{v_{CF}}$ of **HFRC**.

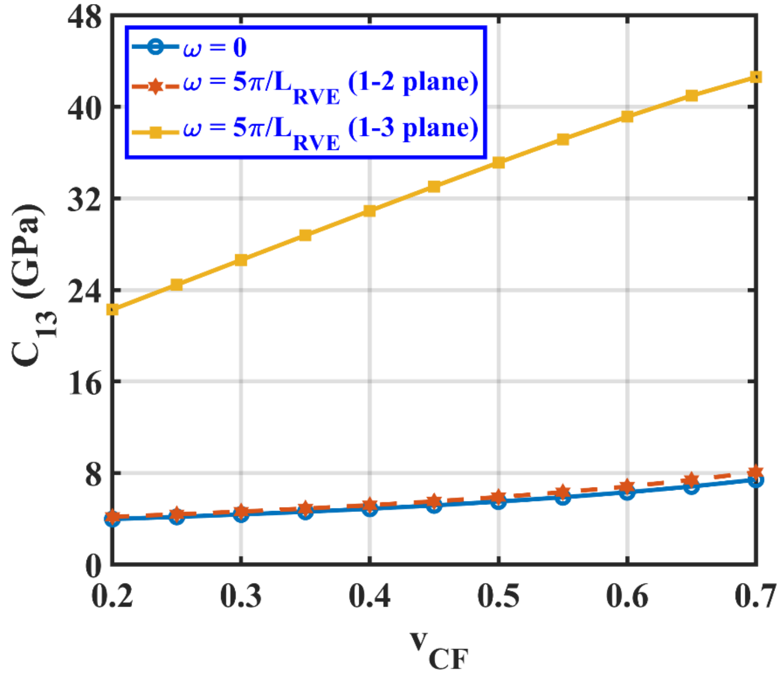

Figure 2.13. Variation of effective elastic coefficient C_{13}^{MSC} with v_{CF} of **HFRC**.

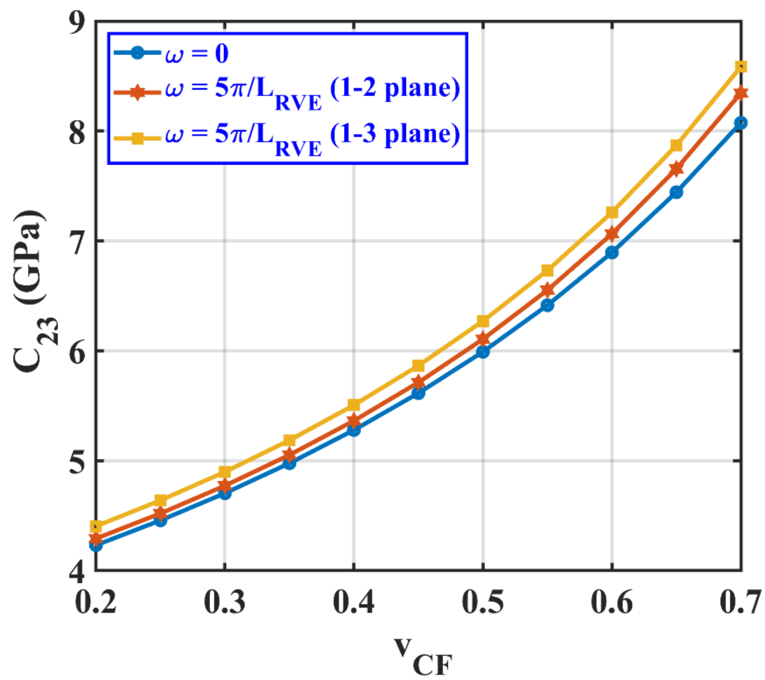

Figure 2.14. Variation of effective elastic coefficient C_{23}^{MSC} with v_{CF} of **HFRC**.

Figure 2.15 illustrates the variation of C_{55}^{MSC} with the v_{CF} of **HFRC**, and we can observe a significant improvement in the values of C_{55}^{MSC} when the waviness of **CNT** is coplanar with **1–3** plane. Similar behavior is observed for the value C_{66}^{MSC}, which depends on the effective elastic coefficients C_{22}^{MSC} and C_{12}^{MSC}. However, the results of C_{66}^{MSC} are not shown here for the sake of brevity.

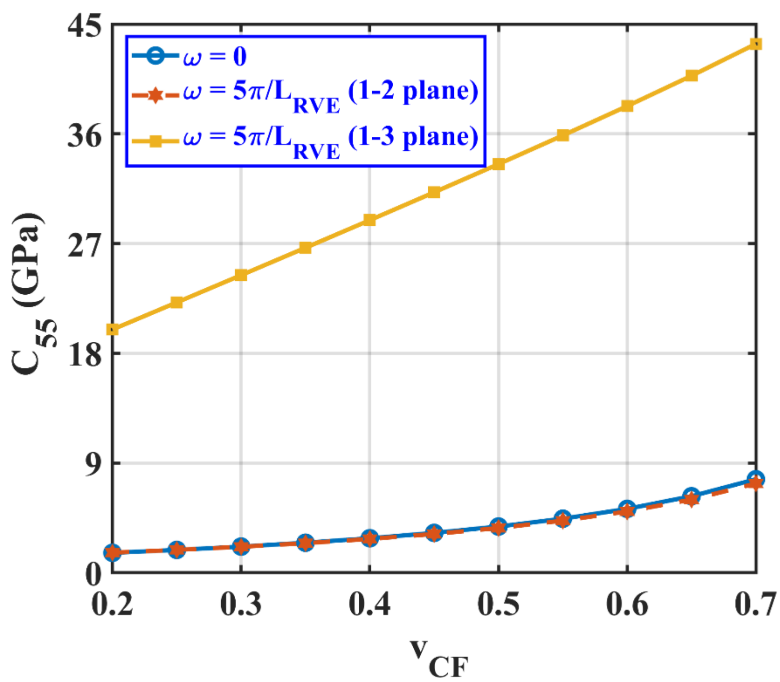

Figure 2.15. Variation of effective elastic coefficient C_{55}^{MSC} with v_{CF} of **HFRC**.

Figure 2.16 demonstrates the effect of **CNT** wave frequency ($\omega = n\pi/L_{RVE}$) on the effective elastic coefficient C_{11}^{MSC} when the **CNT** waves are coplanar with two mutually orthogonal planes (i.e., **1–2** and **1–3** planes). The value of multiplying factor ranges from $n = 0$ to 20. It can be observed from Fig. 2.16 that the value of C_{11}^{MSC} reduces drastically for the value of $n \leq 15$. However, the effect of **CNT** wave frequency on the C_{11}^{MSC} reduces and it approaches a stable value when $n > 15$. Figure 2.17 shows the effect of **CNT** wave frequency on the effective elastic coefficient C_{33}^{MSC}, which demonstrates the significant improvement in the value of C_{33}^{MSC} when the **CNT** waves are coplanar with **1–3** plane. However, the improvement in the value C_{33}^{MSC} is insignificant when **CNT** waves are coplanar with **1–2** planes.

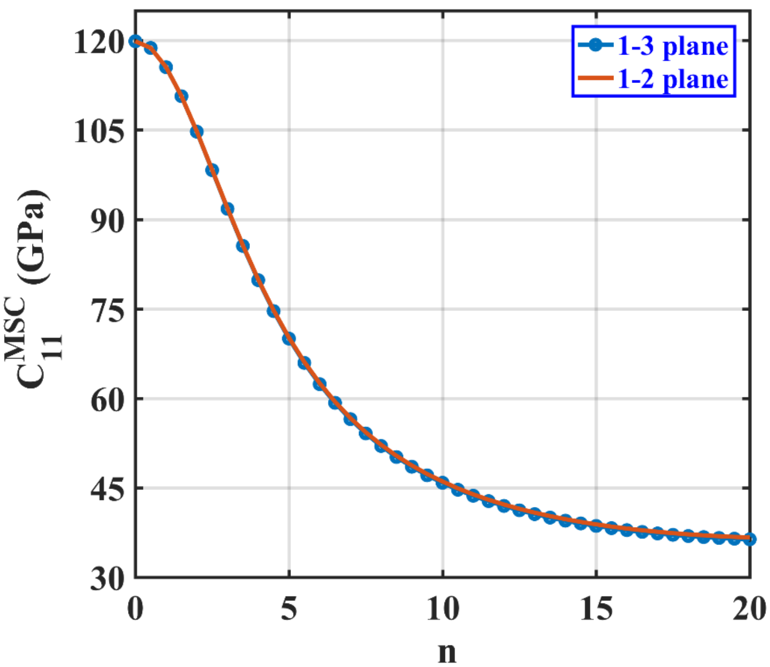

Figure 2.16. Variation of effective elastic coefficient C_{11}^{MSC} of **HFRC** with respect to multiplying factor '$\boldsymbol{n}$' ($\boldsymbol{\omega} = \boldsymbol{n\pi}/\boldsymbol{L_{RVE}}$; $\boldsymbol{n}$ = 0 to 20)

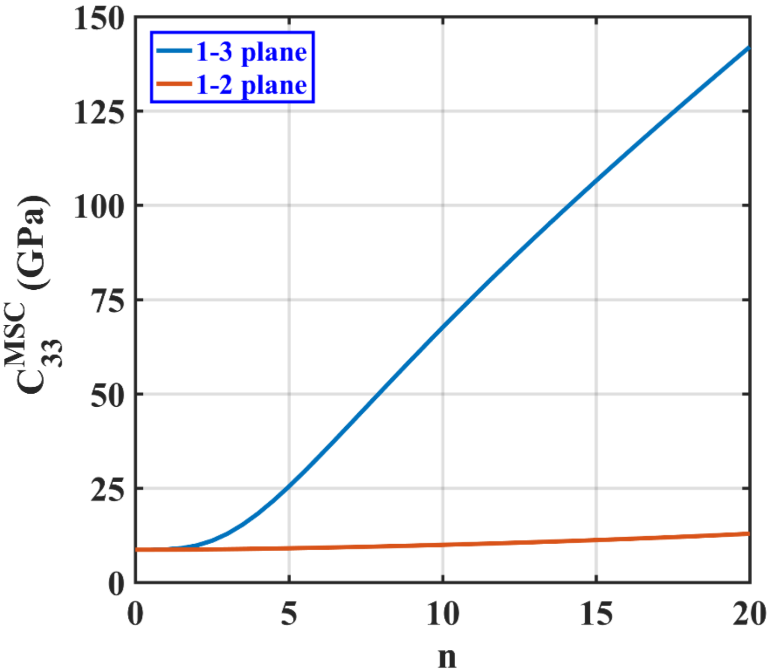

Figure 2.17. Variation of effective elastic coefficient C_{33}^{MSC} of **HFRC** with respect to multiplying factor '$\boldsymbol{n}$' ($\boldsymbol{\omega} = \boldsymbol{n\pi}/\boldsymbol{L_{RVE}}$; $\boldsymbol{n}$ = 0 to 20)

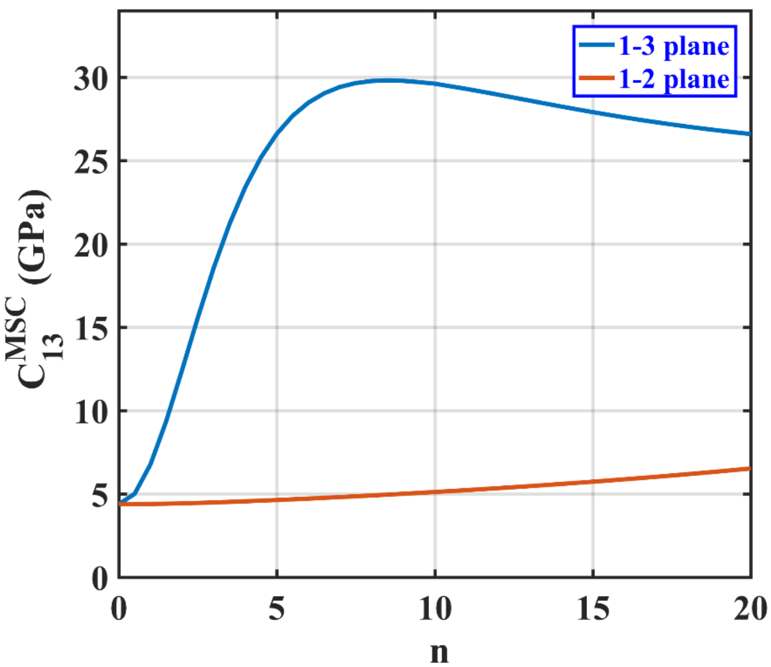

Figure 2.18. Variation of effective elastic coefficient $\boldsymbol{C_{13}^{MSC}}$ of **HFRC** with respect to multiplying factor '$\boldsymbol{n}$' ($\boldsymbol{\omega} = \boldsymbol{n\pi}/\boldsymbol{L_{RVE}}$; $\boldsymbol{n} = 0$ to 20)

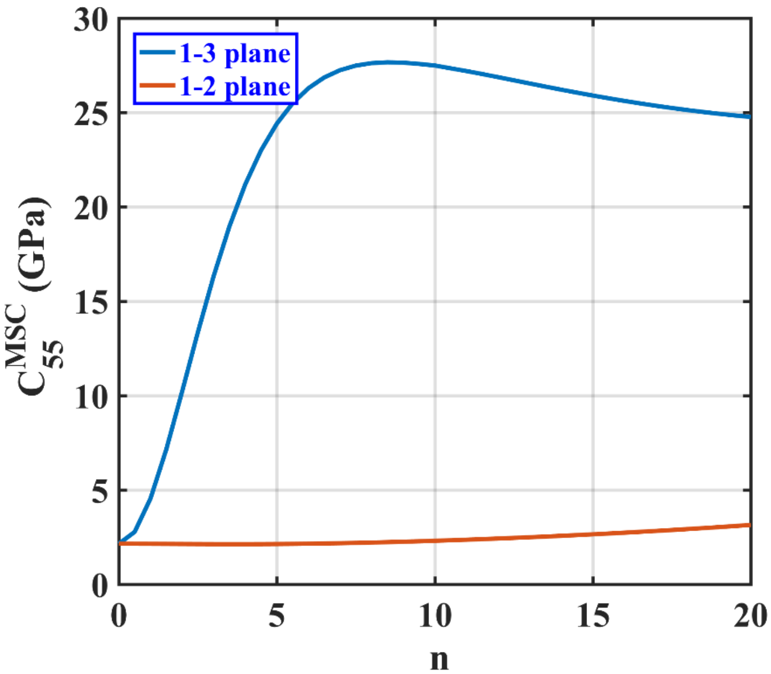

Figure 2.19. Variation of effective elastic coefficient $\boldsymbol{C_{55}^{MSC}}$ of **HFRC** with respect to multiplying factor '$\boldsymbol{n}$' ($\boldsymbol{\omega} = \boldsymbol{n\pi}/\boldsymbol{L_{RVE}}$; $\boldsymbol{n} = 0$ *to* 20)

The influence of **CNT** waviness on the effective elastic coefficient $\boldsymbol{C_{13}^{MSC}}$ is presented in Fig. 2.18. The figure shows that the value of $\boldsymbol{C_{13}^{MSC}}$ increases with the **CNT** wave frequency. The maximum value is observed at $\boldsymbol{n}$ = 8.5 when the **CNT** waves are coplanar with **1–3** plane. Figure 2.19 illustrates the influence of **CNT** waviness on the effective elastic coefficient $\boldsymbol{C_{55}^{MSC}}$. The figure reveals a trend similar to $\boldsymbol{C_{13}^{MSC}}$ due to the dependency of $\boldsymbol{C_{55}^{MSC}}$ on the values $\boldsymbol{C_{33}^{MSC}}$ and $\boldsymbol{C_{13}^{MSC}}$. For the sake of brevity, the results of $\boldsymbol{C_{12}^{MSC}}$ and $\boldsymbol{C_{66}^{MSC}}$ are not presented here, although we have observed that the values of $\boldsymbol{C_{12}^{MSC}}$ and $\boldsymbol{C_{66}^{MSC}}$ are analogous with $\boldsymbol{C_{13}^{MSC}}$ and $\boldsymbol{C_{55}^{MSC}}$, showing substantial increments when the **CNT** waves are coplanar with **1–2** plane. It may be concluded from Figs. 2.10 to 2.19 that the effective elastic properties of multiscale **HFRC** are influenced by the **CNT's** waviness. The axial elastic coefficients decrease, and transverse elastic coefficients increase due to the **CNT** waviness. Also, based on our findings we can conclude that if **CNTs** of different wave amplitude are present in the microstructure then the rate of increment and decrement in the transverse and longitudinal coefficients, respectively, will be a function of the average of the **CNT** wave amplitudes present in the structure. Thus, the inherent issue of wavy **CNTs** can be utilized carefully to tailor the elastic properties of multiscale composites, which is why it is interesting to study the effect of wavy **CNT** on the damping performance of multiscale **HFRC** smart structures discussed in the next Chapters.

2.6 Summary

Micromechanical analysis of a multiscale **HFRC** composed of armchair **CNTs**, carbon fibers, and polyimide matrix has been carried out. The carbon fiber and **CNT** nanofillers reinforcements are horizontally aligned and uniformly distributed in the matrix phase of **HFRC**. Two analytical models based on the two- and three-phase micromechanics paradigms such as the **MOM** approach and the **MT** method are derived to predict the effective elastic properties of a lamina made of base composites (without **CNTs**) and **HFRC**, respectively. In addition, an analytical model is derived to study the effects of **CNT** waviness on the effective elastic properties of the **HFRC**. We observed that the outcomes of both **MOM** and **MT** models are in good agreement with the **MOM** model slightly overpredicting the values, compared to the **MT** model. Due to the incorporation of **CNTs** in the matrix phase, the material properties of **HFRC** lamina show substantial improvement. Next, we investigated the influence of the waviness of **CNTs** on the effective elastic properties of the **HFRC** by considering the wavy **CNTs** to be coplanar with either of the two mutually orthogonal planes using the **MT** approach. When the wavy **CNTs** are coplanar with the **1–2** or **1–3** plane then the transverse effective elastic properties of the **HFRC** are significantly improved over their values with the straight **CNTs** for the higher values of the wave frequencies and the amplitudes of the **CNTs**. However, due to the waviness, the **CNTs** are flexible in the longitudinal direction and, hence, the load-transfer capacity of **CNTs** in the longitudinal direction degrades drastically as compared to the straight **CNTs**. Thus, we observed the reduction in the longitudinal effective elastic coefficient of **HFRC** due to the **CNT** waves. The present study reveals that the wavy **CNTs** can be properly used to construct nanocomposites with superior elastic properties. The results presented here may also be used for comparing the experimental estimations.

Chapter 3

Active Vibration Damping of Smart Multiscale Hybrid Fiber Reinforced Composite Beams Using 1–3 Piezoelectric Composites

This Chapter (Gupta et al., 2021) describes the active vibration damping of multiscale laminated hybrid fiber-reinforced composite ***(HFRC)*** *substrate beams, using* ***1–3*** *piezoelectric composite* ***(PZC)*** *as the material of the constraining layer of active constrained layer damping* ***(ACLD)*** *treatment. Based on a layerwise first order shear deformation theory* ***(FSDT)****, a finite element* ***(FE)*** *model is developed for the smart laminated* ***HFRC*** *beam integrated with the* ***ACLD*** *treatment patch. The effect of in-plane and transverse-plane actuation of the integrated* ***ACLD*** *treatment layer on the damping characteristics of the smart cantilever* ***HFRC*** *beam is investigated. The parameters affecting the damping characteristics of the* ***HFRC*** *substrate beam such as the volume fraction of both carbon nanotubes* ***(CNTs)*** *and carbon fiber, and the aspect ratio are also studied.*

3.1 Introduction

The analytical micromechanics models based on the **MOM** approach and the **MT** method derived in the previous Chapter reveal that the **HFRC** being studied here is characterized by significantly improved effective longitudinal and transverse elastic properties. In this chapter, a **FE** model is developed to investigate the performance of the patches of the **ACLD** treatment for causing the active control of vibrations of laminated multiscale **HFRC** smart beams. The constraining layer of the **ACLD** treatment is considered to be made of the vertically reinforced **1–3 PZC** material; while the constrained layer is made of a viscoelastic material. The substrate **HFRC** beam is composed of multiscale reinforcements of nanoscale **CNT** nanofillers and macroscale carbon fibers. The multiscale reinforcements are considered to be uniformly distributed along the longitudinal direction of **HFRC** lamina. Also, for the present analysis, the **CNTs** are considered to be straight. The displacement field equations for the multiscale **HFRC** beams integrated with the **ACLD** patch at its top surface have been considered according to a layer wise **FSDT**. Based on the displacement field equations **FE** model is derived using the **FSDT** incorporating the inherent zig-zag effects. For the active vibration control of the laminated **HFRC** smart beam, a closed-loop model is also presented based on the simple velocity feedback control law. The performance of the patches for controlling the vibrations of the multiscale **HFRC** smart beam has been thoroughly investigated. The numerical results indicate that the **ACLD** patches significantly improve the damping characteristics of the multiscale **HFRC** smart beam for suppressing their geometrical vibrations. To bring more clarity, the quantitative relative performance of **HFRC** is also presented and the results are compared with the base composite beam.

3.2 Finite Element Modelling of a Smart Beam

The **FE** model is derived to investigate the performance of the novel laminated **HFRC** smart beam attached with **ACLD** treatment constraining layer of **1–3 PZC** material at the upper surface of the beam, comprising $\boldsymbol{N}$ numbers of **HFRC** lamina as shown in Fig 3.1. All the layers of the **HFRC** beam are assumed transversely isotropic, uniformly homogeneous, and linearly elastic. The **ACLD** layer is composed of viscoelastic material.

The volume of the **HFRC** substrate beam is determined using a simple relation: $\boldsymbol{L} \times \boldsymbol{b} \times \boldsymbol{h}$, where $\boldsymbol{L}$, $\boldsymbol{b}$, and $\boldsymbol{h}$ denote the respective length, width, and height of the beam. While $\boldsymbol{L_a}$ denotes the length of **ACLD** treatment constraining layer of piezo material; $\boldsymbol{h_v}$ and $\boldsymbol{h_p}$ denote the respective thickness of **ACLD** and the **1–3 PZC** layer. The reference plane of the laminated **HFRC** smart beam is considered as the mid-plane of the substrate beam. The global coordinate system is defined in such a way that its origin is situated on the reference plane. The smart beam is subjected to cantilevered boundary conditions ($\boldsymbol{x} = 0$, and $\boldsymbol{L}$). Here, the **FSDT** is used for modelling the axial displacement in each layer of an overall beam which can be considered as a thin beam. According to the **FSDTs**, Fig. 3.2 illustrates the kinematics of deformation of the laminated **HFRC** smart beam in the axial direction. Here, the generalized translational displacement at any point on the reference plane ($z = 0$) is denoted by u_0 . θ_x, ϕ_x and γ_x represent the generalized rotations of the normals to the mid planes of the **HFRC** substrate beam, the **ACLD**, and the **1–3 PZC**, respectively, in the xz plane. In Fig 3.2, the coordinate (z) in the thickness direction of the upper and lower surface of any (k_{th}) layer of the overall composite beam is given by h_{k+1} and h_k ($k = 1, 2, 3, \ldots, N + 2$), respectively. According to the **FSDT**, the axial displacement u at any point of the beam in the x-direction can be written as:

$$u(x, z, t) = u_0(x, t) + (z - \langle z - h/2 \rangle)\theta_x(x, t) + (\langle z - h/2 \rangle - \langle z - h_{N+2} \rangle)\phi_x(x, t) + \langle z - h_{N+2} \rangle \gamma_x(x, t) \tag{3.1}$$

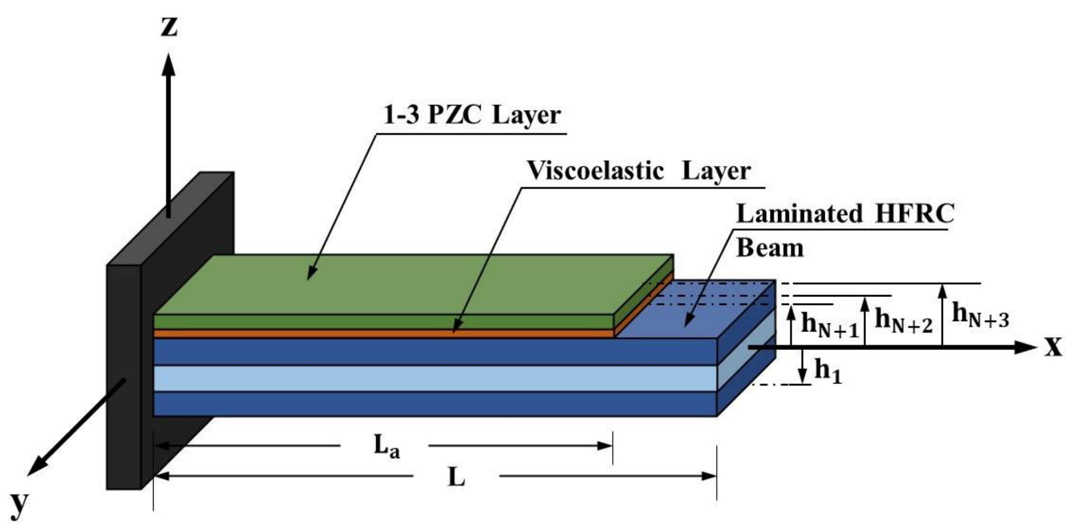

Figure 3.1. Laminated **HFRC** smart beam attached with viscoelastic and **1–3 PZC** layer.

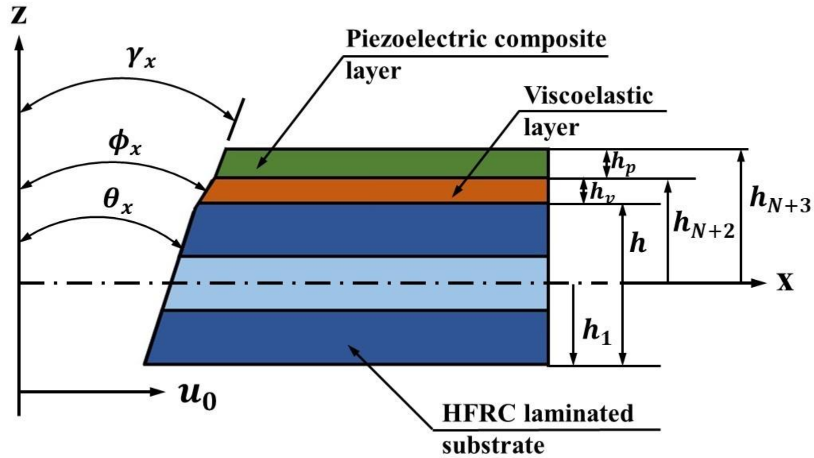

Figure 3.2. Kinematics of axial deformation of **HFRC** smart beam.

where the function within brackets ⟨ ⟩ denote suitable singularity function also termed as zig-zag function. In a general layer-wise formulation of a beam theory, for the modeling of axial deformation, the zig-zag beam theory is used as shown in Eq. (3.1). The axial displacement field could be modeled as a piecewise continuous function that is a collection of linear functions defined for each layer. This theory consists of three such piecewise continuous expressions that account for the displacements in the **HFRC** substrate beam, **ACLD** layer, and the **1–3 PZC** layer, respectively. The proposed zigzag function vanishes at the top and bottom surfaces of the beam and does not require full shear-stress continuity across the thickness laminated beam. Also, this theory appears as a natural extension to the **FSDT** for laminated-composite beams. We considered the transverse normal strain in the model. The transverse actuation is used to control the transverse amplitudes of deflection. Due to the consideration of thin beam analysis, the variation of the transverse displacement ($\boldsymbol{w}$) in the thickness direction at any point of the **HFRC** base beam, **ACLD**, and constraining layer are considered to be affine across the thickness direction. Hence, in the case of the overall beam, the transverse displacement can be expressed as:

$$\boldsymbol{w}(\boldsymbol{x},\boldsymbol{z},\boldsymbol{t}) = \boldsymbol{w_0}(\boldsymbol{x},\boldsymbol{t}) + (\boldsymbol{z} - \langle \boldsymbol{z} - \boldsymbol{h}/2\rangle)\boldsymbol{\theta_z}(\boldsymbol{x},\boldsymbol{t}) + (\langle \boldsymbol{z} - \boldsymbol{h}/2\rangle - \langle \boldsymbol{z} - \boldsymbol{h_{N+2}}\rangle)\boldsymbol{\phi_z}(\boldsymbol{x},\boldsymbol{t})$$
$$+\langle \boldsymbol{z} - \boldsymbol{h_{N+2}}\rangle \boldsymbol{\gamma_z}(\boldsymbol{x},\boldsymbol{t}) \tag{3.2}$$

where $\boldsymbol{w_0}$ denotes the transverse displacement; $\boldsymbol{\theta_z}, \boldsymbol{\phi_z}$ and $\boldsymbol{\gamma_z}$ denote the generalized displacements signifying the gradients corresponding to $\boldsymbol{z}$-direction of **HFRC** base beam, **ACLD**, and the constraining layer, respectively.

To simplify the mathematical formulation, the generalized displacement variables divided into two vectors are written as:

$$\{\boldsymbol{d_t}\} = [\boldsymbol{u_0} \quad \boldsymbol{w_0}]^{\boldsymbol{T}} \qquad \text{and}$$

$$\{\boldsymbol{d_r}\} = [\boldsymbol{\theta_x} \quad \boldsymbol{\theta_z} \quad \boldsymbol{\phi_x} \quad \boldsymbol{\phi_z} \quad \boldsymbol{\gamma_x} \quad \boldsymbol{\gamma_z}]^{\boldsymbol{T}} \tag{3.3}$$

The normal strains ($\boldsymbol{\epsilon_x^k}$ and $\boldsymbol{\epsilon_z^k}$) represent the state of strain at any layer of the laminated **HFRC** smart beam with respect to the $\boldsymbol{x}$– and $\boldsymbol{z}$–axis, respectively, and $\boldsymbol{\epsilon_{xz}^k}$ is the transverse shear strain.

Using Eqs. (3.1) and (3.2) the state of strain can be obtained by considering plane strain condition and the relations of linear strain displacement:

$$\begin{aligned}
&\{\boldsymbol{\epsilon_b^k}\} = \{\boldsymbol{\epsilon_{bt}}\} + [\boldsymbol{Z_1}]\{\boldsymbol{\epsilon_{br}}\}, \\
&\boldsymbol{\epsilon_{xz}^k} = \boldsymbol{\epsilon_{st}} + [\boldsymbol{Z}_4]\{\boldsymbol{\epsilon_{sr}}\}, \qquad \boldsymbol{k} = 1,2,3,\ldots,\boldsymbol{N} \\
&\{\boldsymbol{\epsilon_b^k}\} = \{\boldsymbol{\epsilon_{bt}}\} + [\boldsymbol{Z}_2]\{\boldsymbol{\epsilon_{br}}\}, \\
&\boldsymbol{\epsilon_{xz}^k} = \boldsymbol{\epsilon_{st}} + [\boldsymbol{Z}_5]\{\boldsymbol{\epsilon_{sr}}\}, \qquad \boldsymbol{k} = \boldsymbol{N} + 1 \\
&\{\boldsymbol{\epsilon_b^k}\} = \{\boldsymbol{\epsilon_{bt}}\} + [\boldsymbol{Z}_3]\{\boldsymbol{\epsilon_{br}}\}, \\
&\boldsymbol{\epsilon_{xz}^k} = \boldsymbol{\epsilon_{st}} + [\boldsymbol{Z_6}]\{\boldsymbol{\epsilon_{sr}}\}, \qquad \boldsymbol{k} = \boldsymbol{N} + 2
\end{aligned} \tag{3.4}$$

In which $\{\boldsymbol{\epsilon_b^k}\}$ is the strain vector, $\{\boldsymbol{\epsilon_{bt}}\}, \{\boldsymbol{\epsilon_{br}}\}, \{\boldsymbol{\epsilon_{st}}\}$, and $\{\boldsymbol{\epsilon_{sr}}\}$ are the generalized strains and $[\boldsymbol{Z_1}], [\boldsymbol{Z_2}], [\boldsymbol{Z_3}], [\boldsymbol{Z_4}], [\boldsymbol{Z_5}]$ and $[\boldsymbol{Z_6}]$ are the transformation matrices that are written as:

$$\{\boldsymbol{\epsilon_b^k}\} = [\{\epsilon_x^k\} \quad \{\epsilon_z^k\}]^{\boldsymbol{T}}, \qquad \{\boldsymbol{\epsilon_{bt}}\} = \left[\frac{\boldsymbol{\delta u_0}}{\boldsymbol{\delta x}} \quad 0\right]^{\boldsymbol{T}},$$

$$\{\boldsymbol{\epsilon_{br}}\} = \left[\frac{\boldsymbol{\delta\theta_x}}{\boldsymbol{\delta x}} \quad \frac{\boldsymbol{\delta\phi_x}}{\boldsymbol{\delta x}} \quad \frac{\boldsymbol{\delta\gamma_x}}{\boldsymbol{\delta x}} \quad \boldsymbol{\theta_z} \quad \boldsymbol{\phi_z} \quad \boldsymbol{\gamma_z}\right]^{\boldsymbol{T}},$$

$$\boldsymbol{\epsilon_{st}} = \frac{\boldsymbol{\delta w_0}}{\boldsymbol{\delta x}}, \qquad \{\boldsymbol{\epsilon_{sr}}\} = \left[\boldsymbol{\theta_z} \quad \boldsymbol{\phi_z} \quad \boldsymbol{\gamma_z} \quad \frac{\boldsymbol{\delta\theta_x}}{\boldsymbol{\delta x}} \quad \frac{\boldsymbol{\delta\phi_x}}{\boldsymbol{\delta x}} \quad \frac{\boldsymbol{\delta\gamma_x}}{\boldsymbol{\delta x}}\right]^{\boldsymbol{T}}, \tag{3.5}$$

$$[\boldsymbol{Z_1}] = \begin{bmatrix} \boldsymbol{z} & 0 & 0 & 0 & 0 & 0 \\ 0 & 0 & 0 & 1 & 0 & 0 \end{bmatrix},$$

$$[\boldsymbol{Z_2}] = \begin{bmatrix} \boldsymbol{h}/2 & (\boldsymbol{z} - \boldsymbol{h}/2) & 0 & 0 & 0 & 0 \\ 0 & 0 & 0 & 0 & 1 & 0 \end{bmatrix},$$

$$[\boldsymbol{Z_3}] = \begin{bmatrix} \boldsymbol{h}/2 & \boldsymbol{h_v} & (\boldsymbol{z} - \boldsymbol{h_{N+2}}) & 0 & 0 & 0 \\ 0 & 0 & 0 & 0 & 0 & 1 \end{bmatrix},$$

$$[\boldsymbol{Z_4}] = [1 \quad 0 \quad 0 \quad \boldsymbol{z} \quad 0 \quad 0],$$

$$[\boldsymbol{Z_5}] = [0 \quad 1 \quad 0 \quad \boldsymbol{h}/2 \quad (\boldsymbol{z} - \boldsymbol{h}/2) \quad 0],$$

$$[\boldsymbol{Z_6}] = [0 \quad 0 \quad 1 \quad \boldsymbol{h}/2 \quad \boldsymbol{h_v} \quad (\boldsymbol{z} - \boldsymbol{h_{N+2}})]$$

For the transversely isotropic layers of the base beam, the constitutive relations are obtained as:

$$\{\boldsymbol{\sigma_b^k}\} = [\boldsymbol{C_b^k}]\{\boldsymbol{\epsilon_b^k}\} \qquad \text{and}$$

$$\boldsymbol{\sigma_{xz}^k} = \boldsymbol{\overline{C}_{55}^k}\boldsymbol{\epsilon_{xz}^k}; \qquad (\boldsymbol{k} = 1, 2, 3, \ldots, \boldsymbol{N}) \tag{3.6}$$

where

$$\{\boldsymbol{\sigma_b^k}\} = [\boldsymbol{\sigma_x^k} \quad \boldsymbol{\sigma_z^k}]^{\boldsymbol{T}}, \quad [\boldsymbol{C_b^k}] = \begin{bmatrix} \boldsymbol{\overline{C}_{11}^k} & \boldsymbol{\overline{C}_{13}^k} \\ \boldsymbol{\overline{C}_{13}^k} & \boldsymbol{\overline{C}_{33}^k} \end{bmatrix}$$

and the transformed elastic stiffness constants corresponding to the reference coordinate system are $\boldsymbol{\overline{C}_{ij}^k}$ $(\boldsymbol{i}, \boldsymbol{j} = 1, 3 \text{ and } 5)$. It is assumed that the viscoelastic layer is isotropic and linearly viscoelastic. Eq. (3.6) represented constitutive relation of the viscoelastic layer $(\boldsymbol{k} = \boldsymbol{N} + 1)$ obtained by using the approach of dynamic modulus, with $\boldsymbol{\overline{C}_{ij}^{N+1}}$ $(\boldsymbol{i}, \boldsymbol{j} = 1, 3 \text{ and } 5)$ being the complex elastic constants (Chantalakhana and Stanway, 2001; Jeung and Shen, 2001). For the piezo layer, the constitutive relations can be obtained as:

$$\{\boldsymbol{\sigma}_b^k\} = [\boldsymbol{C}_b^k]\{\boldsymbol{\epsilon}_b^k\} - \{\boldsymbol{e}\}\boldsymbol{E}_z,$$

$$\boldsymbol{D}_z = \{\boldsymbol{e}\}^T\{\boldsymbol{\epsilon}_b^k\} + \boldsymbol{\varepsilon}_{33}\boldsymbol{E}_k \qquad \text{and} \tag{3.7}$$

$$\boldsymbol{\sigma}_{xz}^k = \overline{\boldsymbol{C}}_{55}^k\boldsymbol{\epsilon}_{xz}^k; \qquad \boldsymbol{k} = \boldsymbol{N} + 2$$

where $\{\boldsymbol{e}\}$ indicates the **1–3 PZC** constant matrix and $\boldsymbol{E}_z$ indicates the applied electric field and these terms can be given by:

$$\{\boldsymbol{e}\} = [\boldsymbol{e}_{31} \quad \boldsymbol{e}_{33}]^T \quad \text{and} \quad \boldsymbol{E}_z = -\boldsymbol{V}/\boldsymbol{h}_p \tag{3.8}$$

where $\boldsymbol{V}$ denotes a voltage difference applied over the thickness of **1–3 PZC** layer.

$\boldsymbol{T}_p$ and $\boldsymbol{T}_k$ indicate the total potential and the kinetic energy of the overall beam and calculated as (Ro and Baz, 2002):

$$\boldsymbol{T}_p = \frac{\boldsymbol{1}}{2}\sum_{\boldsymbol{k}=\boldsymbol{1}}^{\boldsymbol{N}+\boldsymbol{2}}\int_{\boldsymbol{\Omega}}\left(\{\boldsymbol{\epsilon}^k\}^T\{\boldsymbol{\sigma}^k\} + \boldsymbol{\epsilon}_{xz}^k\boldsymbol{\sigma}_{xz}^k\right)\boldsymbol{d\Omega} - \frac{\boldsymbol{1}}{2}\int_{\boldsymbol{\Omega}}\boldsymbol{D}_z\boldsymbol{E}_z\boldsymbol{d\Omega} - \int_{\boldsymbol{A}}\overline{\boldsymbol{p}}\boldsymbol{w}\boldsymbol{dA} \tag{3.9}$$

and

$$\boldsymbol{T}_k = \frac{\boldsymbol{1}}{2}\sum_{\boldsymbol{k}=1}^{\boldsymbol{N}+\boldsymbol{2}}\int_{\boldsymbol{\Omega}}\boldsymbol{\rho}^k\{\dot{\boldsymbol{d}}_t\}^T\{\dot{\boldsymbol{d}}_t\}\boldsymbol{d\Omega} \tag{3.10}$$

in which mass density of any $\boldsymbol{k}^{th}$ layer is denoted by $\boldsymbol{\rho}^k$; $\overline{\boldsymbol{p}}$ denotes the surface traction applied externally over a surface area $\boldsymbol{A}$ and volume $\boldsymbol{\Omega}$. While evaluating the kinetic energy, the rotary inertia was ignored as the beam is considered to be a thin beam. The discretization of the overall beam is carried out by using three noded isoparametric bar elements.

Making use of Eq. (3.3), the generalized displacement vectors with respect to $\boldsymbol{i}^{th}$ $(\boldsymbol{i} = 1, 2, 3)$ node of the element are expressed as:

$$\{\boldsymbol{d}_{ti}\} = [\boldsymbol{u}_{0i} \quad \boldsymbol{w}_{0i}]^T \qquad \text{and}$$

$$\{\boldsymbol{d}_{ri}\} = [\boldsymbol{\theta}_{xi} \quad \boldsymbol{\theta}_{zi} \quad \boldsymbol{\phi}_{xi} \quad \boldsymbol{\phi}_{zi} \quad \boldsymbol{\gamma}_{xi} \quad \boldsymbol{\gamma}_{zi}]^T \tag{3.11}$$

Therefore, the generalized displacement vectors at any point within the element are expressed as:

$$\{\boldsymbol{d_t}\} = [\boldsymbol{N_t}]\{\boldsymbol{d_t^e}\} \qquad \text{and} \qquad \{\boldsymbol{d_r}\} = [\boldsymbol{N_r}]\{\boldsymbol{d_r^e}\} \tag{3.12}$$

where

$$\{\boldsymbol{d_t^e}\} = [\{\boldsymbol{d_{t1}^e}\}^{\boldsymbol{T}} \quad \{\boldsymbol{d_{t2}^e}\}^{\boldsymbol{T}} \quad \{\boldsymbol{d_{t3}^e}\}^{\boldsymbol{T}}]^{\boldsymbol{T}},\ \{\boldsymbol{d_r^e}\} = [\{\boldsymbol{d_{r1}^e}\}^{\boldsymbol{T}} \quad \{\boldsymbol{d_{r2}^e}\}^{\boldsymbol{T}} \quad \{\boldsymbol{d_{r3}^e}\}^{\boldsymbol{T}}]^{\boldsymbol{T}},$$

$$[\boldsymbol{N_t}] = [\boldsymbol{N_{t1}} \quad \boldsymbol{N_{t2}} \quad \boldsymbol{N_{t3}}]^{\boldsymbol{T}}, \quad [\boldsymbol{N_r}] = [\boldsymbol{N_{r1}} \quad \boldsymbol{N_{r2}} \quad \boldsymbol{N_{r3}}]^{\boldsymbol{T}},$$

$$\boldsymbol{N_{ti}} = \boldsymbol{n_i I_t} \qquad \text{and} \qquad \boldsymbol{N_{ri}} = \boldsymbol{n_i I_r}$$

with $\boldsymbol{I_t}$ and $\boldsymbol{I_r}$ are respective 2×2 and 6×6 unit matrices, and $\boldsymbol{n_i}$ is the shape function of natural coordinates with respect to $\boldsymbol{i^{th}}$ node. Employing Eqs. (3.3), (3.5), (3.11), and (3.12), the generalized strain vectors at any point within the element that can be written as:

$$\{\boldsymbol{\epsilon_{bt}}\} = [\boldsymbol{B_{tb}}]\{\boldsymbol{d_t^e}\}, \qquad \{\boldsymbol{\epsilon_{br}}\} = [\boldsymbol{B_{rb}}]\{\boldsymbol{d_r^e}\},$$

$$\boldsymbol{\epsilon_{st}} = [\boldsymbol{B_{ts}}]\{\boldsymbol{d_t^e}\}, \qquad \text{and} \qquad [\boldsymbol{\epsilon_{sr}}] = [\boldsymbol{B_{rs}}]\{\boldsymbol{d_r^e}\} \tag{3.13}$$

where $[\boldsymbol{B_{tb}}]$, $[\boldsymbol{B_{rb}}]$, $[\boldsymbol{B_{ts}}]$, and $[\boldsymbol{B_{rs}}]$ denote the nodal strain–displacement matrices that can be written as:

$$[\boldsymbol{B_{tb}}] = [\boldsymbol{B_{tb1}} \quad \boldsymbol{B_{tb2}} \quad \boldsymbol{B_{tb3}}],$$

$$[\boldsymbol{B_{rb}}] = [\boldsymbol{B_{rb1}} \quad \boldsymbol{B_{rb2}} \quad \boldsymbol{B_{rb3}}],$$

$$[\boldsymbol{B_{ts}}] = [\boldsymbol{B_{ts1}} \quad \boldsymbol{B_{ts2}} \quad \boldsymbol{B_{ts3}}], \qquad \text{and}$$

$$[\boldsymbol{B_{rs}}] = [\boldsymbol{B_{rs1}} \quad \boldsymbol{B_{rs2}} \quad \boldsymbol{B_{rs3}}] \tag{3.14}$$

The submatrices appeared in Eq. (3.14) can be obtained as:

$$\boldsymbol{B_{tbi}} = \begin{bmatrix} \frac{\boldsymbol{\delta n_i}}{\boldsymbol{\delta x}} & 0 \\ 0 & 0 \end{bmatrix}, \qquad \boldsymbol{B_{tsi}} = \begin{bmatrix} 0 & \frac{\boldsymbol{\delta n_i}}{\boldsymbol{\delta x}} \end{bmatrix},$$

$$\boldsymbol{B}_{rbi} = \begin{bmatrix} \frac{\delta n_i}{\delta x} & 0 & 0 & 0 & 0 & 0 \\ 0 & 0 & \frac{\delta n_i}{\delta x} & 0 & 0 & 0 \\ 0 & 0 & 0 & 0 & \frac{\delta n_i}{\delta x} & 0 \\ 0 & \boldsymbol{n}_i & 0 & 0 & 0 & 0 \\ 0 & 0 & 0 & \boldsymbol{n}_i & 0 & 0 \\ 0 & 0 & 0 & 0 & 0 & \boldsymbol{n}_i \end{bmatrix}, \boldsymbol{B}_{rsi} = \begin{bmatrix} \boldsymbol{n}_i & 0 & 0 & 0 & 0 & 0 \\ 0 & 0 & \boldsymbol{n}_i & 0 & 0 & 0 \\ 0 & 0 & 0 & 0 & \boldsymbol{n}_i & 0 \\ 0 & \frac{\delta n_i}{\delta x} & 0 & 0 & 0 & 0 \\ 0 & 0 & 0 & \frac{\delta n_i}{\delta x} & 0 & 0 \\ 0 & 0 & 0 & 0 & 0 & \frac{\delta n_i}{\delta x} \end{bmatrix} \quad (3.15)$$

Finally, by making use of Eqs. (3.12) and (3.13) into Eqs. (3.9) and (3.10), the total potential energy ($\boldsymbol{T_p^e}$) and the kinetic energy ($\boldsymbol{T_k^e}$) of a typical length of element ($\boldsymbol{L_e}$) improved via **ACLD** treatment, and can be written as follows:

$$\boldsymbol{T_p^e} = \frac{1}{2}\boldsymbol{b}\big[\{\boldsymbol{d_t^e}\}^{\boldsymbol{T}}[\boldsymbol{K_{tt}^e}]\{\boldsymbol{d_t^e}\} + \{\boldsymbol{d_t^e}\}^{\boldsymbol{T}}[\boldsymbol{K_{tr}^e}]\{\boldsymbol{d_r^e}\} + \{\boldsymbol{d_r^e}\}^{\boldsymbol{T}}[\boldsymbol{K_{tr}^e}]\{\boldsymbol{d_t^e}\} + \{\boldsymbol{d_r^e}\}^{\boldsymbol{T}}[\boldsymbol{K_{rr}^e}]\{\boldsymbol{d_r^e}\}$$
$$- 2\{\boldsymbol{d_t^e}\}^{\boldsymbol{T}}\{\boldsymbol{F_{tp}^e}\}\boldsymbol{V} - 2\,\{\boldsymbol{d_r^e}\}^{\boldsymbol{T}}\,\{\boldsymbol{F_{rp}^e}\}\,\boldsymbol{V} - 2\,\{\boldsymbol{d_t^e}\}^{\boldsymbol{T}}\{\boldsymbol{F^e}\}\boldsymbol{V} - \boldsymbol{\varepsilon_{33}V^2/h_p}\big] \quad (3.16)$$

and

$$\mathbf{T_k^e} = \frac{1}{2}\mathbf{b}\int_{\mathbf{0}}^{\mathbf{L_e}} \bar{\mathbf{m}}\{\dot{\mathbf{d}}_{\mathbf{t}}^{\mathbf{e}}\}^{\mathbf{T}}[\mathbf{N}]^{\mathbf{T}}[\mathbf{N}]\,\{\dot{\mathbf{d}}_{\mathbf{t}}^{\mathbf{e}}\}\mathbf{dx} \quad (3.17)$$

In Eqs. (3.16) and (3.17), the elemental stiffness matrices $[\boldsymbol{K_{tt}^e}]$, $[\boldsymbol{K_{tr}^e}]$, $[\boldsymbol{K_{rr}^e}]$, elemental electrostatic coupling vector $\{\boldsymbol{F_{tp}^e}\}$, $\{\boldsymbol{F_{rp}^e}\}$, elemental load vector $\{\boldsymbol{F^e}\}$ and the mass parameter ($\bar{\boldsymbol{m}}$) can be obtained as follows:

$$[\boldsymbol{K_{tt}^e}] = \int_{\mathbf{0}}^{\boldsymbol{L_e}}([\boldsymbol{B_{tb}}]^{\boldsymbol{T}}[\boldsymbol{D_{tb}}][\boldsymbol{B_{tb}}] + [\boldsymbol{B_{ts}}]^{\boldsymbol{T}}[\boldsymbol{D_{ts}}][\boldsymbol{B_{ts}}])\boldsymbol{dx},$$

$$[\boldsymbol{K_{tr}^e}] = \int_{\mathbf{0}}^{\boldsymbol{L_e}}([\boldsymbol{B_{tb}}]^{\boldsymbol{T}}[\boldsymbol{D_{trb}}][\boldsymbol{B_{rb}}] + [\boldsymbol{B_{ts}}]^{\boldsymbol{T}}[\boldsymbol{D_{trs}}][\boldsymbol{B_{rs}}])\boldsymbol{dx},$$

$$[\boldsymbol{K_{rr}^e}] = \int_{\mathbf{0}}^{\boldsymbol{L_e}}([\boldsymbol{B_{rb}}]^{\boldsymbol{T}}[\boldsymbol{D_{rrb}}][\boldsymbol{B_{rb}}] + [\boldsymbol{B_{rs}}]^{\boldsymbol{T}}[\boldsymbol{D_{rrs}}][\boldsymbol{B_{rs}}])\boldsymbol{dx},$$

$$\{\boldsymbol{F_{tp}^e}\} = \int_{\mathbf{0}}^{\boldsymbol{L_e}}[\boldsymbol{B_t}]^{\boldsymbol{T}}\{\boldsymbol{D_{tp}}\}\boldsymbol{dx}\,;\;\; \{\boldsymbol{F_{rp}^e}\} = \int_{\mathbf{0}}^{\boldsymbol{L_e}}[\boldsymbol{B_r}]^{\boldsymbol{T}}\{\boldsymbol{D_{rp}}\}\boldsymbol{dx}\,;\;\; \{\boldsymbol{F^e}\}$$
$$= \int_{\mathbf{0}}^{\boldsymbol{L_e}}\bar{\boldsymbol{p}}[\boldsymbol{N_t}]^{\boldsymbol{T}}[0 \quad 1]^{\boldsymbol{T}}\boldsymbol{dx},$$

$$\bar{\boldsymbol{m}} = \sum_{k=1}^{N+2} \boldsymbol{\rho}^k (\boldsymbol{h}_{k+1} - \boldsymbol{h}_k) \tag{3.18}$$

The various rigidity matrices are denoted by $[\boldsymbol{D_{tb}}]$, $[\boldsymbol{D_{trb}}]$, $[\boldsymbol{D_{rrb}}]$, $[\boldsymbol{D_{ts}}]$, $[\boldsymbol{D_{trs}}]$, $[\boldsymbol{D_{rrs}}]$**.** The rigidity vectors for electroelastic coupling $\left(\{\boldsymbol{D_{tp}}\}, \{\boldsymbol{D_{rp}}\}\right)$ appeared in Eq. (3.18) are expressed as follows:

$$[\boldsymbol{D_{tb}}] = \sum_{k=1}^{N+2} \int_{h_k}^{h_{k+1}} [\bar{\boldsymbol{C}}_b^k] \boldsymbol{dz}$$

$$[\boldsymbol{D_{trb}}] = \sum_{k=1}^{N} \int_{h_k}^{h_{k+1}} [\boldsymbol{C}_b^k][\boldsymbol{Z_1}]\boldsymbol{dz} + \int_{h_{N+1}}^{h_{N+2}} [\bar{\boldsymbol{C}}_b^{N+1}][\boldsymbol{Z_2}]\boldsymbol{dz} + \int_{h_{N+2}}^{h_{N+3}} [\bar{\boldsymbol{C}}_b^{N+2}][\boldsymbol{Z_3}]\boldsymbol{dz}$$

$$[\boldsymbol{D_{rrb}}] = \sum_{k=1}^{N} \int_{h_k}^{h_{k+1}} [\boldsymbol{Z_1}]^T [\boldsymbol{C}_b^k][\boldsymbol{Z_1}]\boldsymbol{dz} + \int_{h_{N+1}}^{h_{k+2}} [\boldsymbol{Z_2}]^T [\bar{\boldsymbol{C}}_b^{N+1}][\boldsymbol{Z_2}]\boldsymbol{dz}$$

$$+ \int_{h_{N+2}}^{h_{k+3}} [\boldsymbol{Z_3}]^T [\bar{\boldsymbol{C}}_b^{N+2}][\boldsymbol{Z_2}]\boldsymbol{dz}$$

$$\{\boldsymbol{D_{tp}}\} = \int_{h_{N+2}}^{h_{k+3}} -\{\boldsymbol{e}\}/\boldsymbol{h_p}\boldsymbol{dz},$$

$$\{\boldsymbol{D_{rp}}\} = \int_{h_{N+2}}^{h_{k+3}} -[\boldsymbol{Z_3}]^T \{\boldsymbol{e}\}/\boldsymbol{h_p}\boldsymbol{dz} \tag{3.19}$$

Applying the principle of virtual work (Ro and Baz, 2002), the open loop equation of motion for the coupled beam can be expressed as:

$$[\boldsymbol{M}^e]\{\ddot{\boldsymbol{d}}_t^e\} + [\boldsymbol{K}_{tt}^e]\{\boldsymbol{d}_t^e\} + [\boldsymbol{K}_{tr}^e]\{\boldsymbol{d}_r^e\} = \{\boldsymbol{F}_{tp}^e\}\boldsymbol{V} + \{\boldsymbol{F}^e\} \tag{3.20}$$

$$[\boldsymbol{K}_{rt}^e]\{\boldsymbol{d}_t^e\} + [\boldsymbol{K}_{rr}^e]\{\boldsymbol{d}_r^e\} = \{\boldsymbol{F}_{rp}^e\}\boldsymbol{V} \tag{3.21}$$

It should be noted that as the viscoelastic layer has a complex elastic stiffness matrix. The element improved with the **ACLD** treatment also has a complex stiffness matrix. Thus, for the element improved without the treatment of **ACLD**, the electroelastic coupling matrices are null vectors and elemental stiffness matrices are real. Since the stiffness matrices are combined in two separate parts, namely, bending and transverse shear deformation. Hence, to avoid the condition of shear locking for a thin beam, one can use the reduced order integration rule (2×2). By combining the elemental Eqs., the open loop global Eq. of motion can be expressed as:

$$[\boldsymbol{M}]\{\ddot{\boldsymbol{X}}\} + [\boldsymbol{K_{tt}}]\{\boldsymbol{X}\} + [\boldsymbol{K_{tr}}]\{\boldsymbol{X_r}\} = \{\boldsymbol{F_{tp}}\}\boldsymbol{V} + \{\boldsymbol{F}\} \tag{3.22}$$

and

$$[\boldsymbol{K_{rt}}]\{\boldsymbol{X}\} + [\boldsymbol{K_{rr}}]\{\boldsymbol{X_r}\} = \{\boldsymbol{F_{rp}}\}\boldsymbol{V} \tag{3.23}$$

where the global mass matrix is denoted by $[\boldsymbol{M}]$; the global stiffness matrices are represented by $[\boldsymbol{K_{tt}}]$, $[\boldsymbol{K_{tr}}]$, and $[\boldsymbol{K_{rr}}]$; the global electroelastic coupling vectors are denoted by $\{\boldsymbol{F_{tp}}\}$ and $\{\boldsymbol{F_{rp}}\}$; the global nodal generalized displacement vectors are denoted by $\{\boldsymbol{X}\}$ and $\{\boldsymbol{X_r}\}$; and the global nodal force vector is presented by $\{\boldsymbol{F}\}$. After the application of boundary conditions, the global equation of motion in terms of global nodal translational degrees of freedom (**DOF**) $\{\boldsymbol{X}\}$ is obtained by reducing the global generalized **DOF** $\{\boldsymbol{X_r}\}$, and can be written as follows:

$$[\boldsymbol{M}]\{\ddot{\boldsymbol{X}}\} + [\boldsymbol{K}]\{\boldsymbol{X}\} = \left(\{\boldsymbol{F_{tp}}\} - [\boldsymbol{K_{tr}}][\boldsymbol{K_{rr}}]^{-\boldsymbol{1}}\{\boldsymbol{F_{rp}}\}\right)\boldsymbol{V} + \{\boldsymbol{F}\} \tag{3.24}$$

where the global stiffness matrix $[\boldsymbol{K}]$ can be formulated as:

$$[\boldsymbol{K}] = [\boldsymbol{K_{tt}}] - [\boldsymbol{K_{tr}}][\boldsymbol{K_{rr}}]^{-\boldsymbol{1}}[\boldsymbol{K_{rt}}]$$

When voltage difference is not supplied to the **1–3 PZC** then Eq. (2.24) can be used to show the uncontrolled (passive) constrained layer damping of the **HFRC** substrate beam.

3.2.1 Closed Loop Model

A close loop model is presented to calculate the required control voltage for active damping proportional to the velocity at the free end of the beam. Hence, the control voltage applied across the active layer is given by:

$$\boldsymbol{V} = -\boldsymbol{k_d}\dot{\boldsymbol{w}}(\boldsymbol{L_a}, 0) = -\boldsymbol{k_d}[\boldsymbol{U}]\{\dot{\boldsymbol{X}}\} \tag{3.25}$$

where the required control gain is represented by $\boldsymbol{k_d}$ and row vector $[\boldsymbol{U}]$ is denoting the sensor location.

Making use of Eq. (3.25) into Eq. (3.24), the closed loop characteristics of smart **HFRC** beam system can be obtained using Eq. of motion:

$$[\boldsymbol{M}]\{\ddot{\boldsymbol{X}}\} + [\boldsymbol{C_d}]\{\dot{\boldsymbol{X}}\} + [\boldsymbol{K}]\{\boldsymbol{X}\} = \{\boldsymbol{F}\} \tag{3.26}$$

where $[\boldsymbol{C_d}]$ denotes the matrix of active damping and can be expressed as:

$$[\boldsymbol{C_d}] = \boldsymbol{k_d}\left(\{\boldsymbol{F_{tp}}\} - [\boldsymbol{K_{tr}}][\boldsymbol{K_{rr}}]^{-1}\{\boldsymbol{F_{rp}}\}\right)[\boldsymbol{U}] \tag{3.27}$$

3.3 Results and Discussion

In this section, the numerical outcomes are presented for the active control of a laminated smart beam using the **FE** model derived in Section 3.2. We also present the quantitative analysis of **HFRC** substrate beam for the various $\boldsymbol{v_{CF}}$ and aspect ratio (***L/h***) of the beam.

3.3.1 Active Damping of HFRC Smart Cantilever Beam

To study the performance of the laminated **HFRC** as a damping material for a smart structure, numerical outcomes are estimated employing the **FE** model developed in earlier Section 3.2. For the active damping, the frequency responses of the smart cantilever composite beam are calculated. For this, Eq. (3.18) is formulated with the time-harmonic point load of 2 ***N*** subjected at the tip of the free end to investigate amplitude and frequency response analysis. The further analysis has been carried out by considering the carbon fiber volume fraction as 40% in base composite and **HFRC** substrate. For **1–3 PZC** the fiber volume fraction is taken as 60%. The material properties of the **PZC**, base composite and **HFRC** are tabulated in **Table 3.1** and **Table 3.2**, respectively.

The length of the transversely isotropic **HFRC** substrate beam is taken as 0.5 ***m***. Whereas the thickness of each layer of the **HFRC** substrate, piezoelectric layer, and viscous layer are considered as 0.005 ***m***, 0.001 ***m***, and 0.0002 ***m***, respectively.

Table 3.1. Properties of the piezoelectric material (Ray and Pradhan, 2006).

Material	C_{11} (GPa)	C_{13} (GPa)	C_{33} (GPa)	C_{44} (GPa)	e_{31} $(C\,m^{-2})$	e_{33} $(C\,m^{-2})$	ρ (kg/m^3)
1–3 PZC	9.293	6.182	35.444	1.536	-0.19	18.41	5090
PZT-5H	151	96	124	23	-5.1	27	7750

The length and thickness of each layer of transversely isotropic **HFRC** substrate beam are taken as 0.5 m and 0.005 m, respectively. The viscous layer and piezoelectric layer are having a thickness of 0.0002 m and 0.001 m, respectively, and the length of **ACLD** patch is covering 3/5th of the beam. The properties of the viscoelastic constraining layer such as density, Poisson's ratio, and complex shear modulus are considered as 1140 kg/m^3, 0.3 and $20(1+i)$ $MN\,m^{-2}$, respectively (Ro and Baz, 2002; Ray and Pradhan, 2006; Ray and Kundalwal, 2014).

Table 3.2. Effective elastic properties of **HFRC** lamina.

Eff. elastic constant	Two-phase ($v_{CNT} = 0\%$)		Three-phase ($v_{CNT} = 5\%$)		Three-phase ($v_{CNT} = 10\%$)	
	$v_{CF} = 40\%$	$v_{CF} = 60\%$	$v_{CF} = 40\%$	$v_{CF} = 60\%$	$v_{CF} = 40\%$	$v_{CF} = 60\%$
C_{11} (GPa)	96.6451	142.5567	125.5864	171.5618	154.537	200.5939
C_{12} (GPa)	4.1219	5.0647	4.2920	5.3836	4.4906	5.7748
C_{13} (GPa)	4.1219	5.0647	4.2719	5.3559	4.4469	5.7124
C_{23} (GPa)	4.3856	5.521	4.7174	6.0547	5.1033	6.7013
C_{33} (GPa)	7.7068	9.9779	8.3094	11.0133	9.0142	12.2889
C_{44} (GPa)	1.0054	1.407	1.091	1.5806	1.1926	1.8031

To verify the validation of the **FE** model derived in Section 3.2 for active damping of laminated **HFRC** substrate beam integrated with **ACLD** treatment constraining layer of **1–3 PZC**, we compare the frequency response with existing models for the identical beam adopting the similar boundary conditions. These results are tabulated in **Table 3.3** for symmetric cross-ply $(0°/90°/0°)$ and anti-symmetric angle-ply $(-45°/45°/-45°/45°)$ substrate. **Table 3.3** shows a good agreement between the present **FE** model and the existing literature. The convergence study of laminated **HFRC** beam integrated with **ACLD** treatment is presented in **Table 3.4**. Considering the convergence study, the frequency response analysis of laminated beam is done by meshing the beam into 20 elements.

Table 3.3. Frequency response **ACLD** integrated beam.

Beams	**Source**	**1st mode**	**2nd mode**	**3rd mode**
$0°/90°/0°$	Present **FEM**	34	204	561
	Ray and Pradhan (Ray and Pradhan, 2006)	33	207	568
	Ray and Malik (Ray and Mallik, 2003)	35	210	572
$-45°/45°/-45°/45°$	Present **FEM**	20.3	114.8	312.6
	Ray and Pradhan (Ray and Pradhan, 2006)	18.3	113.5	314.6
	Ray and Malik (Ray and Mallik, 2003)	19.2	115.6	316.7
Al substrate beam	Present **FEM**	84	266	518
	Experimental (Vasques, 2006)	92	258.5	502

Figure 3.3 illustrates the uncontrolled variation of amplitude $\boldsymbol{w}(\boldsymbol{L}, 0)$ with the frequency response of $0°/90°/0°$ **HFRC** smart beam for different percentage of **CNT** $(5, 5)$ ($\boldsymbol{v_{CNT}} = 0$ and 10 %). The figure illustrates that the laminated **HFRC** attenuates the amplitude of deflection of cantilever beam at free end significantly for the small value of $\boldsymbol{v_{CNT}}$. Thus, a slight enhancement in the damping characteristic of the system is observed for the passive damping (uncontrolled or gain = 0). For designing a smart structure, the fundamental frequency (i.e., the first mode of natural frequency) is an important parameter to be considered. The amplitude of fundamental frequency decreases from $3.49 \times 10^{-4}\, \boldsymbol{m}$ to $3.46 \times 10^{-4}\, \boldsymbol{m}$ (see **Table 3.5**) due to the incorporation of **CNTs** ($\boldsymbol{v_{CNT}} = 10$ %). It may be observed from passive damping that slight attenuation in the amplitudes of deflection is achieved with laminated **HFRC** beam. It will be very interesting to see the active performance of laminated **HFRC** beam and hence, the further analysis of the laminated **HFRC** beam for active damping (gain $\neq$ 0) and control voltage are shown in Figs. 3.4 and 3.5.

Table 3.4: Convergence study of **HFRC** beam integrated with **ACLD** treatment.

Beams	**Elements**	**Frequency (Hz)**		
		1st mode	**2nd mode**	**3rd mode**
	5	32	169	454
	10	33	171	471
$0°/90°/0$	15	33	172	475
	20	33	172	475
	25	33	172	475
	5	23	120	324
	10	24	122	337
$0°/90°/0°/90°$	15	24	123	339
	20	24	123	340
	25	24	123	340
	5	18	97	263
	10	19	99	273
$-45°/45°/-45°/45°$	15	19	99	275
	20	19	99	275
	25	19	99	275

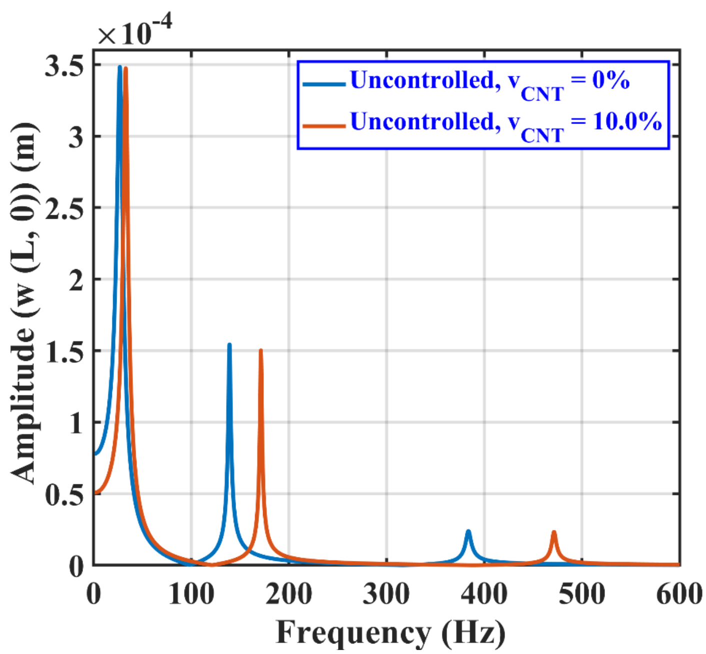

Figure 3.3. Variation of uncontrolled amplitude of deflection with respect to frequency response of $0°/90°/0°$ **HFRC** substrate beam.

Table 3.5. Amplitudes and fundamental natural frequencies of **HFRC** substrate smart beam corresponding to ply type.

Ply	**Gain**	$\boldsymbol{v_{CNT} = 0}$		$\boldsymbol{v_{CNT} = 10}$	
		Amplitude ($\boldsymbol{m}$)	**Frequency (1st mode) ($\boldsymbol{Hz}$)**	**Amplitude ($\boldsymbol{m}$)**	**Frequency (1st mode) ($\boldsymbol{Hz}$)**
$(0°/90°/0°)$	Uncontrolled	3.49×10^{-4}	26	3.46×10^{-4}	33
	2000	2.11×10^{-4}	26	1.92×10^{-4}	33
	3000	1.77×10^{-4}	26	1.57×10^{-4}	33
$(0°/90°/0°/90°)$	Uncontrolled	3.55×10^{-4}	19	3.51×10^{-4}	24
	2000	2.28×10^{-4}	19	2.09×10^{-4}	24
	3000	1.95×10^{-4}	19	1.76×10^{-4}	24
$(-45°/45°/-45°/45°)$	Uncontrolled	3.52×10^{-4}	16	3.48×10^{-4}	19
	2000	2.59×10^{-4}	16	2.40×10^{-4}	19
	3000	2.30×10^{-4}	16	2.11×10^{-4}	19

The frequency v/s amplitude of deflection $\boldsymbol{w}(\boldsymbol{L}, 0)$ of $0°/90°/0°$ **HFRC** and base composite substrate beam is shown in Fig. 3.4. This figure depicts both uncontrolled (passive damping or gain = 0) and controlled (active damping or gain ≠ 0) gain. It may be seen that for the given gain the **HFRC** substrate attenuates the amplitude of deflection significantly as compared to the base composite. **Table 3.5** summarizes the values of the maximum amplitude corresponding to the fundamental natural frequency for the 1st mode. From **Table 3.5** and Fig. 3.4, it may be observed that the reduction in amplitude of the **HFRC** substrate beam is ~ 10 % and ~ 12 % corresponding to the value of gain $(\boldsymbol{k_d}) = 2000$ and 3000. Due to the incorporation of **CNTs** both stiffness and density of the **HFRC** substrate enhanced. The higher stiffness and mass of the **HFRC** substrate beam reduces the amplitudes of deflection. Hence, due to the improved stiffness of the **HFRC** substrate higher damping is achieved in case of overall **ACLD/HFRC** substrate beam as compared to the base composite beam. This reveals that the addition of **CNTs** enhances the damping characteristic of the **HFRC** substrate beam for controlled or active damping.

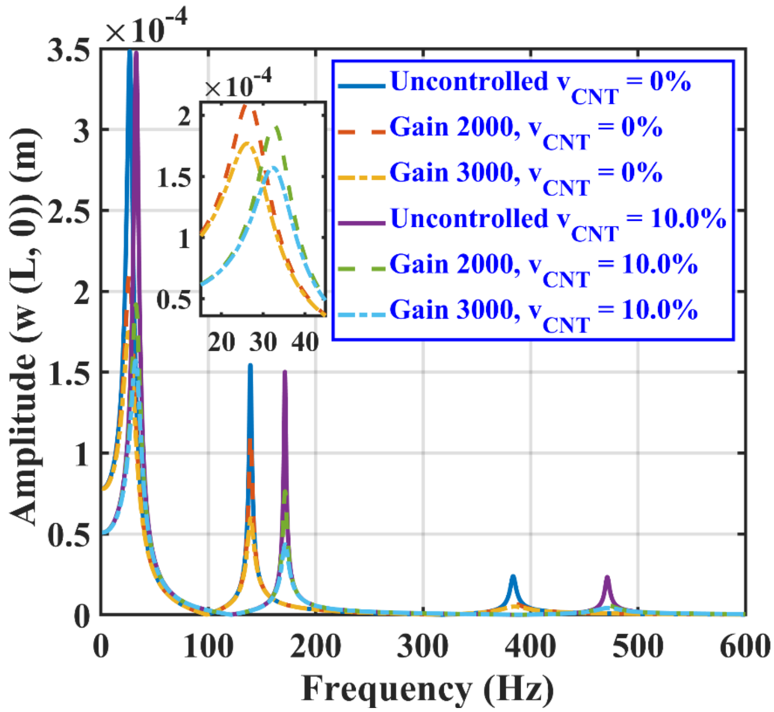

Figure 3.4. Variation of amplitude of deflection with frequency response of $0°/90°/0°$ **HFRC** substrate beam.

Figure 3.5 illustrates the voltage required to control the different modes of the amplitude of the deflection of the cantilever **HFRC** substrate beam at the free end. It may be seen from Fig. 3.5 that for the **HFRC** substrate beam the maximum control voltage for the value of gain $(\boldsymbol{k_d}) = 2000$ is $71.33\ \boldsymbol{V}$ which is $\sim 15\ \%$ less as compared to the voltage required for base composite. The difference in control voltage required for the **HFRC** and base composite substrate beam is considerably high. In practice, such a less value of control voltage can be easily arranged.

Figure 3.6 illustrates the damping performance of smart structure for the value of gain = 2000, with and without considering the piezoelectric constant $\boldsymbol{e_{31}}$ and $\boldsymbol{e_{33}}$. From Fig. 3.6, it may be seen that when the value of the piezoelectric constant $\boldsymbol{e_{31}} \neq 0$ and $\boldsymbol{e_{33}} = 0$, much higher amplitudes of deflections are observed when compared to the case of $\boldsymbol{e_{31}} = 0$ and $\boldsymbol{e_{33}} \neq 0$. From this, it may be concluded that the constraining layer of **ACLD** is mainly responsible for the attenuation of vertical shear deformation. This also means that the out-of-plane actuation has a much higher contribution in vibration attenuation than in-plane actuation of the laminated smart beam. In both cases of $\boldsymbol{e_{33}} = 0$

and $\boldsymbol{e_{33}} \neq 0$, the smart beam with the **HFRC** substrate due to incorporation of **CNTs** ($\boldsymbol{v_{CNT}}$ = 10 %) shows better damping behavior.

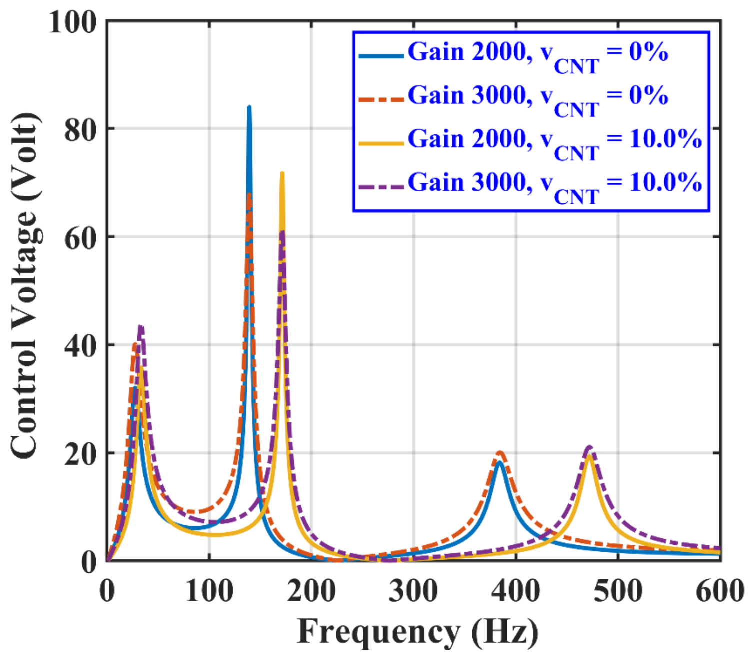

Figure 3.5. Variation of control voltage of 0°/90°/0° **HFRC** substrate beam with frequency.

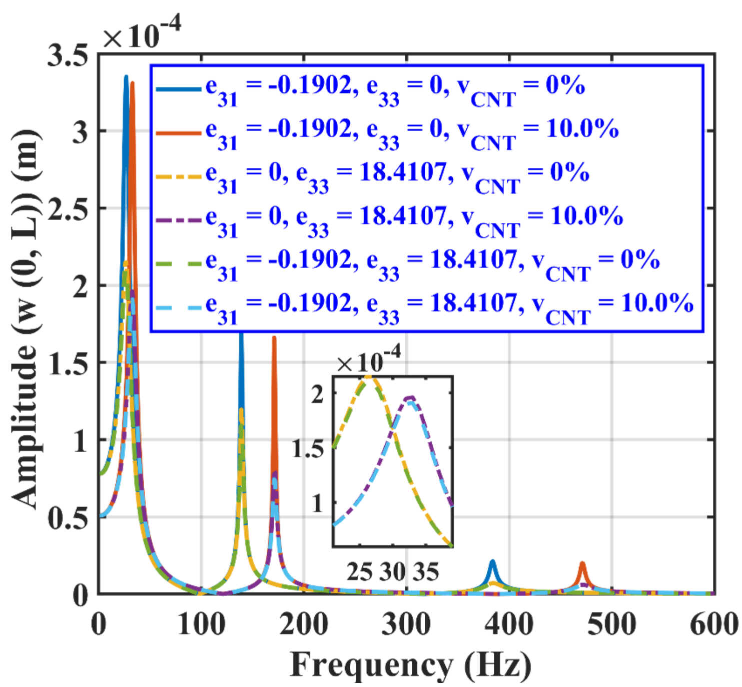

Figure 3.6. Effect of piezoelectric constant ($\boldsymbol{e_{33}}$) on the amplitude of deflection 0°/90°/0° **HFRC** substrate beam with value of $\boldsymbol{k_d}$ = 2000.

Figure 3.7 illustrates the performance of **1–3 PZC** over **PZT–5H** on the uncontrolled amplitude $\boldsymbol{w}(\boldsymbol{L}, 0)$ vs frequency response of $0°/90°/0°$ **HFRC** substrate beam. The figure shows that the **1–3 PZC** attenuates the vibration of beam better than **PZT–5H** and the enhancement in the damping characteristics is $\sim$17 %. It is to be noted that the density of **1–3 PZC** is very less compared to **PZT–5H**, as **1–3 PZC** is a tailor-made **PZC** material. Thus, **1–3 PZC** is a suitable candidate for the development of lightweight and high-performance **MEMS** smart structures.

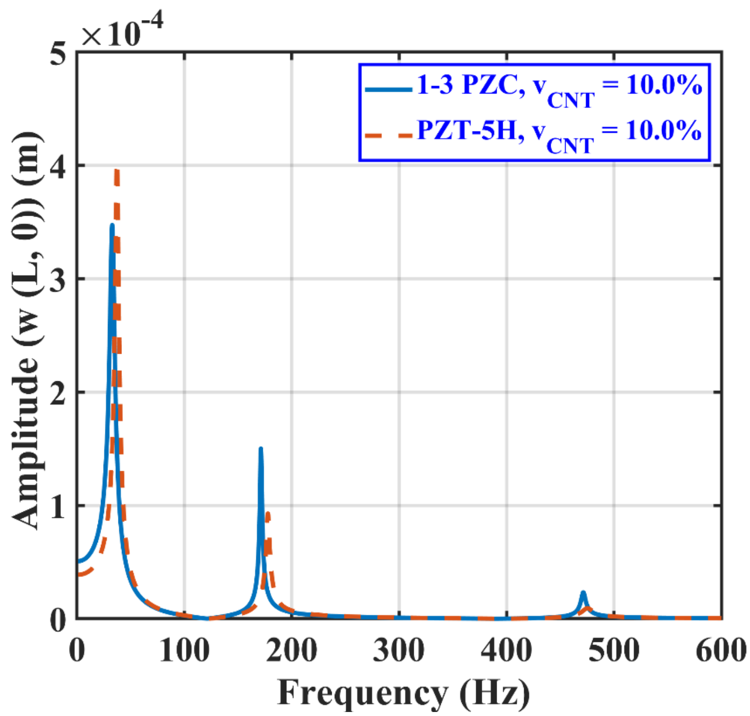

Figure 3.7. Comparison of **1–3 PZC** with **PZT**–5**H** on the uncontrolled amplitude of deflection of the $0°/90°/0°$ **HFRC** smart beam.

To investigate the performance of anti-symmetric cross-ply $(0°/90°/0°/90°)$ **HFRC** substrate beam, the frequency response for both passive and active control are demonstrated in Fig. 3.8 with respect to the amplitude of deflection of cantilever smart beam at free end $\boldsymbol{w}(\boldsymbol{L}, 0)$. It is noticed that the first mode shows much higher peaks compared to the other modes of natural frequency which is highly controlled for the $0°/90°/0°/90°$ **HFRC** substrate beam over the passive damping (gain = 0). The overall smart **HFRC** substrate beam shows the improved damping characteristic and the modes of natural frequency shifted slightly towards the higher side of the frequency as compared to the base composite substrate beam, this difference increases for the higher modes of natural frequency. To determine the performance of anti-symmetric angle-ply $(-45°/45°/-45°/45°)$ **HFRC** substrate beam, the frequency response with respect to the amplitude of deflection of cantilever smart beam at the free end $\boldsymbol{w}(\boldsymbol{L}, 0)$ are shown in Fig. 3.9. It may be observed that for the given gain the **HFRC** substrate beam attenuates the amplitude of deflection significantly as compared to base composite substrate beam. For the gain of 2000, the second mode of natural frequency showing higher peaks; however, for the effective control of higher mode, one can change the value of gain. It is clear from Fig. 3.9 that by changing the value of gain from 2000 to 3000 the higher modes are controlled significantly.

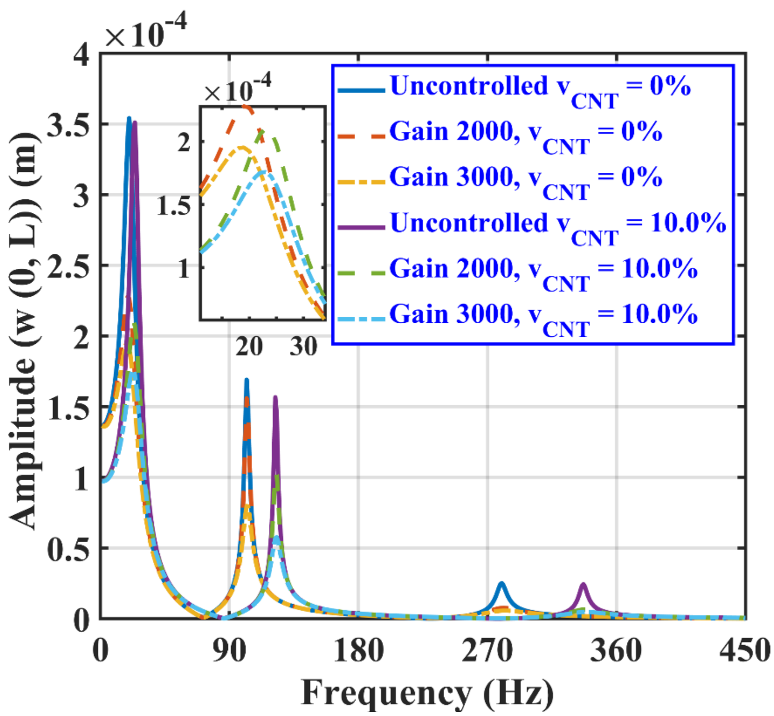

Figure 3.8. Variation of amplitude of deflection with respect to frequency response of $0°/90°/0°/90°$ **HFRC** substrate beam.

Figures 3.10 and 3.11 illustrate the voltage required to control the different modes of the amplitude of deflection of cantilever $0°/90°/0°/90°$ and **HFRC** substrate beam $-45°/45°/-45°/45°$ at the free end. The estimated value for the maximum control voltage required for $0°/90°/0°/90°$ base composite beam is 87.71 $\boldsymbol{V}$ and for the **HFRC** beam is 69.95 $\boldsymbol{V}$. The difference between the two values is $\sim 20\%$, which shows substantial improvement. Similarly, from Fig. 18, the estimated value for the maximum control voltage required for $-45°/45°/-45°/45°$ base composite beam is 182.2 $\boldsymbol{V}$ and for the **HFRC** beam is 128.4 $\boldsymbol{V}$. The difference between the two values is ~30 %. It is noticed that the control voltage required for $-45°/45°/-45°/45°$ ply is significantly high, this due to the higher amplitude of deflection observed in Fig. 3.9.

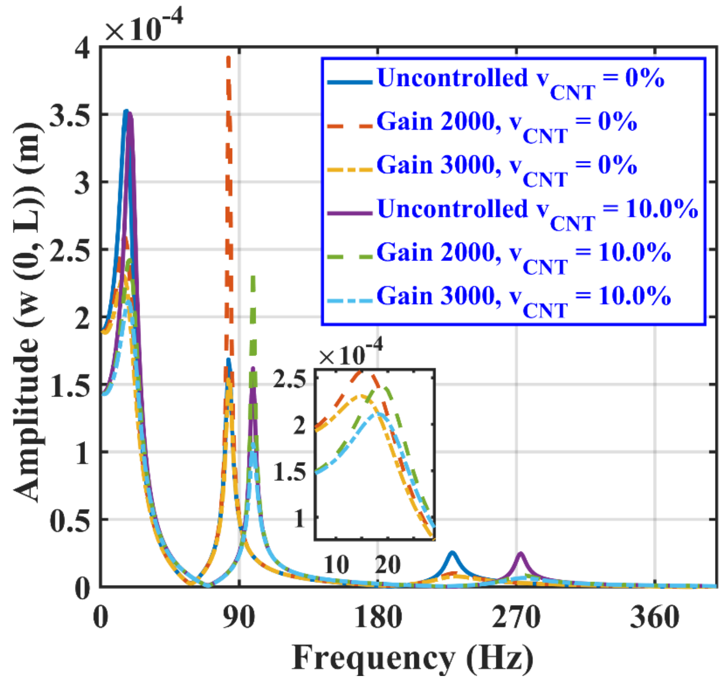

Figure 3.9. Variation of amplitude of deflection with respect to frequency response of $-45°/45°/-45°/45°$ **HFRC** substrate beam.

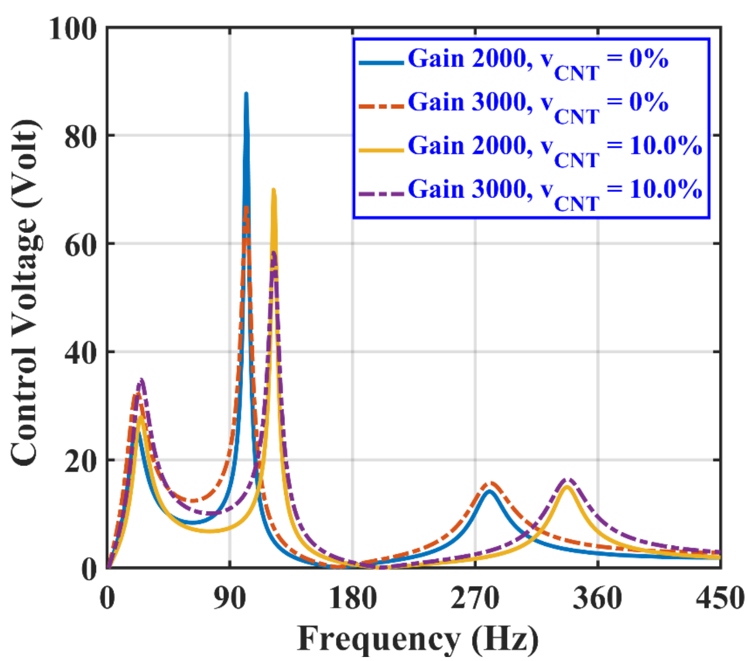

Figure 3.10. Variation of the control voltage of $0°/90°/0°/90°$ **HFRC** substrate beam with frequency.

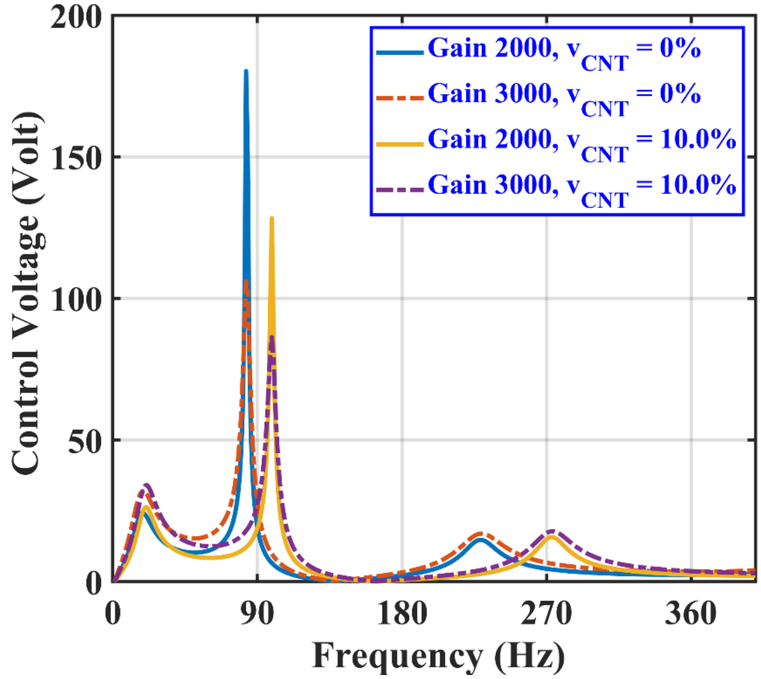

Figure 3.11. Variation of the control voltage of $-45°/45°/-45°/45°$ **HFRC** substrate beam with frequency.

3.3.2 Parametric Analysis of 0°/90°/0° HFRC Substrate Beam

Figure 3.12 illustrates the effect of change in the effective length of the constraining layer on the frequency response with respect to the amplitude of deflection of symmetric cross-ply **HFRC** beam ($\boldsymbol{k_d} = 2000$). The figure shows that the laminated **HFRC** beam attenuates the amplitude of deflection significantly as the effective length of the **PZC** patch ($\boldsymbol{L_a}$) increased from 60 % to 80 % of the beam length ($\boldsymbol{L}$).When the value of effective length changes from $\boldsymbol{L_a} = 0.6\boldsymbol{L}$ to $\boldsymbol{L_a} = 0.8\boldsymbol{L}$, the maximum value of the amplitude of the first mode for base composite decreases from 2.1×10^{-4} $\boldsymbol{m}$ to 1.24×10^{-4} $\boldsymbol{m}$, respectively. Whereas for **HFRC** the amplitude decreases from 1.9×10^{-4} $\boldsymbol{m}$ to 1.13×10^{-4} $\boldsymbol{m}$. This indicates that for $\boldsymbol{L_a} = 0.8\boldsymbol{L}$ the damping characteristics of smart beam enhance approximately around 40% for both base composite and **HFRC** beam. Whereas, for the second mode when the value of effective length changes from $\boldsymbol{L_a} = 0.6\boldsymbol{L}$ to $\boldsymbol{L_a} = 0.8\boldsymbol{L}$, the improvement in the damping characteristic for base composite is ~70 % and for the **HFRC** beam is ~60 %. Although the percentage reduction for the second mode in the case of **HFRC** beam is slightly less compared to the base composite beam, the laminated **HFRC** beam overall shows better damping characteristics. From this, we can conclude that the damping characteristic of the system can be improved by increasing the effective length of piezoelectric composite material.

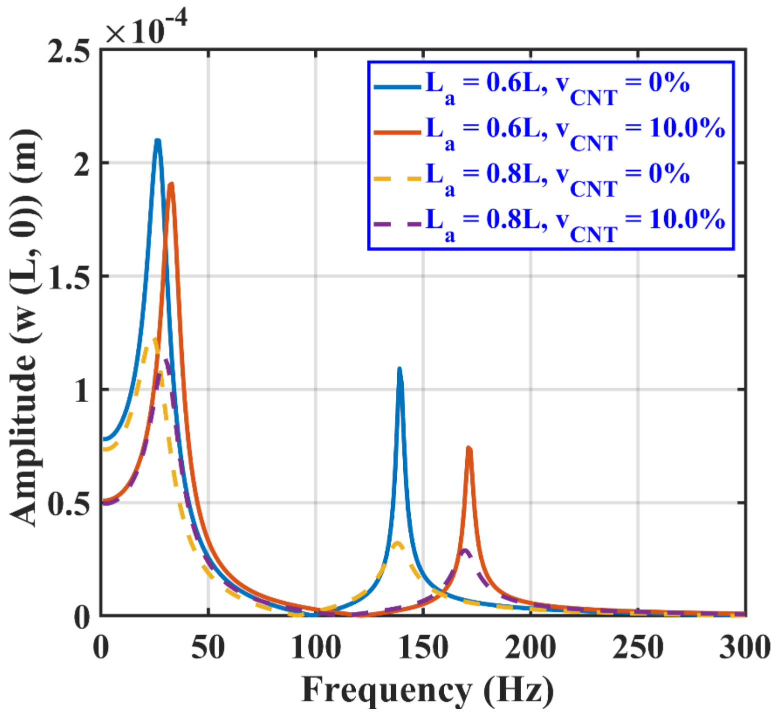

Figure 3.12. Effect of the effective length of **1–3 PZC** patch on the amplitude of deflection of $0°/90°/0°$ **HFRC** substrate beam ($\boldsymbol{k_d} = 2000$).

The effect of the thickness of **PZC** patch on the frequency response for the amplitude of the deflection of the smart beam is demonstrated in Fig. 3.13. Here, it can be noted that the **HFRC** substrate beam shows improved damping characteristics as compared to the base composite beam. By increasing the thickness of **PZC** layer the amplitudes of 1st mode attenuates approximately by ~5% for both **HFRC** and base composite beam; hence the damping characteristics improves significantly. Although for the second mode, it may be seen from Fig. 3.13 that by increasing the effective thickness of **PZC** layer results in the higher amplitudes, also a significant change in the natural frequency of the beam. For base composite substrate beam, the frequency shifted from 139 to 130 ***Hz***; for the **HFRC** substrate beam, frequency shifted from 171 to 158 ***Hz*** when thickness changed from 0.001 to 0.002 ***m***, respectively. Figure 3.14 demonstrates the effect of force on the frequency response for the amplitude of the deflection of the cantilever **HFRC** smart beam at the free end.

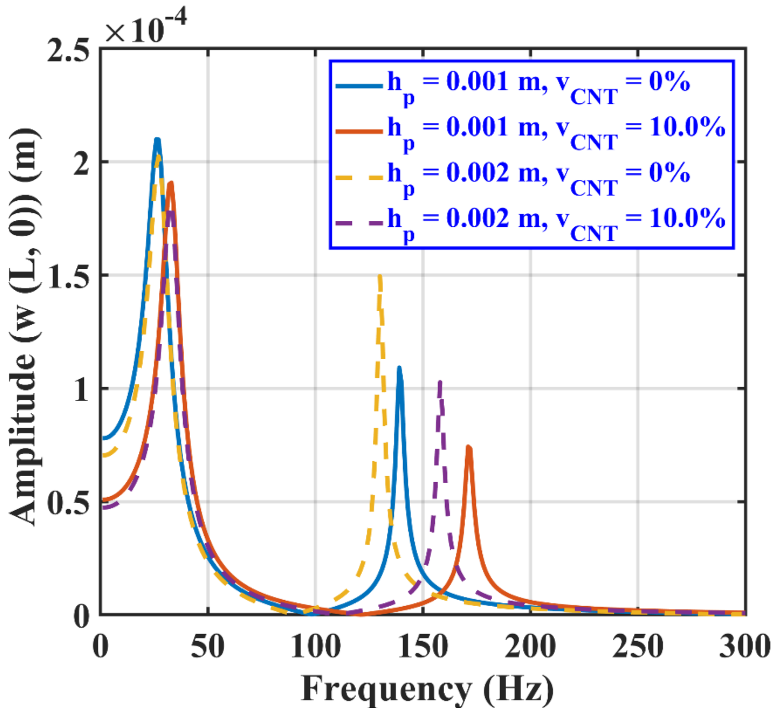

Figure 3.13. Effect of effective thickness of **1–3 PZC** patch on the amplitude of deflection of 0°/90°/0° **HFRC** smart beam ($\boldsymbol{k_d} = 2000$).

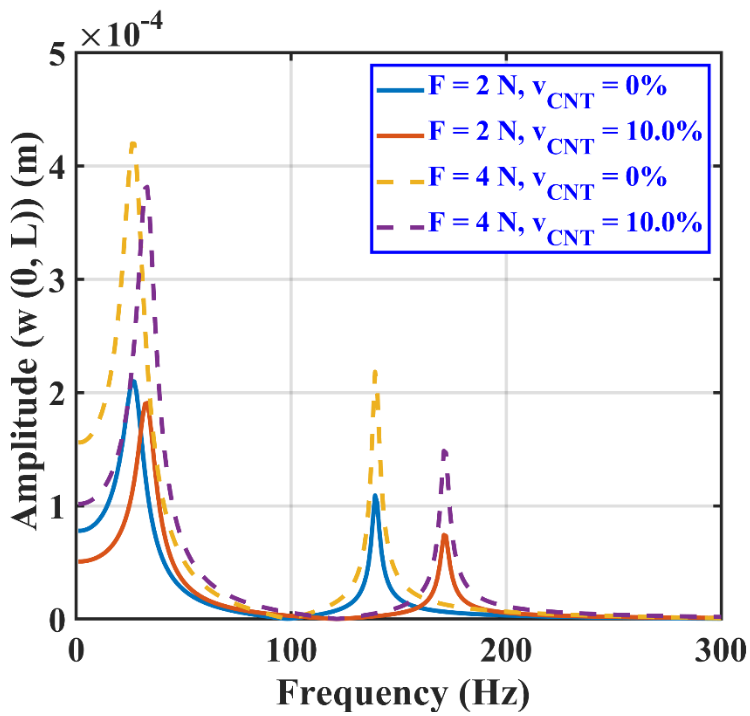

Figure 3.14. Effect of force on the amplitude of deflection of 0°/90°/0° **HFRC** substrate beam ($\boldsymbol{k_d} = 2000$).

Many times, these structures are subjected to variable loading conditions, thus it is important to understand the effect of force on the frequency response for the amplitude of deflection while designing the smart structure as a sensor and actuator. Figure 3.14 illustrates higher amplitude (twice as compared to the amplitude when force F = 2 $\boldsymbol{N}$) as the magnitude of force increases from 2 to 4 $\boldsymbol{N}$ and shows the substantial reduction of the amplitude of deflection with consideration of **CNTs** ($\boldsymbol{v_{CNT}} = 10$ %). In actual practice, this variation might not be twice, but it can be concluded that the increase in the magnitude of force will result in higher amplitudes.

3.3.3 Quantitative Relative Performance of HFRC Substrate Beam

In this section, we present the quantitative analysis of **HFRC** substrate beam for the various $\boldsymbol{v_{CF}}$ and aspect ratio (***L/h***) of the beam. The quantitative analysis is important for selecting, the optimum range of fiber in the composite material and the aspect ratio of the structure to achieve the maximum efficiency of the overall structure.

To demonstrate the enhancement in the damping characteristic of the **HFRC** laminated substrate beam, a damping characteristic enhancement factor (**DCEF**) is defined. This enhancement factor **DCEF** shows the reduction in amplitudes of deflection in terms of percentage of the **HFRC** substrate beam as compared to the base composite beam and hence, **DCEF** can be given by:

$$\boldsymbol{DCEF} = \frac{\boldsymbol{A_0} - \boldsymbol{A_{CNT}}}{\boldsymbol{A_0}}\% \tag{3.28}$$

where $\boldsymbol{A_0}$ is the amplitude of deflection of base composite beam and $\boldsymbol{A_{CNT}}$ is the amplitude of deflection of the **HFRC** beam.

Figures 3.15–3.17 illustrate the **DCEF** of various ply for the first mode of amplitudes of deflection at $\boldsymbol{v_{CNT}} = 5$ and 10%. The results were obtained at the value of gain ($\boldsymbol{k_d}$) = 2000 and it may be seen from the figure that a similar trend like Fig 3.15 was observed as the $\boldsymbol{v_{CF}}$ increases the **DCEF** decreases. This is mainly because the carbon fiber and **CNTs** are aligned in the 1–direction and thus $\boldsymbol{C_{11}}$ of the composite has a major impact on the attenuation of vibrational amplitudes. It may also be observed from Figs. 3.15–3.17 that the significant enhancement in the damping characteristics can be achieved by incorporating 5% and 10% $\boldsymbol{v_{CNT}}$ in the base composite. In Figs. 3.15 and 3.16, at $\boldsymbol{v_{CF}} = 0.2$, the maximum value of **DCEF** in the case of symmetric and anti-symmetric cross-ply for $\boldsymbol{v_{CNT}} =$ 5% and 10% was around ~8% and 13%, respectively. Similarly, at $\boldsymbol{v_{CF}} = 0.2$, for anti-symmetric angle-ply (see Fig. 3.17), the maximum value of the **DCEF** is also observed, which is approx. ~6% and ~10% for $\boldsymbol{v_{CNT}} =$ 5% and 10%, respectively. This value of **DCEF** decreases as $\boldsymbol{v_{CF}}$ increases from 0.2 to 0.8 as shown in Figs. 3.15–3.17. From these results, we can conclude that the **HFRC** substrate beam is very much effective at lower $\boldsymbol{v_{CF}}$. Also, it is noticed that the attenuation in amplitudes of vibration obtained at higher $\boldsymbol{v_{CF}}$ of the base composite could be achievable with the **HFRC** at a much lower $\boldsymbol{v_{CF}}$ by considering a certain volume fraction of **CNTs**.

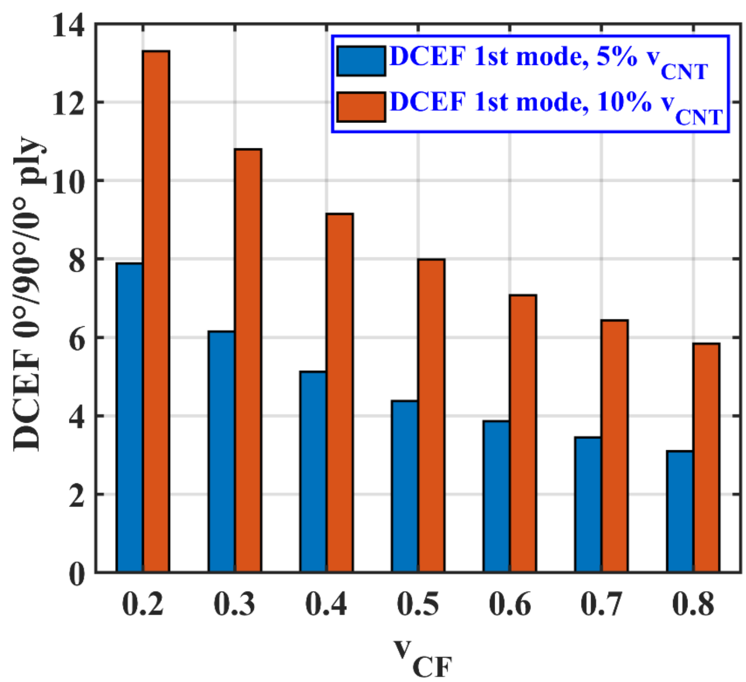

Figure 3.15. Variation of **DCEF** of 0°/90°/0° for the 1st mode of the amplitude of deflection at a gain ($\boldsymbol{k_d}$) of 2000 and $\boldsymbol{v_{CNT}} = 5$ and 10% with $\boldsymbol{v_{CF}}$.

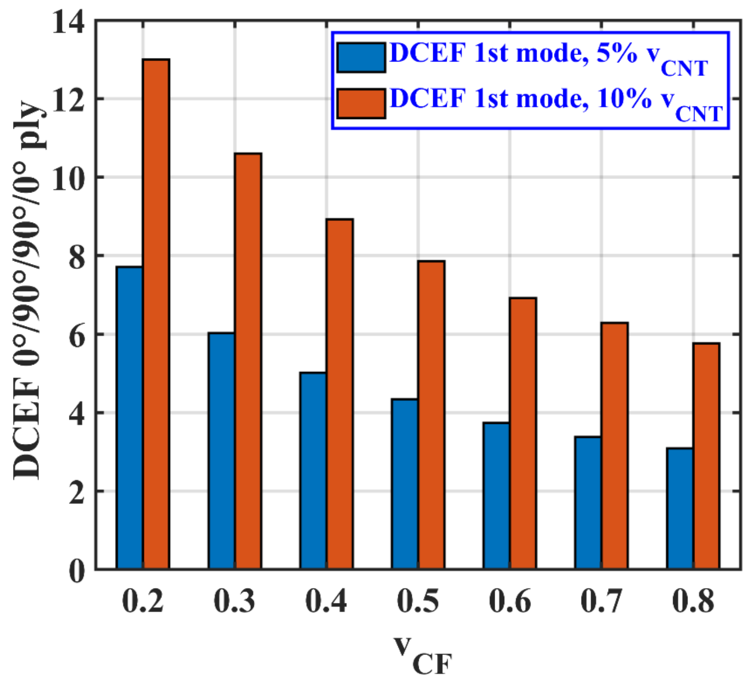

Figure 3.16. Variation of **DCEF** of $0°/90°/90°/0°$ for the 1st mode of the amplitude of deflection at a gain ($\boldsymbol{k_d}$) of 2000 and $\boldsymbol{v_{CNT}} = 5$ and 10% with $\boldsymbol{v_{CF}}$.

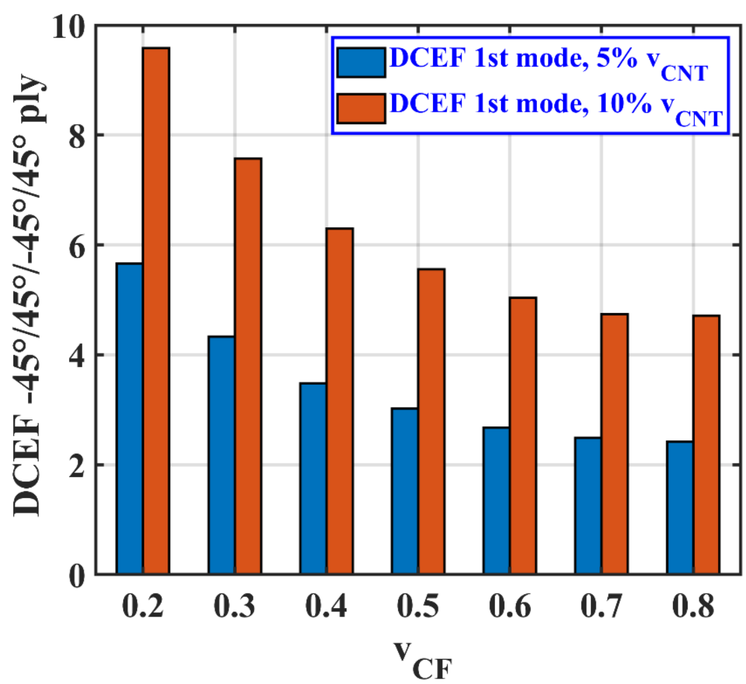

Figure 3.17. Variation of **DCEF** of $-45°/45°/-45°/45°$ for the 1st mode of the amplitude of deflection at a gain ($\boldsymbol{k_d}$) of 2000 and $\boldsymbol{v_{CNT}} = 5$ and 10% with $\boldsymbol{v_{CF}}$.

The structural parameters such as mass, aspect ratio (length, width, and thickness), and stiffness affect the natural frequency and vibrational amplitudes of the system. The effect of length to thickness ratio (***L/h***) on **DCEF** of the **HFRC** laminated beam for the 1st mode of amplitudes of vibration is demonstrated in Figs. 3.18 to 3.20. It may be seen from Fig. that the **DCEF** enhanced as the aspect ratio decreases and it is maximum at the ***L/h*** = 20. It was observed that as the aspect ratio of the substrate decreases, the amplitudes of vibration attenuate, and the frequency of the overall system improves. This is due to the inherent property of **CNTs**. **CNTs** have excellent strength to weight ratio, thus the stiffness of the **HFRC** substrate enhanced significantly, therefore the damping performance of the laminated **HFRC** improved as compared to the base composite.

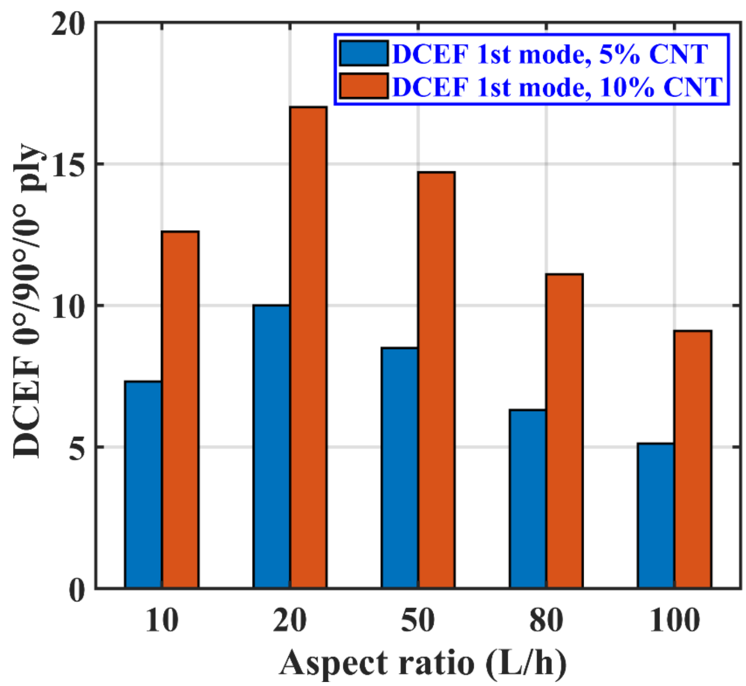

Figure 3.18. Variation of **DCEF** with respect to the aspect ratio of the substrate beam for various ply type 0°/90°/0° at a gain ($\boldsymbol{k_d}$) of 2000 and $\boldsymbol{v_{CNT}} = 5$ and 10%.

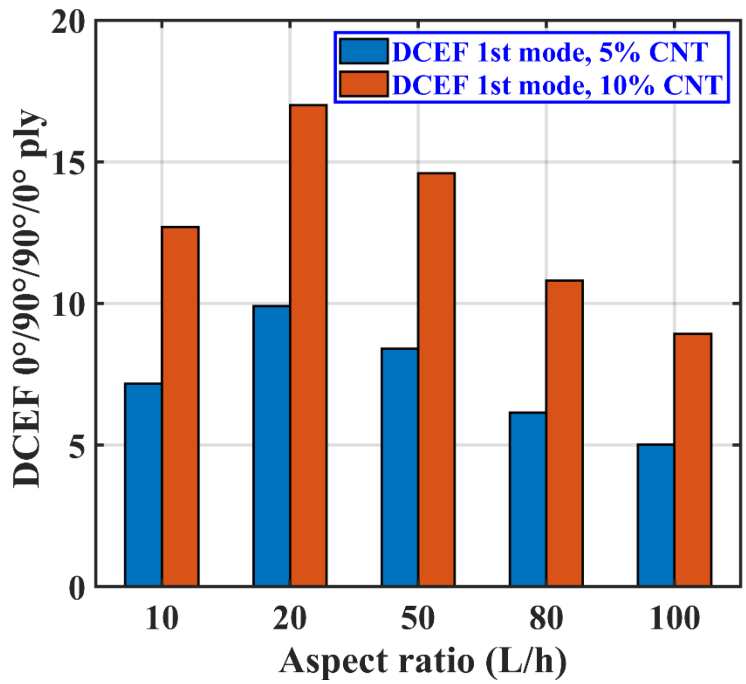

Figure 3.19. Variation of **DCEF** with respect to the aspect ratio of the substrate beam for various ply type $0°/90°/90°/0°$ at a gain ($\boldsymbol{k_d}$) of 2000 and $\boldsymbol{v_{CNT}} = 5$ and 10%.

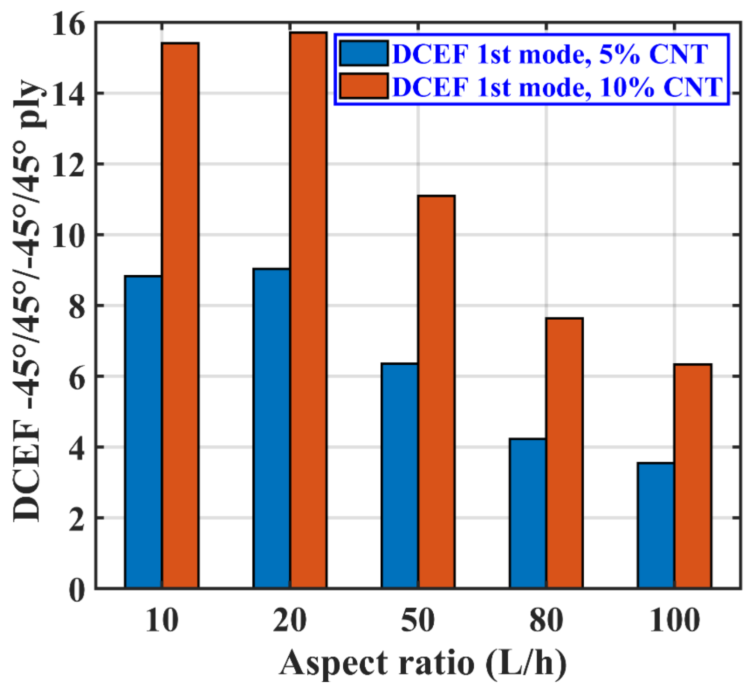

Figure 3.20. Variation of **DCEF** with respect to the aspect ratio of the substrate beam for various ply type $-45°/45°/-45°/45°$ at a gain ($\boldsymbol{k_d}$) of 2000 and $\boldsymbol{v_{CNT}} = 5$ and 10% a

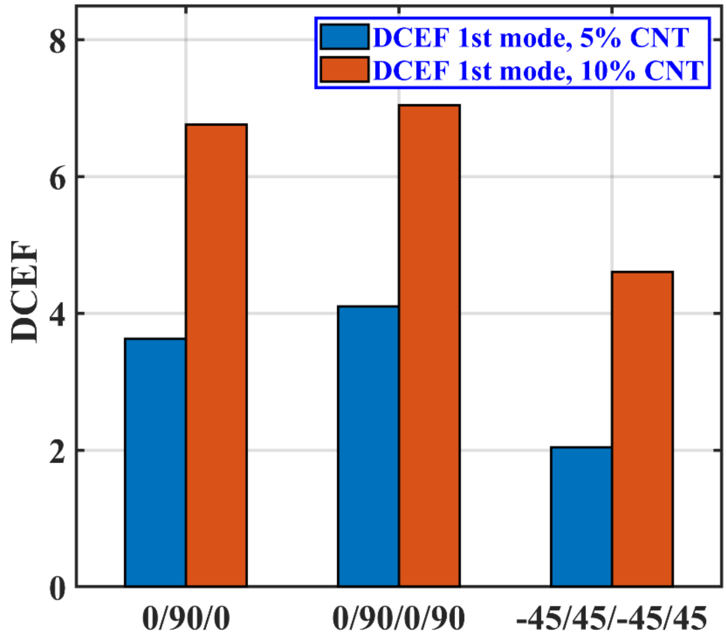

Figure 3.21. Variation of **DCEF** with respect to the aspect ratio of the substrate beam for various ply type at a gain ($\boldsymbol{k_d}$) of 2000, $\boldsymbol{v_{CNT}} = 5$ and 10%, and aspect ratio (***L/h***) = 100 by keeping the overall fiber volume fraction same for base composite and **HFRC**.

The effect of length to thickness ratio (***L/h***) on **DCEF** of the **HFRC** laminated beam for the 1st mode of amplitudes of vibration by keeping the overall volume fraction of base composite and **HFRC** the same is demonstrated in Figs. 3.21 for the various ply types. The fiber volume fraction in the base composite is taken as 40%, while in **HFRC,** the total fiber volume fraction (i.e. $\boldsymbol{v_{CNT}} + \boldsymbol{v_{CF}}$) is taken as 40%. The results show that due to the consideration of **CNTs** the overall structural damping characteristics of **HFRC** significantly improved for all the ply types, and the best results are observed for the anti-symmetric cross-ply.

The results demonstrated in Figs. 3.3 to 3.21 clearly show the significant enhancement in the damping characteristics of the novel smart **HFRC** laminated cantilever beam with consideration of **CNTs**. The quantitative relative performance of **HFRC** and base composite can be presented by defining a factor: **DCEF** for the change in damping characteristics, which are shown as a bar chart in Figs. 3.15 to 3.20. Based on these results one can determine the required response of smart structures by varying different parameters such as length and thickness of piezoelectric patch, applied force, angle of composite ply, aspect ratio of the composite beam, and the volume fraction of fiber and nanofillers.

3.4 Summary

The damping characteristics of the **HFRC** laminated smart cantilever beam is performed. The effect of **CNTs** on the damping characteristic of the laminated **HFRC** smart beam is analyzed. A **FE** model is developed to study the active damping of symmetric and anti-symmetric cross-ply, and anti-symmetric angle-ply **HFRC** smart composite beam attached with **ACLD** patch treatment. From the present investigation following main conclusions are carried out:

1. The damping characteristics of the novel **HFRC** laminated beam considering the $\boldsymbol{v_{CNT}} = 10\%$ for both symmetric and anti-symmetric cross-ply is improved when compared to the base composite with $\boldsymbol{v_{CNT}} = 0\%$. This is mainly because of the high stiffness and density offered by **CNTs**, which improves the overall damping performance of the laminated **HFRC** smart beam. This implies that the **HFRC** is a suitable candidate for developing a high-performance composite structure.
2. It may be concluded from the control voltage results that considerably low voltage is required to control the amplitude of **HFRC** smart beam as compared to the base composite beam.
3. Among the various ply, the performance of $(0°/90°/0°)$ symmetric cross-ply is better considering both the passive and active damping.
4. The contribution of vertical actuation of **ACLD** treatment constraining the layer of **1–3 PZC** material in the vibration damping is significantly higher as compared to in-plane actuation.
5. The performance of tailor made **1–3 PZC** is better as compared to **PZT**–5**H**, making **1–3 PZC** a suitable candidate for the development of the efficient smart structure.
6. It may be concluded from the parametric analysis that the effective length of **1–3 PZC** layer is a more sensitive parameter as compared to the effective thickness of **1–3 PZC** layer. Because comparatively high enhancement in the damping

characteristic of **HFRC** is observed for the change in the effective length of **1–3 PZC** layer.

7. In the quantitative relative performance, we defined a factor **DCEF** to analyse the enhanced performance of the laminated **HFRC** smart beam at various parameters. Based on these factors, it is observed that the same performance can be achieved with the **HFRC** substrate beam with an adequate amount of **CNTs** at a much lower range of $\boldsymbol{v_{CF}}$, which was obtained at the higher range of $\boldsymbol{v_{CF}}$ in case of base composite substrate beam.
8. From the quantitative analysis, optimum performance of the laminated **HFRC** smart beam is observed at a range of 0.2 to 0.5 $\boldsymbol{v_{CF}}$.

Chapter 4

Active Vibration Damping of a Simply Supported Smart Multiscale Hybrid Fiber Reinforced Composite Plates Using 1–3 Piezoelectric Composites

This Chapter (Gupta *et al*., 2022c) *presents the finite element* ***(FE)*** *model using the first-order shear deformation theory* ***(FSDT)*** *to investigate the damping performance of laminated hybrid fiber-reinforced composite* ***(HFRC)*** *smart plates via the active constrained layer damping* ***(ACLD)*** *treatment. A unique feature of the* ***HFRC*** *is that the nanoscale carbon nanotubes* ***(CNTs)*** *are embedded in the matrix phase of carbon fiber composite to improve the overall properties, especially the damping characteristics of the resulting* ***HFRC****. The constraining layer of the* ***ACLD*** *treatment is considered to be made of vertically reinforced* ***1–3*** *piezoelectric composite* ***(PZC)*** *material. The system consists of a laminated* ***HFRC*** *plate integrated with the two patches of* ***ACLD*** *treatment and the numerical results are computed for three cases: symmetric and anti-symmetric cross-ply, and anti-symmetric angle-ply. The effect of in-plane and transverse actuation of* ***1–3 PZC*** *on the damping characteristics of the overall plate is also studied.*

4.1 Introduction

A laminated composite plate is an important structural element and hence, the present research is directed to study the damping performance of simply supported **(SS)** laminated **HFRC** plates. The present work considers the uniform dispersion of aligned **CNTs** in the matrix phase of **HFRC** to achieve the full potential of **CNTs**. The damping performance of smart laminated **HFRC** plates is investigated via the finite element approach using modified **FSDT**. The smart plate is composed of **HFRC** substrate and

ACLD treatment layer with a constrained layer of viscoelastic material and a constraining layer of **1–3 PZC**. Two such **ACLD** treatment layers are installed at the top surface of the substrate **HFRC**. The **ACLD** layers are responsible for the active damping when voltage is supplied. In the absence of voltage, the same **ACLD** treatment layer act as passive damping. In this context, a closed-loop model is developed to supply control voltage to the **ACLD** treatment patch based on simple velocity feedback control law. We present the comparison of the frequency response of the laminated **HFRC** with base composite plates considering three cases: symmetric and anti-symmetric cross-ply, and anti-symmetric angle-ply. The effect of the aspect ratio of the laminated **HFRC** plates on the fundamental frequency and amplitudes of deformation is also studied.

4.2 Theoretical FE Formulation

This section deals with the development of the **FE** model to investigate the **ACLD** of the laminated **HFRC** plates including $\boldsymbol{N}$ number of laminae. Figure 4.1 shows the schematic of the **HFRC** substrate plate with **ACLD** and **1–3 PZC** patches attached to its upper surface. The piezo fibers in the **1–3 PZC** are oriented along the $\boldsymbol{z}$-axis. The thickness of piezo and viscoelastic **(VE)** layers of the **ACLD** treatment is shown by $\boldsymbol{h_p}$ and $\boldsymbol{h_v}$, respectively. We consider the reference plane as the mid-plane of the **HFRC** substrate plate. The coordinate system ($\boldsymbol{x, y, z}$) on this reference plane is chosen such that $\boldsymbol{x} = 0$, $\boldsymbol{a}$ and $\boldsymbol{y} = 0$, $\boldsymbol{b}$ which represent the boundary conditions or dimensions of the **HFRC** substrate plate. The thickness of upper and lower surfaces of any ($\boldsymbol{k^{th}}$) layer of the complete plate system is denoted by $\boldsymbol{h_{k+1}}$ and $\boldsymbol{h_k}$ ($\boldsymbol{k} = 1, 2, 3, \ldots, \boldsymbol{N} + 2$).

4.2.1 Displacement Fields

According to the **FSDT**, the kinematics of axial deformations of the overall plate is demonstrated in Fig. 4.2(a) in which $\boldsymbol{\theta_x}, \boldsymbol{\phi_x},$ and $\boldsymbol{\gamma_x}$ indicate the corresponding generalized rotations of the normal to the mid-plane of the **HFRC** substrate plate, **VE**, and **1–3 PZC** layer in the $\boldsymbol{xz}$ plane. While $\boldsymbol{\theta_y}, \boldsymbol{\phi_y},$ and $\boldsymbol{\gamma_y}$ denote the generalized rotations of the **HFRC** substrate plate, **VE**, and **1–3 PZC** layer in the $\boldsymbol{yz}$ plane, respectively. Terms $\boldsymbol{u_0}$ and $\boldsymbol{v_0}$ represent the generalized translational displacements of a reference point ($\boldsymbol{x, y}$) on the mid-plane ($\boldsymbol{z} = 0$) of the **HFRC** substrate plate along the $\boldsymbol{x}$-

and $\boldsymbol{y}$- axes, respectively. Variables $\boldsymbol{u}$ and $\boldsymbol{v}$ denote the axial displacements at any point in the overall plate attached with the **ACLD** patches, which are obtained by using **FSDT** (Ray and Pradhan, 2006), such as:

$$\mathbf{u}(\boldsymbol{x},\boldsymbol{y},\boldsymbol{z},\boldsymbol{t}) = \boldsymbol{u_0}(\boldsymbol{x},\boldsymbol{y},\boldsymbol{t}) + (\boldsymbol{z} - \langle \boldsymbol{z} - \boldsymbol{h}/2\rangle)\boldsymbol{\theta_x}(\boldsymbol{x},\boldsymbol{y},\boldsymbol{t}) + (\langle \boldsymbol{z} - \boldsymbol{h}/2\rangle - \langle \boldsymbol{z} - \boldsymbol{h_{N+2}}\rangle)\boldsymbol{\phi_x}(\boldsymbol{x},\boldsymbol{y},\boldsymbol{t}) + \langle \boldsymbol{z} - \boldsymbol{h_{N+2}}\rangle \boldsymbol{\gamma_x}(\boldsymbol{x},\boldsymbol{y},\boldsymbol{t}) \quad (4.1)$$

$$\boldsymbol{v}(\boldsymbol{x},\boldsymbol{y},\boldsymbol{z},\boldsymbol{t}) = \boldsymbol{v_0}(\boldsymbol{x},\boldsymbol{y},\boldsymbol{t}) + (\boldsymbol{z} - \langle \boldsymbol{z} - \boldsymbol{h}/2\rangle)\boldsymbol{\theta_y}(\boldsymbol{x},\boldsymbol{y},\boldsymbol{t}) + (\langle \boldsymbol{z} - \boldsymbol{h}/2\rangle - \langle \boldsymbol{z} - \boldsymbol{h_{N+2}}\rangle)\boldsymbol{\phi_y}(\boldsymbol{x},\boldsymbol{y},\boldsymbol{t}) + \langle \boldsymbol{z} - \boldsymbol{h_{N+2}}\rangle \boldsymbol{\gamma_y}(\boldsymbol{x},\boldsymbol{y},\boldsymbol{t}) \quad (4.2)$$

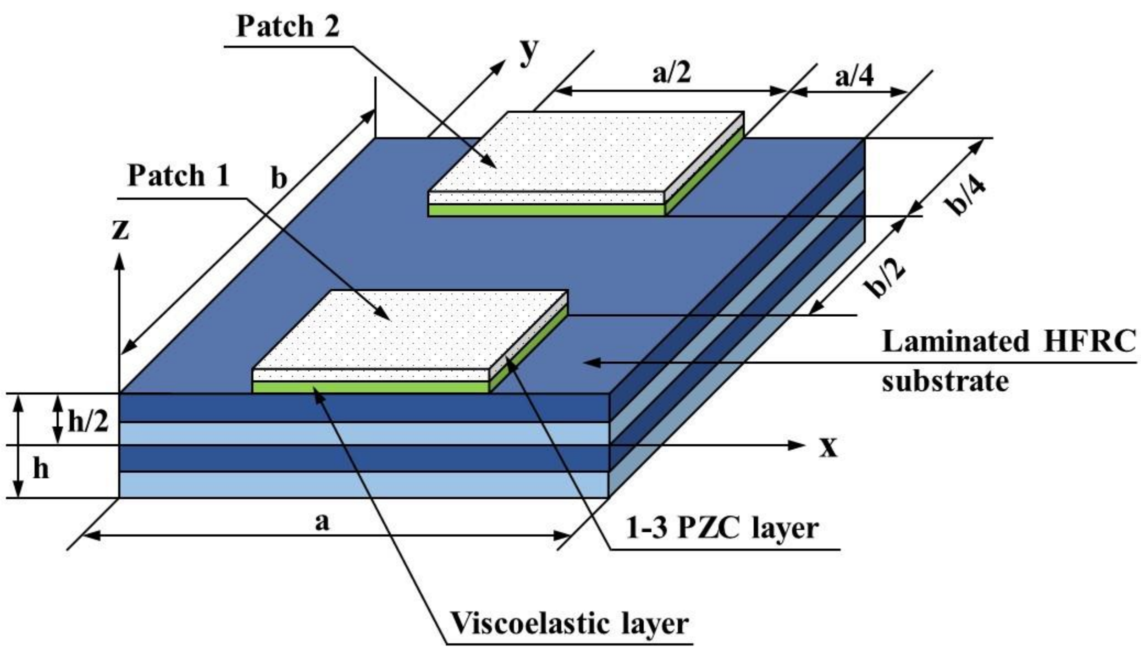

Figure 4.1. Schematic of laminated **HFRC** substrate plate integrated with the **ACLD** treatment and **1–3 PZC** patches.

In Eqs. (4.1) and (4.2), the terms in the bracket ⟨ ⟩ denote the singularity function known as zig-zag function. The multilayered structures like plates consist of relatively thin layers of different material compositions which may influence the different degrees of axial compliance. As a result, the axial displacement of anisotropic structures varies nonlinearly along the thickness of the plate. In a general layer-wise formulation of a plate theory, the axial displacement field could be modeled as a piecewise continuous function, that is, a collection of linear functions defined for each layer of thin plate. Such a function is referred as a "zig-zag" function. The theories based on the zig-zag function are known as zig-zag theory. The zig-zag theory appears like a natural extension to **FSDT**. Thus, in the present study, the layer-wise zig-zag function is added with the axial displacement field of **FSDT**. The proposed zig-zag function vanishes at the top and bottom surfaces of the plate and the full shear-stress continuity across the depth of the multilayered plate is not required. The idea behind such zig-zag formulation is to add a piecewise linear continuous function in such a way that the equilibrium of transverse shear stresses is satisfied in the laminate thickness. In the case of thin structures, the normal strain in the transverse direction is generally assumed as insignificant. However, the transverse actuation of **1–3 PZC**, constraining layer of **ACLD** patches may influence the flexural vibration of the plate. Thus, the transverse normal strains must be considered for modeling smart plates. The radial displacement ($\boldsymbol{w}$) is considered to be linearly varying along the thickness of the substrate composite plate, the **VE** layer, and the piezo layer. Hence, the transverse displacement ($\boldsymbol{w}$) of the overall plate at any point in the reference plane is considered as:

$$\begin{aligned}\boldsymbol{w}(\boldsymbol{x},\boldsymbol{y},\boldsymbol{z},\boldsymbol{t}) &= \boldsymbol{w_0}(\boldsymbol{x},\boldsymbol{y},\boldsymbol{t}) + (\boldsymbol{z} - \langle \boldsymbol{z} - \boldsymbol{h}/2\rangle)\boldsymbol{\theta_z}(\boldsymbol{x},\boldsymbol{y},\boldsymbol{t}) \\ &+ (\langle \boldsymbol{z} - \boldsymbol{h}/2\rangle - \langle \boldsymbol{z} - \boldsymbol{h_{N+2}}\rangle)\boldsymbol{\phi_z}(\boldsymbol{x},\boldsymbol{y},\boldsymbol{t}) + \langle \boldsymbol{z} - \boldsymbol{h_{N+2}}\rangle \boldsymbol{\gamma_z}(\boldsymbol{x},\boldsymbol{y},\boldsymbol{t}) \qquad (4.3)\end{aligned}$$

where, $\boldsymbol{\theta_z}, \boldsymbol{\phi_z}$ and $\boldsymbol{\gamma_z}$ represent the corresponding generalized rotations indicating the gradients of the transverse displacement with the $\boldsymbol{z}$-direction of the substrate composite plates, **VE** layer and **1–3 PZC** layer.

For the sake of simplicity, the generalized displacement of a system under consideration can be further split into two parts, translational displacements $\{\boldsymbol{d_t}\}$ and rotational displacements $\{\boldsymbol{d_r}\}$, and can be written as:

$$\{\boldsymbol{d_t}\} = [\boldsymbol{u_0} \quad \boldsymbol{v_0} \quad \boldsymbol{w_0}]^{\boldsymbol{T}},$$

$$\{\boldsymbol{d_r}\} = [\boldsymbol{\theta_x} \quad \boldsymbol{\theta_y} \quad \boldsymbol{\theta_z} \quad \boldsymbol{\phi_x} \quad \boldsymbol{\phi_y} \quad \boldsymbol{\phi_z} \quad \boldsymbol{\gamma_x} \quad \boldsymbol{\gamma_y} \quad \boldsymbol{\gamma_z}]^{\boldsymbol{T}} \qquad (4.4)$$

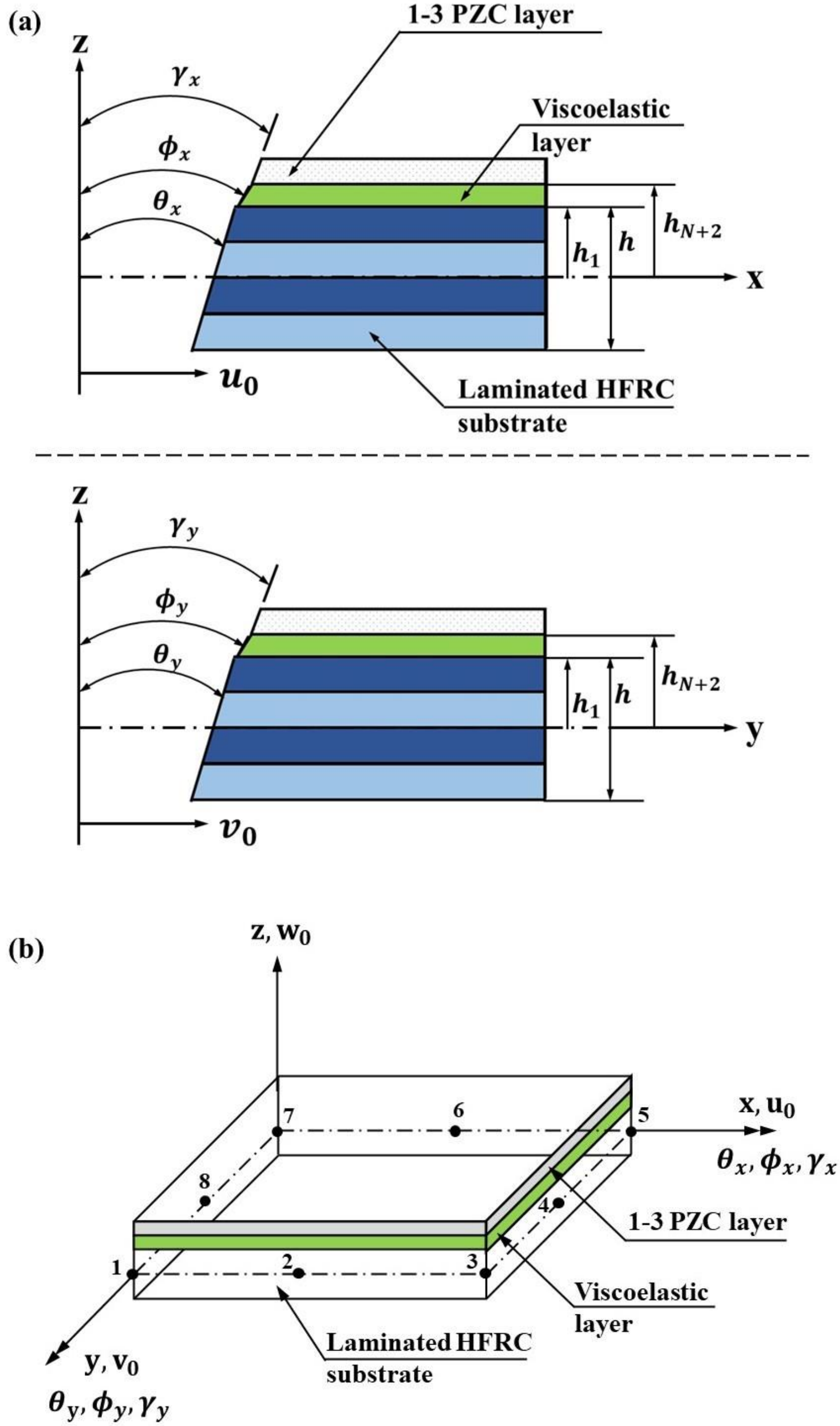

Figure 4.2. (a) Kinematics of deformation of a smart laminated **HFRC** plate, and (b) element topology and nodal degrees of freedom.

4.2.2 Strain-Displacement Relations

The selective integration rule can be applied to overcome the shear locking issue. At any point in the **HFRC** plate system, the state of strains can be assembled in two strain vectors, that is, in-plane $\{\boldsymbol{\epsilon_b}\}$ and out-of-plane $\{\boldsymbol{\epsilon_s}\}$ shear strains, which can be expressed as:

$$\{\boldsymbol{\epsilon_b}\} = [\boldsymbol{\epsilon_x} \quad \boldsymbol{\epsilon_y} \quad \boldsymbol{\epsilon_{xy}} \quad \boldsymbol{\epsilon_z}]^{\boldsymbol{T}};$$

$$\{\boldsymbol{\epsilon_s}\} = [\boldsymbol{\epsilon_{xz}} \quad \boldsymbol{\epsilon_{yz}}]^{\boldsymbol{T}} \tag{4.5}$$

where, $\boldsymbol{\epsilon_x}, \boldsymbol{\epsilon_y}$ and $\boldsymbol{\epsilon_z}$ denote the normal strains in corresponding directions; $\boldsymbol{\epsilon_{xy}}$ denotes the in-plane shear strain while $\boldsymbol{\epsilon_{xz}}$ and $\boldsymbol{\epsilon_{yz}}$ denote the out-of-plane shear strains.

Using the linear strain-displacement relations, the displacement field Eqs. (4.1)-(4.3) and strain field Eq. (4.5), the vectors $\{\boldsymbol{\epsilon_b}\}_{\boldsymbol{p}}$, $\{\boldsymbol{\epsilon_b}\}_{\boldsymbol{v}}$ and $\{\boldsymbol{\epsilon_b}\}_{\boldsymbol{c}}$ can be obtained which indicate the in-plane normal strain at any point in the **1–3 PZC**, **VE** layer, and **HFRC** substrate plate, respectively, and are represented as:

$$\{\boldsymbol{\epsilon_b}\}_{\boldsymbol{p}} = \{\boldsymbol{\epsilon_{bt}}\} + [\boldsymbol{Z_3}]\{\boldsymbol{\epsilon_{br}}\} ;$$

$$\{\boldsymbol{\epsilon_b}\}_{\boldsymbol{v}} = \{\boldsymbol{\epsilon_{bt}}\} + [\boldsymbol{Z_2}]\{\boldsymbol{\epsilon_{br}}\} ;$$

$$\{\boldsymbol{\epsilon_b}\}_{\boldsymbol{c}} = \{\boldsymbol{\epsilon_{bt}}\} + [\boldsymbol{Z_1}]\{\boldsymbol{\epsilon_{br}}\} \tag{4.6}$$

where the vectors $\{\boldsymbol{\epsilon_s}\}_{\boldsymbol{p}}$, $\{\boldsymbol{\epsilon_s}\}_{\boldsymbol{v}}$, and $\{\boldsymbol{\epsilon_s}\}_{\boldsymbol{c}}$ represent the state of out-of-plane shear strains at any point in the **1–3 PZC**, **VE** layer, and **HFRC** substrate plate, respectively, and are given by:

$$\{\boldsymbol{\epsilon_s}\}_{\boldsymbol{p}} = \{\boldsymbol{\epsilon_{st}}\} + [\boldsymbol{Z_6}]\{\boldsymbol{\epsilon_{sr}}\};$$

$$\{\boldsymbol{\epsilon_s}\}_{\boldsymbol{v}} = \{\boldsymbol{\epsilon_{st}}\} + [\boldsymbol{Z_5}]\{\boldsymbol{\epsilon_{sr}}\};$$

$$\{\boldsymbol{\epsilon_s}\}_{\boldsymbol{c}} = \{\boldsymbol{\epsilon_{st}}\} + [\boldsymbol{Z_4}]\{\boldsymbol{\epsilon_{sr}}\} \tag{4.7}$$

The matrices appeared in Eqs. (4.6) and (4.7) are as follows:

$$[\boldsymbol{Z_1}] = [[\bar{\boldsymbol{Z}}_1] \quad \tilde{\boldsymbol{o}} \quad \tilde{\boldsymbol{o}}],$$

$$[\boldsymbol{Z_2}] = [(\boldsymbol{h}/2)\boldsymbol{I} \quad [\bar{\boldsymbol{Z}}_2] \quad \tilde{\boldsymbol{o}}],$$

$$[\boldsymbol{Z_3}] = [(\boldsymbol{h}/2)\boldsymbol{I} \quad \boldsymbol{h_v I} \quad [\bar{\boldsymbol{Z}}_3]],$$

$$[\boldsymbol{Z_4}] = [\bar{\boldsymbol{I}} \quad \bar{\boldsymbol{o}} \quad \bar{\boldsymbol{o}} \quad \boldsymbol{z}\bar{\boldsymbol{I}} \quad \bar{\boldsymbol{o}} \quad \bar{\boldsymbol{o}}],$$

$$[\boldsymbol{Z_5}] = [\bar{\boldsymbol{o}} \quad \bar{\boldsymbol{I}} \quad \bar{\boldsymbol{o}} \quad (\boldsymbol{h}/2)\bar{\boldsymbol{I}} \quad (\boldsymbol{z}-\boldsymbol{h}/2)\bar{\boldsymbol{I}} \quad \bar{\boldsymbol{o}}],$$

$$[\boldsymbol{Z_6}] = [\bar{\boldsymbol{o}} \quad \bar{\boldsymbol{o}} \quad \bar{\boldsymbol{I}} \quad (\boldsymbol{h}/2)\bar{\boldsymbol{I}} \quad \boldsymbol{h_v I} \quad (\boldsymbol{z}-\boldsymbol{h_{N+2}})\bar{\boldsymbol{I}}]$$

in which

$$[\bar{\boldsymbol{Z}}_1] = \begin{bmatrix} \boldsymbol{z} & 0 & 0 & 0 \\ 0 & \boldsymbol{z} & 0 & 0 \\ 0 & 0 & \boldsymbol{z} & 0 \\ 0 & 0 & 0 & 1 \end{bmatrix}, \quad [\bar{\boldsymbol{Z}}_2] = \begin{bmatrix} (\boldsymbol{z}-\boldsymbol{h}/2) & 0 & 0 & 0 \\ 0 & (\boldsymbol{z}-\boldsymbol{h}/2) & 0 & 0 \\ 0 & 0 & (\boldsymbol{z}-\boldsymbol{h}/2) & 0 \\ 0 & 0 & 0 & 1 \end{bmatrix},$$

$$[\bar{\boldsymbol{Z}}_3] = \begin{bmatrix} (\boldsymbol{z}-\boldsymbol{h_{N+2}}) & 0 & 0 & 0 \\ 0 & (\boldsymbol{z}-\boldsymbol{h_{N+2}}) & 0 & 0 \\ 0 & 0 & (\boldsymbol{z}-\boldsymbol{h_{N+2}}) & 0 \\ 0 & 0 & 0 & 1 \end{bmatrix}, [\boldsymbol{I}] = \begin{bmatrix} 1 & 0 & 0 & 0 \\ 0 & 1 & 0 & 0 \\ 0 & 0 & 1 & 0 \\ 0 & 0 & 0 & 1 \end{bmatrix},$$

$$[\bar{\boldsymbol{I}}] = \begin{bmatrix} 1 & 0 \\ 0 & 1 \end{bmatrix}, \qquad [\bar{\boldsymbol{o}}] = \begin{bmatrix} 0 & 0 \\ 0 & 0 \end{bmatrix}, \qquad [\tilde{\boldsymbol{o}}] = \begin{bmatrix} \bar{\boldsymbol{o}} & \bar{\boldsymbol{o}} \\ \bar{\boldsymbol{o}} & \bar{\boldsymbol{o}} \end{bmatrix},$$

The generalized strain vectors can be expressed as,

$$\{\boldsymbol{\epsilon_{bt}}\} = \begin{bmatrix} \frac{\partial \boldsymbol{u_0}}{\partial \boldsymbol{x}} & \frac{\partial \boldsymbol{v_0}}{\partial \boldsymbol{y}} & \frac{\partial \boldsymbol{u_0}}{\partial \boldsymbol{y}} + \frac{\partial \boldsymbol{v_0}}{\partial \boldsymbol{x}} & 0 \end{bmatrix}^{\boldsymbol{T}},$$

$$\{\boldsymbol{\epsilon_{st}}\} = \begin{bmatrix} \frac{\partial \boldsymbol{w_0}}{\partial \boldsymbol{x}} & \frac{\partial \boldsymbol{w_0}}{\partial \boldsymbol{y}} \end{bmatrix}^{\boldsymbol{T}} \tag{4.8}$$

$$\{\boldsymbol{\epsilon_{br}}\} = \begin{bmatrix} \frac{\partial \boldsymbol{\theta_x}}{\partial \boldsymbol{x}} & \frac{\partial \boldsymbol{\theta_y}}{\partial \boldsymbol{y}} & \frac{\partial \boldsymbol{\theta_x}}{\partial \boldsymbol{y}} + \frac{\partial \boldsymbol{\theta_y}}{\partial \boldsymbol{x}} & \boldsymbol{\theta_z} & \frac{\partial \boldsymbol{\phi_x}}{\partial \boldsymbol{x}} & \frac{\partial \boldsymbol{\phi_y}}{\partial \boldsymbol{y}} & \frac{\partial \boldsymbol{\phi_x}}{\partial \boldsymbol{y}} + \frac{\partial \boldsymbol{\phi_y}}{\partial \boldsymbol{x}} & \boldsymbol{\phi_z} & \frac{\partial \boldsymbol{\gamma_x}}{\partial \boldsymbol{x}} & \frac{\partial \boldsymbol{\gamma_y}}{\partial \boldsymbol{y}} & \frac{\partial \boldsymbol{\gamma_x}}{\partial \boldsymbol{y}} + \frac{\partial \boldsymbol{\gamma_y}}{\partial \boldsymbol{x}} & \boldsymbol{\gamma_z} \end{bmatrix}^{\boldsymbol{T}}$$

$$\{\epsilon_{sr}\} = \left[\theta_x \quad \theta_y \quad \phi_x \quad \phi_y \quad \gamma_x \quad \gamma_y \quad \frac{\partial\theta_z}{\partial x} \quad \frac{\partial\theta_z}{\partial y} \quad \frac{\partial\phi_z}{\partial x} \quad \frac{\partial\phi_z}{\partial y} \quad \frac{\partial\gamma_z}{\partial x} \quad \frac{\partial\gamma_z}{\partial y}\right]^T \tag{4.9}$$

4.2.3 Constitutive Relations

For the overall continuum plate at any point, the state of stresses are defined by $\{\boldsymbol{\sigma_b}\}$ and $\{\boldsymbol{\sigma_s}\}$, and are given by:

$$\{\boldsymbol{\sigma_b}\} = [\boldsymbol{\sigma_x} \quad \boldsymbol{\sigma_y} \quad \boldsymbol{\sigma_{xy}} \quad \boldsymbol{\sigma_z}]^T; \qquad \{\boldsymbol{\sigma_s}\} = [\boldsymbol{\sigma_{xz}} \quad \boldsymbol{\sigma_{yz}}]^T \tag{4.10}$$

where $\boldsymbol{\sigma_x}$, $\boldsymbol{\sigma_y}$ and $\boldsymbol{\sigma_z}$ present the normal stresses, and $\boldsymbol{\sigma_{xy}}$ represents the in-plane shear stress while $\boldsymbol{\sigma_{xz}}$ and $\boldsymbol{\sigma_{yz}}$ represent the out-of-plane shear stresses.

In case of any orthotropic layered material of the substrate composite plate, the constitutive relations can be written as follows:

$$\{\boldsymbol{\sigma_s^k}\} = [\boldsymbol{C_s^k}]\{\boldsymbol{\epsilon_b^k}\}; \quad \{\boldsymbol{\sigma_b^k}\} = [\boldsymbol{C_b^k}]\{\boldsymbol{\epsilon_b^k}\}, \qquad (\boldsymbol{k} = 1, 2, 3, \ldots, \boldsymbol{N}) \tag{4.11}$$

in which

$$[\boldsymbol{C_b^k}] = \begin{bmatrix} \bar{C}_{11}^k & \bar{C}_{12}^k & \bar{C}_{16}^k & \bar{C}_{13}^k \\ \bar{C}_{12}^k & \bar{C}_{22}^k & \bar{C}_{26}^k & \bar{C}_{23}^k \\ \bar{C}_{16}^k & \bar{C}_{26}^k & \bar{C}_{66}^k & \bar{C}_{36}^k \\ \bar{C}_{13}^k & \bar{C}_{23}^k & \bar{C}_{36}^k & \bar{C}_{33}^k \end{bmatrix}, \qquad [\boldsymbol{C_s^k}] = \begin{bmatrix} \bar{C}_{55}^k & \bar{C}_{45}^k \\ \bar{C}_{45}^k & \bar{C}_{44}^k \end{bmatrix}$$

where, $\boldsymbol{\bar{C}_{ij}^k}$ represents the transformed elastic stiffness constants corresponding to the reference coordinate system. The electric field is applied to the constraining **1–3 PZC** layer in the $\boldsymbol{z}$-axis and accordingly, the constitutive relationship for the stresses and strains considering the piezoelectric effect can be written as (Ray and Pradhan, 2006).

$$\{\boldsymbol{\sigma_b^k}\} = [\boldsymbol{C_b^k}]\{\boldsymbol{\epsilon_b^k}\} + [\boldsymbol{C_{bs}^k}]\{\boldsymbol{\epsilon_s^k}\} - \{\boldsymbol{e_b}\}\boldsymbol{E_z}$$

$$\{\boldsymbol{\sigma_s^k}\} = [\boldsymbol{C_{bs}^k}]\{\boldsymbol{\epsilon_b^k}\} + [\boldsymbol{C_s^k}]\{\boldsymbol{\epsilon_s^k}\} - \{\boldsymbol{e_b}\}\boldsymbol{E_z} \tag{4.12}$$

$$\boldsymbol{D_z} = \{\boldsymbol{e_b}\}^T\{\boldsymbol{\epsilon_b^k}\} + \{\boldsymbol{e_s}\}^T\{\boldsymbol{\epsilon_s^k}\} + \bar{\boldsymbol{\varepsilon}}_{33}\boldsymbol{E_z}; \qquad \boldsymbol{k} = \boldsymbol{N} + 2$$

where $\boldsymbol{E_z}$ is the electric field in the $\boldsymbol{z}$-direction, $\boldsymbol{D_z}$ is the electric displacement, and $\bar{\boldsymbol{\varepsilon}}_{\boldsymbol{33}}$ represents the dielectric coefficient. Eq. (4.12) shows the coupled relation of out-of-plane shear strains and in-plane strains due to the orientation of piezo fiber in the $\boldsymbol{xz}$ or $\boldsymbol{yz}$ plane of the **1–3 PZC** layer. The respective coupling elastic stiffness constants matrices $[\boldsymbol{C}_{bs}^{N+2}]$ can be expressed as follows (Ray and Baz, 1997; Ray and Pradhan, 2006):

$$[\boldsymbol{C}_{bs}^{N+2}] = \begin{bmatrix} \overline{\boldsymbol{C}}_{15}^{N+2} & \overline{\boldsymbol{C}}_{25}^{N+2} & 0 & \overline{\boldsymbol{C}}_{35}^{N+2} \\ 0 & 0 & \overline{\boldsymbol{C}}_{46}^{N+2} & 0 \end{bmatrix}^{\boldsymbol{T}} \qquad \text{or}$$

$$[\boldsymbol{C}_{bs}^{N+2}] = \begin{bmatrix} 0 & 0 & \overline{\boldsymbol{C}}_{56}^{N+2} & 0 \\ \overline{\boldsymbol{C}}_{14}^{N+2} & \overline{\boldsymbol{C}}_{24}^{N+2} & 0 & \overline{\boldsymbol{C}}_{34}^{N+2} \end{bmatrix}^{\boldsymbol{T}} \tag{4.13}$$

It can be observed that the elastic coupling matrix that appeared in Eq. (4.13) becomes a null matrix due to the fact that the piezo fibers are coplanar either with the vertical ***yz*** plane or ***xz*** plane as a general case. The piezo coefficients appeared in Eq. (4.12) are given as (Ray and Baz, 1997):

$$\{\boldsymbol{e}_b\} = [\bar{\boldsymbol{e}}_{31} \quad \bar{\boldsymbol{e}}_{32} \quad \bar{\boldsymbol{e}}_{36} \quad \bar{\boldsymbol{e}}_{33}]^{\boldsymbol{T}}; \qquad \{\boldsymbol{e}_s\} = [\bar{\boldsymbol{e}}_{35} \quad \bar{\boldsymbol{e}}_{34}]^{\boldsymbol{T}} \tag{4.14}$$

The **VE** material is modeled based on the dynamic modulus method and it is considered isotropic and linear. Here, $\boldsymbol{E}$ and $\boldsymbol{G}$ denote Young's and shear moduli of the **VE** layer which can be expressed as (Shen, 1996):

$$\boldsymbol{E} = 2\boldsymbol{G}(1+\boldsymbol{\nu}); \qquad \boldsymbol{G} = \boldsymbol{G}'(1+\boldsymbol{i\eta}) \tag{4.15}$$

in which $\boldsymbol{G}'$, $\boldsymbol{\nu}$, and $\boldsymbol{\eta}$ represent the storage modulus, Poisson's ratio, and loss factor, respectively. Making use of Eq. (4.15), the elastic stiffness constants of the **VE** material can be estimated and the subsequent elastic stiffness constants matrix $[\boldsymbol{C}_{ij}^{N+1}]$ becomes a complex matrix (Shen, 1996; Ray and Baz, 1997).

4.2.4 FE Formulation

The governing equation of the overall **HFRC** plate/**ACLD** system is derived using the principle of virtual work, as follows (Jeung and Shen, 2001):

$$\sum_{k=1}^{N+2} \int_{\Omega} \left(\{\boldsymbol{\epsilon}_b^k\}^{\boldsymbol{T}} \{\boldsymbol{\sigma}_b^k\} + \{\boldsymbol{\epsilon}_s^k\}^{\boldsymbol{T}} \{\boldsymbol{\sigma}_s^k\} \right) d\boldsymbol{\Omega} - \int_{\Omega} \boldsymbol{D}_z \boldsymbol{E}_z d\boldsymbol{\Omega} - \int_{\Omega} \{\boldsymbol{d}_t\}^{\boldsymbol{T}} \boldsymbol{\rho}^k \{\ddot{\boldsymbol{d}}_t\} d\boldsymbol{\Omega}$$

$$-\int_A \delta\{\boldsymbol{d_t}\}^T\{\boldsymbol{f}\}\boldsymbol{dA} = 0 \tag{4.16}$$

where, $\boldsymbol{\rho^k}$ represents the mass density of the $\boldsymbol{k^{th}}$ layer, $\boldsymbol{\Omega}$ denotes the volume of the respective layer, and $\{\boldsymbol{f}\}$ represents the external surface traction applied over a surface area ($\boldsymbol{A}$).

The discretization of the overall plate was carried out using "8 noded isoparametric **QUAD** elements". The element topology and nodal degrees of freedom of such elements are shown in Fig. 4.2(b). Using Eq. (4.4), the generalized displacement vectors related to the $\boldsymbol{i^{th}}$ node of the element ($\boldsymbol{i} = 1, 2, 3, \ldots, 8$) is given by:

$$\{\boldsymbol{d_{ti}}\} = [\boldsymbol{u_{0i}} \quad \boldsymbol{v_{0i}} \quad \boldsymbol{w_{0i}}]^{\boldsymbol{T}}$$

$$\{\boldsymbol{d_{ri}}\} = [\boldsymbol{\theta_{xi}} \quad \boldsymbol{\theta_{yi}} \quad \boldsymbol{\theta_{zi}} \quad \boldsymbol{\phi_{xi}} \quad \boldsymbol{\phi_{yi}} \quad \boldsymbol{\phi_{zi}} \quad \boldsymbol{\gamma_{xi}} \quad \boldsymbol{\gamma_{yi}} \quad \boldsymbol{\gamma_{zi}}]^{\boldsymbol{T}} \tag{4.17}$$

Therefore, the displacement vectors $\{\boldsymbol{d_t}\}$ and $\{\boldsymbol{d_r}\}$ are re-expressed in the form of the nodal generalized displacement vectors $\{\boldsymbol{d_t^e}\}$ and $\{\boldsymbol{d_r^e}\}$, as follows:

$$\{\boldsymbol{d_t}\} = [\boldsymbol{N_t}]\{\boldsymbol{d_t^e}\}; \qquad \{\boldsymbol{d_r}\} = [\boldsymbol{N_r}]\{\boldsymbol{d_r^e}\} \tag{4.18}$$

where,

$$[\boldsymbol{N_t}] = [\boldsymbol{N_{t1}} \quad \boldsymbol{N_{t2}} \quad \ldots \quad \boldsymbol{N_{t8}}]^{\boldsymbol{T}},$$

$$[\boldsymbol{N_r}] = [\boldsymbol{N_{r1}} \quad \boldsymbol{N_{r2}} \quad \ldots \quad \boldsymbol{N_{r8}}]^{\boldsymbol{T}}, \qquad \boldsymbol{N_{ti}} = \boldsymbol{n_i I_t},$$

$$\boldsymbol{N_{ri}} = \boldsymbol{n_i I_r}\{\boldsymbol{d_t^e}\} = [\{\boldsymbol{d_{t1}^e}\}^{\boldsymbol{T}} \quad \{\boldsymbol{d_{t2}^e}\}^{\boldsymbol{T}} \quad \ldots \quad \{\boldsymbol{d_{t8}^e}\}^{\boldsymbol{T}}]^{\boldsymbol{T}}, \tag{4.19}$$

$$\{\boldsymbol{d_r^e}\} = [\{\boldsymbol{d_{r1}^e}\}^{\boldsymbol{T}} \quad \{\boldsymbol{d_{r2}^e}\}^{\boldsymbol{T}} \quad \ldots \quad \{\boldsymbol{d_{r8}^e}\}^{\boldsymbol{T}}]^{\boldsymbol{T}}$$

in which $\boldsymbol{I_r}$ and $\boldsymbol{I_t}$ denote (9×9) and (3×3) identity matrices, respectively, and $\boldsymbol{n_i}$ represents the shape function of the natural coordinates related to the $\boldsymbol{i^{th}}$ node. Using Eqs. (4.6)-(4.8) and (4.18), the strain vectors can be written in the form of nodal generalized displacement vectors at any point within the element, as follows:

$$\{\boldsymbol{\epsilon_b}\}_{\boldsymbol{c}} = [\boldsymbol{B_{tb}}]\{\boldsymbol{d_t^e}\} + [\boldsymbol{Z_1}]\{\boldsymbol{B_{rb}}\}\{\boldsymbol{d_r^e}\},$$

$$\{\boldsymbol{\epsilon_b}\}_{\boldsymbol{v}} = [\boldsymbol{B_{tb}}]\{\boldsymbol{d_t^e}\} + [\boldsymbol{Z_2}]\{\boldsymbol{B_{rb}}\}\{\boldsymbol{d_r^e}\},$$

$$\{\boldsymbol{\epsilon_b}\}_{\boldsymbol{p}} = [\boldsymbol{B_{tb}}]\{\boldsymbol{d_t^e}\} + [\boldsymbol{Z_3}]\{\boldsymbol{B_{rb}}\}\{\boldsymbol{d_r^e}\}, \tag{4.20}$$

$$\{\boldsymbol{\epsilon_s}\}_{\boldsymbol{c}} = [\boldsymbol{B_{ts}}]\{\boldsymbol{d_t^e}\} + [\boldsymbol{Z_4}]\{\boldsymbol{B_{rs}}\}\{\boldsymbol{d_r^e}\},$$

$$\{\boldsymbol{\epsilon_s}\}_{\boldsymbol{v}} = [\boldsymbol{B_{ts}}]\{\boldsymbol{d_t^e}\} + [\boldsymbol{Z_5}]\{\boldsymbol{B_{rs}}\}\{\boldsymbol{d_r^e}\},$$

$$\{\boldsymbol{\epsilon_s}\}_{\boldsymbol{p}} = [\boldsymbol{B_{ts}}]\{\boldsymbol{d_t^e}\} + [\boldsymbol{Z_6}]\{\boldsymbol{B_{rs}}\}\{\boldsymbol{d_r^e}\}$$

whereas $[\boldsymbol{B_{tb}}]$, $[\boldsymbol{B_{rb}}]$, $[\boldsymbol{B_{ts}}]$ and $[\boldsymbol{B_{rs}}]$ denote the nodal strain-displacement matrices which can be written as:

$$[\boldsymbol{B_{tb}}] = [\boldsymbol{B_{tb1}} \quad \boldsymbol{B_{tb2}} \quad \dots \quad \boldsymbol{B_{tb8}}]^{\boldsymbol{T}},$$

$$[\boldsymbol{B_{rb}}] = [\boldsymbol{B_{rb1}} \quad \boldsymbol{B_{rb2}} \quad \dots \quad \boldsymbol{B_{rb8}}]^{\boldsymbol{T}},$$

$$[\boldsymbol{B_{ts}}] = [\boldsymbol{B_{ts1}} \quad \boldsymbol{B_{ts2}} \quad \dots \quad \boldsymbol{B_{ts8}}]^{\boldsymbol{T}}, \tag{4.21}$$

$$[\boldsymbol{B_{rs}}] = [\boldsymbol{B_{rs1}} \quad \boldsymbol{B_{rs2}} \quad \dots \quad \boldsymbol{B_{rs8}}]^{\boldsymbol{T}}$$

The sub-matrices $\boldsymbol{B_{tbi}}$, $\boldsymbol{B_{tsi}}$, $\boldsymbol{B_{rbi}}$ and $\boldsymbol{B_{rsi}}$ $(\boldsymbol{i} = 1, 2, 3, \dots, 8)$ are as follows:

$$\boldsymbol{B_{tbi}} = \begin{bmatrix} \frac{\partial \boldsymbol{n_i}}{\partial \boldsymbol{x}} & 0 & 0 \\ 0 & \frac{\partial \boldsymbol{n_i}}{\partial \boldsymbol{y}} & 0 \\ \frac{\partial \boldsymbol{n_i}}{\partial \boldsymbol{y}} & \frac{\partial \boldsymbol{n_i}}{\partial \boldsymbol{x}} & 0 \\ 0 & 0 & 0 \end{bmatrix}, \quad \boldsymbol{B_{tsi}} = \begin{bmatrix} 0 & 0 & \frac{\partial \boldsymbol{n_i}}{\partial \boldsymbol{x}} \\ 0 & 0 & \frac{\partial \boldsymbol{n_i}}{\partial \boldsymbol{y}} \end{bmatrix},$$

$$\boldsymbol{B_{rbi}} = \begin{bmatrix} \overline{\boldsymbol{B}}_{\boldsymbol{rbi}} & \breve{\boldsymbol{o}} & \breve{\boldsymbol{o}} \\ \breve{\boldsymbol{o}} & \overline{\boldsymbol{B}}_{\boldsymbol{rbi}} & \breve{\boldsymbol{o}} \\ \breve{\boldsymbol{o}} & \breve{\boldsymbol{o}} & \overline{\boldsymbol{B}}_{\boldsymbol{rbi}} \end{bmatrix}, \quad \overline{\boldsymbol{B}}_{\boldsymbol{rbi}} = \begin{bmatrix} \frac{\partial \boldsymbol{n_i}}{\partial \boldsymbol{x}} & 0 & 0 \\ 0 & \frac{\partial \boldsymbol{n_i}}{\partial \boldsymbol{y}} & 0 \\ \frac{\partial \boldsymbol{n_i}}{\partial \boldsymbol{y}} & \frac{\partial \boldsymbol{n_i}}{\partial \boldsymbol{x}} & 0 \\ 0 & 0 & 1 \end{bmatrix},$$

$$\boldsymbol{B}_{rsi} = \begin{bmatrix} \breve{\boldsymbol{I}} & \widehat{\boldsymbol{o}} & \widehat{\boldsymbol{o}} \\ \widehat{\boldsymbol{o}} & \breve{\boldsymbol{I}} & \widehat{\boldsymbol{o}} \\ \widehat{\boldsymbol{o}} & \widehat{\boldsymbol{o}} & \breve{\boldsymbol{I}} \\ \overline{\boldsymbol{B}}_{rsi} & \widehat{\boldsymbol{o}} & \widehat{\boldsymbol{o}} \\ \widehat{\boldsymbol{o}} & \overline{\boldsymbol{B}}_{rsi} & \widehat{\boldsymbol{o}} \\ \widehat{\boldsymbol{o}} & \widehat{\boldsymbol{o}} & \overline{\boldsymbol{B}}_{rsi} \end{bmatrix}, \qquad \overline{\boldsymbol{B}}_{rsi} = \begin{bmatrix} 0 & 0 & \dfrac{\partial \boldsymbol{n}_i}{\partial \boldsymbol{x}} \\ 0 & 0 & \dfrac{\partial \boldsymbol{n}_i}{\partial \boldsymbol{y}} \end{bmatrix},$$

$$\breve{\boldsymbol{o}} = \begin{bmatrix} 0 & 0 & 0 \\ 0 & 0 & 0 \\ 0 & 0 & 0 \\ 0 & 0 & 0 \end{bmatrix}, \quad \widehat{\boldsymbol{o}} = \begin{bmatrix} 0 & 0 & 0 \\ 0 & 0 & 0 \end{bmatrix} \text{ and } \breve{\boldsymbol{I}} = \begin{bmatrix} 1 & 0 & 0 \\ 0 & 1 & 0 \end{bmatrix}$$

Considering a thin piezoelectric actuator sheet with constant thickness, the applied electric field can be taken as $\boldsymbol{E_z = -V/h_p}$, with $\boldsymbol{V}$ is the voltage applied along the thickness of **1–3 PZC** layer (Baz and Ro, 1995b). By making use of Eqs. (4.13) and (4.20) into Eq. (4.16) the open-loop equations of motion of an element attached with the **ACLD** treatment are obtained as follows:

$$[\boldsymbol{M}^e]\{\ddot{\boldsymbol{d}}_t^e\} + [\boldsymbol{K}_{tt}^e]\{\boldsymbol{d}_t^e\} + [\boldsymbol{K}_{tr}^e]\{\boldsymbol{d}_r^e\} = [\boldsymbol{F}_{tp}^e]\boldsymbol{V} + \{\boldsymbol{F}^e\} \tag{4.22}$$

$$[\boldsymbol{K}_{rt}^e]\{\boldsymbol{d}_t^e\} + [\boldsymbol{K}_{rr}^e]\{\boldsymbol{d}_r^e\} = [\boldsymbol{F}_{rp}^e]\boldsymbol{V} \tag{4.23}$$

where the elemental mass matrix is denoted by $[\boldsymbol{M}^e]$; the elemental stiffness matrices are denoted by $[\boldsymbol{K}_{tt}^e]$, $[\boldsymbol{K}_{tr}^e]$, $[\boldsymbol{K}_{rt}^e]$, and $[\boldsymbol{K}_{rr}^e]$; the elemental load vector is denoted by $\{\boldsymbol{F}^e\}$; the elemental electroelastic coupling vectors are denoted by $\{\boldsymbol{F}_{tp}^e\}$, $\{\boldsymbol{F}_{rp}^e\}$; and $[\boldsymbol{M}^e]$ is the mass parameter which can be obtained as follows:

$$[\boldsymbol{M}^e] = \int_0^{a_e}\int_0^{b_e} \overline{\boldsymbol{m}}[\boldsymbol{N}_t]^T[\boldsymbol{N}_t]\boldsymbol{dx}\,\boldsymbol{dy},$$

$$[\boldsymbol{K}_{tt}^e] = [\boldsymbol{K}_{tb}^e] + [\boldsymbol{K}_{ts}^e] + [\boldsymbol{K}_{tbs}^e]_{pb} + [\boldsymbol{K}_{tbs}^e]_{ps},$$

$$[\boldsymbol{K}_{tr}^e] = [\boldsymbol{K}_{trb}^e] + [\boldsymbol{K}_{trs}^e] + \frac{1}{2}\left([\boldsymbol{K}_{trbs}^e]_{pb} + [\boldsymbol{K}_{rtbs}^e]_{pb}^T + [\boldsymbol{K}_{trbs}^e]_{ps} + [\boldsymbol{K}_{rtbs}^e]_{ps}^T\right),$$

$$[\boldsymbol{K}_{rt}^e] = [\boldsymbol{K}_{tr}^e]^T,$$

$$[\boldsymbol{K}_{rr}^e] = [\boldsymbol{K}_{rrb}^e] + [\boldsymbol{K}_{rrs}^e] + [\boldsymbol{K}_{rt}^e] + [\boldsymbol{K}_{rrbs}^e]_{pb} + [\boldsymbol{K}_{rrbs}^e]_{ps},$$

$$\left\{\boldsymbol{F}_{tp}^{e}\right\} = \left\{\boldsymbol{F}_{tp}^{e}\right\}_{p} + \{\boldsymbol{F}_{ts}^{e}\}_{p}, \quad \left\{\boldsymbol{F}_{rp}^{e}\right\} = \{\boldsymbol{F}_{rb}^{e}\}_{p} + \{\boldsymbol{F}_{rs}^{e}\}_{p},$$

$$\{\boldsymbol{F}^{e}\} = \int_{0}^{a_e}\int_{0}^{b_e} [\boldsymbol{N}_{t}]^{T}\{\boldsymbol{f}\}\boldsymbol{dx}\,\boldsymbol{dy} \tag{4.24}$$

$$\bar{\boldsymbol{m}} = \sum_{k=1}^{N+2} \boldsymbol{\rho}^{k}\,(\boldsymbol{h}_{k+1} - \boldsymbol{h}_{k})$$

where, $\bar{\boldsymbol{m}}$ is the mass parameter, and $\boldsymbol{a_e}$ and $\boldsymbol{b_e}$ are the length and circumferential width of the corresponding element.

The electroelastic coupling vectors and elemental stiffness matrices appeared in Eq. (4.24) are follows:

$$[\boldsymbol{K}_{tb}^{e}] = \int_{A} [\boldsymbol{B}_{tb}]^{T}\big([\boldsymbol{D}_{tb}] + [\boldsymbol{D}_{tb}]_{v} + [\boldsymbol{D}_{tb}]_{p}\big)\,[\boldsymbol{B}_{tb}]\boldsymbol{dx}\,\boldsymbol{dy},$$

$$[\boldsymbol{K}_{ts}^{e}] = \int_{A} [\boldsymbol{B}_{ts}]^{T}\big([\boldsymbol{D}_{ts}] + [\boldsymbol{D}_{ts}]_{v} + [\boldsymbol{D}_{ts}]_{p}\big)\,[\boldsymbol{B}_{ts}]\boldsymbol{dx}\,\boldsymbol{dy},$$

$$[\boldsymbol{K}_{tbs}^{e}]_{pb} = \int_{A} [\boldsymbol{B}_{tb}]^{T}[\boldsymbol{D}_{tbs}]_{p}[\boldsymbol{B}_{ts}]\,\boldsymbol{dx}\,\boldsymbol{dy},$$

$$[\boldsymbol{K}_{tbs}^{e}]_{ps} = \int_{A} [\boldsymbol{B}_{ts}]^{T}[\boldsymbol{D}_{tbs}]_{p}[\boldsymbol{B}_{tb}]\,\boldsymbol{dx}\,\boldsymbol{dy},$$

$$[\boldsymbol{K}_{trb}^{e}] = \int_{A} [\boldsymbol{B}_{trb}]^{T}\big([\boldsymbol{D}_{trb}] + [\boldsymbol{D}_{trb}]_{v} + [\boldsymbol{D}_{trb}]_{p}\big)\,[\boldsymbol{B}_{rb}]\boldsymbol{dx}\,\boldsymbol{dy},$$

$$[\boldsymbol{K}_{trbs}^{e}]_{pb} = \int_{A} [\boldsymbol{B}_{tb}]^{T}[\boldsymbol{D}_{trbs}]_{p}[\boldsymbol{B}_{rs}]\,\boldsymbol{dx}\,\boldsymbol{dy},$$

$$[\boldsymbol{K}_{rtbs}^{e}]_{pb} = \int_{A} [\boldsymbol{B}_{rb}]^{T}[\boldsymbol{D}_{rtbs}]_{p}[\boldsymbol{B}_{ts}]\,\boldsymbol{dx}\,\boldsymbol{dy},$$

$$[\boldsymbol{K}_{trbs}^{e}]_{ps} = \int_{A} [\boldsymbol{B}_{ts}]^{T}[\boldsymbol{D}_{rtbs}]_{p}^{T}[\boldsymbol{B}_{rb}]\,\boldsymbol{dx}\,\boldsymbol{dy},$$

$$[\boldsymbol{K}^{e}_{rtbs}]_{ps} = \int_{A} [\boldsymbol{B}_{rs}]^{T} [\boldsymbol{D}_{trbs}]_{p}^{T} [\boldsymbol{B}_{tb}]\, \boldsymbol{dx}\, \boldsymbol{dy},$$

$$[\boldsymbol{K}^{e}_{trs}] = \int_{A} [\boldsymbol{B}_{ts}]^{T} \left([\boldsymbol{D}_{trs}] + [\boldsymbol{D}_{trs}]_{v} + [\boldsymbol{D}_{trs}]_{p}\right) [\boldsymbol{B}_{rs}] \boldsymbol{dx}\, \boldsymbol{dy},$$

$$[\boldsymbol{K}^{e}_{rrb}] = \int_{A} [\boldsymbol{B}_{rb}]^{T} \left([\boldsymbol{D}_{rrb}] + [\boldsymbol{D}_{rrb}]_{v} + [\boldsymbol{D}_{rrb}]_{p}\right) [\boldsymbol{B}_{rb}] \boldsymbol{dx}\, \boldsymbol{dy},$$

$$[\boldsymbol{K}^{e}_{rrs}] = \int_{A} [\boldsymbol{B}_{rs}]^{T} \left([\boldsymbol{D}_{rrs}] + [\boldsymbol{D}_{rrs}]_{v} + [\boldsymbol{D}_{rrs}]_{p}\right) [\boldsymbol{B}_{rs}] \boldsymbol{dx}\, \boldsymbol{dy},$$

$$[\boldsymbol{K}^{e}_{rrbs}]_{pb} = \int_{A} [\boldsymbol{B}_{rb}]^{T} [\boldsymbol{D}_{rrbs}]_{p} [\boldsymbol{B}_{rs}]\, \boldsymbol{dx}\, \boldsymbol{dy},$$

$$[\boldsymbol{K}^{e}_{rrbs}]_{ps} = \int_{A} [\boldsymbol{B}_{rs}]^{T} [\boldsymbol{D}_{rrbs}]_{p}^{T} [\boldsymbol{B}_{rb}]\, \boldsymbol{dx}\, \boldsymbol{dy},$$

$$[\boldsymbol{F}^{e}_{tb}]_{p} = \int_{A} [\boldsymbol{B}_{tb}]^{T} \{\boldsymbol{D}_{tb}\}_{p}\, \boldsymbol{dx}\, \boldsymbol{dy},$$

$$[\boldsymbol{F}^{e}_{rb}]_{p} = \int_{A} [\boldsymbol{B}_{rb}]^{T} \{\boldsymbol{D}_{rb}\}_{p}\, \boldsymbol{dx}\, \boldsymbol{dy},$$

$$[\boldsymbol{F}^{e}_{ts}]_{p} = \int_{A} [\boldsymbol{B}_{ts}]^{T} \{\boldsymbol{D}_{ts}\}_{p}\, \boldsymbol{dx}\, \boldsymbol{dy},$$

$$[\boldsymbol{F}^{e}_{rs}]_{p} = \int_{A} [\boldsymbol{B}_{rs}]^{T} \{\boldsymbol{D}_{rs}\}_{p}\, \boldsymbol{dx}\, \boldsymbol{dy}$$

The vectors and rigidity matrices that appeared in the elemental matrices can be written as follows:

$$[\boldsymbol{D}_{tb}] = \sum_{k=1}^{N}\int_{h_k}^{h_{k+1}}[\bar{\boldsymbol{C}}_b^k]\boldsymbol{dz}\,,\qquad [\boldsymbol{D}_{trb}] = \sum_{k=1}^{N}\int_{h_k}^{h_{k+1}}[\bar{\boldsymbol{C}}_b^k][\boldsymbol{Z}_1]\boldsymbol{dz}\,,$$

$$[\boldsymbol{D}_{rrb}] = \sum_{k=1}^{N}\int_{h_k}^{h_{k+1}}[\boldsymbol{Z}_1]^T[\bar{\boldsymbol{C}}_b^k][\boldsymbol{Z}_1]\boldsymbol{dz},$$

$$[\boldsymbol{D}_{ts}] = \sum_{k=1}^{N}\int_{h_k}^{h_{k+1}}[\bar{\boldsymbol{C}}_s^k]\boldsymbol{dz}\,,\qquad [\boldsymbol{D}_{trs}] = \sum_{k=1}^{N}\int_{h_k}^{h_{k+1}}[\bar{\boldsymbol{C}}_b^k][\boldsymbol{Z}_4]\boldsymbol{dz}\,,$$

$$[\boldsymbol{D}_{rrs}] = \sum_{k=1}^{N}\int_{h_k}^{h_{k+1}}[\boldsymbol{Z}_4]^T[\bar{\boldsymbol{C}}_s^k][\boldsymbol{Z}_4]\boldsymbol{dz},$$

$$[\boldsymbol{D}_{tb}]_v = \boldsymbol{h}_v[\bar{\boldsymbol{C}}_b^{N+1}],\quad [\boldsymbol{D}_{trb}]_v = \int_{h_{N+1}}^{h_{N+2}}[\bar{\boldsymbol{C}}_b^{N+1}][\boldsymbol{Z}_2]\boldsymbol{dz},$$

$$[\boldsymbol{D}_{rrb}]_v = \int_{h_{N+1}}^{h_{N+2}}[\boldsymbol{Z}_2]^T[\bar{\boldsymbol{C}}_b^{N+1}][\boldsymbol{Z}_2]\boldsymbol{dz},\quad [\boldsymbol{D}_{ts}]_v = \boldsymbol{h}_v[\bar{\boldsymbol{C}}_b^{N+1}],$$

$$[\boldsymbol{D}_{trs}]_v = \int_{h_{N+1}}^{h_{N+2}}[\bar{\boldsymbol{C}}_s^{N+1}][\boldsymbol{Z}_5]\boldsymbol{dz}\,, [\boldsymbol{D}_{rrb}]_v = \int_{h_{N+1}}^{h_{N+2}}[\boldsymbol{Z}_5]^T[\bar{\boldsymbol{C}}_b^{N+1}][\boldsymbol{Z}_5]\boldsymbol{dz},$$

$$[\boldsymbol{D}_{tb}]_p = \boldsymbol{h}_p[\bar{\boldsymbol{C}}_b^{N+2}],$$

$$[\boldsymbol{D}_{trb}]_p = \int_{h_{N+2}}^{h_{N+3}}[\bar{\boldsymbol{C}}_b^{N+2}][\boldsymbol{Z}_3]\boldsymbol{dz},\quad [\boldsymbol{D}_{rrb}]_p = \int_{h_{N+2}}^{h_{N+3}}[\boldsymbol{Z}_3]^T[\bar{\boldsymbol{C}}_b^{N+2}][\boldsymbol{Z}_3]\boldsymbol{dz},$$

$$[\boldsymbol{D}_{ts}]_p = \boldsymbol{h}_p[\bar{\boldsymbol{C}}_s^{N+2}],$$

$$[\boldsymbol{D}_{trs}]_p = \int_{h_{N+2}}^{h_{N+3}}[\bar{\boldsymbol{C}}_s^{N+2}][\boldsymbol{Z}_6]\boldsymbol{dz},\quad [\boldsymbol{D}_{rrs}]_p = \int_{h_{N+2}}^{h_{N+3}}[\boldsymbol{Z}_6]^T[\bar{\boldsymbol{C}}_s^{N+2}][\boldsymbol{Z}_6]\boldsymbol{dz},$$

$$[\boldsymbol{D}_{tbs}]_p = \int_{h_{N+2}}^{h_{N+3}}[\bar{\boldsymbol{C}}_{bs}^{N+2}]\boldsymbol{dz},\qquad [\boldsymbol{D}_{trbs}]_p = \int_{h_{N+2}}^{h_{N+3}}[\bar{\boldsymbol{C}}_{bs}^{N+2}][\boldsymbol{Z}_6]\boldsymbol{dz},$$

$$[\boldsymbol{D}_{rtbs}]_p = \int_{h_{N+2}}^{h_{N+3}} [\boldsymbol{Z}_3]^T [\bar{\boldsymbol{C}}_{bs}^{N+2}] \boldsymbol{dz}, \qquad [\boldsymbol{D}_{rrbs}]_p = \int_{h_{N+2}}^{h_{N+3}} [\boldsymbol{Z}_3]^T [\bar{\boldsymbol{C}}_{bs}^{N+2}][\boldsymbol{Z}_6] \boldsymbol{dz},$$

$$\{\boldsymbol{D}_{tb}\}_p = \int_{h_{N+2}}^{h_{N+3}} -\{\bar{\boldsymbol{e}}_b\}/\boldsymbol{h}_p \boldsymbol{dz}, \qquad \{\boldsymbol{D}_{rb}\}_p = \int_{h_{N+2}}^{h_{N+3}} -[\boldsymbol{Z}_3]^T \{\bar{\boldsymbol{e}}_b\}/\boldsymbol{h}_p \boldsymbol{dz},$$

$$\{\boldsymbol{D}_{ts}\}_p = \int_{h_{N+2}}^{h_{N+3}} -\{\bar{\boldsymbol{e}}_s\}/\boldsymbol{h}_p \boldsymbol{dz}, \qquad \{\boldsymbol{D}_{rs}\}_p = \int_{h_{N+2}}^{h_{N+3}} -[\boldsymbol{Z}_6]^T \{\bar{\boldsymbol{e}}_s\}/\boldsymbol{h}_p \boldsymbol{dz}$$

For the estimation of the open-loop global equation of motion, the rotary inertia of **FE** elements can be ignored since the **HFRC** substrate plate is thin. Finally, the open-loop global equation of motion of the overall plate/**ACLD** system can be obtained by assembling the elemental equations of motion, as follows:

$$[\boldsymbol{M}]\{\ddot{\boldsymbol{X}}\} + [\boldsymbol{K}_{tt}]\{\boldsymbol{X}\} + [\boldsymbol{K}_{tr}]\{\boldsymbol{X}_r\} = \sum_{j=1}^{q} \{\boldsymbol{F}_{tp}^j\}\boldsymbol{V}^j + \{\boldsymbol{F}\} \tag{4.25}$$

$$[\boldsymbol{K}_{rt}]\{\boldsymbol{X}\} + [\boldsymbol{K}_{rr}]\{\boldsymbol{X}_r\} = \sum_{j=1}^{q} \{\boldsymbol{F}_{rp}^j\}\boldsymbol{V}^j \tag{4.26}$$

in which $[\boldsymbol{M}]$ represents the global mass matrix; $[\boldsymbol{K}_{tt}]$, $[\boldsymbol{K}_{tr}]$, $[\boldsymbol{K}_{rt}]$ and $[\boldsymbol{K}_{rr}]$ represent the global stiffness matrices; $\{\boldsymbol{X}_r\}$ and $\{\boldsymbol{X}\}$ denote the global nodal rotational and translational degrees of freedom (**DOF**); $\{\boldsymbol{F}\}$ represents the global nodal force vector; $\{\boldsymbol{F}_{tp}\}$ and $\{\boldsymbol{F}_{rp}\}$ denote global electro-elastic coupling matrices with respect to $\boldsymbol{j}^{th}$ patch; and $\boldsymbol{q}$ and $\boldsymbol{V}^j$ denote the number of patches and the voltage supplied to these patches, respectively.

4.3 Closed-Loop Model

In the active control strategy, a simple velocity feedback control law can be used to activate the **ACLD** patches. Accordingly, the control voltage applied across the active layer is given by (Beheshti-Aval and Lezgy-Nazargah, 2010):

$$\boldsymbol{V}^j = -\boldsymbol{k}_d^j \dot{\boldsymbol{w}} = -\boldsymbol{k}_d^j [\boldsymbol{U}_t^j]\{\dot{\boldsymbol{X}}\} - \boldsymbol{k}_d^j (\boldsymbol{h}/\boldsymbol{2})[\boldsymbol{U}_r^j]\{\dot{\boldsymbol{X}}_r\} \tag{4.27}$$

in which $\boldsymbol{k_d^j}$ represents the control gain for the $\boldsymbol{j^{th}}$ patch, $[\boldsymbol{U_t^j}]$ and $[\boldsymbol{U_r^j}]$ denote the unit vectors to express the transverse velocity of the point with respect to the differentiation of the global nodal generalized displacements. The final equation of motion evaluating the closed-loop dynamics of the **HFRC** plates/**ACLD** system is obtained by substituting Eq. (4.27) into Eqs. (4.25) and (4.26), as follows:

$$[\boldsymbol{M}]\{\ddot{\boldsymbol{X}}\} + [\boldsymbol{K_{tt}}]\{\boldsymbol{X}\} + [\boldsymbol{K_{tr}}]\{\boldsymbol{X_r}\} + \sum_{j=1}^{q} \boldsymbol{k_d^j}\{\boldsymbol{F_{tp}^j}\}\{\boldsymbol{U_t^j}\}\{\dot{\boldsymbol{X}}\}$$

$$+ \sum_{j=1}^{q} \boldsymbol{k_d^j}(\boldsymbol{h}/2)\{\boldsymbol{F_{tp}^j}\}\{\boldsymbol{U_r^j}\}\{\dot{\boldsymbol{X}}_{\boldsymbol{r}}\} = \{\boldsymbol{F}\} \qquad (4.28)$$

and

$$[\boldsymbol{K_{rt}}]\{\boldsymbol{X}\} + [\boldsymbol{K_{rr}}]\{\boldsymbol{X_r}\} + \sum_{j=1}^{q} \boldsymbol{k_d^j}\{\boldsymbol{F_{rp}^j}\}\{\boldsymbol{U_t^j}\}\{\dot{\boldsymbol{X}}\} + \sum_{j=1}^{q} \boldsymbol{k_d^j}(\boldsymbol{h}/2)\{\boldsymbol{F_{rp}^j}\}\{\boldsymbol{U_r^j}\}\{\dot{\boldsymbol{X}}_{\boldsymbol{r}}\} = 0 \qquad (4.29)$$

4.4 Results and Discussions

First, we verified our results with the available results in the literature to validate the above developed **FE** model herein. Second, we discussed the results for the laminated symmetric cross-ply $(0°/90°/0°)$ and anti-symmetric cross-ply $(0°/90°/0°/90°)$ as well as anti-symmetric angle-ply $(-45/45°/-45°/45°)$ **HFRC** plates attached with two patches of **1–3 PZC**. For the analysis of the vibrational characteristics of the laminated **HFRC** substrate plates, the volume fraction of the carbon fiber and **CNT** was taken as 0.4 and 0.1, respectively. The results of the laminated **HFRC** plates are compared with the laminated base composite plates (without **CNTs**) (i.e., $\boldsymbol{v_{CF}} = 0.4$ and $\boldsymbol{v_{CNT}} = 0$). Finally, we demonstrated the enhancement of the damping characteristics of laminated **HFRC** square plates through a quantitative relative analysis. The effective elastic properties of base composite and **HFRC** were estimated using the two-phase and three-phase micromechanical models based on the **MOM** approach, respectively. **Table 4.1** summarizes the effective elastic properties of the base composite and **HFRC** (Gupta *et al.*, 2021).

Table 4.1. Effective elastic properties of base composite and **HFRC**.

Effective elastic constant	**Two-phase** ($v_{CNT}=0\%$)		**Three-phase** ($v_{CNT}=5\%$)		**Three-phase** ($v_{CNT}=10\%$)	
	$v_{CF}=40\%$	$v_{CF}=60\%$	$v_{CF}=40\%$	$v_{CF}=60\%$	$v_{CF}=40\%$	$v_{CF}=60\%$
C_{11} *(GPa)*	96.6451	142.5567	125.5864	171.5618	154.537	200.5939
C_{12} *(GPa)*	4.1219	5.0647	4.2920	5.3836	4.4906	5.7748
C_{13} *(GPa)*	4.1219	5.0647	4.2719	5.3559	4.4469	5.7124
C_{23} *(GPa)*	4.3856	5.521	4.7174	6.0547	5.1033	6.7013
C_{33} *(GPa)*	7.7068	9.9779	8.3094	11.0133	9.0142	12.2889
C_{44} *(GPa)*	1.0054	1.407	1.091	1.5806	1.1926	1.8031
C_{66} *(GPa)*	1.0488	1.5408	1.1423	1.7515	1.2541	2.0289

Table 4.2. Properties of piezoelectric material (Ray and Pradhan, 2006).

Material	C_{11} *(GPa)*	C_{13} *(GPa)*	C_{33} *(GPa)*	C_{44} *(GPa)*	C_{66} *(GPa)*	e_{31} $(C\,m^{-2})$	e_{33} $(C\,m^{-2})$	ρ (kg/m^3)
1–3 PZC	9.293	6.182	35.444	1.584	1.536	–0.19	18.41	5090
PZT–5	121	75.2	111	21.1	21.1	–5.4	15.8	7750
PZT–7**A**	148	74.2	131	25.4	25.4	–2.1	9.5	7750
PZT–5**H**	151	96	124	23	23	–5.1	27	7750

The present work is focused on the influence of **CNTs** on the damping performance of the laminated **HFRC** plates. It can be seen from **Table 4.1** that the effective elastic properties of the **HFRC** improved due to the incorporation of **CNTs**. Unless otherwise mentioned, the v_{CF} is taken as 0.4 by varying the **CNT** volume fraction from 0 and 0.1 for the present analysis. The effective properties of **1–3 PZC** considering **PZT** fiber volume fraction (v_F) as 0.6 are shown in **Table 4.2**. For the **HFRC** square substrate plate, the thickness was taken as 0.003 m, while the aspect ratio (***a/h***) was taken as 100. The thickness of **VE** and piezo layers was taken as 51 μm and 250 μm, respectively. The properties of the viscoelastic constraining layer such as density, Poisson's ratio, and complex shear modulus were considered as 1140 kg/m^3, 0.49, and $20(1+i)\ MN\ m^{-2}$, respectively (Chantalakhana and Stanway, 2001; Ray and Pradhan, 2006).

To verify the **FE** model developed in Section 4.2, the fundamental natural frequencies of the **SS** laminated substrate plates attached with negligible thickness and inactivated **ACLD** treatment patches are verified with available analytical results (Reddy, 2003) for the similar layered composite plates without **ACLD** treatment. A non-dimensional frequency parameter $\boldsymbol{\lambda}$ was used for validation, which is given by:

$$\boldsymbol{\lambda} = \overline{\boldsymbol{\omega}}(\boldsymbol{a}^2/\boldsymbol{h})\sqrt{\boldsymbol{\rho}/\boldsymbol{E_T}} \tag{4.30}$$

where the natural frequency of the overall plate is given by $\overline{\boldsymbol{\omega}}$, and density and transverse Young's modulus of the laminated substrate are denoted by $\boldsymbol{\rho}$ and $\boldsymbol{E_T}$, respectively. **Table 4.3** presents the comparison of the present **FE** model with the available results (Reddy, 2003). The comparison shows good agreement which validates the **FE** model developed herein.

Table 4.3. Non-dimensional frequencies ($\boldsymbol{\lambda}$) of laminated substrate plates.

Substrate laminates	Source	$\boldsymbol{\lambda}$	
		***a/h* = 10**	***a/h* = 100**
$0°/90°/0°$	Present **FE** model	12.197	15.182
	Analytical (Reddy, 2003)	12.223	15.185
$0°/90°/0°/90°$	Present **FE** model	8.887	9.682
	Analytical (Reddy, 2003)	8.90	9.687
$-45°/45°/-45°/45°$	Present **FE** model	10.833	13.625
	Analytical (Reddy, 2003)	10.895	13.629

Next, the damping performance of the laminated **HFRC** plate integrated with two **ACLD** patches is investigated considering the **CNT** volume fraction as 0.1. To compute the frequency response, Eqs. (4.28) and (4.29) are formulated with the harmonic excitation of 1 $\boldsymbol{N}$ force applied at a point $(\boldsymbol{a}/2, \boldsymbol{b}/4, \boldsymbol{h}/2)$. For the first **ACLD** treatment patch, the applied control voltage is negatively proportional to the velocity of a point $(\boldsymbol{a}/2, \boldsymbol{b}/4, \boldsymbol{h}/2)$, whereas, for the second **ACLD** treatment patch, the control voltage applied is negatively proportional to the velocity of a point $(\mathbf{a}/2, 3\mathbf{b}/4, \mathbf{h}/2)$. **Table 4.4** summarizes the values of the maximum amplitude corresponding to the fundamental natural frequency of the first mode of **HFRC** plates. It can be observed from **Table 4.4** that the active damping is effectively attenuated the vibrational amplitudes of composite plates compared to the passive damping (uncontrolled case).

Table 4.4. Amplitudes and fundamental natural frequencies of base composite and **HFRC** substrate smart plates.

Ply	Gain	Base composite Amplitude $(\mathbf{10^{-4}})$ $(\boldsymbol{m})$	Base composite Frequency ($\mathbf{1^{st}}$ mode) $(\boldsymbol{Hz})$	HFRC Amplitude $(\mathbf{10^{-4}})$ $(\boldsymbol{m})$	HFRC Frequency ($\mathbf{1^{st}}$ mode) $(\boldsymbol{Hz})$
$(0°/90°/0°)$	Uncontrolled	1.22	133	1.20	162
	500	0.688	133	0.622	162
	800	0.554	133	0485	162
$(0°/90°/0°/90°)$	Uncontrolled	1.21	125	1.19	151
	500	0.686	125	0.624	151
	800	0.545	125	0.483	151
$(-45°/45°/-45°/45°)$	Uncontrolled	1.19	165	1.16	202
	500	0.604	165	0.538	202
	800	0.466	165	0.405	202

The variation of the amplitude of deflection vs frequency response of the **SS** laminated **HFRC** plate with active damping is shown in Fig. 4.3 for the symmetric cross-ply $(0°/90°/0°)$ case. It can be seen that the laminated **HFRC** plates (incorporated with **CNTs**) attenuate the transverse vibrational amplitudes significantly over those of the base composite plates (without **CNTs**). For the first mode, laminated **HFRC** plate attenuates the amplitude of vibration $\sim 11\ \%$ and $\sim 13\ \%$ corresponding to the value of gain $(\boldsymbol{k_d})$ 500 and 800, respectively, compared to the base composite case. The required maximum control voltage is around 31.46 $\boldsymbol{V}$ and 39.25 $\boldsymbol{V}$ for the value of gain $(\boldsymbol{k_d})$ 500 and 800, respectively, to achieve the attenuation of the amplitude of vibration $\sim 11\ \%$ and $\sim 13\ \%$ of the laminated **HFRC** plate. The respective maximum control voltage is 28.97 $\boldsymbol{V}$ and 37.08 $\boldsymbol{V}$ for the base composite plates as shown in Fig. 4.4. This finding is consistent with an experimental investigation of smart plate by (Baz and Ro, 1996). They observed that the required control voltage is around 28.68 $\boldsymbol{V}$ to achieve 76% of amplitude attenuation of the plate. It may be observed from Fig. 4.3 and Fig. 4.4 that the laminated

HFRC plate shows better damping characteristics due to the incorporation of **CNTs** in terms of attenuation of amplitudes and enhancement in the first few natural frequencies.

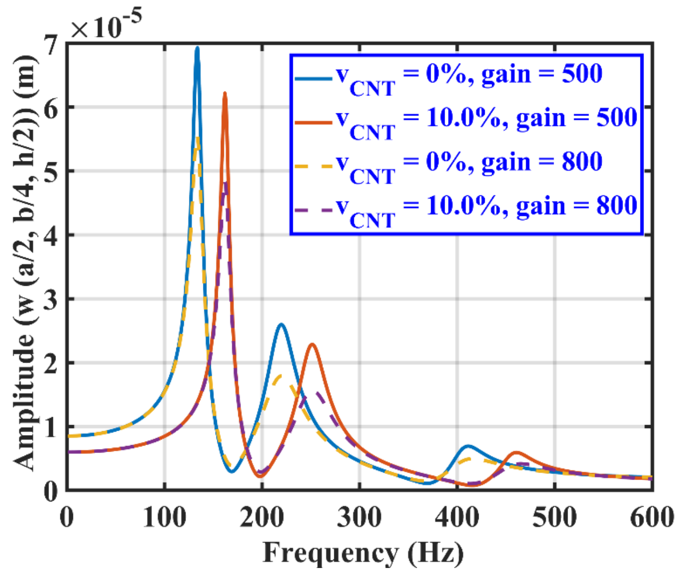

Figure 4.3 Variation of amplitude of deflection with the frequency response of **SS** 0°/90°/0° laminated square composite plates.

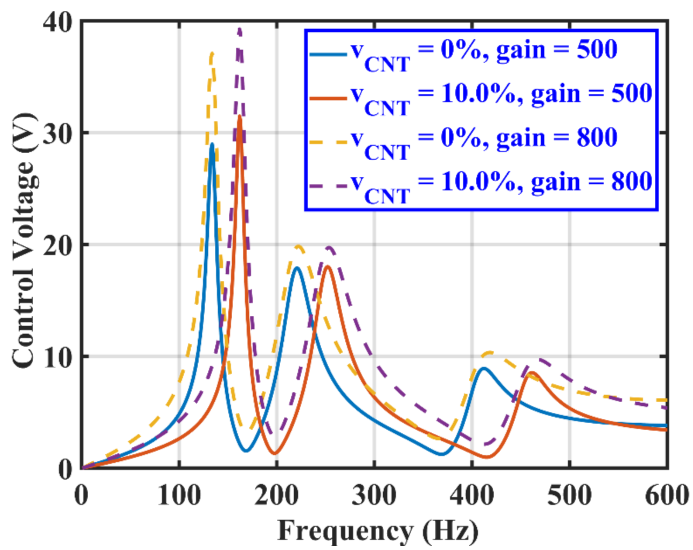

Figure 4.4 Variation of control voltage with the frequency response of **SS** 0°/90°/0° laminated square composite plates.

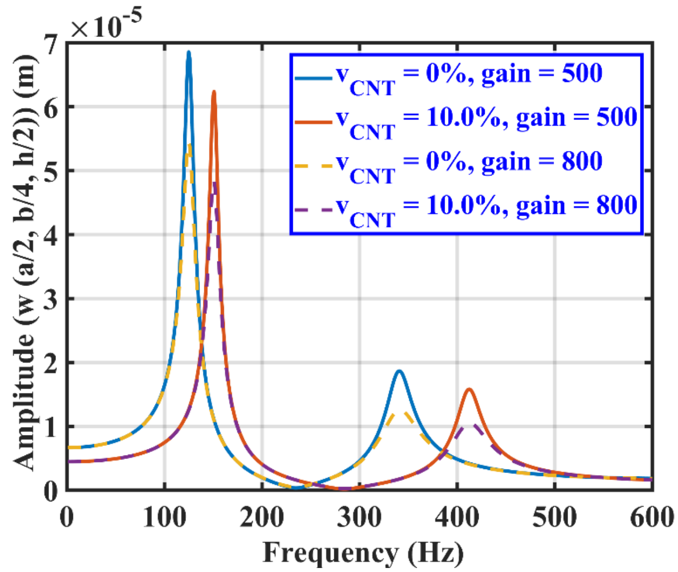

Figure 4.5 Variation of amplitude of deflection with the frequency response of **SS** 0°/90°/0°/90° laminated square composite plates.

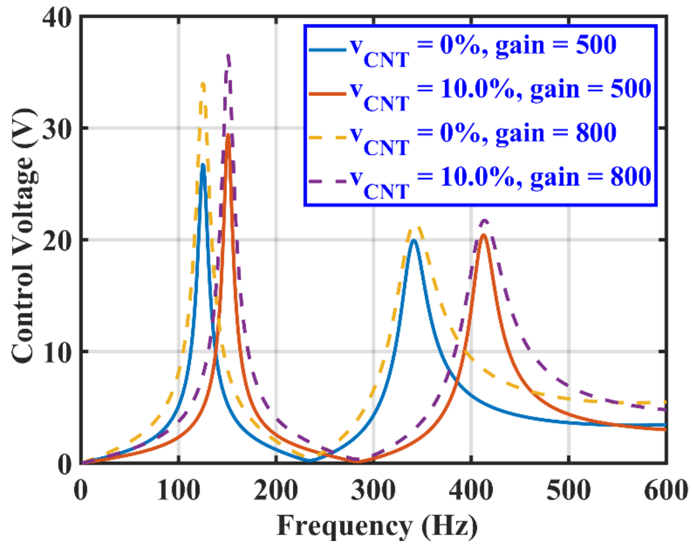

Figure 4.6 Variation of control voltage with the frequency response of **SS** 0°/90°/0°/90° laminated square composite plates.

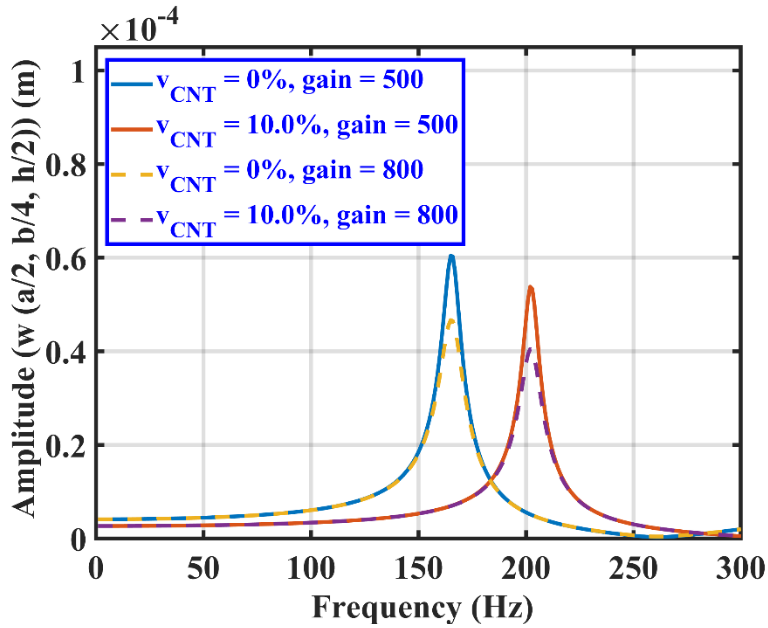

Figure 4.7 Variation of amplitude of deflection with the frequency response of **SS** $-45/45°/-45°/45°$ laminated square composite plates.

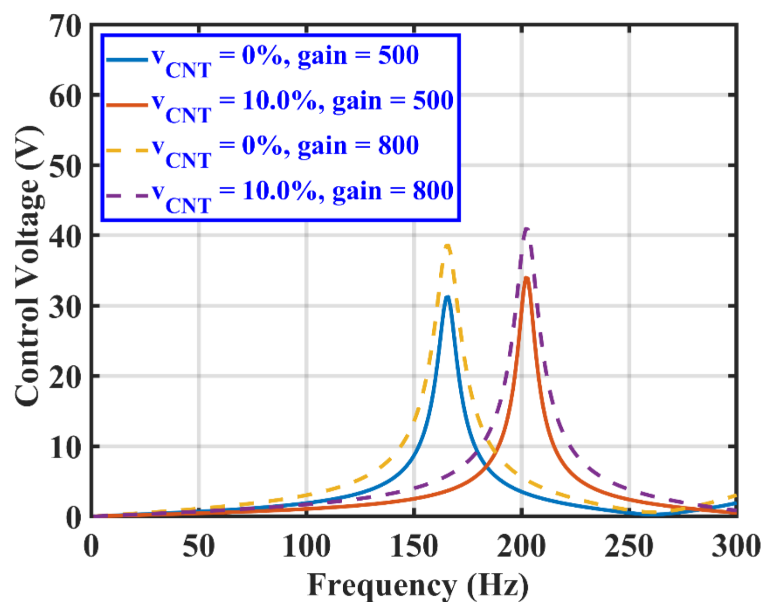

Figure 4.8 Variation of control voltage with the frequency response of **SS** $-45/45°/-45°/45°$ laminated square composite plates.

The frequency response of **SS** laminated smart composite square plates with respect to the amplitude of deflection $\boldsymbol{w}\ (\boldsymbol{a}/2\,,\boldsymbol{b}/4\,,\boldsymbol{h}/2)$ is demonstrated in Fig. 4.5 for the anti-symmetric cross-ply $(0°/90°/0°/90°)$ case. This figure displays that the anti-symmetric cross-ply laminated **HFRC** plate shows better damping characteristics due to the incorporation of **CNTs** in terms of attenuation of amplitudes and enhancement in the first few natural frequencies. For the first mode of natural frequency, the reduction in the vibrational amplitudes of the laminated **HFRC** square plate is $\sim 9\ \%$ and $\sim 11\%$ corresponding to the value of gain $(\boldsymbol{k_d})$ 500 and 800, respectively, compared to the reference composite. Figure 4.6 illustrates the required control voltage to attenuate vibration amplitudes of the **SS** anti-symmetric cross-ply laminated base composite and **HFRC** plates. This figure displays that the laminated **HFRC** square plate requires the maximum voltage to control the vibration amplitudes, which is 29.41 $\boldsymbol{V}$ and 36.48 $\boldsymbol{V}$ with the gain $(\boldsymbol{k_d})$ of 500 and 800, respectively. Figure 4.7 demonstrates the variation of vibrational amplitudes with natural frequency for the **SS** laminated anti-symmetric angle-ply square composite plates. The figure shows that the laminated **HFRC** square plate shows better damping performance compared to the laminated base composite plate for the same value of gain. The percentage of amplitude reduction for the laminated anti-symmetric angle-ply **HFRC** plate with respect to the base composite plate is $\sim 11\ \%$ and $\sim 13\ \%$ for the value of gain $(\boldsymbol{k_d})$ of 500 and 800, respectively. The maximum control voltage required to achieve respective percentage amplitude reduction is 33.98 $\boldsymbol{V}$ and 40.91 $\boldsymbol{V}$, as shown in Fig. 4.8.

Figure 4.9 illustrates the effect piezoelectric constants $\boldsymbol{e_{31}}$ and $\boldsymbol{e_{33}}$ of the **1–3 PZC** reinforced with vertically aligned piezoelectric fibers responsible for the in-plane and transverse plane actuations, respectively, for enhancing the overall damping behavior of the smart laminated symmetric cross-ply **HFRC** square plate. The results are computed considering the gain value of 500 while one of the piezoelectric coefficients ($\boldsymbol{e_{31}}$or $\boldsymbol{e_{33}}$) was set to zero. An electric field is applied to the constraining layer of **1–3 PZC** to induce the out-of-plane actuation when $\boldsymbol{e_{31}} = 0$ and $\boldsymbol{e_{33}} \neq 0$, whereas the case $\boldsymbol{e_{33}} = 0$ and $\boldsymbol{e_{31}} \neq 0$ causes the in-plane actuation in the **1–3 PZC** patches. It is noted that both the piezoelectric constants contribute towards actuation in unison and improves the damping performance of laminated **HFRC** square plate. However, the attenuation capability of out-of-plane actuation (due to $\boldsymbol{e_{33}}$) is much higher than the in-plane actuation (due to $\boldsymbol{e_{31}}$) and the value of $\boldsymbol{e_{33}}$ significantly influences the active vibrational performance of the smart laminated **HFRC** square plate. Figure 4.10 demonstrates the effect of $\boldsymbol{v_{CF}}$ on the damping characteristics of the **SS** laminated symmetric cross-ply **HFRC** square plate. As expected, it can be seen from Fig. 4.10 that the vibrational amplitudes of plates attenuated as the v_{CF} increases from 40% to 60%. The damping characteristics of the laminated symmetric cross-ply **HFRC** square plate is enhanced by ~9 % and ~11% when the value of gain ($\boldsymbol{k_d}$) is 500 and 800, respectively. The corresponding maximum required control voltage is 32.7 $\boldsymbol{V}$ and 40 $\boldsymbol{V}$ to achieve such attenuation, as shown in Fig. 4.11.

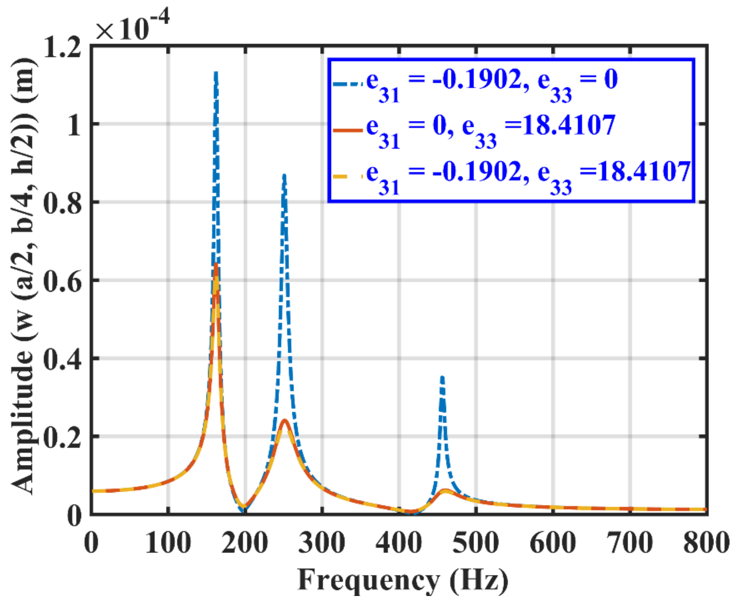

Figure 4.9. Effect of piezoelectric constants on the amplitude of deflection of laminated symmetric cross-ply **HFRC** square plate for $\boldsymbol{k_d} = 500$ and $\boldsymbol{v_{CF}}$ = 10%.

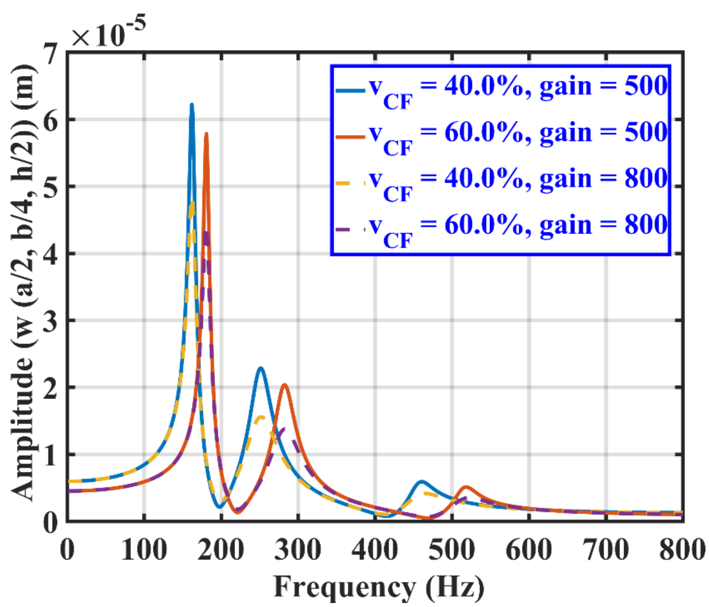

Figure 4.10. Effect of $\boldsymbol{v_{CF}}$ on the amplitude of deflection of laminated symmetric cross-ply **HFRC** square plate.

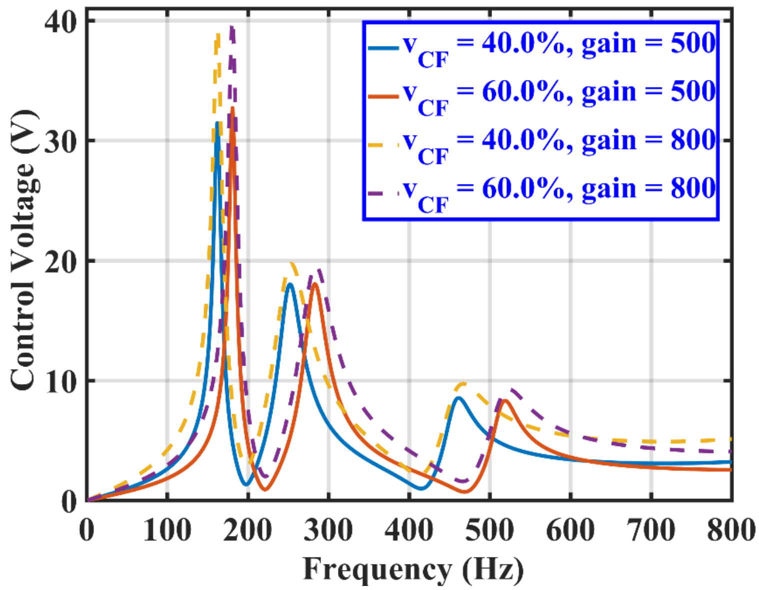

Figure 4.11. Effect $\boldsymbol{v_{CF}}$ on the variation of the control voltage with respect to the frequency response of **SS** laminated symmetric cross-ply **HFRC** square plate.

Figures 4.12-4.14 demonstrate the variation of non-dimensional fundamental natural frequencies ($\boldsymbol{\lambda}$) of the laminated plate with the aspect ratio by varying the thickness of the plate and keeping the in-plane dimensions of the substrate plate constant. Here, we computed the results for the base composite and **HFRC** with $\boldsymbol{v_{CNT}} =$ 5% and 10 %. As expected, the non-dimensional fundamental natural frequencies increase with increasing the $\boldsymbol{v_{CNT}}$. For the symmetric cross-ply case (Fig. 4.12), it can be observed that the value of $\boldsymbol{\lambda}$ of laminated square plates increases as the aspect ratio increases from 20 to 60 and them remain almost constant in the range of 60 to 100. The maximum value of $\boldsymbol{\lambda}$ is found when $\boldsymbol{a/h} = 80$, which is 14.95, 14.21, and 13.19 corresponding to the value of $\boldsymbol{v_{CNT}}$ = 10, 5 and 0 %. Similar results were obtained for the anti-symmetric cross-ply $(0°/90°/0°/90°)$ and anti-symmetric angle-ply $(-45/45°/-45°/45°)$ cases and the same are presented in the supplementary file for the sake of brevity in Figs. 4.13 and 4.14. For the anti-symmetric cross-ply case, the maximum value of $\boldsymbol{\lambda}$ is 13.9, 13.25, and 12.24, whereas the maximum value of $\boldsymbol{\lambda}$ is 18.66, 17.68, and 16.33 for the anti-symmetric angle-ply corresponding to the value of $\boldsymbol{v_{CNT}}$ = 10, 5 and 0 %.

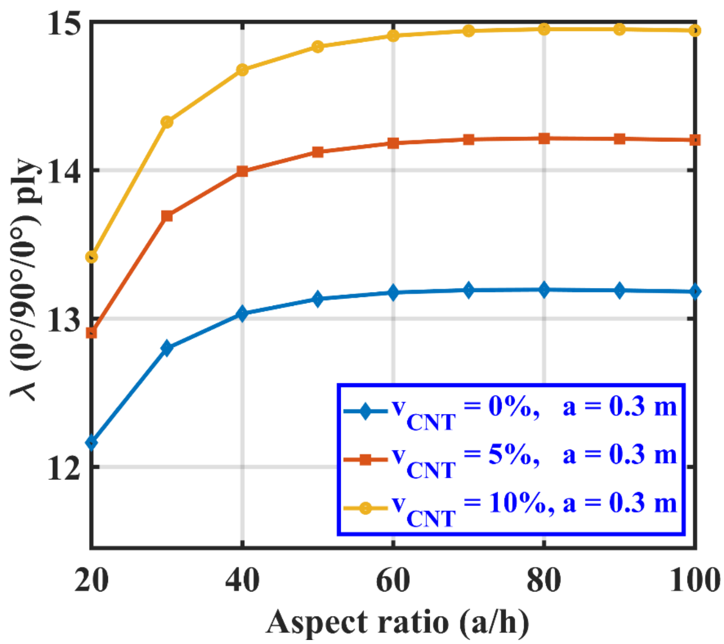

Figure 4.12. Variation of non-dimensional frequency parameter ($\boldsymbol{\lambda}$) with aspect ratio of the laminated square plate by varying the thickness and keeping in-plane dimensions of plate constant for the symmetric cross-ply plates ($\boldsymbol{k_d}$ = 500).

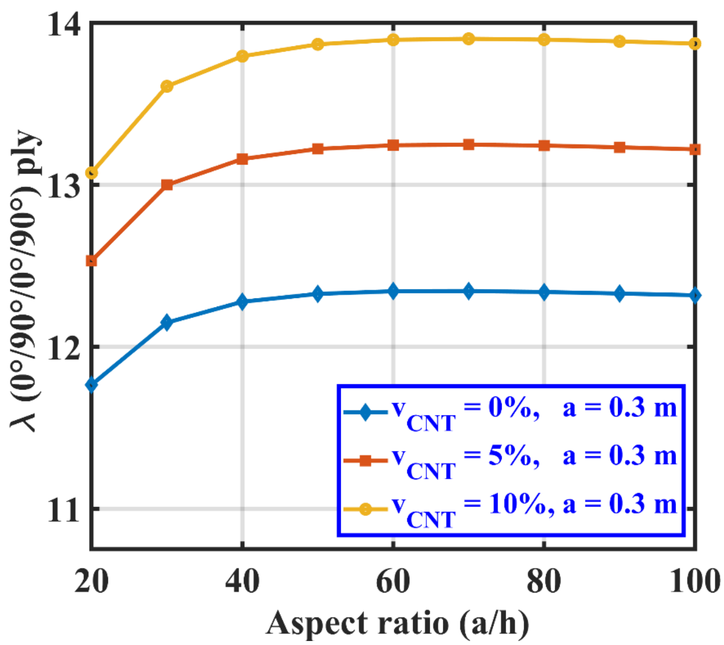

Figure 4.13. Variation of non-dimensional frequency parameter ($\boldsymbol{\lambda}$) with aspect ratio of the laminated square plate by varying the thickness and keeping in-plane dimensions of plate constant for the anti-symmetric cross-ply plates ($\boldsymbol{k_d}$ = 500).

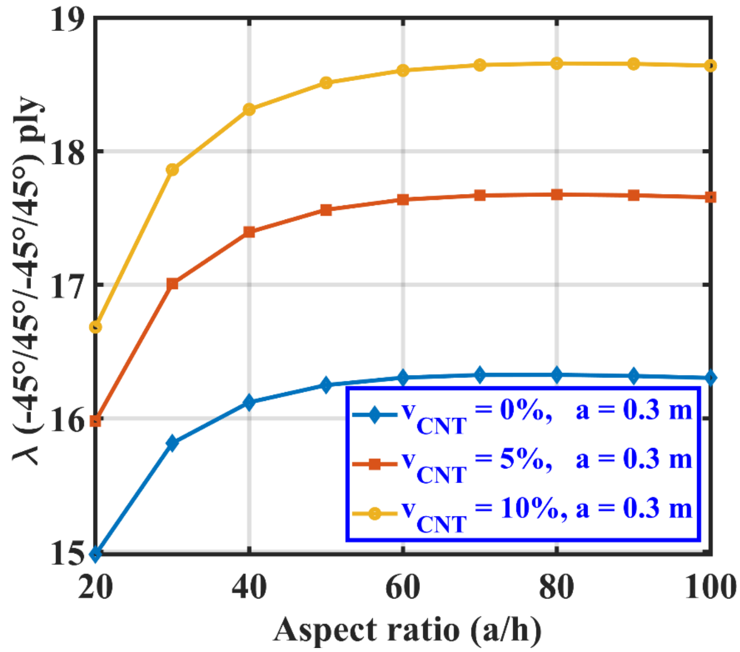

Figure 4.14. Variation of non-dimensional frequency parameter ($\boldsymbol{\lambda}$) with aspect ratio of the laminated square plate by varying the thickness and keeping in-plane dimensions of plate constant for the anti-symmetric angle-ply plates ($\boldsymbol{k_d}$ = 500).

Figure 4.15 demonstrates the variation of non-dimensional fundamental natural frequencies of the laminated square plate with respect to the aspect ratio by varying the in-plane dimensions of plate and keeping the thickness of the substrate plate constant. It can be noted that the value of $\boldsymbol{\lambda}$ improves as the $\boldsymbol{v_{CNT}}$ increases. The maximum value of $\boldsymbol{\lambda}$ for the symmetric cross-ply case is 14.94, 14.20, and 13.18 corresponding to the value of $\boldsymbol{v_{CNT}} = 10, 5,$ and 0 %. Likewise, the maximum value of $\boldsymbol{\lambda}$ is 13.87, 13.22, and 12.32 for the anti-symmetric cross-ply case, whereas the values are 18.64, 17.66, and 16.30 for the anti-symmetric angle-ply case corresponding to $\boldsymbol{v_{CNT}}$ = 10, 5 and 0 %. The results of anti-symmetric cross-ply and anti-symmetric angle-ply cases are presented in the supplementary file in Figs. 4.16 and 4.17.

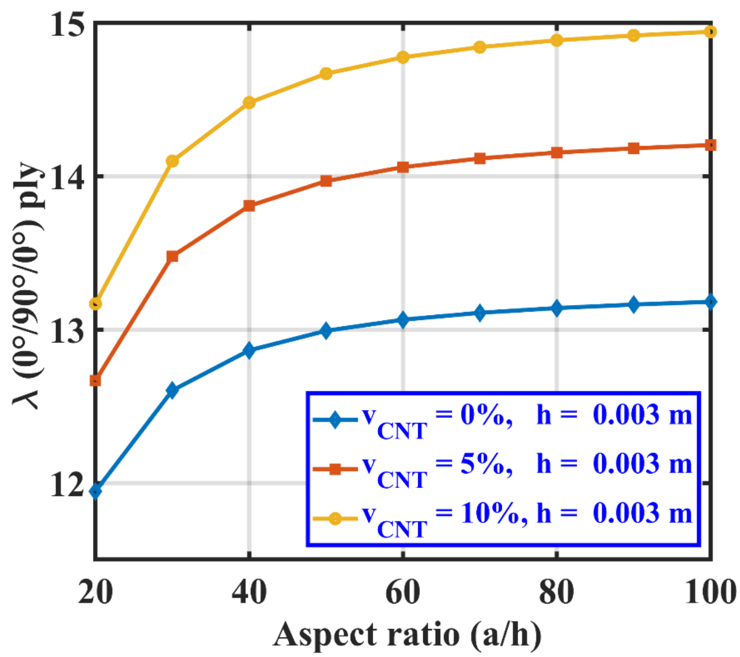

Figure 4.15. Variation of non-dimensional frequency parameter ($\boldsymbol{\lambda}$) with aspect ratio of the laminated square plate by varying the in-plane dimensions and keeping thickness of plate constant for the symmetric cross-ply plates ($\boldsymbol{k_d}$ = 500).

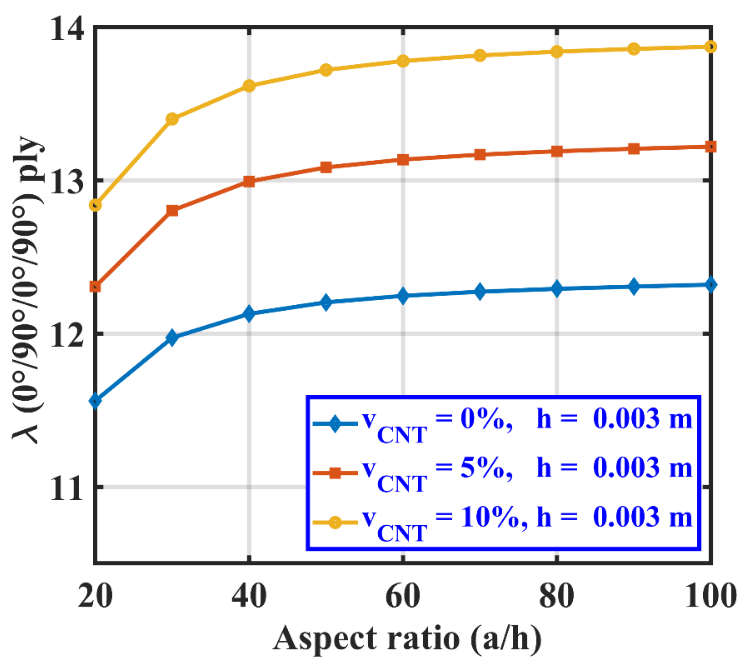

Figure 4.16. Variation of non-dimensional frequency parameter ($\boldsymbol{\lambda}$) with aspect ratio of the laminated square plate by varying the in-plane dimensions and keeping thickness of plate constant for the anti-symmetric cross-ply plates ($\boldsymbol{k_d}$ = 500).

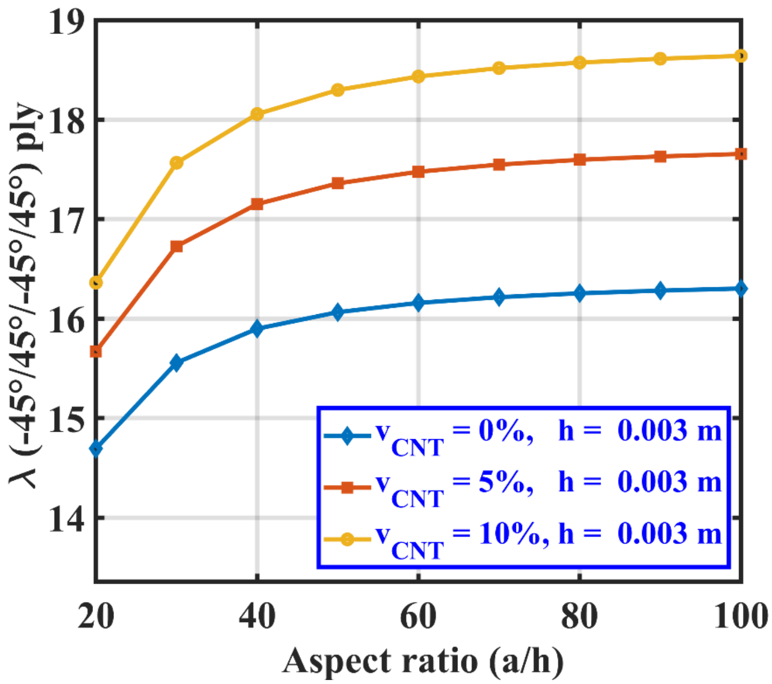

Figure 4.17. Variation of non-dimensional frequency parameter ($\boldsymbol{\lambda}$) with aspect ratio of the laminated square plate by varying the in-plane dimensions and keeping thickness of plate constant for the anti-symmetric angle-ply plates ($\boldsymbol{k_d}$ = 500).

Furthermore, we performed the quantitative relative analysis to demonstrate the enhancement of the damping characteristics of laminated **HFRC** square plates. For this, we defined a damping characteristics enhancement factor (**DCEF**) which indicates the reduction of the amplitudes of deflection of laminated **HFRC** plate compared to the base composite substrate plate, as follows:

$$\boldsymbol{DCEF} = \frac{\boldsymbol{A_0} - \boldsymbol{A_{CNT}}}{\boldsymbol{A_0}}\ \% \tag{4.31}$$

where, $\boldsymbol{A_0}$ is the amplitude of deflection of base composite plate, and $\boldsymbol{A_{CNT}}$ is the amplitude of deflection of **HFRC** plate.

Figures 4.18-4.20 demonstrates the effect of thickness variation ($\boldsymbol{h} = \boldsymbol{a}/\boldsymbol{X}, \boldsymbol{X} =$ 20 to 100) on the **DCEF** of the laminated **HFRC** plates for the first mode of amplitudes of deflection. A higher Young's modulus and excellent strength to weight ratio of **CNTs** improves the stiffness of **HFRC** significantly. This results in the enhancement in the damping performance of the **HFRC** plates compared to the base composite plates. It can be observed that the amplitudes of deflections are attenuated substantially by incorporating the **CNTs** and hence, improving the overall performance of the system. It can also be noted that the value of **DCEF** increases as the aspect ratio of the plate decreases. For the symmetric cross-ply case, maximum value of **DCEF** is approximately $\sim$8.6% and $\sim$16 % when the value of $\boldsymbol{v_{CNT}}$ is 5% and 10 %, respectively, as shown in Fig. 4.18. The results for the other two cases (anti-symmetric cross-ply and anti-symmetric angle-ply) are explicitly shown in the supplementary file in Figs. 4.19 and 4.20. In case of anti-symmetric cross-ply case, the maximum value of **DCEF** is $\sim$8.5% and $\sim$14.8 %, and it is $\sim$9.1% and $\sim$15.7% for the anti-symmetric angle-ply case when the value of $\boldsymbol{v_{CNT}}$ is 5% and 10 %, respectively.

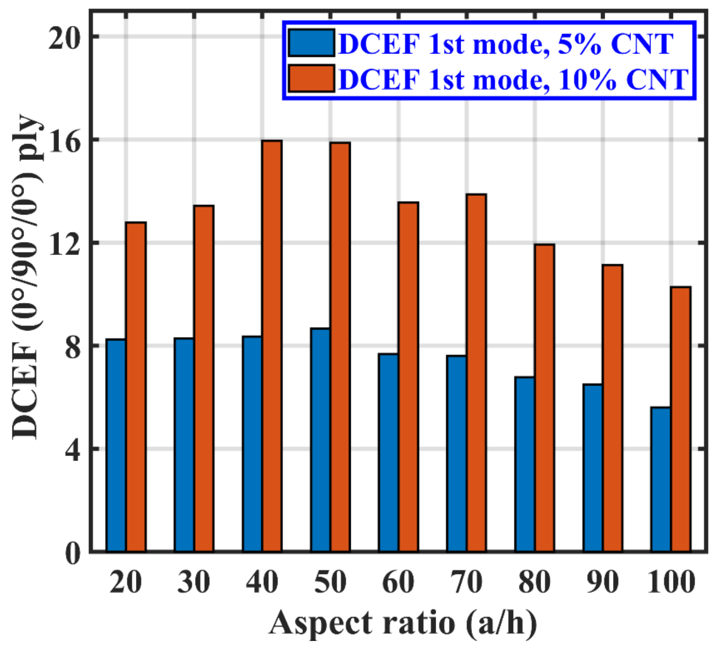

Figure 4.18. Variation of **DCEF** with aspect ratio of the laminated symmetric cross-ply square plate by varying the thickness and keeping in-plane dimensions constant ($\boldsymbol{k_d}$ = 500).

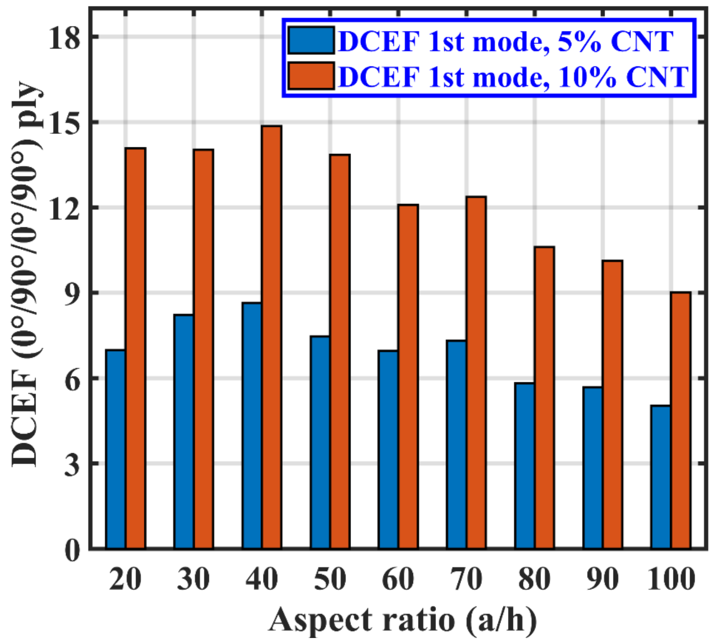

Figure 4.19. Variation of **DCEF** with aspect ratio of the laminated anti-symmetric cross-ply square plate by varying the thickness and keeping in-plane dimensions constant ($\boldsymbol{k_d}$ = 500).

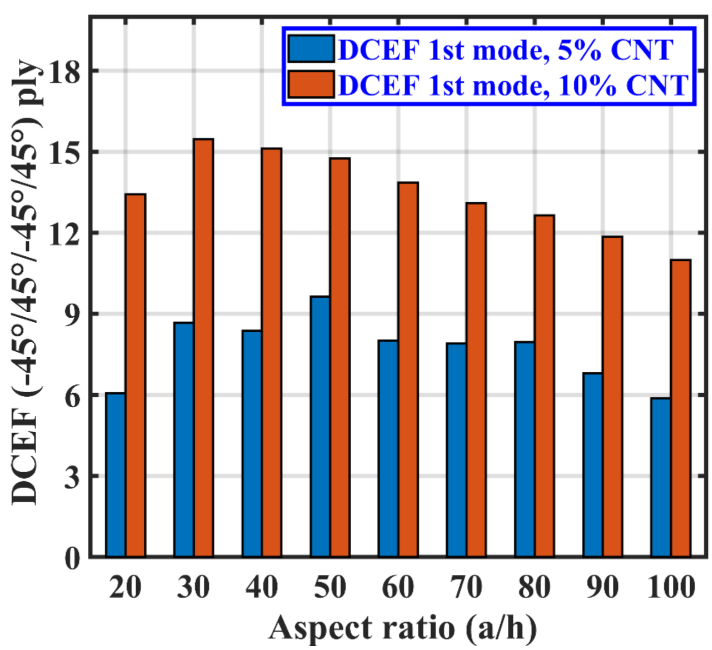

Figure 4.20. Variation of **DCEF** with aspect ratio of the laminated anti-symmetric angle-ply square plate by varying the thickness and keeping in-plane dimensions constant ($\boldsymbol{k_d}$ = 500).

The variation of **DCEF** with respect to the aspect ratio of substrate plates by varying in-plane dimensions and keeping thickness constant is shown in Fig. 4.21. Again, it can be observed that the **DCEF** increases as the aspect ratio of plate decreases. The maximum value of **DCEF** is observed in the range of $\boldsymbol{a/h} = 30$ to 50. The maximum value of **DCEF** of the symmetric cross-ply case is ~9.4% and ~15.7 % when the value of $\boldsymbol{v_{CNT}}$ is 5% and 10 %, respectively, as shown in Fig. 4.21. The maximum value of **DCEF** is ~8.5% and ~14.8 % for the anti-symmetric cross-ply case and it is ~9.1% and ~15.7 % for the anti-symmetric angle-ply case when the value of $\boldsymbol{v_{CNT}}$ is 5% and 10 %, respectively. These results are explicitly presented in the supplementary file in Figs. 4.22 and 4.23 for the sake of brevity. It can be observed from Figs. 4.18 to 4.23 that the addition of **CNTs** in the matrix material improves the performance of the **HFRC** substrate plates significantly.

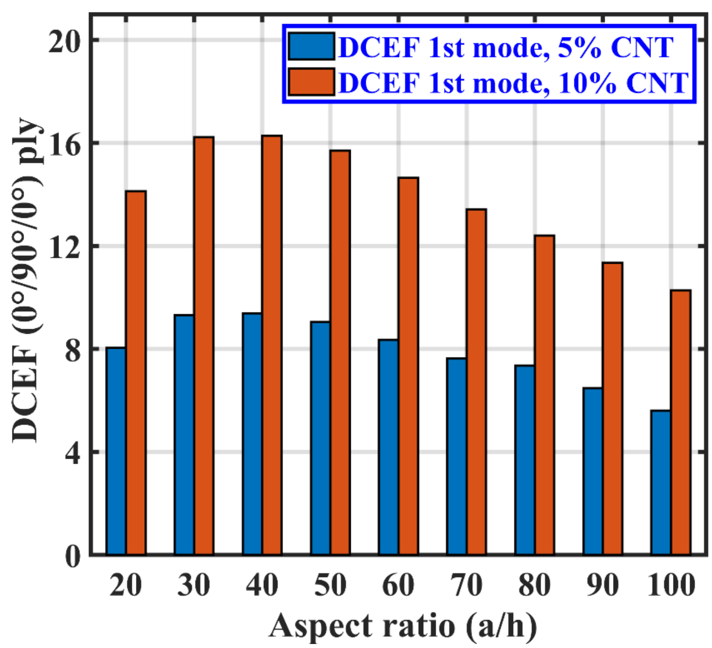

Figure 4.21. Variation of **DCEF** with aspect ratio of the laminated symmetric cross-ply square plate by varying the in-plane dimensions and keeping thickness constant ($\boldsymbol{k_d}$ = 500).

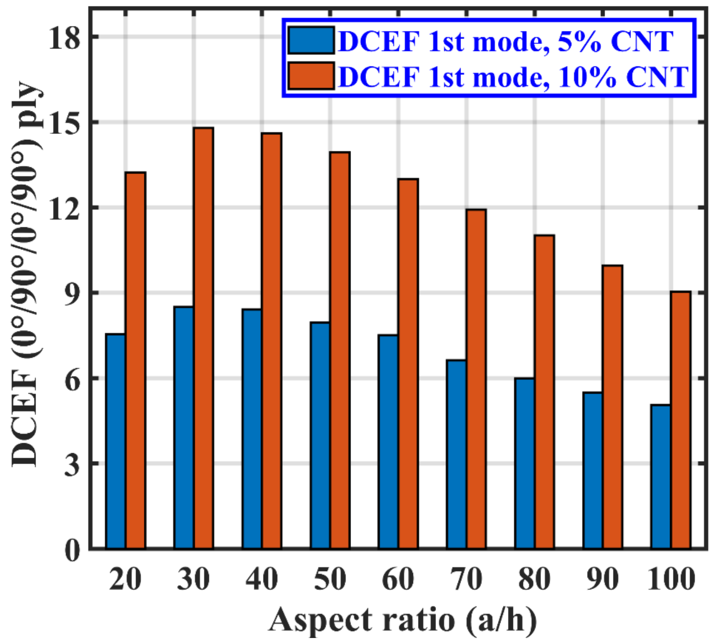

Figure 4.22. Variation of **DCEF** with aspect ratio of the laminated anti-symmetric cross-ply square plate by varying the in-plane dimensions and keeping thickness constant ($\boldsymbol{k_d}$ = 500).

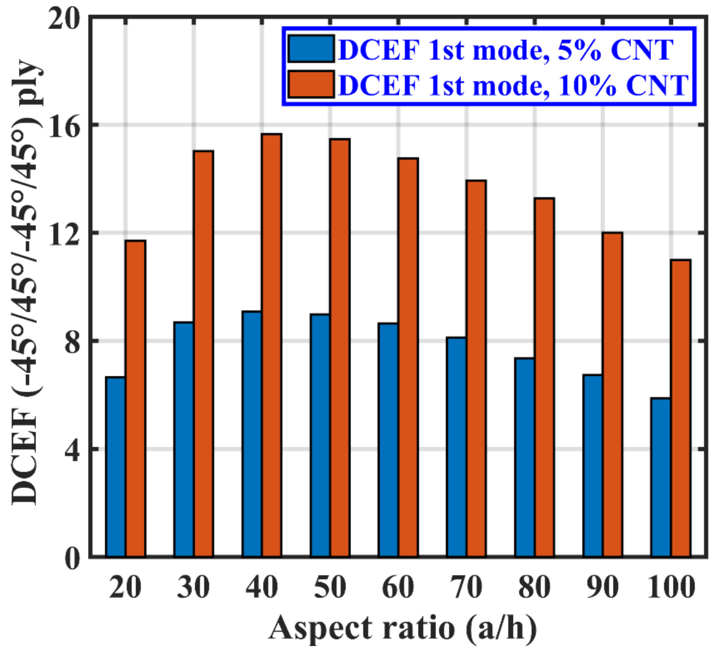

Figure 4.23. Variation of **DCEF** with aspect ratio of the laminated anti-symmetric angle-ply square plate by varying the in-plane dimensions and keeping thickness constant ($\boldsymbol{k_d}$ = 500).

The effect of aspect ratio (***a/h***) on **DCEF** of the **HFRC** laminated beam for the 1st mode of amplitudes of vibration by keeping the overall volume fraction of base composite and **HFRC** the same is demonstrated in Figs. 4.24 for the various ply types. The fiber volume fraction in the base composite is taken as 40%, while in **HFRC,** the total fiber volume fraction (i.e., $\boldsymbol{v_{CNT}} + \boldsymbol{v_{CF}}$) is taken as 40%. The results show that due to the consideration of **CNTs** the overall structural damping characteristics of **HFRC** plate significantly improved for all the ply types, and the best results are observed for the anti-symmetric angle-ply.

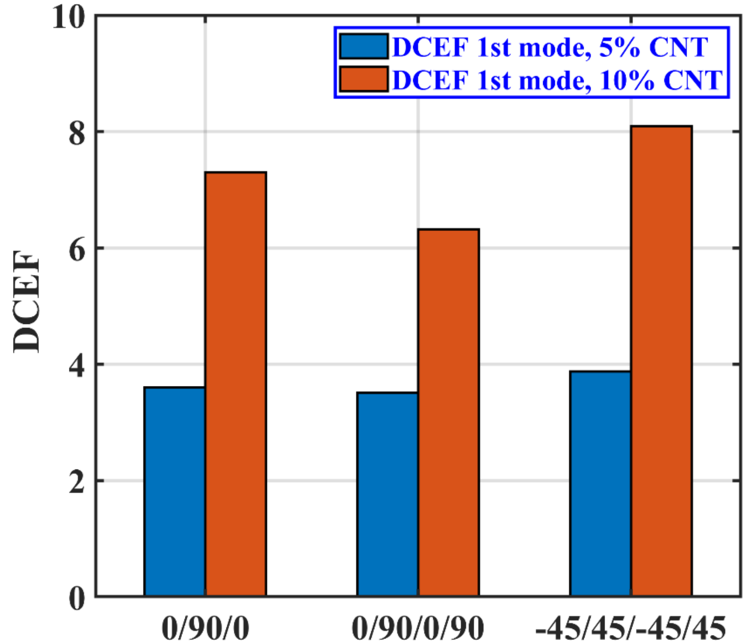

Figure 4.24. Variation of **DCEF** with respect to the aspect ratio of the substrate plate for various ply type at a gain ($\boldsymbol{k_d}$) of 500, $\boldsymbol{v_{CNT}}$ = 5 and 10%, and aspect ratio (***a/h***) = 100 by keeping the overall fiber volume fraction same for base composite and **HFRC**.

4.5 Summary

In the present work, we studied the damping performance of simply supported laminated **CNT**-based carbon fiber reinforced composite plates using the **FE** approach. The **CNTs** are embedded in the matrix phase of carbon fiber composite to improve overall properties, especially the damping properties of the resulting **HFRC**. First, the effective elastic properties of the base composite and **HFRC** are estimated using the mechanics of material approach. Second, the damping performance of smart laminated simply supported **HFRC** plates is investigated via the **FE** approach using modified **FSDT**. The numerical results are shown for the three cases: symmetric and anti-symmetric cross-ply, and anti-symmetric angle-ply. The following main conclusions are drawn from this study.

- The damping characteristics of the **HFRC** plate is significantly improved over the passive damping, that is, about $50\ \%$ improvement in the damping characteristics is observed for the small value of control voltage. The out-of-plane piezoelectric coefficient ($\boldsymbol{e_{33}}$) of the **1–3 PZC** significantly influences the active damping of laminated composite plates.
- In general, the performance of the laminated **HFRC** square plate is significantly enhanced over that of the laminated base composite plate due to the incorporation of **CNTs**. The anti-symmetric angle-ply case provides better damping than that of symmetric/anti-symmetric cross-ply cases. Analysis of the **HFRC** plate showed that its vibration amplitudes can be attenuated from ~ 8 to $\sim 16\ \%$ by adding a small amount **CNTs**.
- For the variation of thickness of plate, the non-dimensional fundamental natural frequencies parameter ($\boldsymbol{\lambda}$) remains almost constant for the higher aspect ratio (***a/h***) of plate. Whereas it increases as the aspect ratio increases for the variation of in-plane dimensions of the plate.
- Analysis of **HFRC** shows that the damping characteristics enhancement factor varies with the aspect ratio of the plate. Based on the quantitative analysis, the thickness and in-plane dimensions of **HFRC** plates can be selected appropriately to achieve optimum performance.

Thus, from the present investigation, it can be concluded that the **CNTs** as a modifier in the conventional composite have the potential to improve the damping and vibrational characteristics of the resulting composite structures.

Chapter 5

Active Vibration Damping of a Clamped-Clamped Smart Multiscale Hybrid Fiber Reinforced Composite Plates Using 1–3 Piezoelectric Composites

*This Chapter (Gupta et al., 2022b) presents the finite element **(FE)** model using the first-order shear deformation theory **(FSDT)** to investigate the damping performance of laminated hybrid fiber-reinforced composite **(HFRC)** smart plates subjected to clamped-clamped **(CC)** boundary condition via the active constrained layer damping **(ACLD)** treatment. A unique feature of the **HFRC** is that the nanoscale carbon nanotubes **(CNTs)** which are either straight or wavy are embedded in the matrix phase of carbon fiber composite to improve the overall properties, especially the damping characteristics of the resulting **HFRC**. The constraining layer of the **ACLD** treatment is considered to be made of vertically/obliquely reinforced **1–3** piezoelectric composite **(PZC)** material. The system consists of a laminated **HFRC** plate integrated with the two patches of **ACLD** treatment. The research carried out in this chapter brings to light that even the wavy **CNTs** and orientation of piezoelectric fibers can be properly utilized for attaining structural benefits from the exceptional elastic properties of **CNTs**.*

5.1 Introduction

The analyses carried out in chapters 3 and 4 revealed that the active patches of the **ACLD** treatment significantly improve the active damping characteristics of laminated **HFRC** beams and plates for controlling their linear vibrations over the passive counterpart. In the present chapter a similar study has been carried out on the active vibration damping of the **HFRC** plates subjected to **CC** boundary condition. The **HFRC** is a novel composite where the **CNT**s which are either straight or wavy are uniformly distributed along with carbon fiber reinforcements in matrix phase. The plane of waviness of the **CNT**s is coplanar with two mutually orthogonal planes i.e., **1–2** plane and **1–3** plane. The constraining layer of the **ACLD** treatment is composed of the vertically/obliquely reinforced **1–3 PZC**s while the constrained viscoelastic layer has been sandwiched between the **HFRC** substrate and the **PZC** layer. Based on the **FSDT** a three-dimensional **FE** model of smart **HFRC** plates integrated with **ACLD** patches has been developed to investigate the performance of these patches for controlling the vibrations of these plates. This study reveals that the performance of the **ACLD** patches for controlling the vibrations of the **CC** laminated **HFRC** plates is better when the **CNT** waviness is coplanar with **1–3** plane. Emphasis has been placed on investigating the effect of the variation of piezoelectric fiber orientation angle on the performance of the **ACLD** treatment. The base composite and **HFRC** substrate with straight and wavy **CNT**s are considered for presenting the numerical results. Also, the effect of variation of the piezoelectric fiber orientation angle in the **1–3 PZC** constraining layer on the control authority of the **ACLD** patches has been investigated. The evaluated results suggest that even the wavy **CNT**s can be properly utilized for attaining structural benefits from the exceptional elastic properties of **CNT**s.

5.2 Effective Piezoelectric Properties of a Vertically/Obliquely Reinforced 1-3 PZC

5.2.1 Mechanics of Materials (MOM) Approach

In this section, we developed a simple micromechanical model based on the **MOM** approach to predict the electromechanical properties of **1–3 PZC**. Figure 5.1(a) illustrates the schematics of representative volume element **(RVE)** of **1–3 PZC** lamina with fibers aligned vertically in **3**–direction, and Fig. 5.1(b) shows the cross-section of the lamina. The piezoelectric constants play an important role in the control authority of the **1–3 PZC** actuator, which can actively control the vibrations induced in the smart structures.

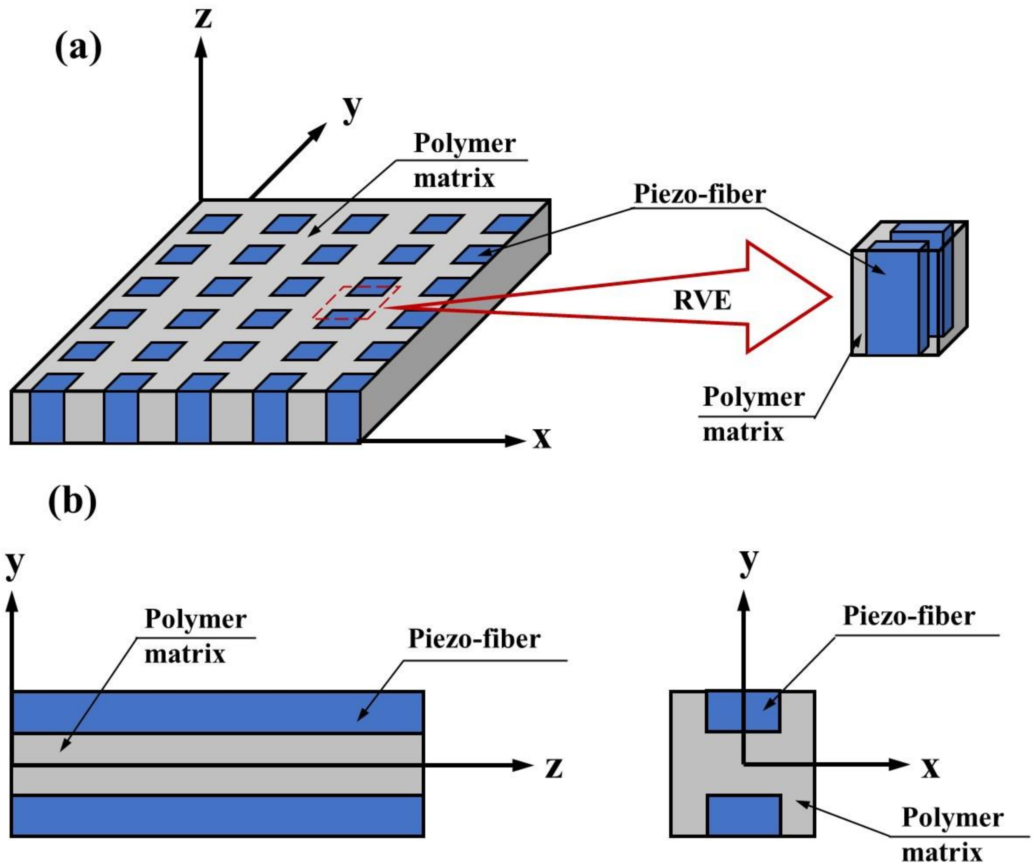

Figure 5.1. (a) Schematic representation of **1–3 PZC** lamina and (b) cross-sections of **RVE** of **1–3 PZC**.

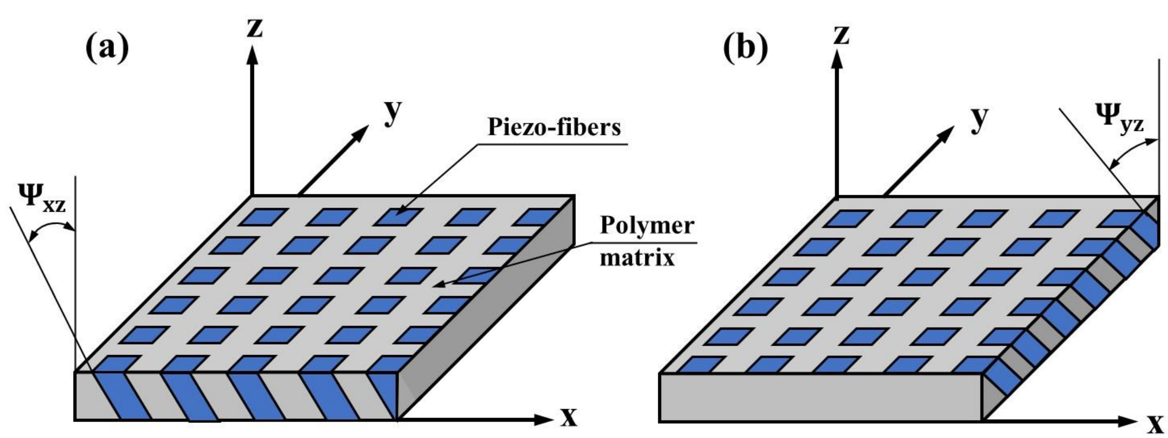

Figure 5.2. Schematic representation of **1–3 PZC** lamina with piezo-fibers coplanar in the (a) ***xz*–** plane and (b) ***yz***–plane.

Considering the principal material coordinate system **(*x*-*y*-*z*)** or problem coordinate system **(1-2-3)**, the constitutive relations for the **1–3 PZC** are given by:

$$\{\boldsymbol{\sigma}^f\} = [\boldsymbol{C}^f]\{\boldsymbol{\varepsilon}^f\} - \{\boldsymbol{e}^f\}\boldsymbol{E_3},$$

$$\{\boldsymbol{\sigma}^m\} = [\boldsymbol{C}^m]\{\boldsymbol{\varepsilon}^m\} \tag{5.1}$$

$$\{\boldsymbol{\sigma}^r\} = \begin{Bmatrix} \boldsymbol{\sigma_1^r} \\ \boldsymbol{\sigma_2^r} \\ \boldsymbol{\sigma_3^r} \\ \boldsymbol{\sigma_{23}^r} \\ \boldsymbol{\sigma_{13}^r} \\ \boldsymbol{\sigma_{12}^r} \end{Bmatrix}, \quad \{\boldsymbol{\epsilon}^r\} = \begin{Bmatrix} \boldsymbol{\varepsilon_1^r} \\ \boldsymbol{\varepsilon_2^r} \\ \boldsymbol{\varepsilon_3^r} \\ \boldsymbol{\varepsilon_{23}^r} \\ \boldsymbol{\varepsilon_{13}^r} \\ \boldsymbol{\varepsilon_{12}^r} \end{Bmatrix}, \tag{5.2}$$

$$[\boldsymbol{C}^r] = \begin{bmatrix} \boldsymbol{C_{11}^r} & \boldsymbol{C_{12}^r} & \boldsymbol{C_{13}^r} & \boldsymbol{0} & \boldsymbol{0} & \boldsymbol{0} \\ \boldsymbol{C_{12}^r} & \boldsymbol{C_{22}^r} & \boldsymbol{C_{23}^r} & \boldsymbol{0} & \boldsymbol{0} & \boldsymbol{0} \\ \boldsymbol{C_{13}^r} & \boldsymbol{C_{23}^r} & \boldsymbol{C_{33}^r} & \boldsymbol{0} & \boldsymbol{0} & \boldsymbol{0} \\ \boldsymbol{0} & \boldsymbol{0} & \boldsymbol{0} & \boldsymbol{C_{44}^r} & \boldsymbol{0} & \boldsymbol{0} \\ \boldsymbol{0} & \boldsymbol{0} & \boldsymbol{0} & \boldsymbol{0} & \boldsymbol{C_{55}^r} & \boldsymbol{0} \\ \boldsymbol{0} & \boldsymbol{0} & \boldsymbol{0} & \boldsymbol{0} & \boldsymbol{0} & \boldsymbol{C_{66}^r} \end{bmatrix}, \quad \{\boldsymbol{e}^f\} = \begin{Bmatrix} \boldsymbol{e_{31}^f} \\ \boldsymbol{e_{32}^f} \\ \boldsymbol{e_{33}^f} \\ \boldsymbol{0} \\ \boldsymbol{0} \\ \boldsymbol{0} \end{Bmatrix}, \quad \boldsymbol{r = m \; and \; f}$$

Here, the notations $\boldsymbol{m}$ and $\boldsymbol{f}$ denote the epoxy matrix and **PZT-5H** phases, respectively; $\boldsymbol{\sigma_1^r}$**,** $\boldsymbol{\sigma_2^r}$, and $\boldsymbol{\sigma_3^r}$ represent the normal stresses along **1**, **2**, and **3** directions, respectively; $\boldsymbol{\varepsilon_1^r}$, $\boldsymbol{\varepsilon_2^r}$, and $\boldsymbol{\varepsilon_3^r}$ denote the corresponding normal strains; shear stresses are given by $\boldsymbol{\sigma_{12}^r}$**,** $\boldsymbol{\sigma_{13}^r}$, and $\boldsymbol{\sigma_{23}^r}$; $\boldsymbol{\varepsilon_{12}^r}$, $\boldsymbol{\varepsilon_{13}^r}$, and $\boldsymbol{\varepsilon_{23}^r}$ are the shear strains; $\boldsymbol{C_{ij}^r}$ ($\boldsymbol{i, j}$ $=$ 1,2 and 6) are the elastic coefficients of ***r*^*th*^** phase; $\boldsymbol{e_{31}^f}$, $\boldsymbol{e_{31}^f}$, and $\boldsymbol{e_{33}^f}$ represent the piezoelectric coefficients and $\boldsymbol{E_3}$ is the applied electric field in the **3**–direction.

Assuming the condition of the perfect bonding between fiber and matrix phases, the iso-field conditions, and the rules of mixture **(ROM)** relation, we can write the following relation:

$$\begin{Bmatrix} \sigma_1^f \\ \sigma_2^f \\ \varepsilon_3^f \\ \sigma_{23}^f \\ \sigma_{13}^f \\ \sigma_{12}^f \end{Bmatrix} = \begin{Bmatrix} \sigma_1^m \\ \sigma_2^m \\ \varepsilon_3^m \\ \sigma_{23}^m \\ \sigma_{13}^m \\ \sigma_{12}^m \end{Bmatrix} = \begin{Bmatrix} \sigma_1 \\ \sigma_2 \\ \varepsilon_3 \\ \sigma_{23} \\ \sigma_{13} \\ \sigma_{12} \end{Bmatrix} \tag{5.3}$$

$$v_f \begin{Bmatrix} \varepsilon_1^{gf} \\ \varepsilon_2^f \\ \sigma_3^f \\ \varepsilon_{23}^f \\ \varepsilon_{13}^f \\ \varepsilon_{12}^f \end{Bmatrix} + v_m \begin{Bmatrix} \varepsilon_1^m \\ \varepsilon_2^m \\ \sigma_3^m \\ \varepsilon_{23}^m \\ \varepsilon_{13}^m \\ \varepsilon_{12}^m \end{Bmatrix} = \begin{Bmatrix} \varepsilon_1 \\ \varepsilon_2 \\ \sigma_3 \\ \varepsilon_{23} \\ \varepsilon_{13} \\ \varepsilon_{12} \end{Bmatrix} \tag{5.4}$$

where v_f and v_m represent the volume fractions of **PZT** fiber and matrix, respectively. Taking Eqs. (5.1)-(5.4) into account, the field vectors of the homogenized composite can be given in terms of stress and strain vectors of the composite, as follows:

$$\{\sigma\} = [C_1]\{\varepsilon^f\} + [C_2]\{\varepsilon^m\} - \{e_1\}E_3,$$

$$[C_3]\{\varepsilon^m\} - [C_4]\{\varepsilon^m\} = \{e_2\}E_3,$$

$$\{\varepsilon\} = [V_1]\{\varepsilon^f\} + [V_2]\{\varepsilon^m\} \tag{5.5}$$

The matrices appeared in Eqs. (5.5) are as follows:

$$[C_1] = \begin{bmatrix} C_{11}^g & C_{12}^g & C_{13}^g & 0 & 0 & 0 \\ C_{12}^g & C_{22}^g & C_{23}^g & 0 & 0 & 0 \\ v_g C_{13}^g & v_g C_{23}^g & v_g C_{33}^g & 0 & 0 & 0 \\ 0 & 0 & 0 & C_{44}^p & 0 & 0 \\ 0 & 0 & 0 & 0 & C_{55}^p & 0 \\ 0 & 0 & 0 & 0 & 0 & C_{66}^p \end{bmatrix}$$

$$[\boldsymbol{C_2}] = \begin{bmatrix} 0 & 0 & 0 & 0 & 0 & 0 \\ 0 & 0 & 0 & 0 & 0 & 0 \\ \boldsymbol{v_m C_{13}^m} & \boldsymbol{v_m C_{23}^m} & \boldsymbol{v_m C_{33}^m} & 0 & 0 & 0 \\ 0 & 0 & 0 & 0 & 0 & 0 \\ 0 & 0 & 0 & 0 & 0 & 0 \\ 0 & 0 & 0 & 0 & 0 & 0 \end{bmatrix},$$

$$\{\boldsymbol{e_1}\} = \begin{Bmatrix} \boldsymbol{e_{31}^g} \\ \boldsymbol{e_{32}^g} \\ \boldsymbol{v_g e_{33}^g} \\ 0 \\ 0 \\ 0 \end{Bmatrix}, \{\boldsymbol{e_2}\} = \begin{Bmatrix} -\boldsymbol{e_{31}^g} \\ -\boldsymbol{e_{32}^g} \\ 0 \\ 0 \\ 0 \\ 0 \end{Bmatrix},$$

$$[\boldsymbol{C_3}] = \begin{bmatrix} \boldsymbol{C_{11}^g} & \boldsymbol{C_{12}^g} & \boldsymbol{C_{13}^g} & 0 & 0 & 0 \\ \boldsymbol{C_{12}^g} & \boldsymbol{C_{22}^g} & \boldsymbol{C_{23}^g} & 0 & 0 & 0 \\ 0 & 0 & 1 & 0 & 0 & 0 \\ 0 & 0 & 0 & \boldsymbol{C_{44}^g} & 0 & 0 \\ 0 & 0 & 0 & 0 & \boldsymbol{C_{55}^g} & 0 \\ 0 & 0 & 0 & 0 & 0 & \boldsymbol{C_{66}^g} \end{bmatrix},$$

$$[\boldsymbol{C_4}] = \begin{bmatrix} \boldsymbol{C_{11}^m} & \boldsymbol{C_{12}^m} & \boldsymbol{C_{13}^m} & 0 & 0 & 0 \\ \boldsymbol{C_{12}^m} & \boldsymbol{C_{22}^m} & \boldsymbol{C_{23}^m} & 0 & 0 & 0 \\ 0 & 0 & 1 & 0 & 0 & 0 \\ 0 & 0 & 0 & \boldsymbol{C_{44}^m} & 0 & 0 \\ 0 & 0 & 0 & 0 & \boldsymbol{C_{55}^m} & 0 \\ 0 & 0 & 0 & 0 & 0 & \boldsymbol{C_{66}^m} \end{bmatrix},$$

$$[\boldsymbol{V_1}] = \begin{bmatrix} \boldsymbol{v_g} & 0 & 0 & 0 & 0 & 0 \\ 0 & \boldsymbol{v_g} & 0 & 0 & 0 & 0 \\ 0 & 0 & 1 & 0 & 0 & 0 \\ 0 & 0 & 0 & \boldsymbol{v_g} & 0 & 0 \\ 0 & 0 & 0 & 0 & \boldsymbol{v_g} & 0 \\ 0 & 0 & 0 & 0 & 0 & \boldsymbol{v_g} \end{bmatrix}, \text{ and } [\boldsymbol{V_2}] = \begin{bmatrix} \boldsymbol{v_m} & 0 & 0 & 0 & 0 & 0 \\ 0 & \boldsymbol{v_m} & 0 & 0 & 0 & 0 \\ 0 & 0 & 0 & 0 & 0 & 0 \\ 0 & 0 & 0 & \boldsymbol{v_m} & 0 & 0 \\ 0 & 0 & 0 & 0 & \boldsymbol{v_m} & 0 \\ 0 & 0 & 0 & 0 & 0 & \boldsymbol{v_m} \end{bmatrix}$$

Substituting Eq. (5.3) into Eq. (5.5), constitutive relation for **1–3 PZC** can be given by:

$$\{\boldsymbol{\sigma}\} = [\boldsymbol{C}]\{\boldsymbol{\varepsilon}\} - \{\boldsymbol{e}\}\boldsymbol{E_3} \tag{5.6}$$

in which $[\boldsymbol{C}\,]$ and $\{\boldsymbol{e}\,\}$ are the respective effective elastic matrix and piezoelectric coefficient vector, respectively. The expansion of matrix appeared in Eq. (5.6) can be given by:

$$[\boldsymbol{C}\,] = [\boldsymbol{C_1}][\boldsymbol{V_3}]^{-\mathbf{1}} + [\boldsymbol{C_2}][\boldsymbol{V_4}]^{-\mathbf{1}}\,,$$

$$[\boldsymbol{V_3}] = [\boldsymbol{V_1}] + [\boldsymbol{V_2}][\boldsymbol{C_4}]^{-\mathbf{1}}[\boldsymbol{C_3}]\,,$$

$$[\boldsymbol{V_4}] = [\boldsymbol{V_2}] + [\boldsymbol{V_1}][\boldsymbol{C_3}]^{-\mathbf{1}}[\boldsymbol{C_4}]$$

$$\{\boldsymbol{e}\,\} = \{\boldsymbol{e_1}\} + [\boldsymbol{C_1}][\boldsymbol{V_3}]^{-\mathbf{1}}[\boldsymbol{V_2}][\boldsymbol{C_4}]^{-\mathbf{1}}\{\boldsymbol{e_2}\} - [\boldsymbol{C_2}][\boldsymbol{V_4}]^{-\mathbf{1}}[\boldsymbol{V_1}][\boldsymbol{C_3}]^{-\mathbf{1}}\{\boldsymbol{e_2}\} \qquad (5.7)$$

The effective dielectric constant $\in_{\mathbf{33}}$ of **1–3 PZC** can be obtained using the following relation.

$$\in_{\mathbf{33}} = \boldsymbol{v_f} \in_{\mathbf{33}}^{\boldsymbol{f}} + \boldsymbol{v_m} \in_{\mathbf{33}}^{\boldsymbol{m}} + \boldsymbol{e_{31}^{f}} \boldsymbol{v_f} \boldsymbol{v_m} \Big/ \left(\boldsymbol{v_m} \boldsymbol{C_{11}^{f}} + \boldsymbol{v_f} \boldsymbol{C_{11}^{m}} \right) \qquad (5.8)$$

The constructional feature of the vertically aligned **1–3 PZC** can be such that the piezoelectric fibers are coplanar with the vertical ***xz***– or ***yz***–plane, making an angle $\boldsymbol{\Psi}$ with ***z***–axis. Based on the law of transformation, the constitutive relations for such **1–3 PZC** can be given by:

$$\{\boldsymbol{\sigma}\,\} = \left[\widehat{\boldsymbol{C}}\,\right]\{\boldsymbol{\varepsilon}\,\} - \{\widehat{\boldsymbol{e}}\,\}\boldsymbol{E_3} \qquad (5.9)$$

where $\left[\widehat{\boldsymbol{C}}\,\right]$ and $\{\widehat{\boldsymbol{e}}\,\}$ are the respective effective stiffness and piezoelectric constant matrices; $\{\widehat{\boldsymbol{\varepsilon}}\,\}$ is the dielectric constant matrix obtained after applying the transformation law and is given by:

$$\left[\widehat{\boldsymbol{C}}\,\right] = [\boldsymbol{T}]^{T}[\boldsymbol{C}][\boldsymbol{T}]\,, \quad \{\widehat{\boldsymbol{e}}\,\} = [\boldsymbol{T}]^{T}\{\boldsymbol{e}\}[\boldsymbol{R}] \quad \text{and}$$

$$\{\widehat{\boldsymbol{\varepsilon}}\,\} = [\boldsymbol{R}]^{-\mathbf{1}}\{\boldsymbol{\varepsilon}\}[\boldsymbol{R}] \qquad (5.10)$$

In above equation (Eq. 5.10), **[*T*]** and **[*R*]** are the transformation matrices, when the fibers are placed in the ***xz***–plane, which are given by:

$$[\boldsymbol{T}]^{-1} = \begin{bmatrix} \boldsymbol{m^2} & 0 & \boldsymbol{n^2} & 0 & -\boldsymbol{mn} & 0 \\ 0 & 1 & 0 & 0 & 0 & 0 \\ \boldsymbol{n^2} & 0 & \boldsymbol{m^2} & 0 & \boldsymbol{mn} & 0 \\ 0 & 0 & 0 & \boldsymbol{m} & 0 & \boldsymbol{n} \\ \boldsymbol{2mn} & 0 & -\boldsymbol{2mn} & 0 & \boldsymbol{m^2-n^2} & 0 \\ 0 & 0 & 0 & -\boldsymbol{n} & 0 & \boldsymbol{m} \end{bmatrix},$$

$$[\boldsymbol{R}] = \begin{bmatrix} \boldsymbol{m} & 0 & \boldsymbol{n} \\ 0 & 1 & 0 \\ -\boldsymbol{n} & 0 & \boldsymbol{m} \end{bmatrix} \tag{5.11}$$

whereas when the fibers are placed in the ***yz***–plane, the transformation matrices are given by:

$$[\boldsymbol{T}]^{-1} = \begin{bmatrix} 1 & 0 & 0 & 0 & 0 & 0 \\ 0 & \boldsymbol{m^2} & \boldsymbol{n^2} & -\boldsymbol{mn} & 0 & 0 \\ 0 & \boldsymbol{n^2} & \boldsymbol{m^2} & \boldsymbol{mn} & 0 & 0 \\ 0 & \boldsymbol{2mn} & -\boldsymbol{2mn} & \boldsymbol{m^2-n^2} & 0 & 0 \\ 0 & 0 & 0 & 0 & \boldsymbol{m} & -\boldsymbol{n} \\ 0 & 0 & 0 & 0 & \boldsymbol{n} & \boldsymbol{m} \end{bmatrix}$$

$$[\boldsymbol{R}] = \begin{bmatrix} 1 & 0 & 0 \\ 0 & \boldsymbol{m} & \boldsymbol{n} \\ 0 & -\boldsymbol{n} & \boldsymbol{m} \end{bmatrix} \tag{5.12}$$

where $\boldsymbol{m = cos\theta}$ and $\boldsymbol{n = sin\theta}$.

Utilizing effective electromechanical properties of **1–3 PZC**, we will discuss the **FE** model in the damping analysis of **HFRC** plates in the next section.

5.3 Theoretical FE Formulation

To investigate the performance of **CC** laminated **HFRC** plates integrated with **ACLD** patches, the boundary condition of the laminated smart plate is changed to **CC**. This section presents the **FE** model similar to the one presented in Chapter 4. Figure 5.3(a-b) shows the vibrating elements and arrangement of **ACLD** patches on the tail of an aircraft. Figure 5.3(c) depicts a systematic representation of square **HFRC** laminae with two rectangular patches of **ACLD** at the top surface to achieve the active damping. The thickness of **HFRC** substrate is $\boldsymbol{h}$, and it includes $\boldsymbol{N}$ numbers of lamina of equal thickness. The **ACLD** treatment patch is composed of a constrained viscoelastic layer and a constraining layer of

1–3 PZC with vertically/obliquely aligned fibers of thickness $\boldsymbol{h_v}$ and $\boldsymbol{h_p}$, respectively. Considering the cartesian coordinate system (***x-y-z***), the mid-plane of the substrate is taken as a reference, such that: $\boldsymbol{x} = 0$, $\boldsymbol{a}$ and $\boldsymbol{y} = 0$, $\boldsymbol{b}$, representing the dimensions of the substrate composite plate. The **1–3 PZC** layer consists of fibers oriented vertically/obliquely (Fig. 5.1a) or coplanar with vertical ***xz***– and ***yz***–plane (Fig. 5.2a-b), making an angle $\boldsymbol{\Psi}$ with the ***z***–axis. The layer numbers ***N+1*** and ***N+2*** represent the viscoelastic layer and the **1–3 PZC** layer, respectively.

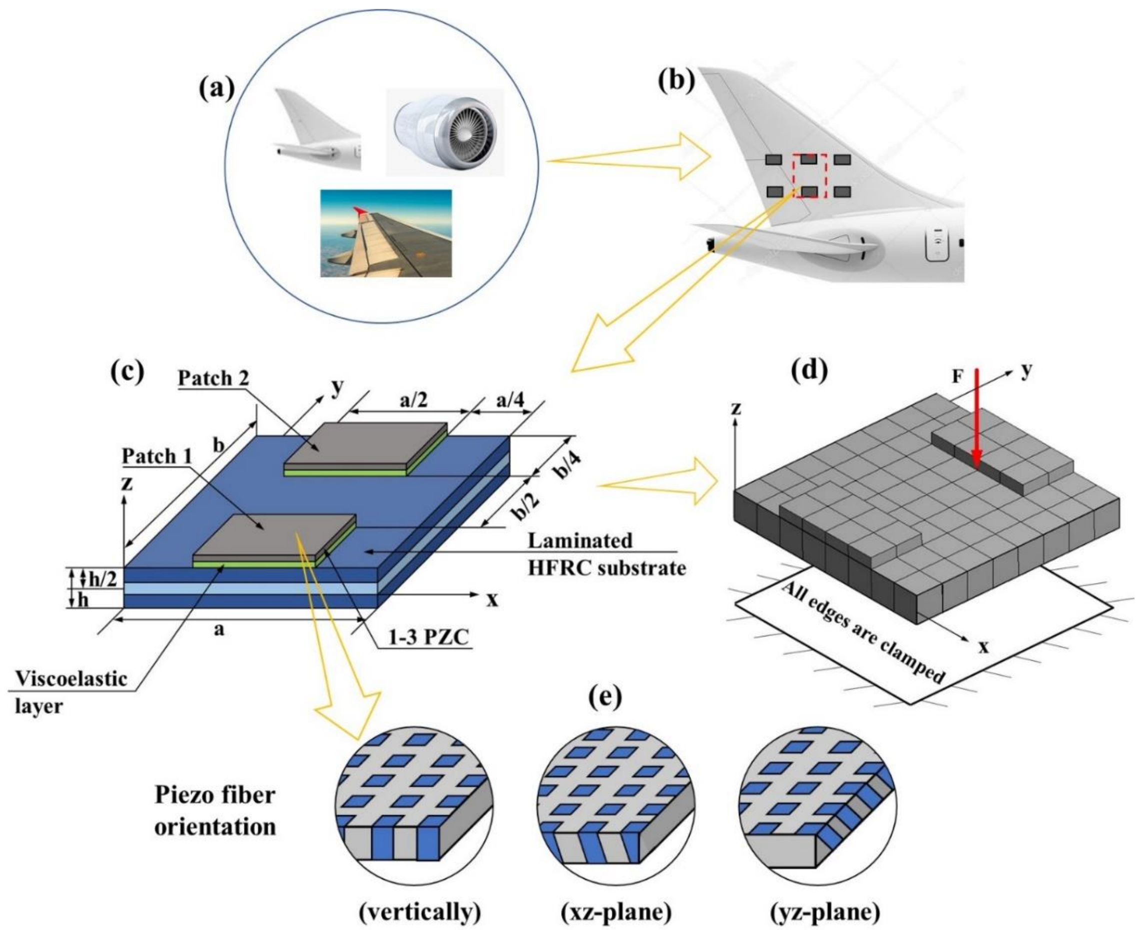

Figure 5.3. (a) Vibrating members of an aircraft, (b) arrangement of multi-patches of **ACLD** on the tail of an aircraft, (c) schematic of layered **HFRC** substrate plate attached with **ACLD** treatment constraining layer of **1–3 PZC** patches, (d) 8-noded mesh model of **HFRC** smart plate, and (e) piezo-fiber orientations in different planes.

5.3.1 Displacement Fields

The notations representing the lateral dimensions of the laminated **HFRC** smart plate integrated with the **ACLD** patches are like those mentioned in Chapter 4. The kinematics of deformations of the overall substrate **HFRC** plate/**ACLD** system are displayed in Fig. 5.4. The axial displacement fields satisfying the continuity conditions between the adjacent layers of the smart **HFRC** plate are similar to the Eqs. (4.1)–(4.3). As presented in the previous analysis, the generalized displacement variables are separated into the translational $\{\boldsymbol{d_t}\}$ and the rotational $\{\boldsymbol{d_r}\}$ variables which are represented by Eq. (4.4). While the state of strains and the state of stresses at any point in the **HFRC** plate are described by Eqs. (4.5)–(4.6) and (4.11), respectively. The generalized strain vectors $\{\boldsymbol{\epsilon_{bt}}\}$, $\{\boldsymbol{\epsilon_{st}}\}$, $\{\boldsymbol{\epsilon_{br}}\}$ and $\{\boldsymbol{\epsilon_{sr}}\}$ are also defined in the same manner as given by Eqs. (4.8)–(4.9). Also, for the overall laminated **HFRC** smart plate, the various matrices $[\boldsymbol{Z_1}]$, $[\boldsymbol{Z_2}]$, $[\boldsymbol{Z_3}]$, $[\boldsymbol{Z_4}]$, $[\boldsymbol{Z_5}]$ and $[\boldsymbol{Z_6}]$ appearing in Eqs. (4.6) and (4.7) are identical to those presented in Chapter 4.

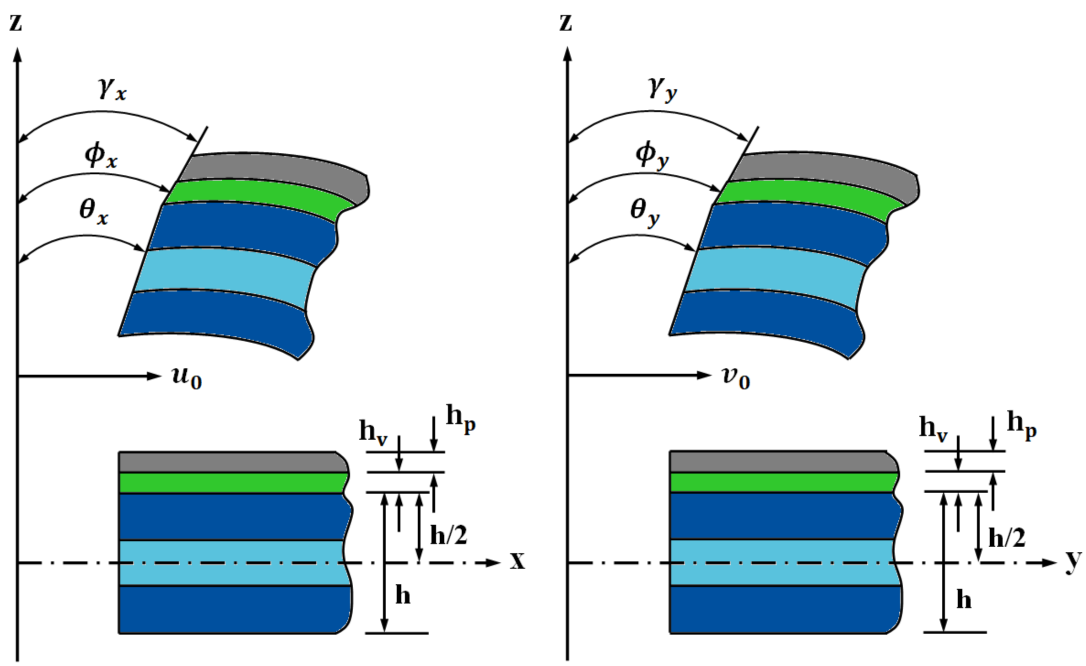

Figure 5.4. Kinematics of deformation of the plate.

5.3.2 Constitutive Relations

The constitutive relations for the laminated **HFRC** substrate plate are given by Eq. (4.11). The constraining **1–3 PZC** layer is also considered to be subjected to the electric field along the direction only. Hence, the constitutive relations for the constraining vertically/obliquely reinforced **1-3 PZC** layer of the **ACLD** treatment (Ray and Pradhan, 2007) used here are also expressed by Eqs. (4.12). The constrained layer of the **ACLD** treatment is made of an isotropic linear viscoelastic material and the stress vector for this layer is also represented by Eq. (4.15). Since the state of stress and the state of strains are considered in the same manner as in the case of the laminated composite plate studied in Chapter 4, the statement of virtual work principle for this smart laminated **HFRC** plate is also expressed by Eq. (4.16).

5.3.3 FE Formulation

The smart sandwich plate has been discretized by using the eight noded isoparametric serendipity quadrilateral elements as shown in Fig. 4.2(b). As a result, description of the generalized displacement variables at any point in the element in terms of the nodal generalized displacement degrees of freedom can be expressed by Eq. (4.18). Also, the expressions for the generalized strain vectors at any point within the element can be expressed in terms of the nodal generalized displacements degrees of freedoms by using Eq. (4.20). Considering a thin piezoelectric actuator sheet with constant thickness, the applied electric field can be taken as $\boldsymbol{E_z = -V/h_p}$, with $\boldsymbol{V}$ is the voltage applied along the thickness of **1–3 PZC** layer (Baz and Ro, 1995b). The open-loop equations of motion of an element attached with the **ACLD** treatment are given by Eqs. (4.22) and (4.23). For the estimation of the open-loop global equation of motion, the rotary inertia of **FE** elements can be ignored since the **HFRC** substrate plate is thin. Finally, the open-loop global equation of motion of the overall plate/**ACLD** system can be obtained by assembling the elemental equations of motion, as follows:

$$[\boldsymbol{M}]\{\ddot{\boldsymbol{X}}\} + [\boldsymbol{K_{tt}}]\{\boldsymbol{X}\} + [\boldsymbol{K_{tr}}]\{\boldsymbol{X_r}\} = \sum_{\boldsymbol{j=1}}^{\boldsymbol{q}} \{\boldsymbol{F_{tp}^j}\}\boldsymbol{V^j} + \{\boldsymbol{F}\} \qquad (5.13)$$

$$[\boldsymbol{K_{rt}}]\{\boldsymbol{X}\} + [\boldsymbol{K_{rr}}]\{\boldsymbol{X_r}\} = \sum_{j=1}^{q} \{\boldsymbol{F_{rp}^j}\}\boldsymbol{V^j} \tag{5.14}$$

in which $[\boldsymbol{M}]$ represents the global mass matrix; $[\boldsymbol{K_{tt}}]$, $[\boldsymbol{K_{tr}}]$, $[\boldsymbol{K_{rt}}]$ and $[\boldsymbol{K_{rr}}]$ represent the global stiffness matrices; $\{\boldsymbol{X_r}\}$ and $\{\boldsymbol{X}\}$ denote the global nodal rotational and translational degrees of freedom (**DOF**); $\{\boldsymbol{F}\}$ represents the global nodal force vector; $\{\boldsymbol{F_{tp}}\}$ and $\{\boldsymbol{F_{rp}}\}$ denote global electro-elastic coupling matrices with respect to $\boldsymbol{j^{th}}$ patch; and $\boldsymbol{q}$ and $\boldsymbol{V^j}$ denote the number of patches and the voltage supplied to these patches, respectively.

5.4 Closed-Loop Model

In the active control strategy, a simple velocity feedback control law can be used to activate the **ACLD** patches. Accordingly, the control voltage applied across the active layer is given by (Beheshti-Aval and Lezgy-Nazargah, 2010):

$$\boldsymbol{V^j} = -\boldsymbol{k_d^j}\dot{\boldsymbol{w}} = -\boldsymbol{k_d^j}[\boldsymbol{U_t^j}]\{\dot{\boldsymbol{X}}\} - \boldsymbol{k_d^j}(\boldsymbol{h}/\boldsymbol{2})[\boldsymbol{U_r^j}]\{\dot{\boldsymbol{X}}_r\} \tag{5.15}$$

in which $\boldsymbol{k_d^j}$ represents the control gain for the $\boldsymbol{j^{th}}$ patch, $[\boldsymbol{U_t^j}]$ and $[\boldsymbol{U_r^j}]$ denote the unit vectors to express the transverse velocity of the point with respect to the differentiation of the global nodal generalized displacements. The final equation of motion evaluating the closed-loop dynamics of the **HFRC** plates/**ACLD** system is obtained by substituting Eq. (4.15) into Eqs. (4.13) and (4.14), as follows:

$$[\boldsymbol{M}]\{\ddot{\boldsymbol{X}}\} + [\boldsymbol{K_{tt}}]\{\boldsymbol{X}\} + [\boldsymbol{K_{tr}}]\{\boldsymbol{X_r}\} + \sum_{j=1}^{q} \boldsymbol{k_d^j}\{\boldsymbol{F_{tp}^j}\}\{\boldsymbol{U_t^j}\}\{\dot{\boldsymbol{X}}\}$$

$$+ \sum_{j=1}^{q} \boldsymbol{k_d^j}(\boldsymbol{h}/\boldsymbol{2})\{\boldsymbol{F_{tp}^j}\}\{\boldsymbol{U_r^j}\}\{\dot{\boldsymbol{X}}_r\} = \{\boldsymbol{F}\} \tag{5.16}$$

and

$$[\boldsymbol{K_{rt}}]\{\boldsymbol{X}\} + [\boldsymbol{K_{rr}}]\{\boldsymbol{X_r}\} + \sum_{j=1}^{q} \boldsymbol{k_d^j}\{\boldsymbol{F_{rp}^j}\}\{\boldsymbol{U_t^j}\}\{\dot{\boldsymbol{X}}\} +$$

$$\sum_{j=1}^{q} \boldsymbol{k}_{\boldsymbol{d}}^{\boldsymbol{j}}\,(\boldsymbol{h}/2)\{\boldsymbol{F}_{\boldsymbol{rp}}^{\boldsymbol{j}}\}\{\boldsymbol{U}_{\boldsymbol{r}}^{\boldsymbol{j}}\}\{\dot{\boldsymbol{X}}_{\boldsymbol{r}}\} = 0 \tag{5.17}$$

5.5 Results and Discussion

In this section, we present the numerical results evaluated using the layer-wise **FSDT** to study the performance of multiscale **HFRC** smart plates. Here, we considered symmetric ($0°/90°/0°$), anti-symmetric cross-ply ($0°/90°/0°/90°$), and anti-symmetric angle-ply ($-45°/45°/-45°/45°$) laminated **HFRC** substrate plates integrated with two **ACLD** patches. To study the damping performance of **HFRC** plates, the volume fractions (unless specified) of carbon fiber, straight **CNTs**, and wavy **CNTs** are taken as 0.3, 0.1, and 0.1243, respectively. The results of laminated base composite plates are compared with the **HFRC** plates by keeping the constant carbon fiber volume fraction (i.e., $\boldsymbol{v_{CF}} = 0.3$). The **CNT** waves are considered coplanar with the **1–2** and **1–3** planes. The geometrical dimensions of base/multiscale **HFRC** substrates are taken as follows: thickness (***h***) = 0.003 $\boldsymbol{m}$ and aspect ratio (***a/h***) = 100. The material properties of base composite and **HFRC** plates with $\boldsymbol{v_{CF}} = 0.3$ are summarized in Table 5.1. The thickness of **1–3 PZC** composed of **PZT 5H**/epoxy composite is taken as $\boldsymbol{h_p} = 250\ \boldsymbol{\mu m}$ and material properties of **PZC** with 60% fiber (**PZT-5H**) and 40% matrix volume fractions are summarized in Table 5.2.

Table 5.1. Effective elastic properties of the base composite and **HFRC** with $\boldsymbol{v_{CF}} = 0.3$.

Elastic constant	C_{11} *(GPa)*	C_{12} *(GPa)*	C_{13} *(GPa)*	C_{22} *(GPa)*	C_{33} *(GPa)*	C_{44} *(GPa)*	C_{55} *(GPa)*	ρ (kg/m^3)
Base composite ($\boldsymbol{v_{CNT}} = 0$)	75.75	3.92	3.92	7.32	7.32	1.63	1.34	1385
HFRC ($\boldsymbol{v_{CNT}} = 0.1$)	119.87	4.69	4.38	8.67	8.67	1.98	1.81	1400
HFRC (**1–2** plane, $\boldsymbol{v_{CNT}} = 0.1243$)	70.01	26.87	4.64	25.58	9.05	10.40	2.14	1403.645

HFRC (**1–3** plane, $v_{CNT} =$ 0.1243)	70.01	4.91	26.61	9.07	25.42	1.93	24.41	1403.645

Table 5.2. Material properties of **PZC**.

Material	C_{11} *(GPa)*	C_{13} *(GPa)*	C_{33} *(GPa)*	C_{44} *(GPa)*	e_{31} $(C\ m^{-2})$	e_{33} $(C\ m^{-2})$	ρ (kg/m^3)
1-3 **PZC**	9.293	6.182	35.444	1.536	–0.19	18.41	5090
PZT-5H (Ray and Pradhan, 2007)	151	96	124	23	–5.1	27	7750
Epoxy (Ray and Pradhan, 2007)	5.3	3.1	5.3	0.9	-	-	1100

The viscoelastic layer material was chosen as **ISD112** with thickness (h_v), density, Poisson's ratio, and complex shear modulus as 51 μm, 1140 kg/m^3, 0.49, and $20(1+\mathbf{i})\ MN\ m^{-2}$, respectively (Chantalakhana and Stanway, 2001). To verify the accuracy of the **FE** model derived in Section 5.3, the natural frequencies for the first mode of substrate plates integrated with **ACLD** treatment are compared with the results presented by Sahoo and Ray (2019b) for the identical composite plates. Table 5.3 shows a good agreement with the available results (Sahoo and Ray, 2019b), which validates the **FE** model in the current work.

Table 5.3. Natural frequencies (ω) of laminated substrate plates integrated with **ACLD** treatment patches.

Substrate laminates	1st mode	
	Present	Source (Sahoo and Ray, 2019b)

$0°/90°/0°$	338	340
$0°/90°/0°/90°$	337	339
$-45°/45°/-45°/45°$	316	317

The effect of **CNT** waves on the laminated **HFRC** plates in attenuating the amplitudes of vibration is investigated and compared with the base composite plates in terms of frequency response functions (**FRFs**). In this context, Eqs. (5.16) and (5.17) were utilized with time-harmonic point force of 1 $\boldsymbol{N}$ subjected at a junction $(\boldsymbol{a}/2, \boldsymbol{b}/4, \boldsymbol{h}/2)$ to excite the fundamental mode of vibration of the plates. Figure 5.5 demonstrates the effect of **CNT** waviness on the **FRF** of **CC** $0°/90°/0°$ ply **HFRC** plate. It can be seen that the laminated **HFRC** plate with **CNT** waves coplanar with **1–3** plane significantly attenuates the amplitudes of vibration compared to the other cases of laminated plates (with or without **CNTs**). This is attributed to the enhanced transverse stiffness of the multiscale **HFRC** substrate due to the waviness of **CNT** in the **1–3** plane. Thus, the energy dissipation capability of the multiscale **HFRC** plate is high, and it significantly attenuates the transverse vibrations. For the multiscale **HFRC** plate with wavy CNTs coplanar with **1–3** plane, the amplitudes are suppressed by $\sim 93\%$ and ~ 77 % corresponding to the value of gain $\boldsymbol{k_d} = 600$ as compared to the amplitudes of base composite and **HFRC** with straight **CNTs**. Further analysis is carried out for $0°/90°/0°/90°$ and $-45°/45°/-45°/45°$ ply plates. Figs. 5.6 and 5.7 show that the **HFRC** plates with **CNT** waves coplanar with the **1–3** plane have better vibration attenuating capability compared to the other cases. However, Fig. 5.7 shows that $-45°/45°/-45°/45°$ ply plates have lower amplitudes of deflection when **CNT** waviness is coplanar with **1–2** plane. This is attributed to the fact that for $-45°/45°/-45°/45°$, ply plate the carbon fiber and CNTs are oriented in the **1**–direction. Therefore, $-45°/45°/-45°/45°$ ply **HFRC** plate shows enhanced stiffness and natural frequencies when **CNT** waviness is coplanar with **1–2** plane compared to other composite plates. Figures. 5.5–5.7 implies that the three cases of plies of **HFRC** plate show higher vibration attenuation capability for the first mode due to the incorporation of wavy **CNTs** compared to base composite plates. It is clear that the **HFRC** plates with **CNT** waves coplanar in the mutually orthogonal planes have better damping characteristics due to the higher transverse stiffness offered by the **HFRC**. Therefore, only **HFRC** plates are considered in the next section to study the effect of orientation of piezo-fiber on the plates' damping performance.

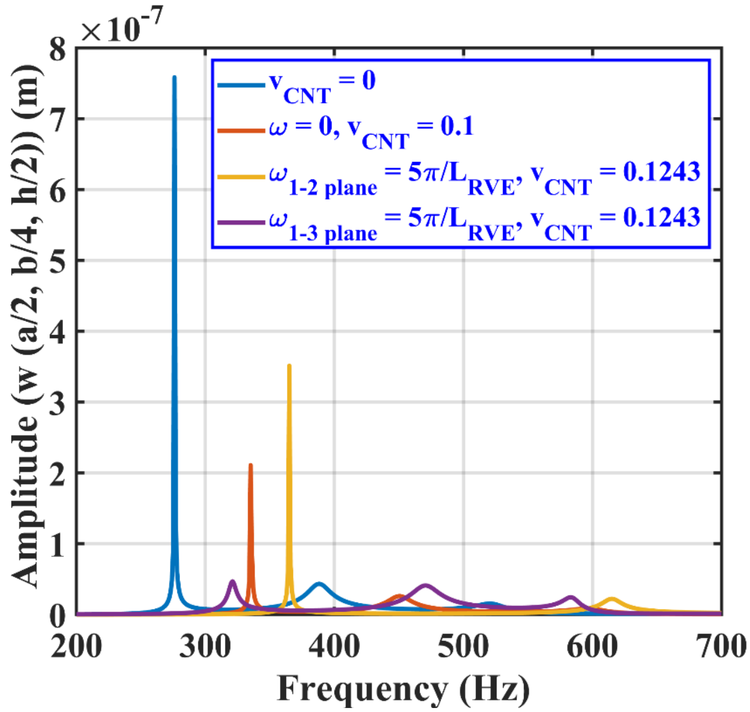

Figure 5.5. Frequency response of symmetric cross-ply **HFRC** and base composite plates when $\boldsymbol{k_d}$ = 600.

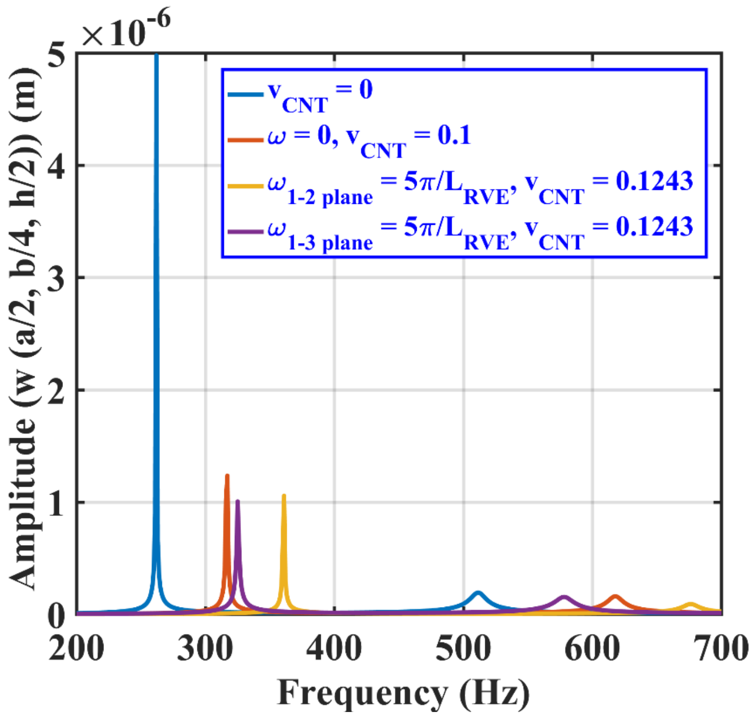

Figure 5.6. Frequency response of anti-symmetric cross-ply **HFRC** and base composite plates when $\boldsymbol{k_d}$ = 600.

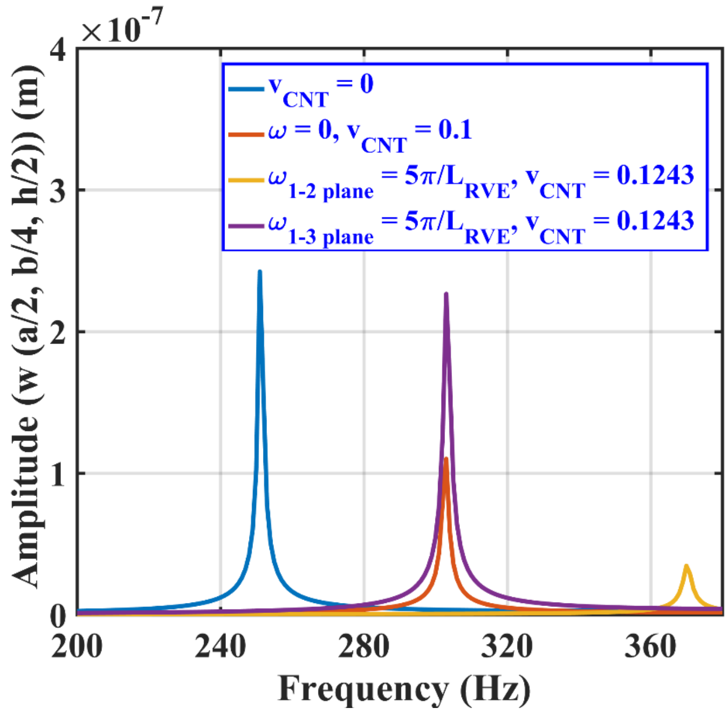

Figure 5.7. Frequency response of anti-symmetric angle-ply **HFRC** and base composite plates when $\boldsymbol{k_d}$ = 600.

We further explored the effect of piezo-fiber orientation angle ($\boldsymbol{\Psi}$) on the damping performance of multiscale **HFRC** plates. In this context, the value of $\boldsymbol{\Psi}$ was chosen such that it varies from 0 to 45° in two mutually orthogonal vertical ***xz***- and ***yz***-planes. However, for the sake of simplicity, the **FRF** corresponding to the values of $\boldsymbol{\Psi} = 0, 15, 30,$ and 45° is presented to demonstrate the effectiveness of **ACLD** treatment. Figures 5.8–5.13 illustrate the effect of piezo-fiber angle in the ***xz***- and ***yz***-planes on the frequency response of various ply configurations of laminated **HFRC** plates. Unless otherwise mentioned, the value of $\boldsymbol{k_d}$ was taken as 600 to investigate the active performance of multiscale **HFRC** plates for the various piezo-fiber orientation angles. Figures 5.8 and 5.9 illustrates the active performance of **CC** $0°/90°/0°$ HFRC plate when the **CNT** waves are coplanar with the **1–3** plane. It can be observed that the piezo-fiber orientation angle affects the damping behavior of laminated **HFRC** plates. The control authority of **ACLD** patches is maximum: (i) at $\boldsymbol{\Psi}$ = 30° when piezo-fibers are coplanar with the ***xz***-plane and (ii) at $\boldsymbol{\Psi}$ = 15° when the piezo-fibers are coplanar with the ***yz***-plane. Note that the higher attenuation was achieved when the piezo-fibers were coplanar with the ***yz***-plane, which was attributed to the configuration of **ACLD** treatment patches. Along the ***x***-axis, the patches are in a parallel configuration, whereas the patches are in a series combination along the ***y***-direction. Thus, we can obtain a combined effect of both configurations when the piezo-fibers are coplanar with the ***yz***-plane. Similar results are obtained for $0°/90°/0°/90°$ and $-45°/45°/-45°/45°$ **HFRC** plates, as shown in Figs 5.10-5.13. For $0°/90°/0°/90°$ **HFRC** plate, the results are evaluated when the **CNT** waviness is coplanar with the **1–3** plane. Whereas, in the case of $-45°/45°/-45°/45°$ **HFRC** plate, the results are evaluated when the CNT waviness is coplanar with the **1–2** plane. Figures 5.10–5.13 show that the maximum attenuation of vibration of plates is achieved when the piezo-fibers are oriented at $\boldsymbol{\Psi}$ = 30°.

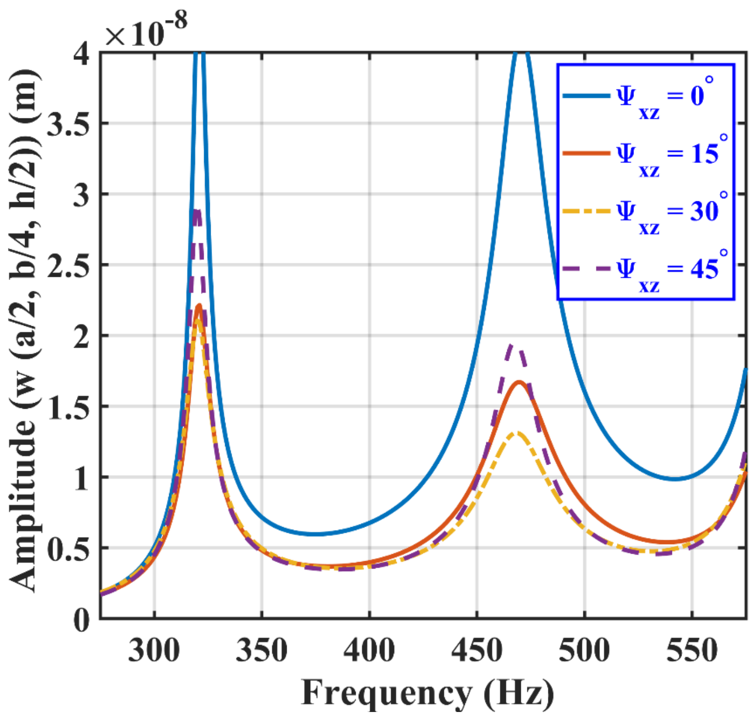

Figure 5.8. Effect of piezo-fiber orientation ($\boldsymbol{\Psi}$) in the ***xz***-plane on the frequency response of symmetric cross-ply **HFRC** plates when $\boldsymbol{k_d}$ = 600.

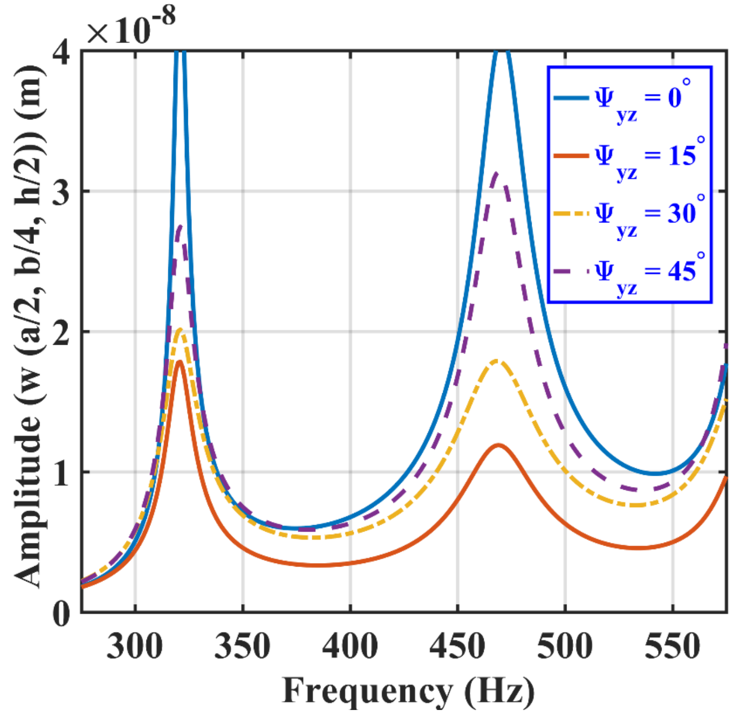

Figure 5.9. Effect of piezo-fiber orientation ($\boldsymbol{\Psi}$) in the ***yz***-plane on the frequency response of symmetric cross-ply **HFRC** plates when $\boldsymbol{k_d}$ = 600.

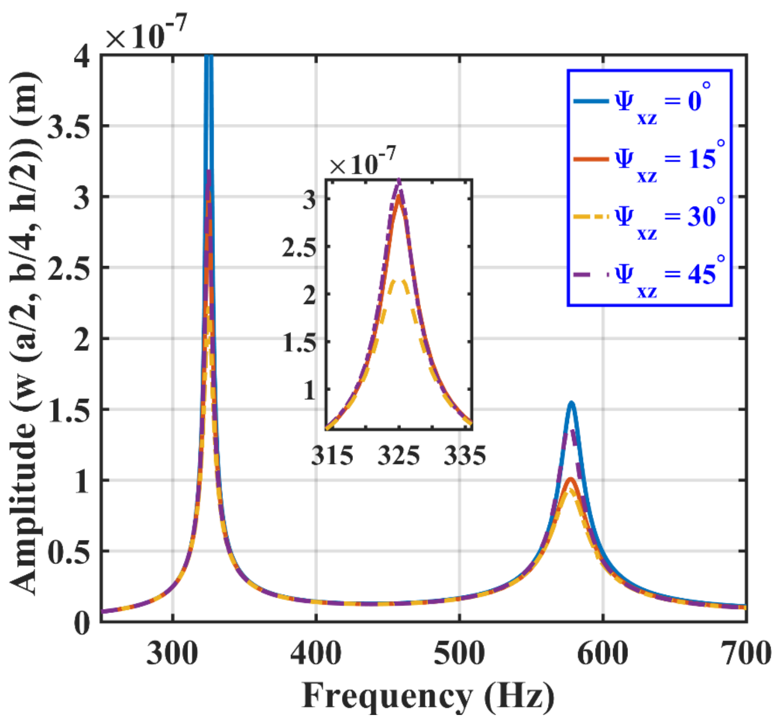

Figure 5.10. Effect of piezo-fiber orientation ($\boldsymbol{\Psi}$) in the ***xz***-plane on the frequency response of anti-symmetric cross-ply **HFRC** plates when $\boldsymbol{k_d}$ = 600.

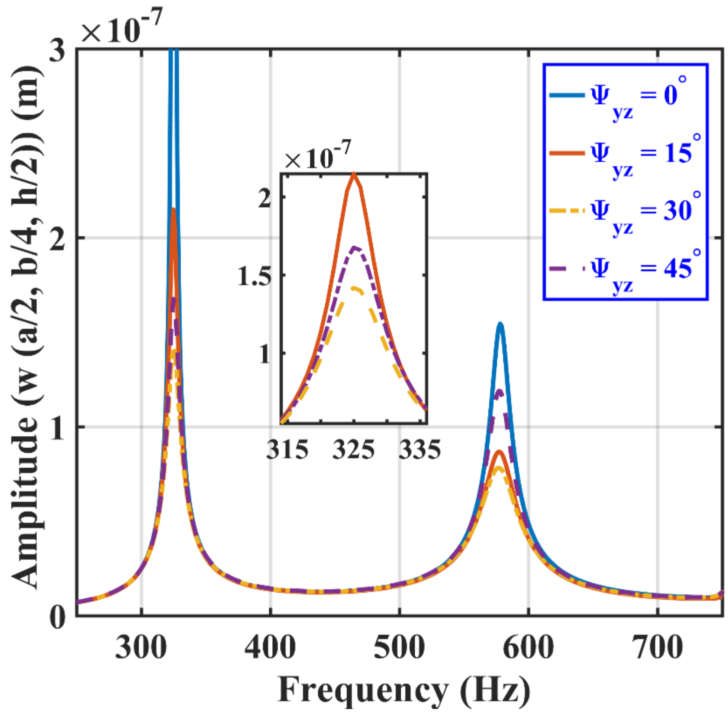

Figure 5.11. Effect of piezo-fiber orientation ($\boldsymbol{\Psi}$) in the ***yz***-plane on the frequency response of anti-symmetric cross-ply **HFRC** plates when $\boldsymbol{k_d}$ = 600.

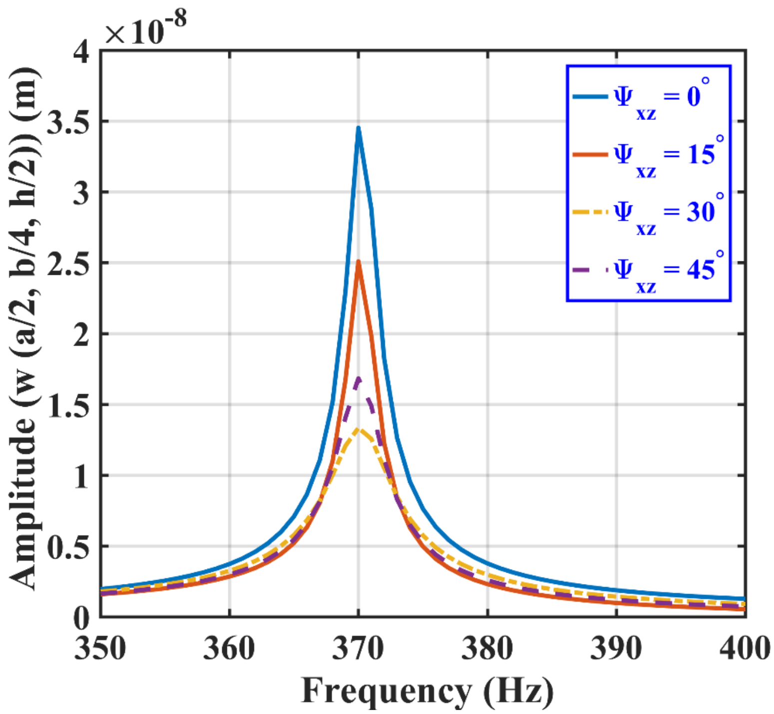

Figure 5.12. Effect of piezo-fiber orientation ($\boldsymbol{\Psi}$) in the ***xz***-plane on the frequency response of anti-symmetric angle-ply **HFRC** plates when $\boldsymbol{k_d}$ = 600.

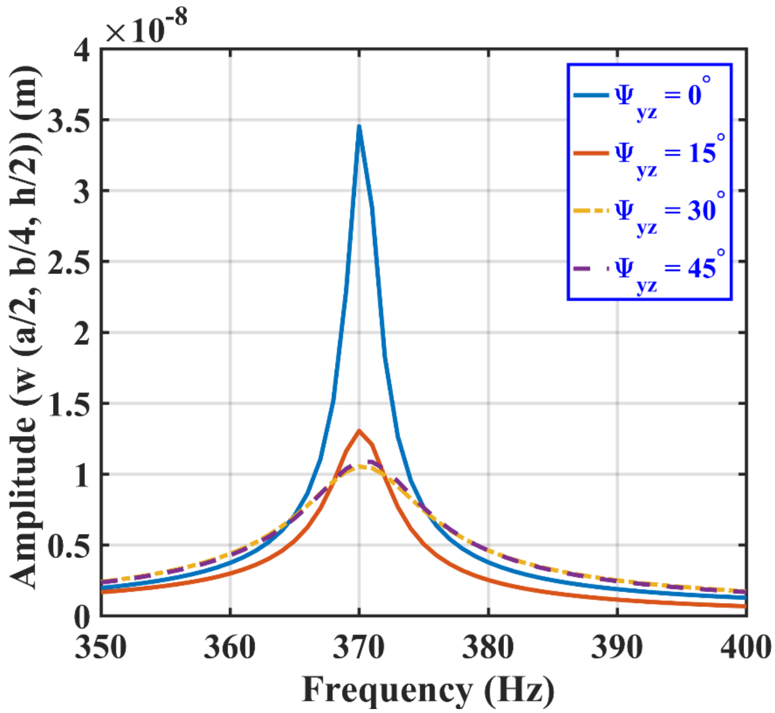

Figure 5.13. Effect of piezo-fiber orientation ($\boldsymbol{\Psi}$) in the $\boldsymbol{yz}$-plane on the frequency response of anti-symmetric angle-ply **HFRC** plates when $\boldsymbol{k_d}$ = 600.

Next, the effect of **1–3 PZC** layer thickness on the controlling ability of **ACLD** treatment is investigated. The thickness of **1–3 PZC** layer varied from 150 $\boldsymbol{\mu m}$ to 450 $\boldsymbol{\mu m}$ under the constant gain, $\boldsymbol{k_d}$ = 600. The outcomes are illustrated in Figs 5.14 and 5.15, which shows that a better performance can be achieved with a thinner **1–3 PZC** layer for $0°/90°/0°$ **HFRC** plate. This is attributed to the fact that the electric field intensity increases for the constant voltage difference when the thickness of **1–3 PZC** decreases. Similar results are obtained for $0°/90°/0°/90°$ and $-45°/45°/-45°/45°$ plies **HFRC** plates, but they are not presented here for the sake of brevity.

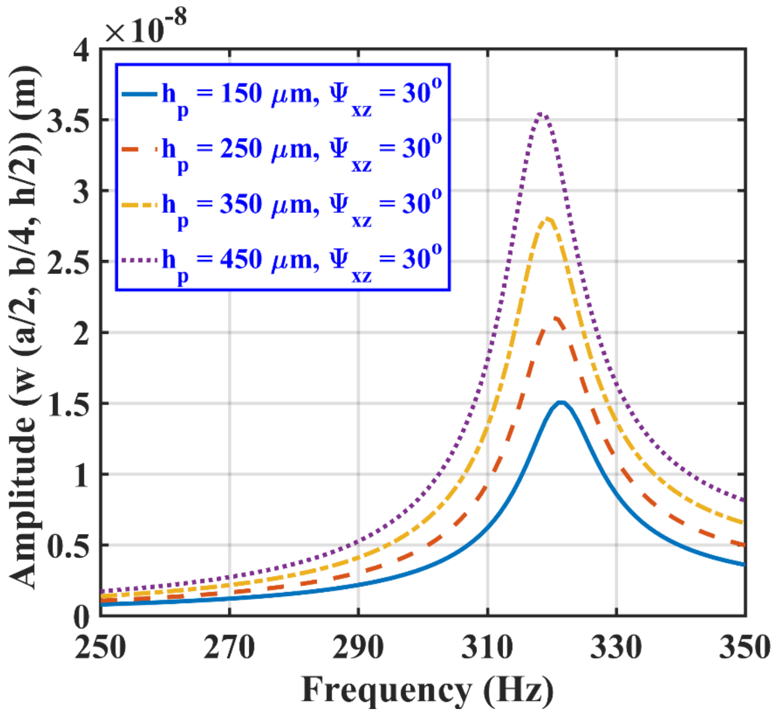

Figure 5.14. Effect of **1–3 PZC** layer thickness on the **FRF** of symmetric cross-ply **HFRC** plates when piezo-fibers are coplanar with the ***xz***-plane.

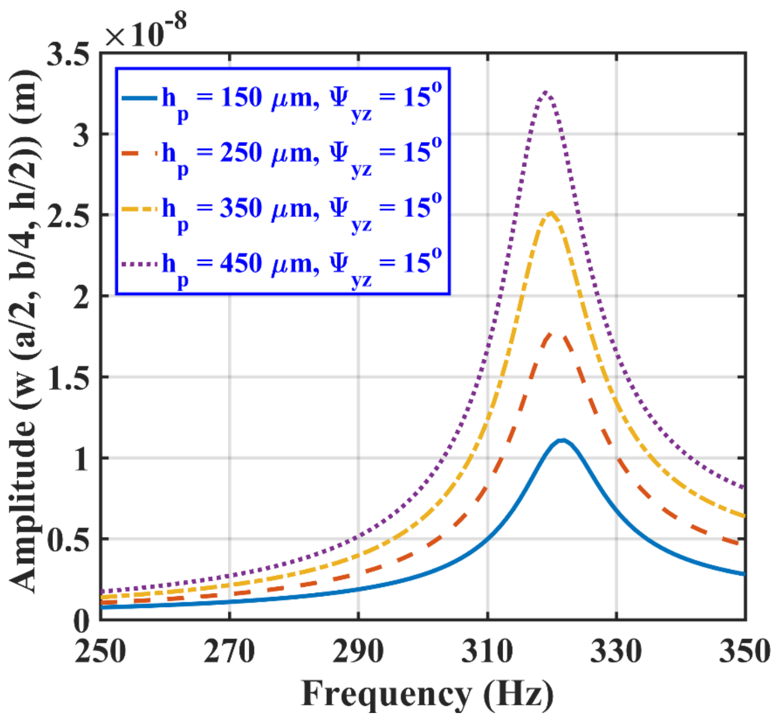

Figure 5.15. Effect of **1–3 PZC** layer thickness on the **FRF** of symmetric cross-ply **HFRC** plates when piezo-fibers are coplanar with the ***yz***-plane.

4. Summary

In this article, we studied the effects of **CNT** waviness on the dynamic response of a laminated **HFRC** smart plate integrated with two **ACLD** patches at the upper surface of the **HFRC** substrate plate. The integrated **ACLD** patches are composed of a viscoelastic layer and a tailor-made constraining **1–3 PZC** layer. Based on the layer-wise **FSDT**, we derived a **FE** model to investigate the active damping performance of laminated **HFRC** plates subjected to **CC** boundary conditions. A simple closed-loop model is used to introduce active damping. The performance of multiscale **HFRC** with wavy **CNT** is compared with the base composite. We observed that, due to the enhanced transverse effective elastic coefficient, the ability of **HFRC** plates to attenuate the transverse vibrations is significantly improved. We also investigated the effect of the piezo-fiber alignment angle on the effectiveness of **ACLD** patches and found that oblique **1–3 PZC** have a maximum control authority. Our investigation reveals that the maximum damping is achieved when the piezo-fibers are coplanar with ***yz***-plane $(\boldsymbol{\Psi}_{\boldsymbol{yz}})$, due to the combination of **ACLD** patches in ***y***-direction. In the parametric analysis, we observed that the **1–3 PZC** is more sensitive for the thinner layer. This is because the electric field intensity increases for the constant voltage difference as the thickness of the **1–3 PZC** layer decreases. Based on the following observation, we can conclude that the wavy **CNTs** can be utilized in conventional composite structures to improve their damping characteristics. Such multiscale composites can be used in the vibrating members of an aircraft, submarine, and missiles along with the combination of **ACLD** patches to actively control the mechanical vibrations. Such smart composites can reduce fatigue and improve the life of the system.

Chapter 6

Active Vibration Damping of a Clamped-Free Smart Multiscale Hybrid Fiber Reinforced Composite Shells Using 1–3 Piezoelectric Composites

This chapter (Gupta *et al.*, 2022d) *deals with the linear vibrations of doubly curved laminated hybrid fiber reinforced composite (**HFRC**) shells integrated with active constrained layer damping (**ACLD**) treatment installed at the upper circumference of the substrate shell. **HFRC** is a novel composite where the carbon nanotubes (**CNT**s) which are either straight or wavy are uniformly distributed along with carbon fiber reinforcements. A three-dimensional finite element (**FE**) model of doubly curved smart **HFRC** shells integrated with **ACLD** patches has been developed to investigate the performance of these patches for controlling the vibrations of these shells. The **FE** model is based on the sinusoidal shear deformation theory incorporating the Murakami's zig-zag function (**SinusZZ** theory), to encounter the inherent zig-zag effects. Emphasis has also been placed on investigating the effect of piezoelectric fiber orientation angle on the frequency response of **HFRC** shells. Also, the research carried out in this chapter brings to light that even the wavy **CNT**s can be properly utilized for attaining structural benefits from the exceptional elastic properties of **CNT**s.*

6.1 Introduction

The laminated composite structures are the fundamental building blocks extensively used in almost all engineering applications due to their remarkable mechanical properties, lightweight, and high performance. These multilayered structures consist of relatively thin layers of different material compositions that may influence the different degrees of axial compliance. As a result, the axial displacement of anisotropic structures varies nonlinearly along the thickness of the structure, which causes discontinuous derivatives between the interface of two individual layers. This change in slope between two adjacent layers is known as the zig-zag (**ZZ**) effect. The low values of the transverse to in-plane modulus led to a higher transverse shear, resulting in the **ZZ** effect that must be accounted for. The shear response of laminated composite structures has been considered accurately by theories like the first-order shear deformation theory (**FSDT**), the higher-order shear deformation theory (**HSDT**), and mixed variational theories (Reddy and Phan, 1985; Narita, *et al.*, 1993; Eisenberger, *et al.*, 1995; Norouzzadeh, *et al.*, 2021). However, these theories do not account for the **ZZ** effects. Hence, efforts have been made in this framework to refine these theories by considering the **ZZ** effects to study the behavior of laminated structures more accurately. The resulting theories are often termed zig-zag theories (**ZZTs**). There are three common **ZZTs**, namely, the Lekhnitskii multilayered theory, the Ambartsumian multilayered theory, and the Reissner multilayered theory (**RMT**); with the **RMT** being the most natural and powerful method to study laminated structures (Carrera, 2003). Based on the **RMT**, Di Sciuva (1985) and Murakami (1986) made early efforts to employ **ZZ**-like displacement fields that satisfy a priori transverse shear stress and displacement continuity conditions at the layer interfaces while keeping the number of kinematic variables independent of the number of layers. In addition, the **ZZ** function vanishes at the top and bottom surfaces of the plate, and the full shear-stress continuity across the depth of the multilayered plate is not required. Carrera (2004) effectively employed Murakami's zig-zag function (**MZZF**) in studying the behavior of laminated shells both statically and dynamically. Using a novel piecewise linear **ZZ** function, Tessler *et al.* (2009) presented a refined theory for laminated composite and sandwich beams based on the kinematics of the Timoshenko beam theory derived from the virtual work principle. Sedira *et al.* (2012) employed **MZZF** and investigated the static response of laminated composite plates by developing a **FE** model using the **FSDT**. Most recently, Khan and Suresh (2021a) investigated the active control response of the smart shell embedded with **ACLD** patches using the **FSDT**, employing **MZZF** to account for the **ZZ** effects. Their findings reveal that the modified **FSDT** shows higher vibration suppression due to the incorporation of **ZZ** effects.

The literature review suggests the importance of the **ZZ** effects. The existing well-known **FSDT** effectively considers the shear response of laminated composites. However, it fails to account for the inherent **ZZ** effects. Additionally, the **FSDT** considers the linear distribution of transverse shear stress that does not satisfy the condition of zero shear stress at the top and bottom surface of the laminated structures. Thus, an attempt has been made in the present work to develop a **FE** model based on the **SinusZZ** theory, which is a combination of the sinusoidal shear deformation (**Sinus**) theory and **MZZF** accounting for the inherent **ZZ** effects induced in laminated structures. The proposed **SinusZZ** theory overcomes these drawbacks of the **FSDT**, thus improving the accuracy of the outcomes. The existing literature also lacks to provide the dynamic analysis of multiscale hybrid composites. This work focuses on the investigation of active damping response of the multiscale **HFRC** smart shells using the **FE** model based on the **SinusZZ** theory. To the best of the present authors' knowledge, there does not exist a single study in the literature that investigates the active damping response of the laminated multiscale **HFRC** smart shell using the **SinusZZ** theory. This is the motivation behind the present work, which aims to develop an advanced laminated multiscale smart shell capable of actively suppressing mechanically induced vibrations. The multiscale **HFRC** shell is composed of nanoscale **CNT** nanofillers and microscale carbon fibers used as reinforcement materials. In the matrix phase, the reinforcement materials are considered to be uniformly distributed along the ***x***-axis. Our outcomes reveal that the multiscale **HFRC** possesses better damping characteristics due to the incorporation of **CNTs**. We also investigated the effects of **CNT** waviness and piezo-fiber orientation on the damping characteristics of laminated multiscale **HFRC** shell and the control authority of **ACLD** treatment patches, respectively. Our observation suggests that **CNT** waviness and piezo-fiber orientation greatly influence both the damping characteristics of laminated multiscale **HFRC** shell and the control authority of **ACLD** treatment patches, respectively. Additionally, the frequency response of the laminated multiscale **HFRC** shell is compared with the base composite for symmetric/anti-symmetric cross-ply and anti-symmetric angle-ply.

6.2 Mathematical Modeling

Figure 6.1 demonstrates the lamination scheme and displacement field configuration for various theories. It can be seen that the displacement and rotation variables are not layer-independent in the thickness direction in case of classical laminate theory (**CLT**) and **FSDT**. Thus, **MZZF** can be introduced to obtain the discontinuous slopes corresponding to the layer interface. Moreover, the **SinusZZ** theory considers the sinusoidal distribution of the displacement field for the individual layer of the laminate along its thickness direction. Thus, shear lag correction factor is not required. This also ensures that better accuracy can be achieved with the implementation of the **SinusZZ** theory.

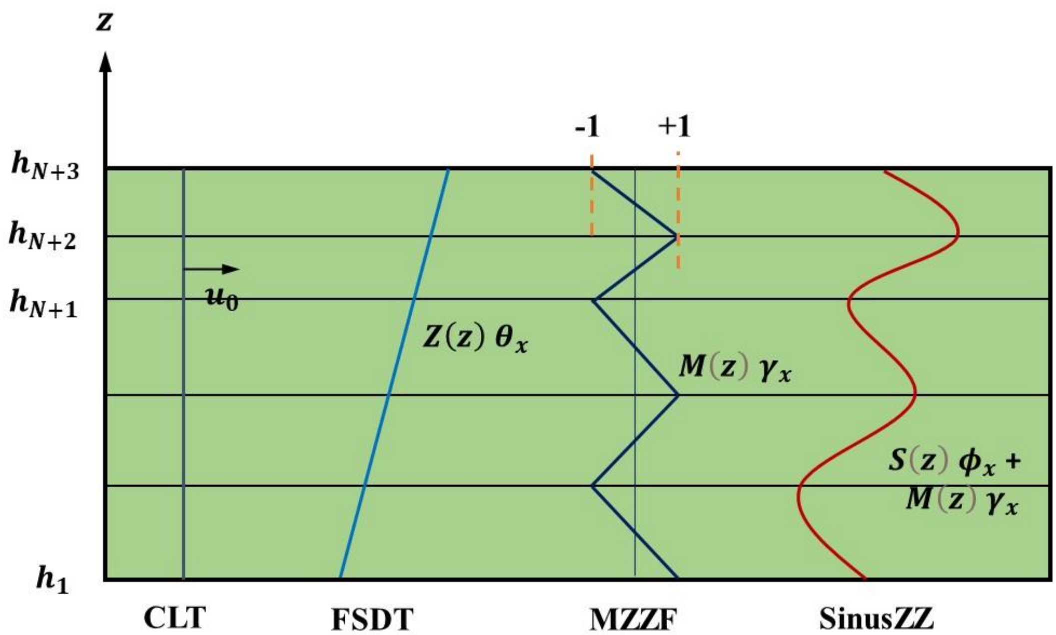

Figure 6.1. Scheme of the expansions involved in the displacement field.

Figure 6.2 illustrates the schematics representation and the cross-sections of the laminated multiscale **HFRC** shell with two **ACLD** treatment patches installed at its top circumferential surface. The laminated multiscale **HFRC** shell comprises N numbers of the unidirectional lamina of equal thickness that are assumed to be perfectly bonded. The cantilever multiscale **HFRC** shell has a length, thickness, and radius of a, h, and R, respectively. The **ACLD** treatment layer is composed of a viscoelastic layer and a constraining layer of **1–3** piezoelectric composite **(PZC)**, having a thickness of h_v and h_p, respectively. The **1–3 PZC** is a tailored-made smart material with piezoelectric fibers oriented vertically or obliquely in the ***xz***-plane and the ***yz***-plane, making an angle $\boldsymbol{\Psi}$ with the ***z***-axis, as shown in Fig. 6.3. The reference plane of the overall **HFRC**/**ACLD** shell system is considered to be the mid-plane of the substrate **HFRC** shell, such that the origin of the coordinate system ($\boldsymbol{x}$, $\boldsymbol{y}$, $\boldsymbol{z}$) is located on the mid-plane of the substrate **HFRC** shell, with $\boldsymbol{x} = 0$ and $\boldsymbol{x} = \boldsymbol{a}$ representing the boundaries of the cantilever multiscale **HFRC** shell. The thickness coordinates ($\boldsymbol{z}$) of the top and bottom surfaces of any ($\boldsymbol{k^{th}}$) layer of the overall multiscale **HFRC** shell are given by $\boldsymbol{z_{k+1}}$ and $\boldsymbol{z_k}(\boldsymbol{k} = 1,2,3,\ldots,\boldsymbol{N} + \mathbf{2})$, respectively, while $\boldsymbol{h_k}$ is the thickness of the $\boldsymbol{k^{th}}$ layer. According to Murakami's **ZZ** theory, the **MZZF** $\boldsymbol{M(z)}$ is the function of the individual layer corresponding to the mid-plane. It is represented by a non-denationalized layer coordinate, $\boldsymbol{\zeta_k}$, which can be expressed as (Carrera, 2004):

$$\boldsymbol{M}(\boldsymbol{z}) = (-\mathbf{1})^{\boldsymbol{k}}\boldsymbol{\zeta_k}, \qquad \boldsymbol{\zeta_k} = \frac{\mathbf{2}}{\boldsymbol{h_k}}\left(\boldsymbol{z} - \frac{\mathbf{1}}{\mathbf{2}}(\boldsymbol{z_k} + \boldsymbol{z_{k+1}})\right) \tag{6.1}$$

where $\boldsymbol{M(z)}$ is a piece-wise linear function of the layer coordinates $\boldsymbol{z_k}$. The $\boldsymbol{M(z)}$ has a unit amplitude ($\pm$) for the $\boldsymbol{k^{th}}$ layer with $\boldsymbol{\zeta_k}$ limiting $-1 \leq \boldsymbol{\zeta_k} \leq 1$. The slope of $\boldsymbol{M'}(\boldsymbol{z})$ assumes the opposite sign between two adjacent layers.

In this article, we present the **SinusZZ** theory, which is the **Sinus** theory incorporating the **MZZF**. The sinusoidal function $\boldsymbol{S(z)}$ is given by (Thai and Kim, 2013):

$$\boldsymbol{S}(\boldsymbol{z}) = \frac{\boldsymbol{\pi}}{\boldsymbol{h}}\boldsymbol{sin}\left(\frac{\boldsymbol{\pi z}}{\boldsymbol{h}}\right) \tag{6.2}$$

where the slope of $\boldsymbol{S'}(\boldsymbol{z}) = \boldsymbol{cos}\left(\frac{\boldsymbol{\pi z}}{\boldsymbol{h}}\right)$. The **SinusZZ** theory includes the sinusoidal function and **MZZF** in the displacement field equations in the ***x***-direction and the ***y***-direction, respectively. While the displacement field equation in the ***z***-direction is of a higher order in the thickness coordinate. The advantages of the sinusoidal functions over polynomial functions are that they are simple and accurate. Also, it guarantees zero transverse shear stress conditions at the top and bottom surfaces of the shell.

A mixed piecewise displacement field theory is considered for the overall **HFRC**/**ACLD** shell system investigation. The kinematics of axial deformations accounting for the **SinusZZ** is demonstrated in Fig. 6.4 (a). $\boldsymbol{u_0}$ and $\boldsymbol{v_0}$ are the generalized axial displacements of a point ($\boldsymbol{x}$, $\boldsymbol{y}$) on the reference plane ($\boldsymbol{z} = 0$) of the substrate **HFRC** shell along the $\boldsymbol{x}$-axis and $\boldsymbol{y}$-axis, respectively. $\boldsymbol{\theta_x}$ and $\boldsymbol{\theta_y}$ are the generalized rotations of the normals to the middle planes of the overall **HFRC** shell. $\boldsymbol{\phi_x}, \boldsymbol{\phi_y}$ and $\boldsymbol{\gamma_x}, \boldsymbol{\gamma_y}$ are the unknown displacement variables associated with the sinusoidal functions and **MZZF** in the $\boldsymbol{x}$-direction and the $\boldsymbol{y}$-direction, respectively. With the help of the kinematic of deformations presented in Fig. 6.4 (a), the axial displacement at any point in the overall **HFRC**/**ACLD** shell system can be expressed as (Neves *et al.*, 2017):

$$\boldsymbol{u}(\boldsymbol{x},\boldsymbol{y},\boldsymbol{z},\boldsymbol{t}) = \boldsymbol{u_0}(\boldsymbol{x},\boldsymbol{y},\boldsymbol{t}) + \boldsymbol{Z}(\boldsymbol{z})\boldsymbol{\theta_x}(\boldsymbol{x},\boldsymbol{y},\boldsymbol{t}) + \boldsymbol{S}(\boldsymbol{z})\boldsymbol{\phi_x}(\boldsymbol{x},\boldsymbol{y},\boldsymbol{t}) + \boldsymbol{M}(\boldsymbol{z})\boldsymbol{\gamma_x}(\boldsymbol{x},\boldsymbol{y},\boldsymbol{t}) \quad (6.3)$$

$$\boldsymbol{v}(\boldsymbol{x},\boldsymbol{y},\boldsymbol{z},\boldsymbol{t}) = \boldsymbol{v_0}(\boldsymbol{x},\boldsymbol{y},\boldsymbol{t}) + \boldsymbol{Z}(\boldsymbol{z})\boldsymbol{\theta_y}(\boldsymbol{x},\boldsymbol{y},\boldsymbol{t}) + \boldsymbol{S}(\boldsymbol{z})\boldsymbol{\phi_y}(\boldsymbol{x},\boldsymbol{y},\boldsymbol{t}) + \boldsymbol{M}(\boldsymbol{z})\boldsymbol{\gamma_y}(\boldsymbol{x},\boldsymbol{y},\boldsymbol{t}) \quad (6.4)$$

where $\boldsymbol{Z}(\boldsymbol{z}) = (\boldsymbol{z_c} + \boldsymbol{z_v} + \boldsymbol{z_p})$,

$$\boldsymbol{z_c} = \boldsymbol{z}, \boldsymbol{z_v} = \boldsymbol{z_p} = 0 \qquad \textit{for } \boldsymbol{k = N+1},$$

$$\boldsymbol{z_c} = \frac{\boldsymbol{h}}{2}, \boldsymbol{z_v} = \left(\boldsymbol{z} - \frac{\boldsymbol{h}}{\boldsymbol{2}}\right), \boldsymbol{z_p} = 0 \qquad \textit{for } \boldsymbol{k = N+2},$$

$$\boldsymbol{z_c} = \frac{\boldsymbol{h}}{2}, \boldsymbol{z_v} = \boldsymbol{h_v}, \boldsymbol{z_p} = \left(\boldsymbol{z} - \frac{\boldsymbol{h}}{2} - \boldsymbol{h_v}\right) \qquad \textit{for } \boldsymbol{k = N+3}$$

The transverse actuation of the constraining layer of **ACLD** patches may influence the flexural vibration of the plate. Thus, for the modeling of active damping of smart plates, the transverse normal strain must be considered. To avoid Poisson's locking phenomenon, one can consider the higher-order transverse displacement field to achieve a parabolic distribution of the transverse shear stress, which can be expressed as:

$$\boldsymbol{w}(\boldsymbol{x},\boldsymbol{y},\boldsymbol{z},\boldsymbol{t}) = \boldsymbol{w_0}(\boldsymbol{x},\boldsymbol{y},\boldsymbol{t}) + \boldsymbol{z}\boldsymbol{\theta_z}(\boldsymbol{x},\boldsymbol{y},\boldsymbol{t}) + \boldsymbol{z^2}\boldsymbol{\phi_z}(\boldsymbol{x},\boldsymbol{y},\boldsymbol{t}) \quad (6.5)$$

where $\boldsymbol{w_0}$ is the transverse displacement at any point on the reference plane ($\boldsymbol{z} = 0$) of the substrate **HFRC** shell; $\boldsymbol{\theta_z}$ and $\boldsymbol{\phi_z}$ are the generalized rotations with the mid-plane of the **HFRC** shell; $\boldsymbol{z}$ and $\boldsymbol{z^2}$ are the first and second-order gradient, respectively, of the transverse displacement of the overall **HFRC**/**ACLD** shell system with respect to the thickness of the z-coordinate.

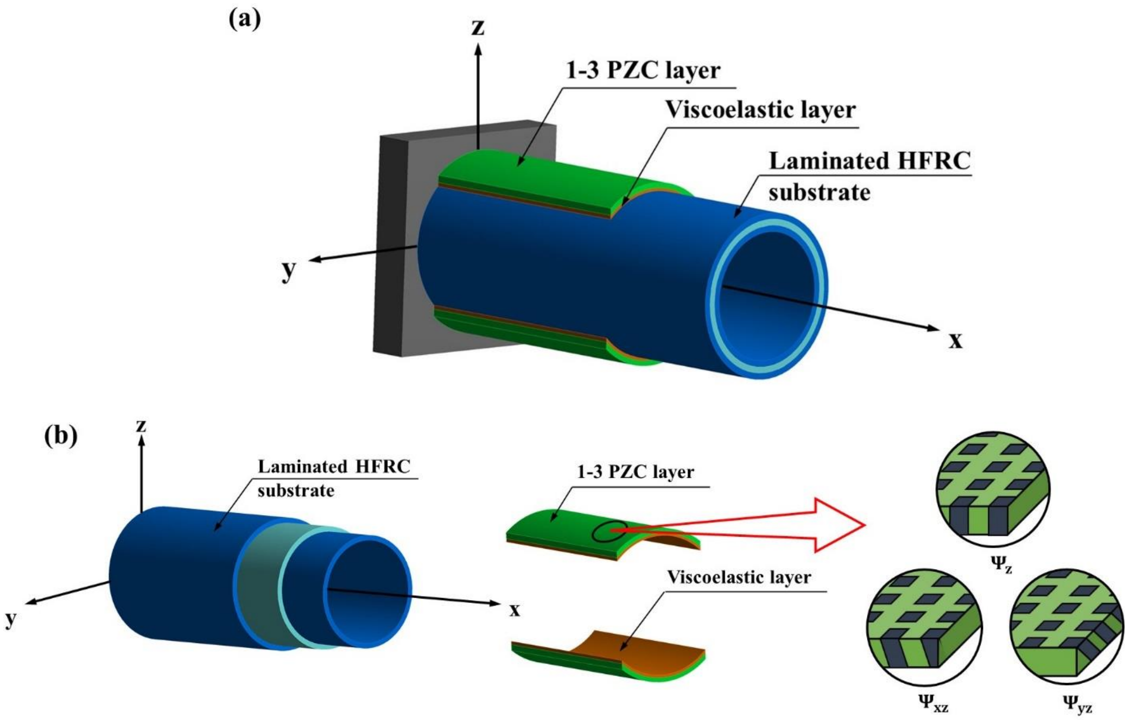

Figure 6.2. (a) Schematic of layered **HFRC** substrate shell attached with **ACLD** treatment constraining layer of **1–3 PZC** patches, (b) individual phases of laminated **HFRC** smart shell.

For the sake of simplicity, the generalized displacement variables are categorized as translational $\{\boldsymbol{d_t}\}$ and rotational $\{\boldsymbol{d_r}\}$ component vectors:

$$\{\boldsymbol{d_t}\} = [\boldsymbol{u_0} \;\; \boldsymbol{v_0} \;\; \boldsymbol{w_0}]^{\boldsymbol{T}}, \qquad \{\boldsymbol{d_r}\} = \left[\boldsymbol{\theta_x} \;\; \boldsymbol{\theta_y} \;\; \boldsymbol{\theta_z} \;\; \phi_{\boldsymbol{x}} \;\; \phi_{\boldsymbol{y}} \;\; \phi_{\boldsymbol{z}} \;\; \boldsymbol{\gamma_x} \;\; \boldsymbol{\gamma_y}\right]^{\boldsymbol{T}} \tag{6.6}$$

The strain vector $\{\boldsymbol{\epsilon}\}$ representing the state of strain at any point in the overall **HFRC** shell system can be classified into the in-plane shear strain $\{\boldsymbol{\epsilon_b}\}$ and transverse shear strain $\{\boldsymbol{\epsilon_s}\}$ vectors:

$$\{\boldsymbol{\epsilon_b}\} = \left[\boldsymbol{\epsilon_x} \;\; \boldsymbol{\epsilon_y} \;\; \boldsymbol{\epsilon_{xy}} \;\; \boldsymbol{\epsilon_z}\right]^{\boldsymbol{T}}, \;\; \{\boldsymbol{\epsilon_s}\} = \left[\boldsymbol{\epsilon_{xz}} \;\; \boldsymbol{\epsilon_{yz}}\right]^{\boldsymbol{T}} \tag{6.7}$$

where ϵ_x, ϵ_y, and ϵ_z are the normal strains along the x, y, and z-directions, respectively; ϵ_{xy} is the in-plane shear strain; ϵ_{xz} and ϵ_{yz} are the transverse shear strains. Using Eqs. (6.3)–(6.5) and (6.7), the vectors $\{\epsilon_b\}_c$, $\{\epsilon_b\}_v$, and $\{\epsilon_b\}_p$ define the in-plane and transverse normal strains, whereas the vectors $\{\epsilon_s\}_c$, $\{\epsilon_s\}_v$, and $\{\epsilon_s\}_p$ define the transverse shear strains for the substrate **HFRC** shell, the viscoelastic layer, and the **1–3 PZC** layer, respectively, as follows:

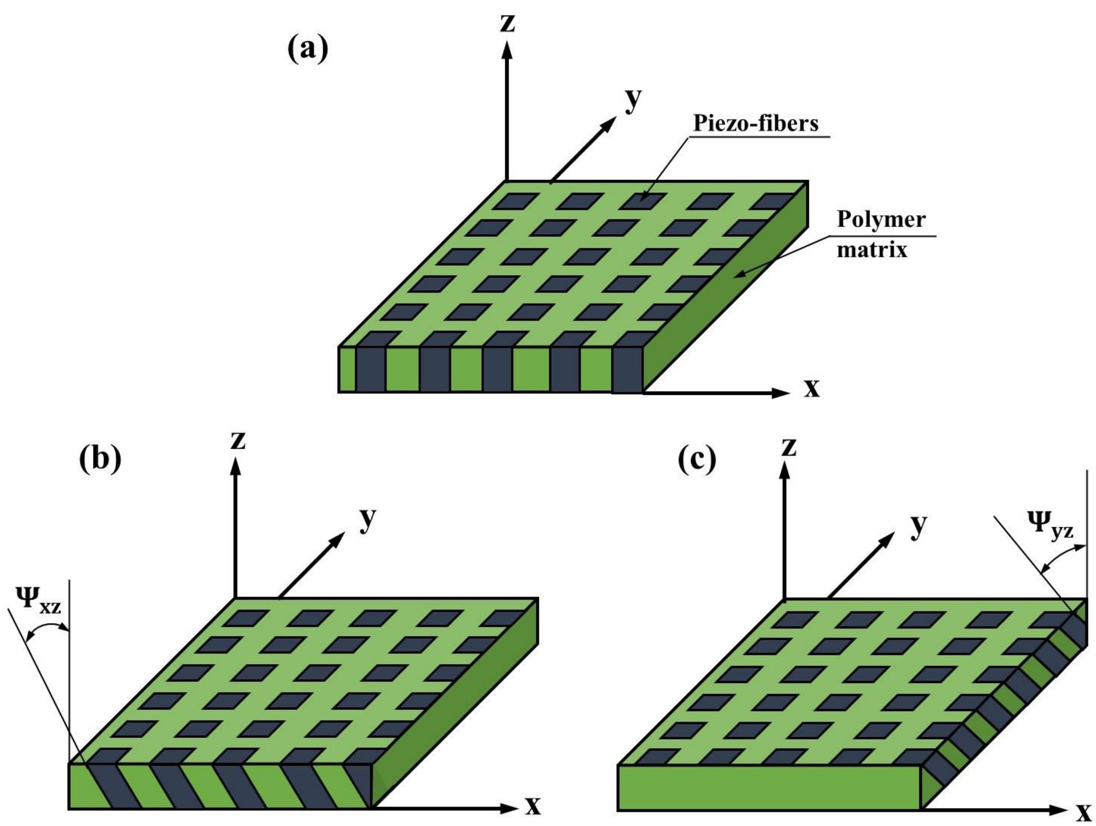

Figure 6.3. Schematic representation of **1–3 PZC** lamina with (a) vertically aligned piezo-fibers, (b) piezo-fibers coplanar in the ***xz***-plane, and (c) piezo-fibers coplanar in the ***yz***-plane.

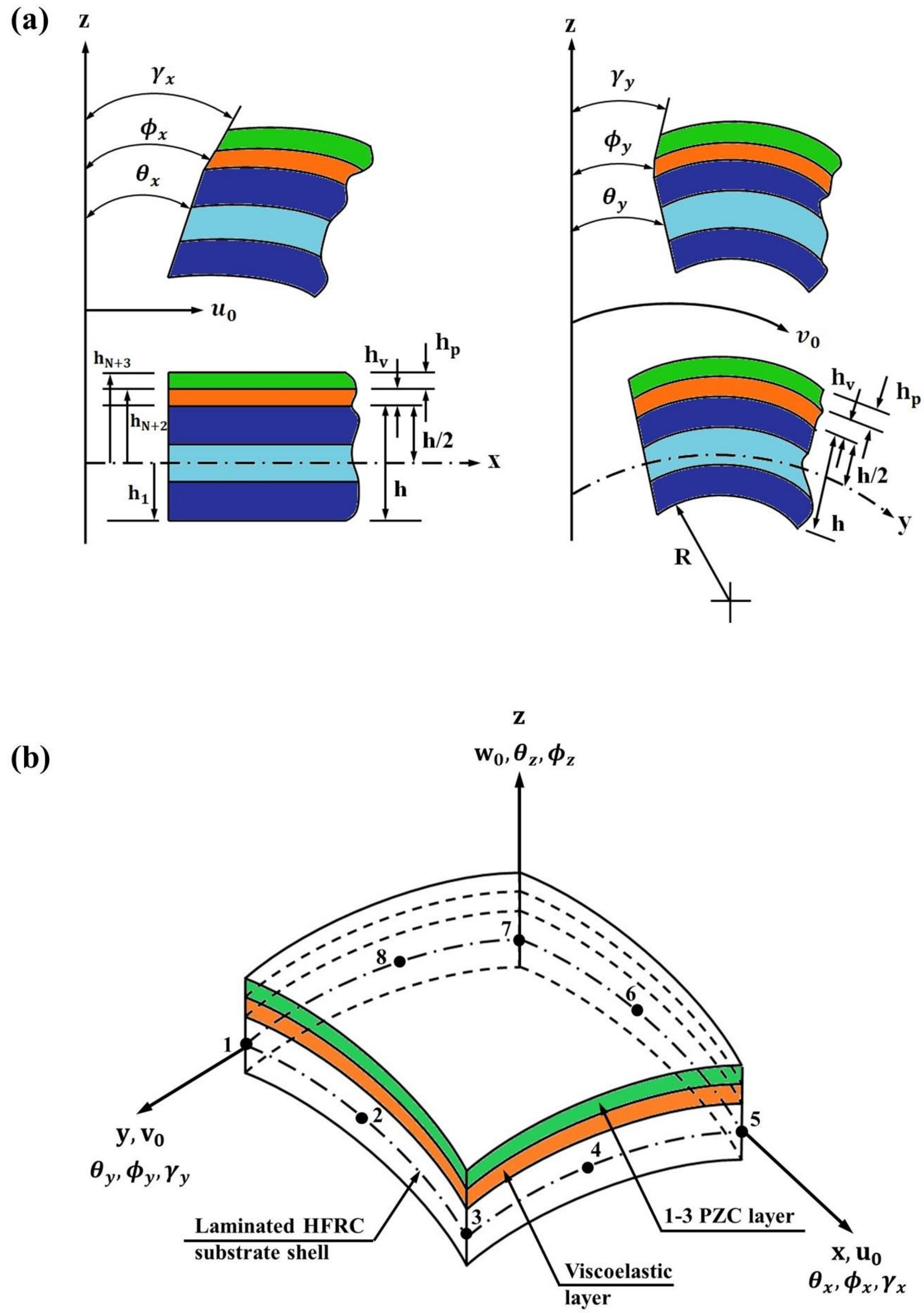

Figure 6.4. (a) Kinematics of deformation of the shell, (b) element topology and nodal degrees of freedom.

$$\{\boldsymbol{\epsilon_b}\}_c = \{\boldsymbol{\epsilon_{bt}}\} + [\boldsymbol{Z_1}]\{\boldsymbol{\epsilon_{br}}\}$$

$$\{\boldsymbol{\epsilon_b}\}_v = \{\boldsymbol{\epsilon_{bt}}\} + [\boldsymbol{Z_2}]\{\boldsymbol{\epsilon_{br}}\}$$

$$\{\boldsymbol{\epsilon_b}\}_p = \{\boldsymbol{\epsilon_{bt}}\} + [\boldsymbol{Z_3}]\{\boldsymbol{\epsilon_{br}}\}$$

$$\{\boldsymbol{\epsilon_s}\}_c = \{\boldsymbol{\epsilon_{st}}\} + [\boldsymbol{Z_4}]\{\boldsymbol{\epsilon_{sr}}\}$$

$$\{\boldsymbol{\epsilon_s}\}_v = \{\boldsymbol{\epsilon_{st}}\} + [\boldsymbol{Z_5}]\{\boldsymbol{\epsilon_{sr}}\}$$

$$\{\boldsymbol{\epsilon_s}\}_p = \{\boldsymbol{\epsilon_{st}}\} + [\boldsymbol{Z_6}]\{\boldsymbol{\epsilon_{sr}}\} \tag{6.8}$$

where $[\boldsymbol{Z_i}]$, (i = 1, 2, …, 6) are the generalized translational matrix appearing in Eq. (6.8) and are given by:

$$[\boldsymbol{Z_1}]_{\boldsymbol{k=1\ to\ N}} = \begin{bmatrix} \boldsymbol{z} & 0 & 0 & 0 & \boldsymbol{S_{z1}} & 0 & 0 & 0 & \boldsymbol{M_{z1}} & 0 & 0 \\ 0 & \boldsymbol{z} & 0 & \boldsymbol{z/R} & 0 & \boldsymbol{S_{z1}} & 0 & \boldsymbol{z^2/R} & 0 & \boldsymbol{M_{z1}} & 0 \\ 0 & 0 & \boldsymbol{z} & 0 & 0 & 0 & \boldsymbol{S_{z1}} & 0 & 0 & 0 & \boldsymbol{M_{z1}} \\ 0 & 0 & 0 & 1 & 0 & 0 & 0 & 2\boldsymbol{z} & 0 & 0 & 0 \end{bmatrix}$$

$$[\boldsymbol{Z_2}]_{\boldsymbol{k=N+1}} = \begin{bmatrix} \boldsymbol{z-h_{N+1}} & 0 & 0 & 0 & \boldsymbol{S_{z2}} & 0 & 0 & 0 & \boldsymbol{M_{z2}} & 0 & 0 \\ 0 & \boldsymbol{z-h_{N+1}} & 0 & \boldsymbol{z/R} & 0 & \boldsymbol{S_{z2}} & 0 & \boldsymbol{z^2/R} & 0 & \boldsymbol{M_{z2}} & 0 \\ 0 & 0 & \boldsymbol{z-h_{N+1}} & 0 & 0 & 0 & \boldsymbol{S_{z2}} & 0 & 0 & 0 & \boldsymbol{M_{z2}} \\ 0 & 0 & 0 & 1 & 0 & 0 & 0 & 2\boldsymbol{z} & 0 & 0 & 0 \end{bmatrix}$$

$$[\boldsymbol{Z_3}]_{\boldsymbol{k=N+2}} = \begin{bmatrix} \boldsymbol{z-h_{N+2}} & 0 & 0 & 0 & \boldsymbol{S_{z3}} & 0 & 0 & 0 & \boldsymbol{M_{z3}} & 0 & 0 \\ 0 & \boldsymbol{z-h_{N+2}} & 0 & \boldsymbol{z/R} & 0 & \boldsymbol{S_{z3}} & 0 & \boldsymbol{z^2/R} & 0 & \boldsymbol{M_{z3}} & 0 \\ 0 & 0 & \boldsymbol{z-h_{N+2}} & 0 & 0 & 0 & \boldsymbol{S_{z3}} & 0 & 0 & 0 & \boldsymbol{M_{z3}} \\ 0 & 0 & 0 & 1 & 0 & 0 & 0 & 2\boldsymbol{z} & 0 & 0 & 0 \end{bmatrix}$$

$$[\boldsymbol{Z_4}]_{\boldsymbol{k=1\ to\ N}} = \begin{bmatrix} 1 & 0 & \boldsymbol{S'_{z1}} & 0 & \boldsymbol{M'_{z1}} & 0 & \boldsymbol{z} & 0 & \boldsymbol{z^2} & 0 \\ 0 & 1-\boldsymbol{z/R} & 0 & \boldsymbol{S_{z1*}} & 0 & \boldsymbol{M_{z1*}} & 0 & \boldsymbol{z} & 0 & \boldsymbol{z^2} \end{bmatrix}$$

$$[\boldsymbol{Z_5}]_{\boldsymbol{k=N+1}} = \begin{bmatrix} 1 & 0 & \boldsymbol{S'_{z2}} & 0 & \boldsymbol{M'_{z2}} & 0 & \boldsymbol{z} & 0 & \boldsymbol{z^2} & 0 \\ 0 & 1-(\boldsymbol{z-h_{N+1}})/\boldsymbol{R} & 0 & \boldsymbol{S_{z2*}} & 0 & \boldsymbol{M_{z2*}} & 0 & \boldsymbol{z} & 0 & \boldsymbol{z^2} \end{bmatrix}$$

$$[\boldsymbol{Z_6}]_{\boldsymbol{k=N+2}} = \begin{bmatrix} 1 & 0 & \boldsymbol{S'_{z3}} & 0 & \boldsymbol{M'_{z3}} & 0 & \boldsymbol{z} & 0 & \boldsymbol{z^2} & 0 \\ 0 & 1-(\boldsymbol{z-h_{N+2}})/\boldsymbol{R} & 0 & \boldsymbol{S_{z3*}} & 0 & \boldsymbol{M_{z3*}} & 0 & \boldsymbol{z} & 0 & \boldsymbol{z^2} \end{bmatrix}$$

where

$$\boldsymbol{S_{z1\,(k=1\ to\ N)}} = \boldsymbol{S_{z2\,(k=N+1)}} = \boldsymbol{S_{z3\,(k=N+2)}} = \frac{\boldsymbol{\pi}}{\boldsymbol{h}}\boldsymbol{sin}\left(\frac{\boldsymbol{\pi z_k}}{\boldsymbol{h}}\right),$$

$$\boldsymbol{S'_{z1\,(k=1\;to\;N)}} = \boldsymbol{S'_{z2\,(k=\,N+1)}} = \boldsymbol{S'_{z1\,(k=N+2)}} = \boldsymbol{cos}\left(\frac{\boldsymbol{\pi z_k}}{\boldsymbol{h}}\right),$$

$$\boldsymbol{M_{z1\,(k=1\;to\;N)}} = \boldsymbol{M_{z2\,(k=N+1)}} = \boldsymbol{M_{z3\,(k=N+2)}} = (-1)^{\boldsymbol{k}}\,\boldsymbol{\zeta_k},$$

$$\boldsymbol{M'_{z1\,(k=1\;to\;N)}} = \boldsymbol{M'_{z2\,(k=\,N+1)}} = \boldsymbol{M'_{z1\,(k=N+2)}} = (-1)^{\boldsymbol{k}}\,\frac{2}{\boldsymbol{h_k}},$$

$$\boldsymbol{S_{z1*\,(k=1\;to\;N)}} = \boldsymbol{S_{z3*\,(k=N+1)}} = \boldsymbol{S_{z3*\,(k=N+2)}} = \boldsymbol{S'_{zi\,(k)}} - \frac{\boldsymbol{S_{zi\,(k)}}}{\boldsymbol{R}},$$

$$\boldsymbol{M_{z1*\,(k=1\;to\;N)}} = \boldsymbol{M_{z3*\,(k=N+1)}} = \boldsymbol{M_{z3*\,(k=N+2)}} = \boldsymbol{M'_{zi\,(k)}} - \frac{\boldsymbol{M_{zi\,(k)}}}{\boldsymbol{R}}$$

$$(\boldsymbol{i} = 1, 2, 3 \text{ and } \boldsymbol{k} = 1\ to\ \boldsymbol{N}, \boldsymbol{N+1}, \boldsymbol{N+2})$$

The generalized strain vectors $\{\boldsymbol{\epsilon_{bt}}\}, \{\boldsymbol{\epsilon_{st}}\}, \{\boldsymbol{\epsilon_{br}}\}$, and $\{\boldsymbol{\epsilon_{sr}}\}$ are given by:

$$\{\boldsymbol{\epsilon_{bt}}\} = \boldsymbol{\nabla_1}\{\boldsymbol{d_t}\}, \qquad \{\boldsymbol{\epsilon_{st}}\} = \boldsymbol{\nabla_2}\{\boldsymbol{d_t}\}, \qquad \{\boldsymbol{\epsilon_{br}}\} = \boldsymbol{\nabla_3}\{\boldsymbol{d_r}\}, \quad \{\boldsymbol{\epsilon_{sr}}\} = \boldsymbol{\nabla_4}\{\boldsymbol{d_r}\} \qquad (6.9)$$

where,

$$\boldsymbol{\nabla_1} = \begin{bmatrix} \frac{\boldsymbol{\partial}}{\boldsymbol{\partial x}} & 0 & 0 \\ 0 & \frac{\boldsymbol{\partial}}{\boldsymbol{\partial y}} & \frac{1}{\boldsymbol{R}} \\ \frac{\boldsymbol{\partial}}{\boldsymbol{\partial y}} & \frac{\boldsymbol{\partial}}{\boldsymbol{\partial x}} & 0 \\ 0 & 0 & 0 \end{bmatrix}, \qquad \boldsymbol{\nabla_2} = \begin{bmatrix} 0 & 0 & \frac{\boldsymbol{\partial}}{\boldsymbol{\partial x}} \\ 0 & \frac{-1}{\boldsymbol{R}} & \frac{\boldsymbol{\partial}}{\boldsymbol{\partial y}} \end{bmatrix},$$

$$\boldsymbol{\nabla_3} = \begin{bmatrix} \widehat{\boldsymbol{\nabla}} & \widehat{\boldsymbol{O}} & \breve{\boldsymbol{O}} \\ \widehat{\boldsymbol{O}} & \widehat{\boldsymbol{\nabla}} & \breve{\boldsymbol{O}} \\ \bar{\bar{\boldsymbol{O}}} & \bar{\bar{\boldsymbol{O}}} & \breve{\boldsymbol{\nabla}} \end{bmatrix}, \qquad \boldsymbol{\nabla_4} = \begin{bmatrix} \hat{\boldsymbol{I}} & \tilde{\boldsymbol{O}} & \bar{\boldsymbol{O}} \\ \tilde{\boldsymbol{O}} & \hat{\boldsymbol{I}} & \bar{\boldsymbol{O}} \\ \tilde{\boldsymbol{O}} & \tilde{\boldsymbol{O}} & \breve{\boldsymbol{I}} \\ \bar{\boldsymbol{\nabla}} & \tilde{\boldsymbol{O}} & \bar{\boldsymbol{O}} \\ \tilde{\boldsymbol{O}} & \bar{\boldsymbol{\nabla}} & \bar{\boldsymbol{O}} \end{bmatrix},$$

$$\widehat{\boldsymbol{\nabla}} = \begin{bmatrix} \frac{\boldsymbol{\partial}}{\boldsymbol{\partial x}} & 0 & 0 \\ 0 & \frac{\boldsymbol{\partial}}{\boldsymbol{\partial y}} & 0 \\ \frac{\boldsymbol{\partial}}{\boldsymbol{\partial y}} & \frac{\boldsymbol{\partial}}{\boldsymbol{\partial x}} & 0 \\ 0 & 0 & 1 \end{bmatrix}, \qquad \breve{\boldsymbol{\nabla}} = \begin{bmatrix} \frac{\boldsymbol{\partial}}{\boldsymbol{\partial x}} & 0 \\ 0 & \frac{\boldsymbol{\partial}}{\boldsymbol{\partial y}} \\ \frac{\boldsymbol{\partial}}{\boldsymbol{\partial y}} & \frac{\boldsymbol{\partial}}{\boldsymbol{\partial x}} \end{bmatrix},$$

$$\bar{\boldsymbol{\nabla}} = \begin{bmatrix} 0 & 0 & \dfrac{\boldsymbol{\partial}}{\boldsymbol{\partial x}} \\ 0 & 0 & \dfrac{\boldsymbol{\partial}}{\boldsymbol{\partial y}} \end{bmatrix}, \qquad \widehat{\boldsymbol{O}} = \begin{bmatrix} \widetilde{\boldsymbol{O}} \\ \breve{\boldsymbol{O}} \end{bmatrix}, \qquad \breve{\boldsymbol{O}} = \begin{bmatrix} \bar{\boldsymbol{O}} \\ \bar{\boldsymbol{O}} \end{bmatrix},$$

$$\bar{\bar{\boldsymbol{O}}} = \begin{bmatrix} 0 & 0 & 0 \\ 0 & 0 & 0 \\ 0 & 0 & 0 \end{bmatrix}, \qquad \widetilde{\boldsymbol{O}} = \begin{bmatrix} 0 & 0 & 0 \\ 0 & 0 & 0 \end{bmatrix},$$

$$\bar{\boldsymbol{O}} = \begin{bmatrix} 0 & 0 \\ 0 & 0 \end{bmatrix}, \qquad \hat{\boldsymbol{I}} = \begin{bmatrix} 1 & 0 & 0 \\ 0 & 1 & 0 \end{bmatrix}, \qquad \breve{\boldsymbol{I}} = \begin{bmatrix} 1 & 0 \\ 0 & 1 \end{bmatrix}$$

Corresponding to the state of strains, the state of stresses in the overall **HFRC** shell are categorized into the state of the in-plane and out-of-plane stresses $\{\boldsymbol{\sigma_b}\}$ and the state of transverse shear stresses $\{\boldsymbol{\sigma_s}\}$ as follows:

$$\{\boldsymbol{\sigma_b}\} = \left[\boldsymbol{\sigma_x} \;\; \boldsymbol{\sigma_y} \;\; \boldsymbol{\sigma_{xy}} \;\; \boldsymbol{\sigma_z}\right]^T, \;\; \{\boldsymbol{\sigma_s}\} = \left[\boldsymbol{\sigma_{xz}} \;\; \boldsymbol{\sigma_{yz}}\right]^T \tag{6.10}$$

where $\boldsymbol{\sigma_x}, \boldsymbol{\sigma_y}$, and $\boldsymbol{\sigma_z}$ are the normal stresses along the $\boldsymbol{x}$, $\boldsymbol{y}$, and $\boldsymbol{z}$ directions, respectively; $\boldsymbol{\sigma_{xy}}$ is the in-plane shear stress; $\boldsymbol{\sigma_{xz}}$ and $\boldsymbol{\sigma_{yz}}$ are the transverse shear stresses.

The constitutive relations for any $\boldsymbol{k^{th}}$ layer of the substrate **HFRC** shell are given by:

$$\{\boldsymbol{\sigma_b^k}\} = [\bar{\boldsymbol{C}}_{\boldsymbol{b}}^{\boldsymbol{k}}]\{\boldsymbol{\epsilon_b^k}\}, \quad \{\boldsymbol{\sigma_s^k}\} = [\bar{\boldsymbol{C}}_{\boldsymbol{s}}^{\boldsymbol{k}}]\{\boldsymbol{\epsilon_s^k}\}; \; (\boldsymbol{k} \; = \; 1,2,3,\ldots,\boldsymbol{N}) \tag{6.11}$$

where,

$$[\bar{\boldsymbol{C}}_{\boldsymbol{b}}^{\boldsymbol{k}}] = \begin{bmatrix} \boldsymbol{C_{11}^k} & \boldsymbol{C_{12}^k} & \boldsymbol{C_{16}^k} & \boldsymbol{C_{13}^k} \\ \boldsymbol{C_{12}^k} & \boldsymbol{C_{22}^k} & \boldsymbol{C_{26}^k} & \boldsymbol{C_{23}^k} \\ \boldsymbol{C_{16}^k} & \boldsymbol{C_{26}^k} & \boldsymbol{C_{66}^k} & \boldsymbol{C_{36}^k} \\ \boldsymbol{C_{13}^k} & \boldsymbol{C_{23}^k} & \boldsymbol{C_{36}^k} & \boldsymbol{C_{33}^k} \end{bmatrix}, \qquad [\bar{\boldsymbol{C}}_{\boldsymbol{s}}^{\boldsymbol{k}}] = \begin{bmatrix} \boldsymbol{C_{55}^k} & \boldsymbol{C_{54}^k} \\ \boldsymbol{C_{45}^k} & \boldsymbol{C_{44}^k} \end{bmatrix}$$

$\boldsymbol{C_{ij}^k}(\boldsymbol{i},\boldsymbol{j} = 1,2,\ldots 6)$ are the transformed elastic coefficients of the laminated multiscale **HFRC** shell.

The viscoelastic material of the constrained **ACLD** layer is assumed to be linearly viscoelastic and isotropic. It is modeled using the complex modulus approach. The constitutive relations for the viscoelastic material are similar to Eq. (6.11) with $\boldsymbol{k} = \boldsymbol{N+1}$, while the complex shear modulus ($\boldsymbol{G}$) and Young's modulus ($\boldsymbol{E}$) of the viscoelastic material are given by (Baz and Ro, 1995c; Shen, 1996):

$$\boldsymbol{G} = \boldsymbol{G}'(1 + \boldsymbol{i\eta}), \qquad \boldsymbol{E} = 2\boldsymbol{G}(1 + \boldsymbol{v}) \tag{6.12}$$

The constraining **1–3 PZC** layer of the **ACLD** treatment is subjected to the applied electric field ($\boldsymbol{E_z}$) along its thickness direction. Accordingly, the constitutive relations for the material of the **PZC** layer can be expressed as (Ray and Pradhan, 2007):

$$\{\boldsymbol{\sigma_b^k}\} = \left[\overline{\boldsymbol{C}}_{\boldsymbol{b}}^{\boldsymbol{k}}\right]\{\boldsymbol{\epsilon_b^k}\} + \left[\overline{\boldsymbol{C}}_{\boldsymbol{bs}}^{\boldsymbol{k}}\right]\{\boldsymbol{\epsilon_s^k}\} - \{\overline{\boldsymbol{e}}_{\boldsymbol{b}}\}\boldsymbol{E_z}; \quad \boldsymbol{k} = \boldsymbol{N} + \boldsymbol{2}$$

$$\{\boldsymbol{\sigma_s^k}\} = \left[\overline{\boldsymbol{C}}_{\boldsymbol{bs}}^{\boldsymbol{k}}\right]^T\{\boldsymbol{\epsilon_b^k}\} + \left[\overline{\boldsymbol{C}}_{\boldsymbol{s}}^{\boldsymbol{k}}\right]\{\boldsymbol{\epsilon_s^k}\} - \{\overline{\boldsymbol{e}}_{\boldsymbol{s}}\}\boldsymbol{E_z}$$

$$\boldsymbol{D_z} = \{\overline{\boldsymbol{e}}_{\boldsymbol{b}}\}^T\{\boldsymbol{\epsilon_b^k}\} + \{\overline{\boldsymbol{e}}_{\boldsymbol{s}}\}^T\{\boldsymbol{\epsilon_s^k}\} + \overline{\boldsymbol{\varepsilon}}_{\boldsymbol{33}}\boldsymbol{E_z} \tag{6.13}$$

in which $\boldsymbol{D_z}$ is the applied electric displacement along the thickness direction, and $\overline{\boldsymbol{\varepsilon}}_{\boldsymbol{33}}$ is the transformed dielectric constant. $\left[\overline{\boldsymbol{C}}_{\boldsymbol{b}}^{\boldsymbol{k}}\right]$ and $\left[\overline{\boldsymbol{C}}_{\boldsymbol{s}}^{\boldsymbol{k}}\right]$ are the transformed elastic coefficient matrices, similar to those in Eq. (6.11) with $\boldsymbol{k} = \boldsymbol{N} + \boldsymbol{2}$. For the **1–3 PZC** layer, the transverse shear strains are coupled with the in-plane strains because of the orientation of the piezoelectric fibers with respect to the vertical $\boldsymbol{xz}$-plane and $\boldsymbol{yz}$-plane. The corresponding coupling matrix $\left[\boldsymbol{C}_{\boldsymbol{bs}}^{\boldsymbol{N+2}}\right]$ is given by:

$$\left[\boldsymbol{C}_{\boldsymbol{bs}}^{\boldsymbol{N+2}}\right] = \begin{bmatrix} \overline{\boldsymbol{C}}_{\boldsymbol{15}}^{\boldsymbol{N+2}} & \overline{\boldsymbol{C}}_{\boldsymbol{25}}^{\boldsymbol{N+2}} & 0 & \overline{\boldsymbol{C}}_{\boldsymbol{35}}^{\boldsymbol{N+2}} \\ 0 & 0 & \overline{\boldsymbol{C}}_{\boldsymbol{46}}^{\boldsymbol{N+2}} & 0 \end{bmatrix}^{\boldsymbol{T}}$$

$$\left[\boldsymbol{C}_{\boldsymbol{bs}}^{\boldsymbol{N+2}}\right] = \begin{bmatrix} 0 & 0 & \overline{\boldsymbol{C}}_{\boldsymbol{56}}^{\boldsymbol{N+2}} & 0 \\ \overline{\boldsymbol{C}}_{\boldsymbol{14}}^{\boldsymbol{N+2}} & \overline{\boldsymbol{C}}_{\boldsymbol{24}}^{\boldsymbol{N+2}} & 0 & \overline{\boldsymbol{C}}_{\boldsymbol{34}}^{\boldsymbol{N+2}} \end{bmatrix}^{\boldsymbol{T}} \tag{6.14}$$

For the orientation of piezoelectric fiber $\boldsymbol{\Psi} = 0$, the matrices shown in Eq. (6.14) will have zero entities. The transformed piezoelectric constant vectors $\{\overline{\boldsymbol{e}}_{\boldsymbol{b}}\}$ and $\{\overline{\boldsymbol{e}}_{\boldsymbol{s}}\}$ appearing in Eq. (6.13) are as follows:

$$\{\boldsymbol{\sigma_b}\} = \left[\boldsymbol{\sigma_x} \ \ \boldsymbol{\sigma_y} \ \ \boldsymbol{\sigma_{xy}} \ \ \boldsymbol{\sigma_z}\right]^T, \qquad \{\boldsymbol{\sigma_s}\} = \left[\boldsymbol{\sigma_{xz}} \ \ \boldsymbol{\sigma_{yz}}\right]^T \tag{6.15}$$

The principle of virtual work is employed to derive the governing equations of the overall **HFRC** shell/**ACLD** system, which can be expressed as (Jeung and Shen, 2001):

$$\sum_{k=1}^{N+2} \int_{\boldsymbol{\Omega}} \left(\boldsymbol{\delta}\left\{\boldsymbol{\epsilon_b^k}\right\}^{\boldsymbol{T}}\left\{\boldsymbol{\sigma_b^k}\right\} + \boldsymbol{\delta}\left\{\boldsymbol{\epsilon_s^k}\right\}^{\boldsymbol{T}}\left\{\boldsymbol{\sigma_s^k}\right\} - \boldsymbol{\delta E_z \bar{\epsilon}_{33} E_z} - \boldsymbol{\delta}\{\boldsymbol{d_t}\}^{\boldsymbol{T}}\boldsymbol{\rho^k}\left\{\ddot{\boldsymbol{d}}_{\boldsymbol{t}}\right\}\right) \boldsymbol{d\Omega}$$

$$- \int_{\boldsymbol{A}} \boldsymbol{\delta}\{\boldsymbol{d_t}\}^{\boldsymbol{T}}\{\boldsymbol{f}\}\boldsymbol{dA} = 0 \tag{6.16}$$

in which $\boldsymbol{\rho^k}$ and $\boldsymbol{\Omega}$ are the mass density of the $\boldsymbol{k^{th}}$ layer, and $\{\boldsymbol{f}\}$ is the externally applied load over the outer surface area ($\boldsymbol{A}$) of the **HFRC** shell.

6.3 Finite Element Modeling

In this section, a **FE** model is developed to investigate the frequency response of the transverse displacement at the free end of the laminated **HFRC** shells. The overall **HFRC**/**ACLD** shell system is discretized by eight-noded quadrilateral isoparametric shell elements (see Fig. 6.4b) with a 12×6 mesh grid. Following Eq. (6.7), the generalized displacement vectors of the concerning $\boldsymbol{i^{th}}$ $(i = 1,2, \dots ,8)$ node of an element can be redefined as:

$$\{\boldsymbol{d_{ti}}\} = [\boldsymbol{u_{0i}} \ \ \boldsymbol{v_{0i}} \ \ \boldsymbol{w_{0i}}]^{\boldsymbol{T}}, \qquad \{\boldsymbol{d_{ri}}\} = \left[\boldsymbol{\theta_{xi}} \ \ \boldsymbol{\theta_{yi}} \ \ \boldsymbol{\theta_{zi}} \ \ \phi_{\boldsymbol{xi}} \ \ \phi_{\boldsymbol{yi}} \ \ \phi_{\boldsymbol{zi}} \ \ \boldsymbol{\gamma_{xi}} \ \ \boldsymbol{\gamma_{yi}} \ \ \boldsymbol{\gamma_{zi}}\right]^{\boldsymbol{T}} \tag{6.17}$$

Thus, the generalized displacement vectors, $\{\boldsymbol{d_t}\}$ and $\{\boldsymbol{d_r}\}$, at any point within the **HFRC** shell element, can be expressed in terms of the nodal generalized displacement vectors as follows:

$$\{\boldsymbol{d_t}\} = [\boldsymbol{N_t}]\{\boldsymbol{d_t^e}\}, \qquad \{\boldsymbol{d_r}\} = [\boldsymbol{N_t}]\{\boldsymbol{d_r^e}\} \tag{6.18}$$

in which,

$$\left[\boldsymbol{N}_{()}\right] = \left[\boldsymbol{N}_{()\boldsymbol{1}}\boldsymbol{N}_{()\boldsymbol{2}} \ . \ . \ . \ \boldsymbol{N}_{()\boldsymbol{8}}\right]^T, \qquad \boldsymbol{N}_{()\boldsymbol{i}} = \boldsymbol{n_i I}_{()},$$

$$\{\boldsymbol{d}^e_{()}\} = \left[\{\boldsymbol{d}^e_{()1}\}^T \{\boldsymbol{d}^e_{()2}\}^T \ . \ . \ . \ \{\boldsymbol{d}^e_{()8}\}^T\right]^T, \qquad () \xrightarrow{either} \begin{cases} \boldsymbol{t - translational} \\ \boldsymbol{r - rotational} \end{cases} \tag{6.19}$$

where $\boldsymbol{I_t}$ and $\boldsymbol{I_r}$ are the 3×3 and 8×8 identity matrices, respectively, and $\boldsymbol{n_i}$ is the shape function of the natural coordinates associated with the $\boldsymbol{i^{th}}$ node. Using Eqs. (6.8) and (6.18), the strain vectors can be expressed in terms of the nodal generalized displacement vectors as:

$$\{\boldsymbol{\epsilon_b}\}_{\boldsymbol{c}} = [\boldsymbol{B_{tb}}]\{\boldsymbol{d^e_t}\} + [\boldsymbol{Z_1}][\boldsymbol{B_{rb}}]\{\boldsymbol{d^e_r}\}, \qquad \{\boldsymbol{\epsilon_s}\}_{\boldsymbol{c}} = [\boldsymbol{B_{ts}}]\{\boldsymbol{d^e_t}\} + [\boldsymbol{Z_4}][\boldsymbol{B_{rs}}]\{\boldsymbol{d^e_r}\},$$

$$\{\boldsymbol{\epsilon_b}\}_{\boldsymbol{v}} = [\boldsymbol{B_{tb}}]\{\boldsymbol{d^e_t}\} + [\boldsymbol{Z_2}][\boldsymbol{B_{rb}}]\{\boldsymbol{d^e_r}\}, \qquad \{\boldsymbol{\epsilon_s}\}_{\boldsymbol{v}} = [\boldsymbol{B_{ts}}]\{\boldsymbol{d^e_t}\} + [\boldsymbol{Z_5}][\boldsymbol{B_{rs}}]\{\boldsymbol{d^e_r}\},$$

$$\{\boldsymbol{\epsilon_b}\}_{\boldsymbol{p}} = [\boldsymbol{B_{tb}}]\{\boldsymbol{d^e_t}\} + [\boldsymbol{Z_3}][\boldsymbol{B_{rb}}]\{\boldsymbol{d^e_r}\}, \qquad \{\boldsymbol{\epsilon_s}\}_{\boldsymbol{p}} = [\boldsymbol{B_{ts}}]\{\boldsymbol{d^e_t}\} + [\boldsymbol{Z_6}][\boldsymbol{B_{rs}}]\{\boldsymbol{d^e_r}\} \tag{6.20}$$

The sub-matrices appearing in Eq. (6.20), $[\boldsymbol{B_{tb}}]$, $[\boldsymbol{B_{rb}}]$, $[\boldsymbol{B_{ts}}]$, and $[\boldsymbol{B_{rs}}]$ are given by:

$$[\boldsymbol{B_{t()}}] = [\boldsymbol{B_{t()1}} \boldsymbol{B_{t()2}} \ . \ . \ . \ \boldsymbol{B_{t()8}}]^T,$$

$$[\boldsymbol{B_{r()}}] = [\boldsymbol{B_{r()1}} \boldsymbol{B_{r()2}} \ . \ . \ . \ \boldsymbol{B_{r()8}}]^T, \qquad () \xrightarrow{either} \begin{cases} \boldsymbol{b - bending} \\ \boldsymbol{s - shear} \end{cases} \tag{6.21}$$

The various sub-matrices $\boldsymbol{B_{tbi}}$, $\boldsymbol{B_{tsi}}$, $\boldsymbol{B_{rbi}}$ and $\boldsymbol{B_{rsi}}$ appearing in Eq. (6.21) are given by:

$$\boldsymbol{B_{tbi}} = \begin{bmatrix} \frac{\partial \boldsymbol{n_i}}{\partial \boldsymbol{x}} & 0 & 0 \\ 0 & \frac{\partial \boldsymbol{n_i}}{\partial \boldsymbol{y}} & \frac{1}{\boldsymbol{R}} \\ \frac{\partial \boldsymbol{n_i}}{\partial \boldsymbol{y}} & \frac{\partial \boldsymbol{n_i}}{\partial \boldsymbol{x}} & 0 \\ 0 & 0 & 0 \end{bmatrix}, \qquad \boldsymbol{B_{tsi}} = \begin{bmatrix} 0 & 0 & \frac{\partial \boldsymbol{n_i}}{\partial \boldsymbol{x}} \\ 0 & -\frac{1}{\boldsymbol{R}} & \frac{\partial \boldsymbol{n_i}}{\partial \boldsymbol{y}} \end{bmatrix},$$

$$\boldsymbol{B_{rbi}} = \begin{bmatrix} \overline{\boldsymbol{B}}_{\boldsymbol{rbi}} & \widehat{\boldsymbol{O}} & \breve{\boldsymbol{O}} \\ \widehat{\boldsymbol{O}} & \overline{\boldsymbol{B}}_{\boldsymbol{rbi}} & \breve{\boldsymbol{O}} \\ \overline{\overline{\boldsymbol{O}}} & \overline{\overline{\boldsymbol{O}}} & \widetilde{\boldsymbol{B}}_{\boldsymbol{rbi}} \end{bmatrix},$$

$$\boldsymbol{B}_{rsi} = \begin{bmatrix} \hat{\boldsymbol{I}} & \widetilde{\boldsymbol{O}} & \overline{\boldsymbol{O}} \\ \widetilde{\boldsymbol{O}} & \hat{\boldsymbol{I}} & \overline{\boldsymbol{O}} \\ \widetilde{\boldsymbol{O}} & \widetilde{\boldsymbol{O}} & \check{\boldsymbol{I}} \\ \overline{\boldsymbol{B}}_{rsi} & \widetilde{\boldsymbol{O}} & \overline{\boldsymbol{O}} \\ \widetilde{\boldsymbol{O}} & \overline{\boldsymbol{B}}_{rsi} & \overline{\boldsymbol{O}} \end{bmatrix}, \overline{\boldsymbol{B}}_{rbi} = \begin{bmatrix} \frac{\partial n_i}{\partial x} & 0 & 0 \\ 0 & \frac{\partial n_i}{\partial y} & 0 \\ \frac{\partial n_i}{\partial y} & \frac{\partial n_i}{\partial x} & 0 \\ 0 & 0 & 1 \end{bmatrix},$$

$$\widetilde{\boldsymbol{B}}_{rbi} = \begin{bmatrix} \frac{\partial n_i}{\partial x} & 0 \\ 0 & \frac{\partial n_i}{\partial y} \\ \frac{\partial n_i}{\partial y} & \frac{\partial n_i}{\partial x} \end{bmatrix}, \overline{\boldsymbol{B}}_{rsi} = \begin{bmatrix} 0 & 0 & \frac{\partial n_i}{\partial x} \\ 0 & 0 & \frac{\partial n_i}{\partial y} \end{bmatrix}$$

Substituting Eqs. (6.11), (6.13), and (6.20) into Eq. (6.16), and identifying that $\boldsymbol{E_z = V/h_p}$, where $\boldsymbol{V}$ is the applied voltage to the **1–3 PZC** layer across the thickness direction. The open-loop equations of motion of the overall **HFRC**/**ACLD** shell system can be written as follows:

$$[\boldsymbol{M^e}]\{\ddot{\boldsymbol{d}}_t^e\} + [\boldsymbol{K_{tt}^e}]\{\boldsymbol{d_t^e}\} + [\boldsymbol{K_{tr}^e}]\{\boldsymbol{d_r^e}\} = \{\boldsymbol{F_{tp}^e}\}\boldsymbol{V} + \{\boldsymbol{F^e}\} \tag{6.22}$$

$$[\boldsymbol{K_{rt}^e}]\{\boldsymbol{d_t^e}\} + [\boldsymbol{K_{rr}^e}]\{\boldsymbol{d_r^e}\} = \{\boldsymbol{F_{rp}^e}\}\boldsymbol{V} \tag{6.23}$$

where $[\boldsymbol{M^e}]$ is the elemental mass matrix; $[\boldsymbol{K_{tt}^e}]$, $[\boldsymbol{K_{tr}^e}]$, $[\boldsymbol{K_{rt}^e}]$, and $[\boldsymbol{K_{rr}^e}]$ are the elemental stiffness matrices; $\{\boldsymbol{F_{tp}^e}\}$ and $\{\boldsymbol{F_{rp}^e}\}$ are the elemental electro-elastic coupling vectors; $\{\boldsymbol{F^e}\}$ is the elemental load vector and $\{\boldsymbol{F^e}\}$ is the elemental load vector, as appearing in Eqs. (6.22) and (6.23), and given by:

$$[\boldsymbol{M^e}] = \int_0^{a_e}\int_0^{b_e} \overline{\boldsymbol{m}}[\boldsymbol{N_t}]^T[\boldsymbol{N_t}]\boldsymbol{dxdy}$$

$$[\boldsymbol{K_{tt}^e}] = [\boldsymbol{K_{tb}^e}] + [\boldsymbol{K_{ts}^e}] + [\boldsymbol{K_{tbs}^e}]_{\boldsymbol{pb}} + [\boldsymbol{K_{tbs}^e}]_{\boldsymbol{ps}}$$

$$[\boldsymbol{K_{tr}^e}] = [\boldsymbol{K_{trb}^e}] + [\boldsymbol{K_{trs}^e}] + \frac{1}{2}\left([\boldsymbol{K_{trbs}^e}]_{\boldsymbol{pb}} + [\boldsymbol{K_{rtbs}^e}]_{\boldsymbol{pb}}^T + [\boldsymbol{K_{trbs}^e}]_{\boldsymbol{ps}} + [\boldsymbol{K_{rtbs}^e}]_{\boldsymbol{ps}}^T\right),$$

$$[\boldsymbol{K_{rt}^e}] = [\boldsymbol{K_{tr}^e}]^T, [\boldsymbol{K_{rr}^e}] = [\boldsymbol{K_{rrb}^e}] + [\boldsymbol{K_{rrs}^e}] + [\boldsymbol{K_{rrbs}^e}]_{\boldsymbol{pb}} + [\boldsymbol{K_{rrbs}^e}]_{\boldsymbol{ps}},$$

$$\{\boldsymbol{F}_{tp}^{e}\} = \{\boldsymbol{F}_{tb}^{e}\}_{p} + \{\boldsymbol{F}_{ts}^{e}\}_{p}, \{\boldsymbol{F}_{rp}^{e}\} = \{\boldsymbol{F}_{rb}^{e}\}_{p} + \{\boldsymbol{F}_{rs}^{e}\}_{p},$$

$$\{\boldsymbol{F}^{e}\} = \int_{0}^{a_e}\int_{0}^{b_e} [\boldsymbol{N}_t]^{T} \{\boldsymbol{f}\} \boldsymbol{dxdy},$$

$$\bar{\boldsymbol{m}} = \sum_{k=1}^{N+2} \boldsymbol{\rho}^{k}(\boldsymbol{h}_{k+1} - \boldsymbol{h}_{k}) \tag{6.24}$$

where $\boldsymbol{a_e}$ and $\boldsymbol{b_e}$ are the length and circumferential width of the corresponding element, respectively, and ($\overline{\boldsymbol{m}}$) is the mass parameter. The various elemental stiffness matrices and the electro-elastic coupling vectors appearing in Eq. (6.24) are given by:

$$[\boldsymbol{K}_{tb}^{e}] = \int_{A} [\boldsymbol{B}_{tb}]^{T}\big([\boldsymbol{D}_{tb}]+[\boldsymbol{D}_{tb}]_{v} + [\boldsymbol{D}_{tb}]_{p}\big)[\boldsymbol{B}_{tb}]\ \boldsymbol{dx\ dy},$$

$$[\boldsymbol{K}_{ts}^{e}] = \int_{A} [\boldsymbol{B}_{ts}]^{T}\big([\boldsymbol{D}_{ts}]+[\boldsymbol{D}_{ts}]_{v} + [\boldsymbol{D}_{ts}]_{p}\big)[\boldsymbol{B}_{ts}]\ \boldsymbol{dx\ dy},$$

$$[\boldsymbol{K}_{tbs}^{e}]_{pb} = \int_{A} [\boldsymbol{B}_{tb}]^{T}[\boldsymbol{D}_{tbs}]_{p}[\boldsymbol{B}_{ts}]\ \boldsymbol{dx\ dy},$$

$$[\boldsymbol{K}_{tbs}^{e}]_{ps} = \int_{A} [\boldsymbol{B}_{ts}]^{T}[\boldsymbol{D}_{tbs}]_{p}[\boldsymbol{B}_{tb}]\ \boldsymbol{dx\ dy},$$

$$[\boldsymbol{K}_{trb}^{e}] = \int_{A} [\boldsymbol{B}_{trb}]^{T}\big([\boldsymbol{D}_{trb}]+[\boldsymbol{D}_{trb}]_{v} + [\boldsymbol{D}_{trb}]_{p}\big)[\boldsymbol{B}_{rb}]\ \boldsymbol{dx\ dy},$$

$$[\boldsymbol{K}_{trbs}^{e}]_{pb} = \int_{A} [\boldsymbol{B}_{tb}]^{T}[\boldsymbol{D}_{trbs}]_{p}[\boldsymbol{B}_{rs}]\ \boldsymbol{dx\ dy},$$

$$[\boldsymbol{K}_{rtbs}^{e}]_{pb} = \int_{A} [\boldsymbol{B}_{rb}]^{T}[\boldsymbol{D}_{rtbs}]_{p}[\boldsymbol{B}_{ts}]\ \boldsymbol{dx\ dy},$$

$$[\boldsymbol{K}_{trbs}^{e}]_{ps} = \int_{A} [\boldsymbol{B}_{ts}]^{T}[\boldsymbol{D}_{rtbs}]^{T}{}_{p}[\boldsymbol{B}_{rb}]\ \boldsymbol{dx\ dy},$$

$$[\boldsymbol{K}_{rtbs}^{e}]_{ps} = \int_{A} [\boldsymbol{B}_{rs}]^{T}[\boldsymbol{D}_{trbs}]^{T}{}_{p}[\boldsymbol{B}_{tb}]\ \boldsymbol{dx\ dy},$$

$$[\boldsymbol{K}_{trs}^{e}] = \int_{A} [\boldsymbol{B}_{ts}]^{T}\big([\boldsymbol{D}_{trs}]+[\boldsymbol{D}_{trs}]_{v} + [\boldsymbol{D}_{trs}]_{p}\big)[\boldsymbol{B}_{rs}]\ \boldsymbol{dx\ dy},$$

$$[\boldsymbol{K}^{e}_{rrb}] = \int_{A} [\boldsymbol{B}_{rb}]^{T} \big([\boldsymbol{D}_{rrb}] + [\boldsymbol{D}_{rrb}]_{v} + [\boldsymbol{D}_{rrb}]_{p}\big)[\boldsymbol{B}_{rb}]\, \boldsymbol{dx}\, \boldsymbol{dy},$$

$$[\boldsymbol{K}^{e}_{rrs}] = \int_{A} [\boldsymbol{B}_{rs}]^{T} \big([\boldsymbol{D}_{rrs}] + [\boldsymbol{D}_{rrs}]_{v} + [\boldsymbol{D}_{rrs}]_{p}\big)[\boldsymbol{B}_{rs}]\, \boldsymbol{dx}\, \boldsymbol{dy},$$

$$[\boldsymbol{K}^{e}_{rrbs}]_{pb} = \int_{A} [\boldsymbol{B}_{rb}]^{T} [\boldsymbol{D}_{rrbs}]_{p} [\boldsymbol{B}_{rs}]\, \boldsymbol{dx}\, \boldsymbol{dy},$$

$$[\boldsymbol{K}^{e}_{rrbs}]_{ps} = \int_{A} [\boldsymbol{B}_{rs}]^{T} [\boldsymbol{D}_{rrbs}]^{T}_{p} [\boldsymbol{B}_{rb}]\, \boldsymbol{dx}\, \boldsymbol{dy},$$

$$\{\boldsymbol{F}^{e}_{tb}\}_{p} = \int_{A} [\boldsymbol{B}_{tb}]^{T} \{\boldsymbol{D}_{tb}\}_{p} \boldsymbol{dx}\, \boldsymbol{dy}, \qquad \{\boldsymbol{F}^{e}_{rb}\}_{p} = \int_{A} [\boldsymbol{B}_{rb}]^{T} \{\boldsymbol{D}_{rb}\}_{p}\, \boldsymbol{dx}\, \boldsymbol{dy},$$

$$\{\boldsymbol{F}^{e}_{ts}\}_{p} = \int_{A} [\boldsymbol{B}_{ts}]^{T} \{\boldsymbol{D}_{ts}\}_{p} \boldsymbol{dx}\, \boldsymbol{dy}, \qquad \{\boldsymbol{F}^{e}_{rs}\}_{p} = \int_{A} [\boldsymbol{B}_{rs}]^{T} \{\boldsymbol{D}_{rs}\}_{p} \boldsymbol{dx}\, \boldsymbol{dy}$$

Also, the various rigidity matrices originated in the above elemental matrices are given by:

$$[\boldsymbol{D}_{tb}] = \sum_{k=1}^{N} \int_{h_k}^{h_{k+1}} [\overline{\boldsymbol{C}}^{k}_{b}]\, \boldsymbol{dz}, \qquad [\boldsymbol{D}_{trb}] = \sum_{k=1}^{N} \int_{h_k}^{h_{k+1}} [\overline{\boldsymbol{C}}^{k}_{b}]\, [\boldsymbol{Z}_{1}]\, \boldsymbol{dz},$$

$$[\boldsymbol{D}_{rrb}] = \sum_{k=1}^{N} \int_{h_k}^{h_{k+1}} [\boldsymbol{Z}_{1}]^{T} [\overline{\boldsymbol{C}}^{k}_{b}]\, [\boldsymbol{Z}_{1}]\, \boldsymbol{dz}, \qquad [\boldsymbol{D}_{ts}] = \sum_{k=1}^{N} \int_{h_k}^{h_{k+1}} [\overline{\boldsymbol{C}}^{k}_{s}]\, \boldsymbol{dz},$$

$$[\boldsymbol{D}_{trs}] = \sum_{k=1}^{N} \int_{h_k}^{h_{k+1}} [\overline{\boldsymbol{C}}^{k}_{b}]\, [\boldsymbol{Z}_{4}]\, \boldsymbol{dz}, \qquad [\boldsymbol{D}_{rrs}] = \sum_{k=1}^{N} \int_{h_k}^{h_{k+1}} [\boldsymbol{Z}_{4}]^{T} [\overline{\boldsymbol{C}}^{k}_{s}]\, [\boldsymbol{Z}_{4}]\, \boldsymbol{dz},$$

$$[\boldsymbol{D}_{tb}]_{v} = \boldsymbol{h}_{v} [\overline{\boldsymbol{C}}^{N+1}_{b}], \qquad [\boldsymbol{D}_{trb}]_{v} = \int_{h_{N+1}}^{h_{N+2}} [\overline{\boldsymbol{C}}^{N+1}_{b}] [\boldsymbol{Z}_{2}]\, \boldsymbol{dz},$$

$$[\boldsymbol{D}_{rrb}]_{v} = \int_{h_{N+1}}^{h_{N+2}} [\boldsymbol{Z}_{2}]^{T} [\overline{\boldsymbol{C}}^{N+1}_{b}] [\boldsymbol{Z}_{2}]\, \boldsymbol{dz}, \qquad [\boldsymbol{D}_{ts}]_{v} = \boldsymbol{h}_{v} [\overline{\boldsymbol{C}}^{N+1}_{s}],$$

$$[\boldsymbol{D}_{trs}]_{v} = \int_{h_{N+1}}^{h_{N+2}} [\overline{\boldsymbol{C}}^{N+1}_{s}] [\boldsymbol{Z}_{5}]\, \boldsymbol{dz}, \qquad [\boldsymbol{D}_{rrs}]_{v} = \int_{h_{N+1}}^{h_{N+2}} [\boldsymbol{Z}_{5}]^{T} [\overline{\boldsymbol{C}}^{N+1}_{s}] [\boldsymbol{Z}_{5}] \boldsymbol{dz},$$

$$[\boldsymbol{D}_{tb}]_{p} = \boldsymbol{h}_{p} [\overline{\boldsymbol{C}}^{N+2}_{b}], \qquad [\boldsymbol{D}_{trb}]_{p} = \int_{h_{N+2}}^{h_{N+3}} [\overline{\boldsymbol{C}}^{N+2}_{b}] [\boldsymbol{Z}_{3}]\, \boldsymbol{dz},$$

$$[\boldsymbol{D_{rrb}}]_{\boldsymbol{p}} = \int_{h_{N+2}}^{h_{N+3}} [\boldsymbol{Z_3}]^T [\overline{\boldsymbol{C}}_b^{N+2}][\boldsymbol{Z_3}]\, d\boldsymbol{z}, \qquad [\boldsymbol{D_{ts}}]_{\boldsymbol{p}} = \boldsymbol{h_p}[\overline{\boldsymbol{C}}_s^{N+2}],$$

$$[\boldsymbol{D_{trs}}]_{\boldsymbol{p}} = \int_{h_{N+2}}^{h_{N+3}} [\overline{\boldsymbol{C}}_s^{N+2}][\boldsymbol{Z_6}]\, d\boldsymbol{z}, \qquad [\boldsymbol{D_{rrs}}]_{\boldsymbol{p}} = \int_{h_{N+2}}^{h_{N+3}} [\boldsymbol{Z_6}]^T [\overline{\boldsymbol{C}}_s^{N+2}][\boldsymbol{Z_6}] d\boldsymbol{z},$$

$$[\boldsymbol{D_{tbs}}]_{\boldsymbol{p}} = \int_{h_{N+2}}^{h_{N+3}} [\overline{\boldsymbol{C}}_{bs}^{N+2}]\, d\boldsymbol{z}, \qquad [\boldsymbol{D_{trbs}}]_{\boldsymbol{p}} = \int_{h_{N+2}}^{h_{N+3}} [\overline{\boldsymbol{C}}_{bs}^{N+2}][\boldsymbol{Z_6}]\, d\boldsymbol{z},$$

$$[\boldsymbol{D_{rtbs}}]_{\boldsymbol{p}} = \int_{h_{N+2}}^{h_{N+3}} [\boldsymbol{Z_3}]^T [\overline{\boldsymbol{C}}_{bs}^{N+2}]\, d\boldsymbol{z}, \qquad [\boldsymbol{D_{rrbs}}]_{\boldsymbol{p}} = \int_{h_{N+2}}^{h_{N+3}} [\boldsymbol{Z_3}]^T [\overline{\boldsymbol{C}}_{bs}^{N+2}][\boldsymbol{Z_6}]\, d\boldsymbol{z},$$

$$\{\boldsymbol{D_{tb}}\}_{\boldsymbol{p}} = \int_{h_{N+2}}^{h_{N+3}} -\{\bar{\boldsymbol{e}}_b\}/\boldsymbol{h_p}\, d\boldsymbol{z}, \qquad \{\boldsymbol{D_{rb}}\}_{\boldsymbol{p}} = \int_{h_{N+2}}^{h_{N+3}} -[\boldsymbol{Z_3}]^T\{\bar{\boldsymbol{e}}_b\}/\boldsymbol{h_p}\, d\boldsymbol{z},$$

$$\{\boldsymbol{D_{ts}}\}_{\boldsymbol{p}} = \int_{h_{N+2}}^{h_{N+3}} -\{\bar{\boldsymbol{e}}_s\}/\boldsymbol{h_p}\, d\boldsymbol{z}, \qquad \{\boldsymbol{D_{rs}}\}_{\boldsymbol{p}} = \int_{h_{N+2}}^{h_{N+3}} -[\boldsymbol{Z_6}]^T\{\bar{\boldsymbol{e}}_s\}/\boldsymbol{h_p}\, d\boldsymbol{z}$$

Finally, the open-loop global equations of motion of the **HFRC**/**ACLD** shell system can be obtained by assembling the elemental equations of motion, as follows:

$$[\boldsymbol{M}]\{\ddot{\boldsymbol{X}}\} + [\boldsymbol{K_{tt}}]\{\boldsymbol{X}\} + [\boldsymbol{K_{tr}}]\{\boldsymbol{X_r}\} = \sum_{j=1}^{q}\{\boldsymbol{F_{tp}^j}\}\boldsymbol{V^j} + \{\boldsymbol{F}\}, \tag{6.25}$$

$$[\boldsymbol{K_{rt}}]\{\boldsymbol{X}\} + [\boldsymbol{K_{rr}}]\{\boldsymbol{X_r}\} = \sum_{j=1}^{q}\{\boldsymbol{F_{rp}^j}\}\boldsymbol{V^j} \tag{6.26}$$

where the matrices appearing in Eqs. (6.25) and (6.26) are in the global form and are similar to the matrices shown in Eqs. (6.22) and (6.23). Vectors $\{\boldsymbol{X}\}$ and $\{\boldsymbol{X_r}\}$ represent the global nodal translational and rotational degrees of freedom, respectively, and $\boldsymbol{V^j}$ is the applied voltage corresponding to the $\boldsymbol{j^{th}}$ **ACLD** patch.

6.4 Control Strategy

To activate the **ACLD** patches, the electric potential applied to the constraining **1–3 PZC** layer is negatively proportional to the transverse velocity at that point of the multiscale

HFRC shell. Thus, the control voltage supplied to activate the **ACLD** patches can be expressed as:

$$\boldsymbol{V^j} = -\boldsymbol{k_d^j}\dot{\boldsymbol{w}} = -\boldsymbol{k_d^j}\{\boldsymbol{U_t^j}\}\{\dot{\boldsymbol{X}}\} - \boldsymbol{k_d^j}(\boldsymbol{h}/2)\{\boldsymbol{U_r^j}\}\{\dot{\boldsymbol{X}}_{\boldsymbol{r}}\} \tag{6.27}$$

Substituting Eq. (6.27) into Eqs. (6.25) and (6.26), the final equations of motion defining the closed-loop dynamics of the overall **HFRC/ACLD** shell system can be expressed as follows:

$$[\boldsymbol{M}]\{\ddot{\boldsymbol{X}}\} + [\boldsymbol{K_{tt}}]\{\boldsymbol{X}\} + [\boldsymbol{K_{tr}}]\{\boldsymbol{X_r}\} + \sum_{j=1}^{q}\boldsymbol{k_d^j}\{\boldsymbol{F_{tp}^j}\}\{\boldsymbol{U_t^j}\}\{\dot{\boldsymbol{X}}\} +$$

$$\sum_{j=1}^{q}\boldsymbol{k_d^j}(\boldsymbol{h}/2)\{\boldsymbol{F_{tp}^j}\}\{\boldsymbol{U_r^j}\}\{\dot{\boldsymbol{X}}_{\boldsymbol{r}}\} = \{\boldsymbol{F}\} \tag{6.28}$$

$$[\boldsymbol{K_{rt}}]\{\boldsymbol{X}\} + [\boldsymbol{K_{rr}}]\{\boldsymbol{X_r}\} + \sum_{j=1}^{q}\boldsymbol{k_d^j}\{\boldsymbol{F_{rp}^j}\}\{\boldsymbol{U_t^j}\}\{\dot{\boldsymbol{X}}\} +$$

$$\sum_{j=1}^{q}\boldsymbol{k_d^j}(\boldsymbol{h}/2)\{\boldsymbol{F_{rp}^j}\}\{\boldsymbol{U_r^j}\}\{\dot{\boldsymbol{X}}_{\boldsymbol{r}}\} = 0 \tag{6.29}$$

6.5 Results and Discussion

In this section, first we validate the proposed **SinusZZ** theory with the analytical model and **FSDT**. Next, the numerical outcomes are evaluated by using the **FE** model developed in the earlier section to investigate the performance of the laminated multiscale **HFRC** smart shell. For this, the laminated symmetric cross-ply $(0°/90°/0°)$, the anti-symmetric cross-ply $(0°/90°/0°/90°)$, and the anti-symmetric angle-ply $(-45°/45°/-45°/45°)$, thin cantilever cylindrical **HFRC** shells, integrated with the two patches of the **ACLD** treatment, are considered. The **ACLD** treatment patches are installed at the outer circumference of the cantilevered **HFRC** shell, $180°$ apart from each other, as shown in Fig. 6.2. The **ACLD** patches cover $2/3$ the length of the shell while it is assumed that the width of the individual patch is $1/6$ of the length of the outer circumferential width of the shell. To study the damping performance of the **HFRC** plates, unless specified, the volume fractions of carbon fiber, straight **CNTs**, and wavy **CNTs** are taken as 0.3, 0.1, and 0.1243, respectively. The results of laminated base composite plates are compared with the **HFRC** plates by keeping the carbon fiber volume fraction constant (i.e., $\boldsymbol{v_{CF}} = 0.3$). The influence of **CNT** waviness on the performance of the laminated **HFRC** shells is also investigated by considering the **CNT** waves coplanar with the **1–2** and **1–3** planes. Unless otherwise mentioned, **CNT** (5, 5) is used for analysis, with a diameter $\boldsymbol{d_n} = 0.78\,\boldsymbol{nm}$, maximum amplitude $\boldsymbol{A} = 100\boldsymbol{d_n}$, and waviness factor $(\boldsymbol{A}/\boldsymbol{L_{RVE}}) = 0.17$, where $\boldsymbol{L_{RVE}}$ as the linear distance between the two ends of the **CNT**. The amplitude variation of **CNT** waviness in the **1–2** and **1–3** planes is predicted by taking the value of wave frequency, $\boldsymbol{\omega} = 5\,\boldsymbol{\pi}/\boldsymbol{L_{RVE}}$. The effective elastic properties of the base composite and the **HFRC** with straight and wavy **CNTs** are summarized in Table 6.1. These properties are predicted using the two- and three-phase Mori-Tanaka model presented in Chapter 2. For the sake of brevity the Mori-Tanaka model is not presented here. It can be observed from Table 6.1 that the effective elastic properties of the **HFRC** significantly enhance in the transverse direction due to the waviness of the **CNT**.

Table 6.1. Effective elastic properties of the base composite and the **HFRC** with $\boldsymbol{v_{CF}} = 0.3$.

Elastic constant	$\boldsymbol{C_{11}}$ **(*GPa*)**	$\boldsymbol{C_{12}}$ **(*GPa*)**	$\boldsymbol{C_{13}}$ **(*GPa*)**	$\boldsymbol{C_{22}}$ **(*GPa*)**	$\boldsymbol{C_{33}}$ **(*GPa*)**	$\boldsymbol{C_{44}}$ **(*GPa*)**	$\boldsymbol{C_{55}}$ **(*GPa*)**	$\boldsymbol{\rho}$ $(\boldsymbol{kg/m^3})$
Base composite ($\boldsymbol{v_{CNT}} = 0$)	75.75	3.92	3.92	7.32	7.32	1.63	1.34	1385
HFRC ($\boldsymbol{v_{CNT}} = 0.1$)	119.87	4.69	4.38	8.67	8.67	1.98	1.81	1400
HFRC (**1–2** plane, $\boldsymbol{v_{CNT}} = 0.1243$)	70.01	26.87	4.64	25.58	9.05	10.40	2.14	1403.645
HFRC (**1–3** plane, $\boldsymbol{v_{CNT}} = 0.1243$)	70.01	4.91	26.61	9.07	25.42	1.93	24.41	1403.645

The thickness of the laminated **HFRC** shell is considered as $\boldsymbol{h} = 0.003\ \boldsymbol{m}$. The thickness of the **1–3 PZC** layer is taken as $\boldsymbol{h_p} = 250\ \boldsymbol{\mu m}$ and the viscoelastic layer is taken as $\boldsymbol{h_v} = 200\ \mu\boldsymbol{m}$. The length and radius of the shell from the reference plane are chosen to be $\boldsymbol{a} = 1\ \boldsymbol{m}$ and $\boldsymbol{R} = 50 \times \boldsymbol{h}$, respectively. The elastic and piezoelectric properties of **1–3 PZC** by considering 60% fiber volume fraction are given as follows (Ray and Pradhan, 2007):

$\boldsymbol{C_{11}}$= 9.293 $\boldsymbol{GPa}$, $\boldsymbol{C_{12}}$= 6.182 $\boldsymbol{GPa}$, $\boldsymbol{C_{13}}$= 6.054 $\boldsymbol{GPa}$, $\boldsymbol{C_{33}}$= 35.44 $\boldsymbol{GPa}$, $\boldsymbol{C_{23}} = \boldsymbol{C_{13}}$, $\boldsymbol{C_{44}}$= 1.58 $\boldsymbol{GPa}$, $\boldsymbol{C_{66}}$= 1.544 $\boldsymbol{GPa}$, $\boldsymbol{C_{55}} = \boldsymbol{C_{44}}$, $\boldsymbol{e_{31}} = -0.1902\ \boldsymbol{C/m^2}$, $\boldsymbol{e_{32}} = \boldsymbol{e_{31}}$, $\boldsymbol{e_{33}}$= 18.4107 $\boldsymbol{C/m^2}$, $\boldsymbol{e_{24}}$= 0.004 $\boldsymbol{C/m^2}$, $\boldsymbol{e_{15}} = \boldsymbol{e_{24}}$ and $\boldsymbol{\rho_p}$= 5090 $\boldsymbol{kg/m^3}$.

The material properties of the viscoelastic layer material **ISD**112 are considered as (Chantalakhana and Stanway, 2001):

$\boldsymbol{\rho_v}$= 1140 $\boldsymbol{kg/m^3}$, $\boldsymbol{\nu_v}$ = 0.49, and $\boldsymbol{G_v} = 20(1 + \boldsymbol{i})\ \boldsymbol{MNm^{-2}}$

6.5.1 Validation of SinusZZ Theory

To validate the present **FE** model developed using the **SinusZZ** theory, the fundamental natural frequencies of the laminated shell are compared with the existing analytical and **FE** models presented in the literature. The outcome of this comparison is shown in Table 6.2, and the results are found to be in good agreement with the existing models. A non-dimensional frequency parameter $\boldsymbol{\lambda}$ was used for validation, which is given by:

$$\boldsymbol{\lambda} = \overline{\boldsymbol{\omega}}(\boldsymbol{a^2}/\boldsymbol{h})\sqrt{\boldsymbol{\rho}/\boldsymbol{E_T}} \tag{6.30}$$

in which $\overline{\boldsymbol{\omega}}$ is the natural frequency of the laminated shell; $\boldsymbol{\rho}$ and $\boldsymbol{E_T}$ are the density and the transverse Young's modulus substrate shell, respectively.

Table 6.2. Non-dimensional frequencies (λ) of cantilever laminated substrate shells.

Substrate laminates	Source	*R/h*	*a/R*	λ
$0^o/90^o/0^o$	Present FE model	20	5	0.4908
	Analytical (Reddy, 2003)	20	5	0.4899
$0^o/90^o$	Present FE model	20	5	0.5598
	Analytical (Reddy, 2003)	20	5	0.5581

Furthermore, we compared the results of **SinusZZ** theory with the existing results of classical **FSDT** by considering the identical smart shell with straight **CNTs** for symmetric cross-ply and anti-symmetric angle-ply (Kundalwal and Meguid, 2015). The results are predicted for both active and passive damping by considering the value of gain $\boldsymbol{k_d} = 1000$. It can be seen from Fig. 6.5 that for both the theories the frequency response shows excellent agreement for the first three modes obtained for symmetric cross-ply **FFRC** smart shell. It can also be observed from this figure that the amplitudes of vibration are significantly attenuated with the **SinusZZ** theory for both active and passive damping. This is attributed to the layer-independent sinusoidal shear distribution obtained along the thickness of laminated shell, due to the implementation of **SinusZZ** theory. Similar results are obtained for the anti-symmetric angle-ply as shown in Fig 6.6.

From Figs. 6.5 and 6.6 we can conclude that the **SinusZZ** theory shows better active damping performance. Thus next, we will compare the active damping performance of multiscale **HFRC** smart shells using **SinusZZ** theory and **FSDT**. Table 6.3 shows the amplitude of deflections corresponding to the frequency response of laminated symmetric cross-ply **HFRF** shell, which is predicted by using the present **SinusZZ** theory and the existing classical **FSDT** (Kundalwal and Meguid, 2015) and the **FSDT** with higher-order function (**FSDT-H**) for the transverse displacement along the thickness direction (Sahoo and Ray, 2019a). It can be seen from this table that the frequency response of the **SinusZZ** theory shows excellent agreement with classical **FSDT** and **FSDT-H**. Also, the present **SinusZZ** theory effectively attenuates the

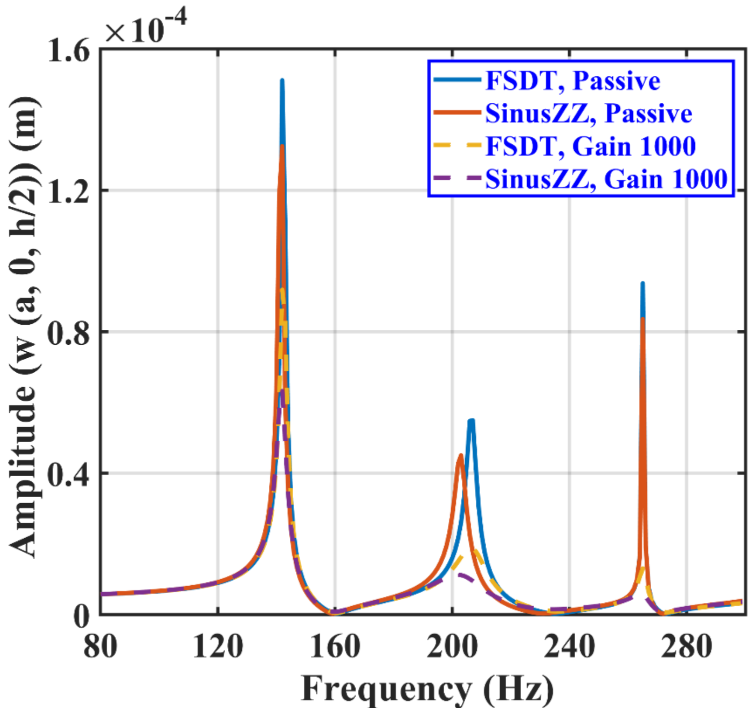

Figure 6.5. Comparison of **SinusZZ** theory and **FSDT** for symmetric cross-ply **FFRC** smart shell with $\boldsymbol{k_d} = 1000$.

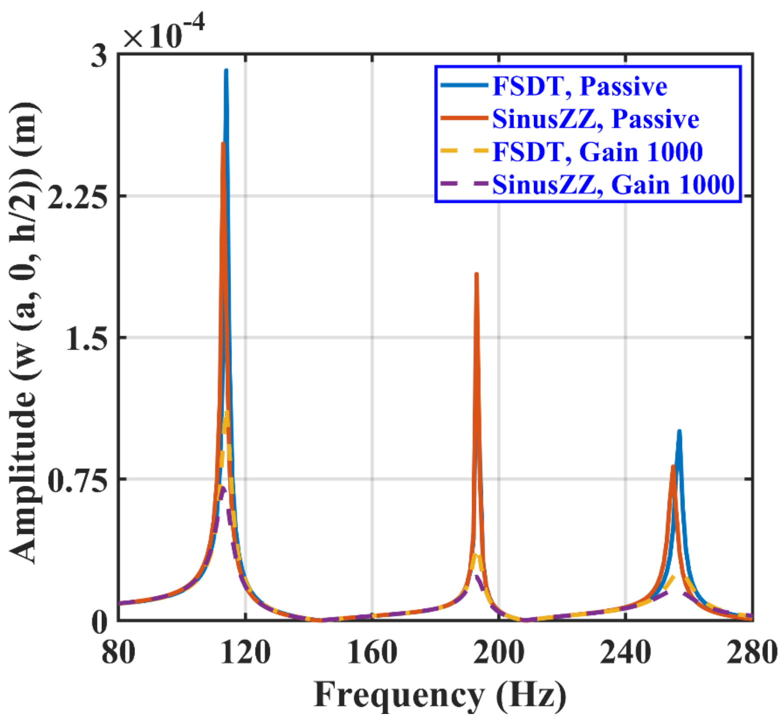

Figure 6.6. Comparison of **SinusZZ** theory and **FSDT** for anti-symmetric angle-ply **FFRC** smart shell with $\boldsymbol{k_d} = 1000$.

amplitude of vibrations as compared to the **FSDT**. The results presented in Table 6.3 verify the successful implementation of the **SinusZZ** theory. Hence, the established **SinusZZ** model is now being used to analyze the damping performance of the proposed laminated multiscale **HFRC** smart shell. The results are compared with the base composite shell. For this, Eqs. (6.28) and (6.29) are formulated, and the harmonic excitation of 1 $\boldsymbol{N}$ force is applied at a point $(\boldsymbol{a}, 0, \boldsymbol{h}/2)$ on the top surface of the limited **HFRC** smart shell to evaluate the frequency response.

Table 6.3. Amplitudes and fundamental natural frequencies of laminated symmetric cross-ply **HFRC** substrate shell with straight and wavy **CNTs** ($\boldsymbol{k_d} = 600$).

Theory	Laminated smart shell	Reference	Amplitude (10^{-4}) **(m)**	Frequency (1st mode) (Hz)
SinusZZ	**HFRC** shell with straight **CNTs**	Present **FE** model	1.033	110
FSDT		(Kundalwal and Meguid, 2015)	1.477	110
FSDT-H		(Sahoo and Ray, 2019a)	1.374	110
SinusZZ	**HFRC** shell with wavy **CNTs** (**1–3** plane)	Present **FE** model	0.917	89
FSDT		(Kundalwal and Meguid, 2015)	1.175	90
FSDT-H		(Sahoo and Ray, 2019a)	1.117	90

6.5.2 *Active Damping of Laminated HFRC Smart Cantilever Shell*

After validation and ensuring the successful implementation of **SinusZZ** theory, it is utilized for the investigation of active damping of laminated **HFRC** smart cantilever shell. In this context, Fig. 6.7 illustrates the frequency response of laminated symmetric cross-ply with respect to the amplitudes of deflection $\boldsymbol{w}(\boldsymbol{a}, 0, \boldsymbol{h}/2)$, considering both active and passive damping. The figure depicts that the developed **SinusZZ** model effectively attenuates the amplitudes of vibration for the active damping. The frequency response of laminated base composite and **HFRC** shell (with straight **CNTs**) is also compared in Fig. 6.7. It can be observed that for both active ($\boldsymbol{k_d} \neq 0$) and passive damping ($\boldsymbol{k_d} = 0$), the **HFRC** shell attenuates the amplitudes of vibrations significantly higher compared to the base composite shell. Corresponding to the value of gain $\boldsymbol{k_d} = 600$, the laminated **HFRC** shell attenuates the amplitudes of vibration approximately 22% higher than the base composite shell, which is a significant improvement. This is attributed to the enhanced stiffness offered due to the incorporation of **CNT** nanofillers in the multiscale **HFRC** substrate shell. The control voltage required to achieve the following vibration attenuation is demonstrated in Fig. 6.8. It can be observed from this figure that for the laminated **HFRC** shell, the maximum required control voltage is 42.66 $\boldsymbol{V}$, which is significantly less as compared to the base composite shell corresponding to the value of gain $\boldsymbol{k_d} = 600$. Similar behavior was also observed for anti-symmetric cross-ply and anti-symmetric angle-ply, but for the sake of brevity, the results are not presented here. Figs. 6.7 and 6.8 reveals that the laminated multiscale **HFRC** smart shell shows better damping performance. Next, we analyze the effect of **CNT** waviness on the damping performance of the laminated symmetric/anti-symmetric cross-ply and the anti-symmetric angle-ply multiscale **HFRC** smart shells.

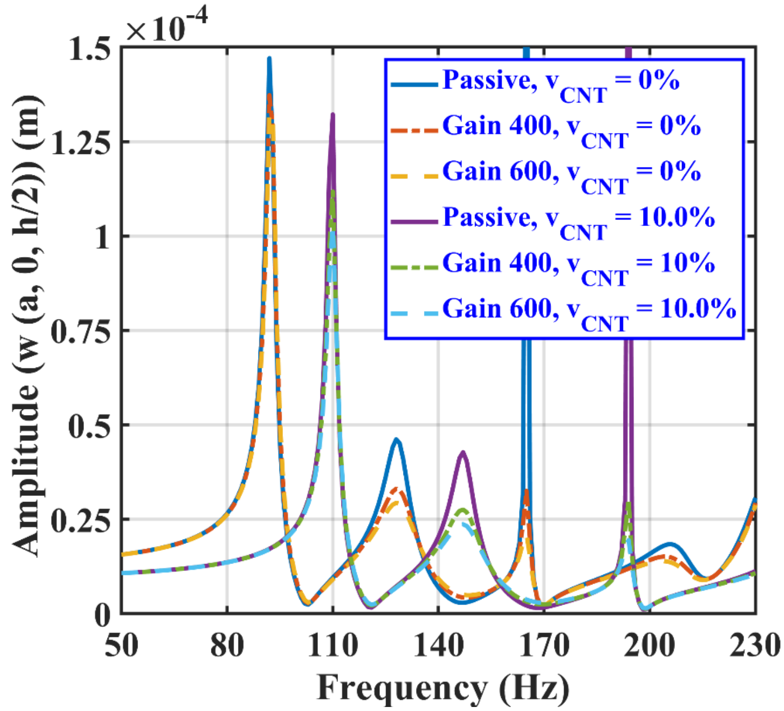

Figure 6.7. Variation of amplitude of deflection with respect to the frequency response of the laminated symmetric cross-ply composite shell ($\boldsymbol{\Psi} = 0°, \boldsymbol{\omega} = 0$).

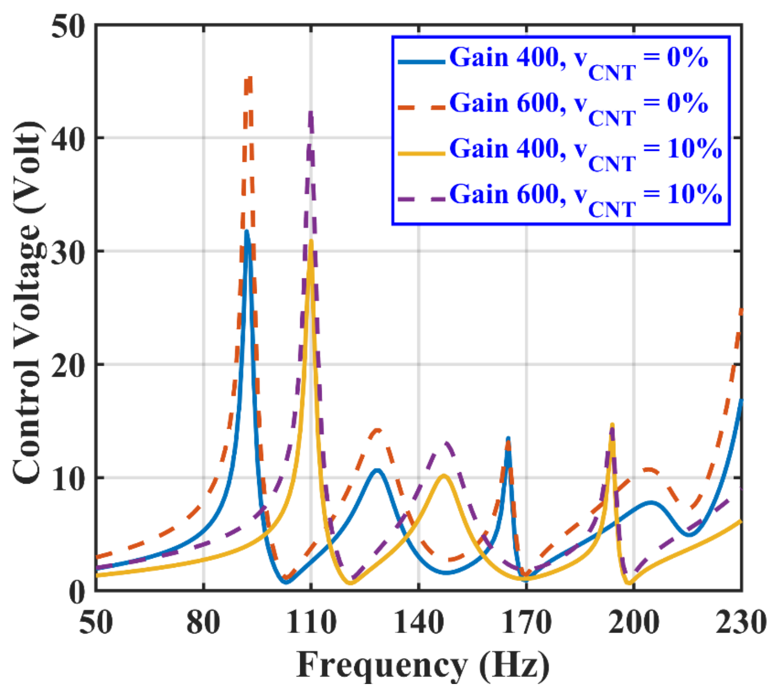

Figure 6.8. Variation of control voltage with respect to the frequency response of the laminated symmetric cross-ply composite shell ($\boldsymbol{\Psi} = 0°, \boldsymbol{\omega} = 0$).

Figure 6.9 represents the effects of **CNT** waviness on the frequency response of the laminated smart composite shell. Unless otherwise stated, the value of gain is considered to be $\boldsymbol{k_d} = 600$, and the piezo-fiber orientation is taken as $\boldsymbol{\Psi} = 0°$. It can be noted that **CNT** waviness significantly influences the damping characteristics of the laminated **HFRC** smart shell. The **HFRC** shell, with the **CNT** waves coplanar with the **1–3** plane shows maximum vibrational attenuation compared to the composites with or without considering **CNTs**. For the first mode of natural frequency, the multiscale **HFRC** shell with **CNT** waviness coplanar with the **1–3** plane shows 30% and 11.5% higher vibrational attenuation compared to the base composite and **HFRC** shell with straight **CNTs**. This is attributed to the enhanced transverse stiffness of the multiscale **HFRC** substrate shells due to the incorporation of **CNTs** mutually orthogonal planes. Hence, improving the energy dissipation capability of the multiscale **HFRC** shell shows better suppression of transverse vibrations. Similar behavior is also observed for anti-symmetric cross-ply and anti-symmetric angle-ply, as shown in Fig. 6.10 and Fig. 6.11, respectively. The multiscale **HFRC** shell having **CNT** waviness coplanar with the **1–3** plane suppresses amplitudes of the first mode of natural frequency by 64% and 60% higher than the base composite and **HFRC** shell with straight **CNTs**. Figures 6.9–6.11 shows that the multiscale **HFRC** shell having **CNT** waviness coplanar with the **1–3** plane shows better damping characteristics compared to other composite shells (with or without **CNTs**). Thus, further investigation has been carried out using the multiscale **HFRC** shell having **CNT** waviness coplanar with the **1–3** plane.

The control authority of the **ACLD** treatment patches depends on the constraining layer of **1–3 PZC**. The effective elastic and piezoelectric properties of **1–3 PZC** layer can be altered by varying the piezo fiber orientation ($\boldsymbol{\Psi}$) in two mutually orthogonal vertical ***xz***-plane and ***yz***-plane. In this context, the value of $\boldsymbol{\Psi}$ is considered to vary between 0° to $45°$. For the sake of simplicity, the effectiveness of the control authority of the **ACLD** treatment patches has been investigated for the values of $\boldsymbol{\Psi} = 0°, 15°, 30°,$ and $45°$. Figure 6.12–6.13 illustrate the effect of the piezo-fiber orientation on the control authority of the **ACLD** treatment patches for the laminated symmetric cross-ply **HFRC** smart shell incorporated with wavy **CNTs**. The figures depict that the piezo-fiber orientation significantly influences the control authority of the **ACLD** patches, and for the first mode of the natural frequency, the maximum attenuation is observed at $\boldsymbol{\Psi} = 0°$ for both cases. However, for the anti-symmetric cross-ply, when the piezo-fibers are oriented in the vertical ***xz***-plane, the maximum attenuation is observed at $\boldsymbol{\Psi} = 45°$, as shown in Fig. 6.14. Whereas when the piezo-fibers are oriented in the vertical ***yz***-plane, the maximum attenuation is observed at $\boldsymbol{\Psi} = 0°$, as shown in Fig. 6.15. For the anti-symmetric angle-ply, the results are similar to the anti-symmetric cross-ply as shown in Figs. 6.16 and 6.17. From Figs. 6.12–6.17, it can be noted that the performance of the **ACLD** treatment patches is much better when the piezo-fibers are oriented along the ***xz***-plane. However, when the piezo-fibers are oriented along the ***yz***-plane, the magnitude of the amplitudes of vibration are much higher. Thus, we can say that the control authority of the **ACLD** patches for this case is comparatively poor. This is attributed to the fact that the out-of-plane piezoelectric coefficient is maximum when the piezo-fibers are oriented along the ***xz***-plane, compared to when the piezo-fibers are oriented along the ***yz***-plane.

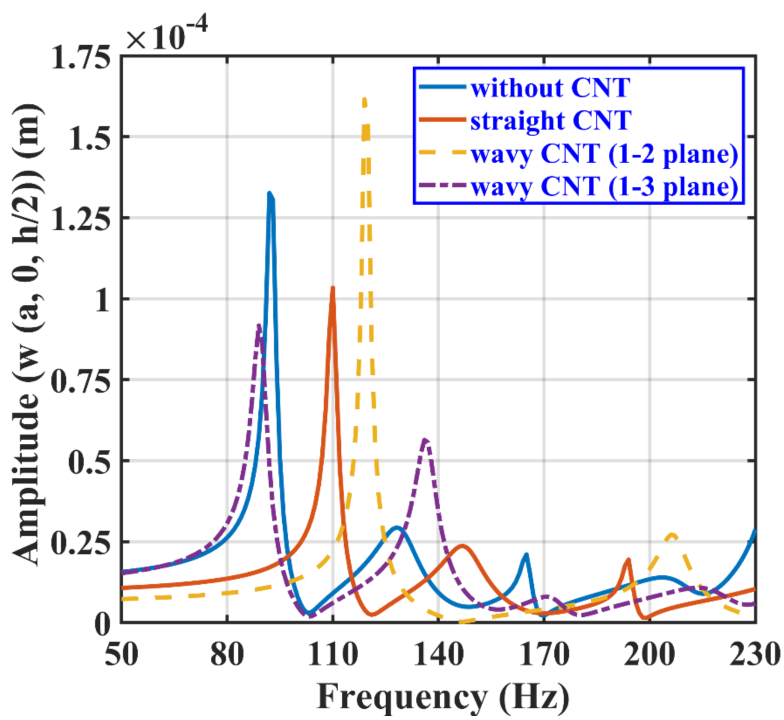

Figure 6.9. Frequency response for transverse displacement $\boldsymbol{w}(\boldsymbol{a}, 0, \boldsymbol{h}/2)$ of the cantilever laminated symmetric cross-ply composite smart shell ($\boldsymbol{\Psi} = 0°$).

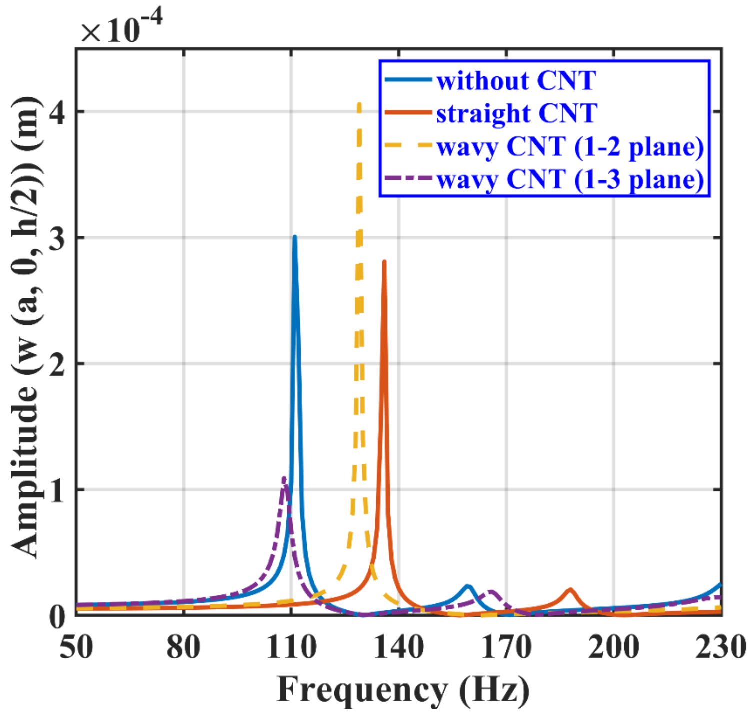

Figure 6.10. Frequency response for transverse displacement $\boldsymbol{w}(\boldsymbol{a}, 0, \boldsymbol{h}/2)$ of the cantilever laminated anti-symmetric cross-ply composite smart shell ($\boldsymbol{\Psi} = 0°$).

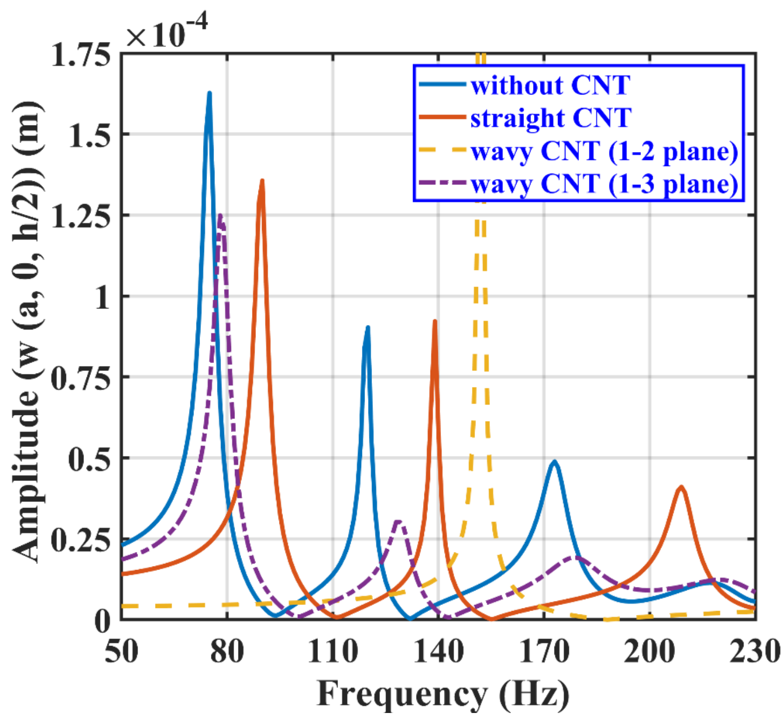

Figure 6.11. Frequency response for transverse displacement $\boldsymbol{w}(\boldsymbol{a}, 0, \boldsymbol{h}/2)$ of the cantilever laminated anti-symmetric angle-ply composite smart shell ($\boldsymbol{\Psi} = 0°$).

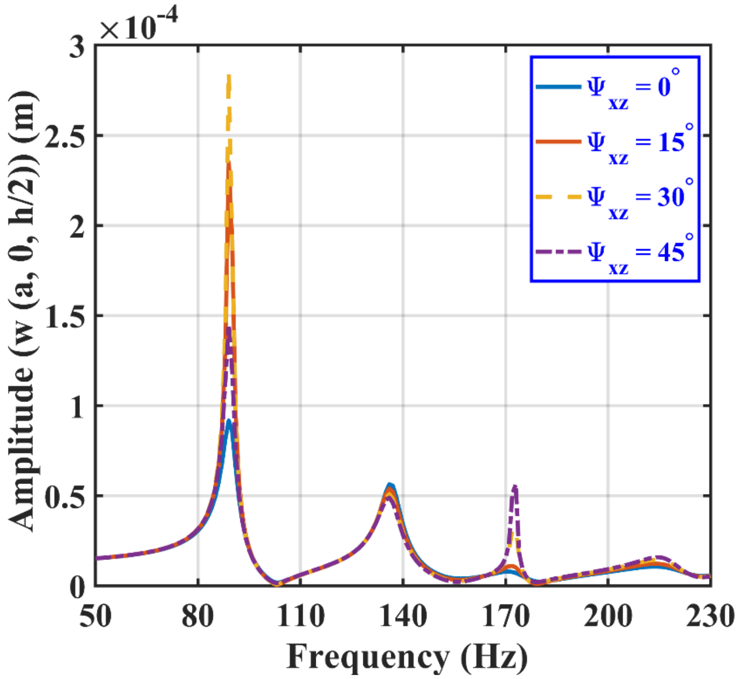

Figure 6.12. Effect of piezo-fiber orientation ($\boldsymbol{\Psi}$) in the ***xz***-plane on the frequency response of laminated symmetric cross-ply multiscale **HFRC** smart shell having wavy **CNTs**.

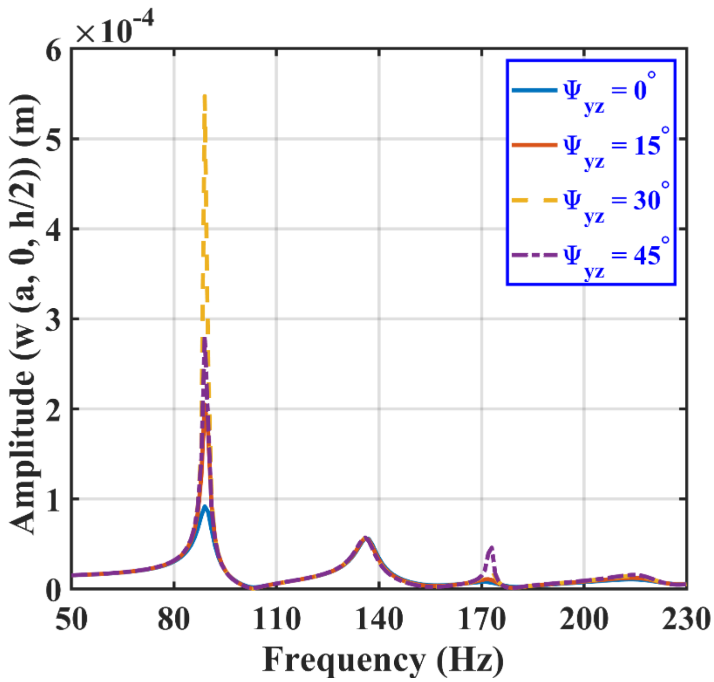

Figure 6.13. Effect of piezo-fiber orientation ($\boldsymbol{\Psi}$) in the ***yz***-plane on the frequency response of laminated symmetric cross-ply multiscale **HFRC** smart shell having wavy **CNTs**.

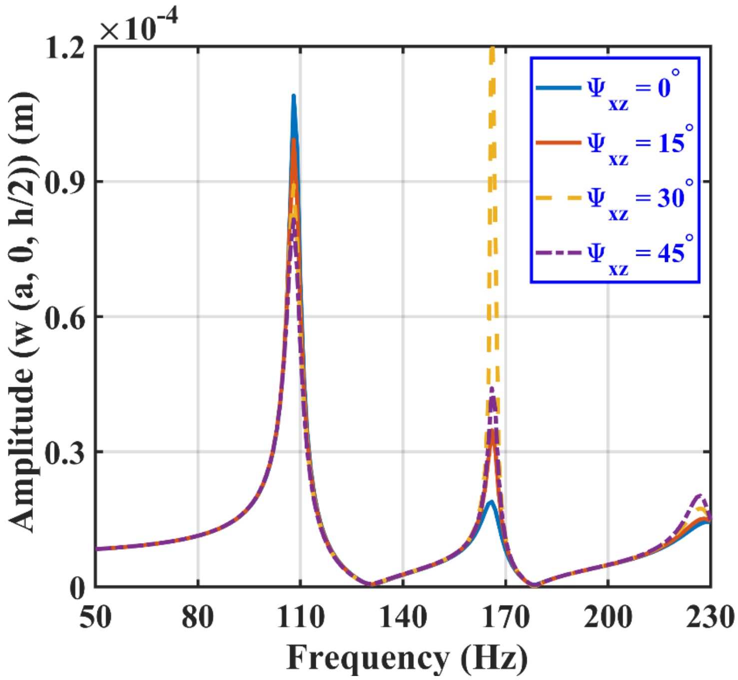

Figure 6.14. Effect of piezo-fiber orientation ($\boldsymbol{\Psi}$) in the ***xz***-plane on the frequency response of laminated anti-symmetric cross-ply multiscale **HFRC** smart shell having wavy **CNTs**.

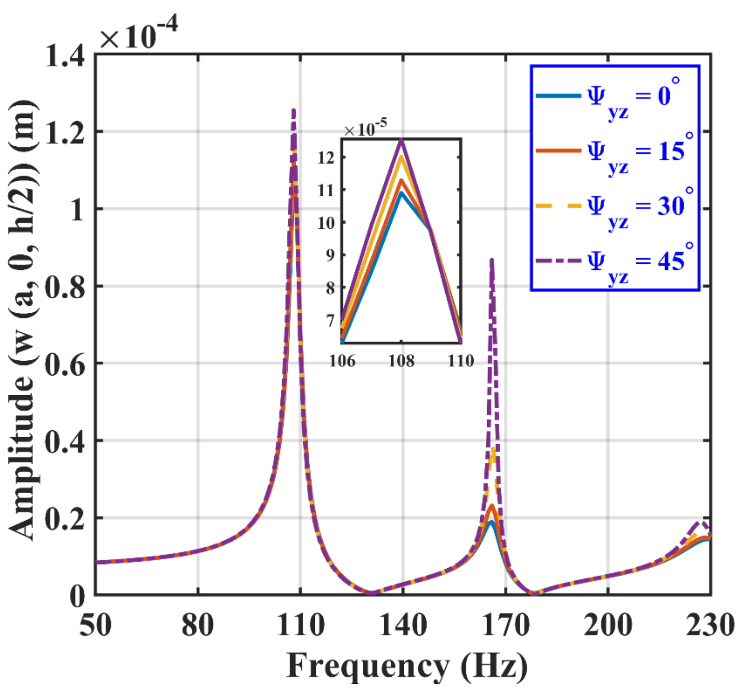

Figure 6.15. Effect of piezo-fiber orientation ($\boldsymbol{\Psi}$) in the ***yz***-plane on the frequency response of laminated anti-symmetric cross-ply multiscale **HFRC** smart shell having wavy **CNTs**.

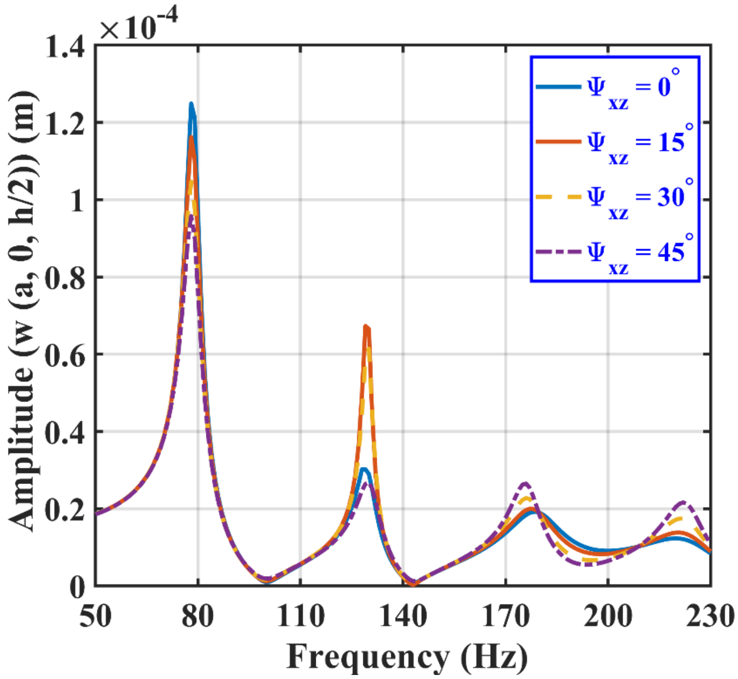

Figure 6.16. Effect of piezo-fiber orientation (***Ψ***) in the ***xz***-plane on the frequency response of laminated anti-symmetric angle-ply multiscale **HFRC** smart shell having wavy **CNTs**.

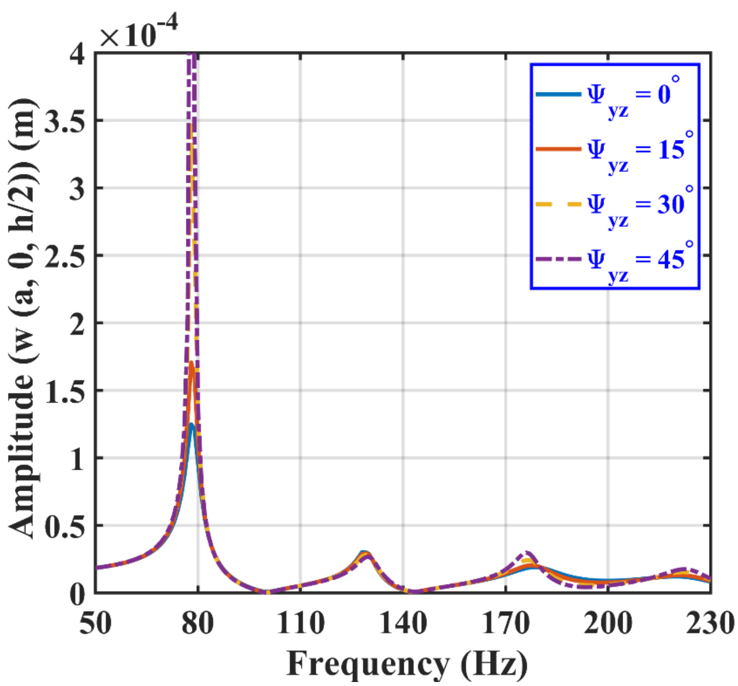

Figure 6.17. Effect of piezo-fiber orientation (***Ψ***) in the ***yz***-plane on the frequency response of laminated anti-symmetric angle-ply multiscale **HFRC** smart shell having wavy **CNTs**.

6.6 Summary

The present work focuses on the influence of **CNT** waviness on the damping behavior of the laminated multiscale **HFRC** smart shell, integrated with two **ACLD** treatment patches installed at the outer circumference of the substrate **HFRC** shell. The **ACLD** treatment patches consist of a viscoelastic layer and a constraining layer of **1–3 PZC**, responsible for the active damping. The effect of piezo-fiber orientation on the control authority of the **ACLD** treatment patches is also investigated. In this context, a **FE** model is developed based on the **Sinus** theory incorporating the **ZZ** effects by considering the **MZZF**. The outcomes of the proposed model are compared with the existing models, and the results are found to be in good agreement. Our findings suggest that considering the **ZZ** effects alleviates the amplitudes of vibrations. Thus, neglecting the **ZZ** effects can compromise the accuracy of the **FE** model. Furthermore, we investigate the active damping response of the laminated multiscale **HFRC** smart shell using the **SinusZZ** theory for the symmetric/anti-symmetric cross-ply and anti-symmetric angle-ply. For this, a simple closed-loop feedback model is used to compare the laminated multiscale **HFRC** smart shell's active damping performance (with straight and wavy **CNTs**) with that of the base composite smart shell. It is observed that the waviness of **CNTs** significantly influences the damping characteristics of the laminated **HFRC** shell. The maximum attenuation of vibrational amplitudes is obtained when the **CNT** waves are coplanar with the **1–3** plane. The results further show that the control authority of the **ACLD** treatment patches is maximum for the piezo-fiber orientation angle $\boldsymbol{\Psi} = 0°$ and $45°$. The control authority of the **ACLD** treatment patches is better when the piezo-fibers are oriented along the $\boldsymbol{xz}$-plane. This is due to the higher transverse piezoelectric coefficient $(\boldsymbol{e_{33}})$ observed when the piezo-fibers are oriented along the $\boldsymbol{xz}$-plane. Our preliminary findings suggest that **CNT** waviness can be utilized to tailor the direction of elastic properties of the proposed multiscale **HFRC**. The proposed **HFRC** can be used to develop superior, lightweight, and high-performance composite materials.

Chapter 7

Conclusions and Future Scope

In this Chapter, major conclusions drawn from the research work executed in this Thesis have been highlighted. Scopes for further research on these novel composites are suggested.

7.1 Major Conclusions

This dissertation is concerned with the investigation of damping performance of laminated multiscale **HFRC** smart beams, plates and shells integrated with **ACLD** treatment patches. In this context, first, two- and three-phase micromechanical models are developed based on the **MOM** and **MT** approaches. The distinct constructional feature of **HFRC** is that the **CNTs** and carbon fibers are considered to be uniformly distributed and reinforced along the axial direction (***x***-axis) of the advanced composite. Analytical micromechanics models have been developed for estimating the effective elastic properties of base composite and **HFRC**. Emphasis has also been placed on investigating the effect of waviness of **CNTs** on the effective elastic properties of the **HFRC**. The plane of waviness of the **CNTs** is coplanar either with the **1**–**2** (**1'**–**2'**) plane or with the **1**–**3** (**1'**–**3'**) plane while the **CNTs** are sinusoidally wavy and the carbon fiber is aligned along the **1**–direction. The micromechanics models developed here are capable of estimating the effective elastic properties of any continuous/short fiber-reinforced composite in which both the fiber and the matrix are homogeneous and orthotropic. The predicted values of the effective properties of the multiscale **HFRC** presented in this Thesis may serve the purpose of validating the further new micromechanics model and experimental investigations.

Second, the investigation is carried out for the **ACLD** of vibration amplitudes of laminated multiscale **HFRC** beams, plates, and shells. The constraining layer of the

ACLD treatment is considered to be composed of vertically/obliquely reinforced **1–3 PZC** material. Based on the layerwise displacement theories, electro-mechanical finite element models of the overall **HFRC/ACLD** beam, plate, and shell system have been derived. A simple velocity feedback control law is used to introduce the active damping in the overall structures. In the case of **HFRC** smart beams, a single patch of **ACLD** treatment is used which is located at the top surface of the cantilever beam while two **ACLD** patches are mounted on the top surface of the **HFRC** smart plates and at the upper circumference of the doubly curved **HFRC** smart shells. The numerical results are shown for the three cases: symmetric and anti-symmetric cross-ply, and antisymmetric angle-ply. The following main conclusions are drawn from the work carried out in this Thesis:

- The incorporation of straight **CNTs** significantly improves the values of the effective elastic constants of the multiscale **HFRC** over their values without **CNTs**. Since the transverse properties of the **HFRC** are significantly improved without the cost of the values of the in-plane effective elastic constants, these **HFRC** will have better strength against the transverse dynamic excitation.
- The effective elastic properties of the **HFRC** estimated by the analytical micromechanics models based on the **MOM** approach and the **MT** method are in excellent agreement, also, these analytical micromechanical models require much less computational time. Hence, for predicting all effective properties of the advanced composite one could adopt the analytical micromechanics models.
- When the sinusoidally wavy **CNTs** are coplanar with the **1**–**2** (**1'**–**2'**) and **1**–**3** (**1'**–**3'**) plane then the transverse effective elastic properties of the multiscale HFRC are significantly improved over their values with straight **CNTs** for the higher values of the wave frequencies and the amplitudes of the wavy **CNTs**. Thus the present study suggests that the wav**y CNTs** can be properly utilized to construct advanced hybrid composites with superior elastic properties.
- The **ACLD** treatment significantly improves the active damping characteristics of the laminated multiscale **HFRC** smart beams, plates, and shells over the passive damping for suppressing their transient vibrations.
- The contribution of transverse actuation by the **1–3 PZC** constraining layer is significantly larger than that of the in-plane actuation by the same for causing the

active damping of laminated multiscale **HFRC** smart beams, plates, and shells.

- The performance of the **ACLD** patches for controlling the transient vibrations of smart laminated multiscale **HFRC** plates and shells is significantly influenced by the piezoelectric fiber orientation angle of **1–3 PZC**.
- The performance of the **ACLD** patches for attenuating the amplitude of vibrations of smart laminated **HFRC** beams, plates, and shells significantly increases as compared to the base composite because of the incorporation of **CNTs**.
- The **HFRC** with wavy **CNTs** being coplanar with the **1**–**3** (**1'–3'**) significantly improves the performance of the **ACLD** patches than the **HFRC** the straight **CNTs**.
- The wavy **CNTs** can be properly exploited for achieving structural benefits from the excellent elastic properties of **CNTs** and high-performance smart structures can be developed which may be superior to the existing ones.

7.2 Scope for Further Research

Although the basic purpose of this Thesis has been fulfilled by the contributions presented in the preceding chapters of this dissertation, further research may still be pursued for the development of high-performance smart structures. Some of the further research works that may be undertaken in line with the present work are as follows:

- Experimental characterization of the **HFRC** for multifunctional structures is a natural extension of this work.
- Predictions of the effective electrical and thermal properties of the **HFRC**.
- Derivation of the accurate micromechanics models for predicting the strength of the **HFRC**.
- Smart control of geometrically nonlinear vibrations of smart laminated **HFRC** beams, plates, and shells is the natural extension of this work and provides scope for further work.
- The experimental verification of the theoretical models developed in this Thesis is also a challenging task that can be taken up for further research.
- More accurate theories like **3D** solutions and mixed variational theories can be adopted for developing the FE models.

References

Agnihotri, P., Basu, S. and Kar, K.K., 2011. Effect of carbon nanotube length and density on the properties of carbon nanotube-coated carbon fiber/polyester composites. *Carbon*, 49(9), pp.3098-3106.

Al-Ostaz, A., Pal, G., Mantena, P.R. and Cheng, A., 2008. Molecular dynamics simulation of SWCNT–polymer nanocomposite and its constituents. *Journal of Materials Science*, 43(1), pp.164-173.

Alian, A.R., El-Borgi, S. and Meguid, S.A., 2016. Multiscale modeling of the effect of waviness and agglomeration of CNTs on the elastic properties of nanocomposites. *Computational Materials Science*, 117, pp.195-204.

Anumandla, V. and Gibson, R.F., 2006. A comprehensive closed form micromechanics model for estimating the elastic modulus of nanotube-reinforced composites. *Composites Part A: Applied Science and Manufactu*ring, 37(12), pp.2178-2185.

Ashrafi, B. and Hubert, P., 2006. Modeling the elastic properties of carbon nanotube array/polymer composites. *Composites Science and Technology*, 66(3-4), pp.387-396.

Ayatollahi, M.R., Shadlou, S. and Shokrieh, M.M., 2011. Multiscale modeling for mechanical properties of carbon nanotube reinforced nanocomposites subjected to different types of loading. *Composite Structures*, 93(9), pp.2250-2259.

Azvine, B., Tomlinson, G.R. and Wynne, R.J., 1995. Use of active constrained-layer damping for controlling resonant vibration. *Smart Materials and Structures*, 4(1), p.1.

Azzouz, M.S. and Ro, J., 2002. Control of sound radiation of an active constrained layer damping plate/cavity system using the structural intensity approach. *Journal of Vibration and Control*, 8(6), pp.903-918.

Bailey, T. and Hubbard Jr, J.E., 1985. Distributed piezoelectric-polymer active vibration control of a cantilever beam. *Journal of Guidance, Control, and Dynamics*, *8*(5), pp.605-611.

Balamurugan, V. and Narayanan, S., 2001a. Active vibration control of smart shells using distributed piezoelectric sensors and actuators. *Smart Materials and Structures*, 10(2), p.173.

Balamurugan, V. and Narayanan, S., 2001b. Shell finite element for smart piezoelectric composite plate/shell structures and its application to the study of active vibration control. *Finite Elements in Analysis and Design*, 37(9), pp.713-738.

Batra, R.C. and Gupta, S.S., 2008. Wall thickness and radial breathing modes of single-walled carbon nanotubes. *Journal of Applied Mechanics*, 75(6).

Batra, R.C., Liang, X.Q. and Yang, J.S., 1996. The vibration of a simply supported rectangular elastic plate due to piezoelectric actuators. *International Journal of Solids and Structures*, 33(11), pp.1597-1618.

Batra, R.C. and Sears, A., 2007. Uniform radial expansion/contraction of carbon nanotubes and their transverse elastic moduli. *Modelling and Simulation in Materials Science and Engineering*, 15(8), p.835.

Baz, A., 1997. Dynamic boundary control of beams using active constrained layer damping. *Mechanical Systems and Signal Processing*, 11(6), pp.811-825.

Baz, A., 2000. Spectral finite-element modeling of the longitudinal wave propagation in rods treated with active constrained layer damping. *Smart Materials and Structures*, 9(3), p.372.

Baz, A. and Chen, T., 2000. Control of axi-symmetric vibrations of cylindrical shells using active constrained layer damping. *Thin-Walled Structures*, 36(1), pp.1-20.

Baz, A. and Poh, S., 1990. Experimental implementation of the modified independent modal space control method. *Journal of Sound and Vibration*, 139(1), pp.133-149.

Baz, A., Poh, S. and Fedor, J., 1992. Independent modal space control with positive position feedback. ASME Journal of Dynamic Systems, *Measurement and Control*, 114(1), pp. 96–103.

Baz, A. and Ro, J., 1995a. Optimum design and control of active constrained layer damping. *Journal of Vibration and Acoustics*, 117(June 1995), pp. 135–144.

Baz, A. and Ro, J., 1995b. Performance characteristics of active constrained layer damping. *Shock and Vibration*, 2(1), pp.33-42.

Baz, A. and Ro, J., 1995c. Vibration control of plates with active constrained-layer damping. in Proceedings SPIE 2445, *Smart Structures and Materials 1995: Passive Damping, San Diego, CA, United States (5 May 1995)*, pp. 393–409.

Baz, A. and Ro, J., 1996. Vibration control of plates with active constrained layer damping. *Smart Materials and Structures*, 5(3), p.272.

Baz, A. and Ro, J., 2001. Vibration control of rotating beams with active constrained layer damping. *Smart Materials and Structures*, 10(1), p.112.

Beheshti-Aval, S.B. and Lezgy-Nazargah, M.J.S.S., 2010. Assessment of velocity-acceleration feedback in optimal control of smart piezoelectric beams. *Smart Structures and Systems*, 6(8), pp.921-938.

Bendary, I.M., Elshafei, M.A. and Riad, A.M., 2010. Finite element model of smart beams with distributed piezoelectric actuators. *Journal of Intelligent Material Systems and Structures*, 21(7), pp.747-758.

Benveniste, Y., 1987. A new approach to the application of Mori-Tanaka's theory in composite materials. *Mechanics of Materials*, 6(2), pp.147-157.

Benveniste, Y. and Dvorak, G.J., 1992. Uniform fields and universal relations in piezoelectric composites. *Journal of the Mechanics and Physics of Solids*, 40(6), pp.1295-1312.

Berhan, L., Yi, Y.B. and Sastry, A.M., 2004. Effect of nanorope waviness on the effective moduli of nanotube sheets. *Journal of Applied Physics*, 95(9), pp.5027-5034.

Bower, C., Zhu, W., Jin, S. and Zhou, O., 2000. Plasma-induced alignment of carbon nanotubes. *Applied Physics Letters*, 77(6), pp.830-832.

Bradbury, C.R., Gomon, J.K., Kollo, L., Kwon, H. and Leparoux, M., 2014. Hardness of multi wall carbon nanotubes reinforced aluminium matrix composites. *Journal of Alloys and Compounds*, 585, pp.362-367.

Bradford, P.D., Wang, X., Zhao, H., Maria, J.P., Jia, Q. and Zhu, Y.T., 2010. A novel approach to fabricate high volume fraction nanocomposites with long aligned carbon nanotubes. *Composites Science and Technology*, 70(13), pp.1980-1985.

Carrera, E., 2003. Historical review of zig-zag theories for multilayered plates and shells. *Applied Mechanics Reviews*, 56(3), pp.287-308.

Carrera, E., 2004. On the use of the Murakami's zig-zag function in the modeling of layered plates and shells. *Computers & Structures*, 82(7-8), pp.541-554.

Chan, H.L.W. and Unsworth, J., 1989. Simple model for piezoelectric ceramic/polymer 1-3 composites used in ultrasonic transducer applications. *IEEE Transactions on Ultrasonics, Ferroelectrics, and Frequency Control*, 36(4), pp.434-441.

Chantalakhana, C. and Stanway, R., 2001. Active constrained layer damping of clamped-clamped plate vibrations. *Journal of Sound and Vibration*, 241(5), pp.755-777.

Chen, L.H., AuBuchon, J.F., Chen, I.C., Daraio, C., Ye, X.R., Gapin, A., Jin, S. and Wang, C.M., 2006. Growth of aligned carbon nanotubes on carbon microfibers by dc plasma-enhanced chemical vapor deposition. *Applied Physics Letters*, 88(3), p.033103.

Chen, X., Beyerlein, I.J. and Brinson, L.C., 2011. Bridged crack models for the toughness of composites reinforced with curved nanotubes. *Journal of the Mechanics and Physics of Solids*, 59(9), pp.1938-1952.

Cheng, H.C., Liu, Y.L., Hsu, Y.C. and Chen, W.H., 2009. Atomistic-continuum modeling for mechanical properties of single-walled carbon nanotubes. *International Journal of Solids and Structures*, 46(7-8), pp.1695-1704.

Ci, L.J., Zhao, Z.G. and Bai, J.B., 2005. Direct growth of carbon nanotubes on the surface of ceramic fibers. *Carbon*, 43(4), pp.883-886.

Crawley, E.F., de Luis, J., Hagood, N.W. and Anderson, E.H., 1988, June. Development of piezoelectric technology for applications in control of intelligent structures. In 1988 *American Control Conference* (pp. 1890-1896). IEEE.

Datta, P. and Ray, M.C., 2016. Three-dimensional fractional derivative model of smart constrained layer damping treatment for composite plates. *Composite Structures*, 156, pp.291-306.

Deepak, B.P., Ganguli, R. and Gopalakrishnan, S., 2012. Dynamics of rotating composite beams: A comparative study between CNT reinforced polymer composite beams and laminated composite beams using spectral finite elements. *International Journal of Mechanical Sciences*, *64*(1), pp.110-126.

Dikin, D.A., Chen, X., Ding, W., Wagner, G. and Ruoff, R.S., 2003. Resonance vibration of amorphous SiO 2 nanowires driven by mechanical or electrical field excitation. *Journal of Applied Physics*, 93(1), pp.226-230.

Dimitriadis, E.K., Fuller, C.R. and Rogers, C.A., 1991. Piezoelectric actuators for distributed vibration excitation of thin plates. *Journal of Vibration and Acoustics*, 113(1), pp. 100–107.

Dong, X.J., Meng, G. and Peng, J.C., 2006. Vibration control of piezoelectric smart structures based on system identification technique: Numerical simulation and experimental study. *Journal of Sound and Vibration*, 297(3-5), pp.680-693.

Dresselhaus, M.S., Dresselhaus, G. and Eklund, P.C., 1996. Science of fullerenes and carbon nanotubes: their properties and applications. *Elsevier*.

Ebrahimi, F. and Dabbagh, A., 2020. Vibration analysis of multi-scale hybrid nanocomposite shells by considering nanofillers' aggregation. *Waves in Random and Complex Media*, pp.1-19.

Ebrahimi, F. and Dabbagh, A., 2021. An analytical solution for static stability of multi-scale hybrid nanocomposite plates. *Engineering with Computers*, 37(1), pp.545-559.

Ebrahimi, F., Nopour, R. and Dabbagh, A., 2021. Effect of viscoelastic properties of polymer and wavy shape of the CNTs on the vibrational behaviors of CNT/glass fiber/polymer plates. *Engineering with Computers*, pp.1-14.

Eisenberger, M., Abramovich, H. and Shulepov, O., 1995. Dynamic stiffness analysis of laminated beams using a first order shear deformation theory. *Composite Structures*, 31(4), pp.265-271.

Esawi, A.M., Morsi, K., Sayed, A., Taher, M. and Lanka, S.J.C.S., 2010. Effect of carbon nanotube (CNT) content on the mechanical properties of CNT-reinforced aluminium composites. *Composites Science and Technology*, 70(16), pp.2237-2241.

Esteva, M. and Spanos, P., 2009. Effective elastic properties of nanotube reinforced composites with slightly weakened interfaces. *Journal of Mechanics of Materials and Structures*, 4(5), pp.887-900.

Fisher, F.T., Bradshaw, R.D. and Brinson, L.C., 2002. Effects of nanotube waviness on the modulus of nanotube-reinforced polymers. *Applied Physics Letters*, 80(24), pp.4647-4649.

Fung, E.H.K. and Yau, D.T.W., 2004. Vibration characteristics of a rotating flexible arm with ACLD treatment. *Journal of Sound and Vibration*, 269(1-2), pp.165-182.

Gao, G., Cagin, T. and Goddard III, W.A., 1998. Energetics, structure, mechanical and vibrational properties of single-walled carbon nanotubes. *Nanotechnology*, 9(3), p.184.

Gao, X.L. and Li, K., 2005. A shear-lag model for carbon nanotube-reinforced polymer composites. *International Journal of Solids and Structures*, 42(5-6), pp.1649-1667.

Gholami, R., Ansari, R. and Gholami, Y., 2018. Numerical study on the nonlinear resonant dynamics of carbon nanotube/fiber/polymer multiscale laminated composite rectangular plates with various boundary conditions. *Aerospace Science and Technology*, 78, pp.118-129.

Gojny, F.H., Wichmann, M.H., Fiedler, B., Bauhofer, W. and Schulte, K., 2005. Influence of nano-modification on the mechanical and electrical properties of conventional fibre-reinforced composites. *Composites Part A: Applied Science and Manufacturing*, 36(11), pp.1525-1535.

Grimmer, C.S. and Dharan, C.K.H., 2008. High-cycle fatigue of hybrid carbon nanotube/glass fiber/polymer composites. *Journal of Materials Science*, 43(13), pp.4487-4492.

Gupta, M., Meguid, S.A. and Kundalwal, S.I., 2022a. Synergistic effect of surface-flexoelectricity on electromechanical response of BN-based nanobeam. *International Journal of Mechanics and Materials in Design*, 18, pp 3–19.

Gupta, M., Ray, M.C., Patil, N.D. and Kundalwal, S.I., 2021. Dynamic modelling and analysis of smart carbon nanotube-based hybrid composite beams: Analytical and finite element study. *Proceedings of the Institution of Mechanical Engineers, Part L: Journal of Materials: Design and Applications*, 235(10), pp.2185-2206.

Gupta, M., Ray, M.C., Patil, N.D. and Kundalwal, S.I., 2022b. Effect of orientation of CNTs and piezoelectric fibers on the damping performance of multiscale composite plate. *Journal of Intelligent Material Systems and Structures*. (Accepted)

Gupta, M., Ray, M.C., Patil, N.D. and Kundalwal, S.I., 2022c. Smart damping of a simply supported laminated CNT-based hybrid composite plate using FE approach. *Thin-Walled Structures*, 171, p.108782.

Gupta, M., Patil, N. D. and Kundalwal, S. I., 2022d. Active damping of multiscale composite shells using Sinus theory incorporated with Murakami's zig-zag function. *Thin-Walled Structures*. (Under revision)

Gupta, S.S., Bosco, F.G. and Batra, R.C., 2010. Wall thickness and elastic moduli of single-walled carbon nanotubes from frequencies of axial, torsional and inextensional modes of vibration. *Computational Materials Science*, *47*(4), pp.1049-1059.

Ha, S.K., Keilers, C. and Chang, F.K., 1992. Finite element analysis of composite structures containing distributed piezoceramic sensors and actuators. *AIAA journal*, 30(3), pp.772-780.

Hamada, N., Sawada, S.I. and Oshiyama, A., 1992. New one-dimensional conductors: Graphitic microtubules. *Physical review letters*, 68(10), p.1579.

Hasanzadeh, M., Ansari, R. and Hassanzadeh-Aghdam, M.K., 2019. Evaluation of effective properties of piezoelectric hybrid composites containing carbon nanotubes. *Mechanics of Materials*, 129, pp.63-79.

Huang, S.C., Inman, D.J. and Austin, E.M., 1996. Some design considerations for active and passive constrained layer damping treatments. *Smart Materials and Structures*, 5(3), p.301.

Huang, X., Zhi, C. and Jiang, P., 2012. Toward effective synergetic effects from graphene nanoplatelets and carbon nanotubes on thermal conductivity of ultrahigh volume fraction nanocarbon epoxy composites. *The Journal of Physical Chemistry C*, 116(44), pp.23812-23820.

Iijima, S., 1991. Helical microtubules of graphitic carbon. *Nature*, 354(6348), pp.56-58.

Iijima, S. and Ichihashi, T., 1993. Single-shell carbon nanotubes of 1-nm diameter. *Nature*, 363(6430), pp.603-605.

Iwahori, Y., Ishiwata, S., Sumizawa, T. and Ishikawa, T., 2005. Mechanical properties improvements in two-phase and three-phase composites using carbon nano-fiber dispersed resin. *Composites Part A: Applied Science and Manufacturing*, 36(10), pp.1430-1439.

Jeung, Y.S. and Shen, I.Y., 2001. Development of isoparametric, degenerate constrained layer element for plate and shell structures. *AIAA journal*, 39(10), pp.1997-2005.

Jiang, B., Liu, C., Zhang, C., Liang, R. and Wang, B., 2009. Maximum nanotube volume fraction and its effect on overall elastic properties of nanotube-reinforced composites. *Composites Part B: Engineering*, 40(3), pp.212-217.

Karousis, N., Tagmatarchis, N. and Tasis, D., 2010. Current progress on the chemical modification of carbon nanotubes. *Chemical reviews*, 110(9), pp.5366-5397.

Kattimani, S.C., 2017. Active damping of multiferroic composite plates using 1–3 piezoelectric composites. *Smart Materials and Structures*, 26(12), p.125021.

Kattimani, S.C. and Ray, M.C., 2014. Smart damping of geometrically nonlinear vibrations of magneto-electro-elastic plates. *Composite Structures*, 114, pp.51-63.

Khan, N.M. and Kumar, R.S., 2021a. Smart control of cylindrical shells incorporating Murakami zig-zag function. *Composite Structures*, 257, p.113044.

Khan, N.M. and Suresh Kumar, R., 2021b. Smart control of laminated plates using Murakami zig-zag functions. *International Journal of Mechanics and Materials in Design*, 17(3), pp.463-487.

Kim, M., Park, Y.B., Okoli, O.I. and Zhang, C., 2009. Processing, characterization, and modeling of carbon nanotube-reinforced multiscale composites. *Composites Science and Technology*, 69(3-4), pp.335-342.

Kim, P., Shi, L., Majumdar, A. and McEuen, P.L., 2001. Thermal transport measurements of individual multiwalled nanotubes. *Physical Review Letters*, 87(21), p.215502.

Klein, M.L. and Shinoda, W., 2008. Large-scale molecular dynamics simulations of self-assembling systems. *Science*, 321(5890), pp.798-800.

Krishnan, A., Dujardin, E., Ebbesen, T.W., Yianilos, P.N. and Treacy, M.M.J., 1998. Young's modulus of single-walled nanotubes. *Physical Review B*, 58(20), p.14013.

Kucuk, I., Sadek, I.S., Zeini, E. and Adali, S., 2011. Optimal vibration control of piezolaminated smart beams by the maximum principle. *Computers & Structures*, 89(9-10), pp.744-749.

Kumar, N. and Singh, S.P., 2009. Vibration and damping characteristics of beams with active constrained layer treatments under parametric variations. *Materials & Design*, 30(10), pp.4162-4174.

Kumar, N. and Singh, S.P., 2012. Vibration control of curved panel using smart damping. *Mechanical Systems and Signal Processing*, 30, pp.232-247.

Kumar, R.S., Kundalwal, S.I. and Ray, M.C., 2017. Control of large amplitude vibrations of doubly curved sandwich shells composed of fuzzy fiber reinforced composite facings. *Aerospace Science and Technology*, 70, pp.10-28.

Kundalwal, S.I., 2018. Review on micromechanics of nano-and micro-fiber reinforced composites. *Polymer Composites*, 39(12), pp.4243-4274.

Kundalwal, S.I. and Meguid, S.A., 2015. Effect of carbon nanotube waviness on active damping of laminated hybrid composite shells. *Acta Mechanica*, 226(6), pp.2035-2052.

Kundalwal, S.I. and Ray, M.C., 2011. Micromechanical analysis of fuzzy fiber reinforced composites. *International Journal of Mechanics and Materials in Design*, 7(2), pp.149-166.

Kundalwal, S.I. and Ray, M.C., 2013. Effect of carbon nanotube waviness on the elastic properties of the fuzzy fiber reinforced composites. *Journal of Applied Mechanics*, 80(2).

Kundalwal, S.I. and Ray, M.C., 2016. Smart damping of fuzzy fiber reinforced composite plates using 1--3 piezoelectric composites. *Journal of Vibration and Control*, 22(6), pp.1526-1546.

Kundalwal, S.I., Ray, M.C. and Meguid, S.A., 2014. Shear lag model for regularly staggered short fuzzy fiber reinforced composite. *Journal of Applied Mechanics*, 81(9).

Kundalwal, S.I., Kumar, R.S. and Ray, M.C., 2013. Smart damping of laminated fuzzy fiber reinforced composite shells using 1–3 piezoelectric composites. *Smart Materials and Structures*, 22(10), p.105001.

Larbi, W., Deü, J.F. and Ohayon, R., 2012. Finite element formulation of smart piezoelectric composite plates coupled with acoustic fluid. *Composite Structures*, 94(2), pp.501-509.

Li, C. and Chou, T.W., 2003. A structural mechanics approach for the analysis of carbon nanotubes. *International Journal of Solids and Structures*, 40(10), pp.2487-2499.

Li, C. and Chou, T.W., 2009. Failure of carbon nanotube/polymer composites and the effect of nanotube waviness. *Composites Part A: Applied Science and Manufacturing*, 40(10), pp.1580-1586.

Li, F.M., Kishimoto, K., Wang, Y.S., Chen, Z.B. and Huang, W.H., 2008. Vibration control of beams with active constrained layer damping. *Smart Materials and Structures*, 17(6), p.065036.

Li, L., Zhang, D. and Guo, Y., 2017. Dynamic modeling and analysis of a rotating flexible beam with smart ACLD treatment. *Composites Part B: Engineering*, 131, pp.221-236.

Lim, Y.H., Varadan, V.V. and Varadan, V.K., 2002. Closed loop finite-element modeling of active constrained layer damping in the time domain analysis. *Smart Materials and Structures*, 11(1), p.89.

Lin, M. and Chang, F.K., 2002. The manufacture of composite structures with a built-in network of piezoceramics. *Composites Science and Technology*, 62(7-8), pp.919-939.

Liu, A., Huang, J.H., Wang, K.W. and Bakis, C.E., 2006. Effects of interfacial friction on the damping characteristics of composites containing randomly oriented carbon nanotube ropes. *Journal of Intelligent Material Systems and Structures*, 17(3), pp.217-229.

Liu, J.Z., Zheng, Q.S., Wang, L.F. and Jiang, Q., 2005. Mechanical properties of single-walled carbon nanotube bundles as bulk materials. *Journal of the Mechanics and Physics of Solids*, 53(1), pp.123-142.

Liu, L., Zhang, Z. and Hua, H., 2007. Dynamic characteristics of rotating cantilever plates with active constrained layer damping treatments. *Smart Materials and Structures*, 16(5), p.1849.

Liu, Y.J. and Chen, X.L., 2003. Evaluations of the effective material properties of carbon nanotube-based composites using a nanoscale representative volume element. *Mechanics of Materials*, 35(1-2), pp.69-81.

Lu, J.P., 1997. Elastic properties of carbon nanotubes and nanoropes. *Physical Review Letters*, 79(7), p.1297.

Lu, J.P. and Han, J., 1998. Carbon nanotubes and nanotube-based nano devices. *International Journal of High speed Electronics and Systems*, 9(01), pp.101-123.

Ma, X., Scarpa, F., Peng, H.X., Allegri, G., Yuan, J. and Ciobanu, R., 2015. Design of a hybrid carbon fibre/carbon nanotube composite for enhanced lightning strike resistance. *Aerospace Science and Technology*, 47, pp.367-377.

Mallek, H., Jrad, H., Wali, M. and Dammak, F., 2021. Nonlinear dynamic analysis of piezoelectric-bonded FG-CNTR composite structures using an improved FSDT theory. *Engineering with Computers*, *37*(2), pp.1389-1407.

Mallik, N. and Ray, M.C., 2003. Effective coefficients of piezoelectric fiber-reinforced composites. *AIAA Journal*, 41(4), pp.704-710.

Mathur, R.B., Chatterjee, S. and Singh, B.P., 2008. Growth of carbon nanotubes on carbon fibre substrates to produce hybrid/phenolic composites with improved mechanical properties. *Composites Science and Technology*, 68(7-8), pp.1608-1615.

Mecklenburg, M., Mizushima, D., Ohtake, N., Bauhofer, W., Fiedler, B. and Schulte, K., 2015. On the manufacturing and electrical and mechanical properties of ultra-high wt.% fraction aligned MWCNT and randomly oriented CNT epoxy composites. *Carbon*, 91, pp.275-290.

Meguid, S.A., Wernik, J.M. and Cheng, Z.Q., 2010. Atomistic-based continuum representation of the effective properties of nano-reinforced epoxies. *International Journal of Solids and Structures*, 47(13), pp.1723-1736.

Meguid, S.A., Wernik, J.M. and Al Jahwari, F., 2013. Toughening mechanisms in multiphase nanocomposites. *International Journal of Mechanics and Materials in Design*, 9(2), pp.115-125.

Mintmire, J.W., Dunlap, B.I. and White, C.T., 1992. Are fullerene tubules metallic?. *Physical Review Letters*, 68(5), p.631.

Mook, G., Pohl, J. and Michel, F., 2003. Non-destructive characterization of smart CFRP structures. *Smart Materials and Structures*, 12(6), p.997.

Murakami, H., 1986. Laminated composite plate theory with improved in-plane responses. *Journal of Applied Mechanics*, 53(3), pp. 661–666.

Narita, Y., Ohta, Y. and Saito, M., 1993. Finite element study for natural frequencies of cross-ply laminated cylindrical shells. *Composite Structures*, 26(1-2), pp.55-62.

Neves, A.M.A., Ferreira, A.J.M., Carrera, E., Cinefra, M., Jorge, R.M.N., Mota Soares, C.M. and Araújo, A.L., 2017. Influence of zig-zag and warping effects on buckling of functionally graded sandwich plates according to sinusoidal shear deformation theories. *Mechanics of Advanced Materials and Structures*, 24(5), pp.360-376.

Ni, Q., Xiang, Y., Huang, Y. and Lu, J., 2013. Modeling and dynamics analysis of shells of revolution by partially active constrained layer damping treatment. *Acta Mechanica Solida Sinica*, 26(5), pp.468-479.

Ning, J., Zhang, J., Pan, Y. and Guo, J., 2003. Fabrication and mechanical properties of SiO2 matrix composites reinforced by carbon nanotube. *Materials Science and Engineering: A*, 357(1-2), pp.392-396.

Norouzzadeh, A., Ansari, R. and Darvizeh, M., 2021. From nonlinear micromorphic to nonlinear micropolar shell theory. *Applied Mathematical Modelling*, 100, pp.689-727.

Odegard, G.M., Gates, T.S., Nicholson, L.M. and Wise, K.E., 2002. Equivalent-continuum modeling of nano-structured materials. *Composites Science and Technology*, 62(14), pp.1869-1880.

Odegard, G.M., Gates, T.S., Wise, K.E., Park, C. and Siochi, E.J., 2003. Constitutive modeling of nanotube–reinforced polymer composites. *Composites Science and Technology*, 63(11), pp.1671-1687.

Pan, Z.W., Xie, S.S., Chang, B.H., Sun, L.F., Zhou, W.Y. and Wang, G., 1999. Direct growth of aligned open carbon nanotubes by chemical vapor deposition. *Chemical Physics Letters*, 299(1), pp.97-102.

Pantano, A.N.T.O.N.I.O. and Cappello, F.R.A.N.C.E.S.C.O., 2008. Numerical model for composite material with polymer matrix reinforced by carbon nanotubes. *Meccanica*, 43(2), pp.263-270.

Park, J.M., Kim, D.S., Lee, J.R. and Kim, T.W., 2003. Nondestructive damage sensitivity and reinforcing effect of carbon nanotube/epoxy composites using electro-micromechanical technique. *Materials Science and Engineering: C*, 23(6-8), pp.971-975.

Peddavarapu, S. and Bharathi, R.J., 2018. Dry sliding wear behaviour of AA6082-5% sic and AA6082-5% tib2 metal matrix composites. *Materials Today: Proceedings*, 5(6), pp.14507-14511.

Pettermann, H.E. and Suresh, S., 2000. A comprehensive unit cell model: a study of coupled effects in piezoelectric 1–3 composites. *International Journal of Solids and Structures*, 37(39), pp.5447-5464.

Poh, S., Baz, A. and Balachandran, B., 1996. Experimental adaptive control of sound radiation from a panel into an acoustic cavity using active constrained layer damping. *Smart Materials and Structures*, 5(5), p.649.

Poncharal, P., Wang, Z.L., Ugarte, D. and De Heer, W.A., 1999. Electrostatic deflections and electromechanical resonances of carbon nanotubes. *Science*, 283(5407), pp.1513-1516.

Providakis, C.P., Voutetaki, M.E., Stauroulaki, M.E. and Kontoni, D.P., 2007. FEM Modeling of electromechanical impedance for the analysis of smart damping treatments. *In Advances in Computer, Information, and Systems Sciences, and Engineering (pp. 129-134). Springer, Dordrecht*.

Qian, D., Dickey, E.C., Andrews, R. and Rantell, T., 2000. Load transfer and deformation mechanisms in carbon nanotube-polystyrene composites. *Applied Physics Letters*, 76(20), pp.2868-2870.

Qiu, Y.P. and Weng, G.J., 1990. On the application of Mori-Tanaka's theory involving transversely isotropic spheroidal inclusions. *International Journal of Engineering Science*, 28(11), pp.1121-1137.

Qiu, Z.C., Zhang, X.M., Wu, H.X. and Zhang, H.H., 2007. Optimal placement and active vibration control for piezoelectric smart flexible cantilever plate. *Journal of sound and Vibration*, 301(3-5), pp.521-543.

Rathi, A., Kundalwal, S., Singh, S. and Kumar, A., 2021. Adhesive and viscoelastic response of MWCNT/ZrO2 hybrid epoxy nanocomposites. *Journal of Mechanics of Materials and Structures*, 16(3), pp.281-292.

Rathi, A. and Kundalwal, S.I., 2020. Mechanical and fracture behavior of MWCNT/ZrO2/epoxy nanocomposite systems: Experimental and numerical study. *Polymer Composites*, 41(6), pp.2491-2507.

Ray, M.C., 1998. Optimal control of laminated plate with piezoelectric sensor and actuator layers. *AIAA Journal*, 36(12), pp.2204-2208.

Ray, M.C., 2003. Optimal control of laminated shells using piezoelectric sensor and actuator layers. *AIAA Journal*, 41(6), pp.1151-1157.

Ray, M.C., 2006. Micromechanics of piezoelectric composites with improved effective piezoelectric constant. *International Journal of Mechanics and Materials in Design*, 3(4), pp.361-371.

Ray, M.C., Faye, A., Patra, S. and Bhattacharyya, R., 2008. Theoretical and experimental investigations on the active structural–acoustic control of a thin plate using a vertically reinforced 1-3 piezoelectric composite. *Smart Materials and Structures*, 18(1), p.015012.

Ray, M.C. and Balaji, R., 2007. Active structural–acoustic control of laminated cylindrical panels using smart damping treatment. *International Journal of Mechanical Sciences*, 49(9), pp.1001-1017.

Ray, M.C. and Batra, R.C., 2007a. A single-walled carbon nanotube reinforced 1–3 piezoelectric composite for active control of smart structures. *Smart Materials and Structures*, 16(5), p.1936.

Ray, M.C. and Batra, R.C., 2007b. Vertically reinforced 1-3 piezoelectric composites for active damping of functionally graded plates. *AIAA Journal*, 45(7), pp.1779-1784.

Ray, M.C. and Batra, R.C., 2008. Smart constrained layer damping of functionally graded shells using vertically/obliquely reinforced 1–3 piezocomposite under a thermal environment. *Smart Materials and Structures*, 17(5), p.055007.

Ray, M.C. and Batra, R.C., 2009. Effective properties of carbon nanotube and piezoelectric fiber reinforced hybrid smart composites. *Journal of Applied Mechanics*, 76(3).

Ray, M.C. and Baz, A., 1997. Optimization of energy dissipation of active constrained layer damping treatments of plates. *Journal of Sound and Vibration*, 208(3), pp.391-406.

Ray, M.C. and Kundalwal, S.I., 2014. Effect of carbon nanotube waviness on the load transfer characteristics of short fuzzy fiber-reinforced composite. *Journal of Nanomechanics and Micromechanics*, 4(2), p.A4013010.

Ray, M.C. and Mallik, N., 2003. Active control of laminated composite beams using a piezoelectric fiber reinforced composite layer. *Smart Materials and Structures*, 13(1), p.146.

Ray, M.C. and Mallik, N., 2005. Performance of smart damping treatment using piezoelectric fiber-reinforced composites. *AIAA Journal*, 43(1), pp.184-193.

Ray, M.C., Oh, J. and Baz, A., 2001. Active constrained layer damping of thin cylindrical shells. *Journal of Sound and Vibration*, 240(5), pp.921-935.

Ray, M.C. and Pradhan, A.K., 2006. The performance of vertically reinforced 1–3 piezoelectric composites in active damping of smart structures. *Smart Materials and Structures*, 15(2), p.631.

Ray, M.C. and Pradhan, A.K., 2007. On the use of vertically reinforced 1-3 piezoelectric composites for hybrid damping of laminated composite plates. *Mechanics of Advanced Materials and Structures*, 14(4), pp.245-261.

Ray, M.C. and Pradhan, A.K., 2010. Active damping of laminated thin cylindrical composite panels using vertically/obliquely reinforced 1–3 piezoelectric composites. *Acta Mechanica*, 209(3), pp.201-218.

Ray, M.C., Rao, K.M. and Samanta, B., 1993. Exact solution for static analysis of an intelligent structure under cylindrical bending. *Computers & Structures*, *47*(6), pp.1031-1042.

Ray, M.C. and Reddy, J.N., 2004a. Effect of delamination on active constrained layer damping of smart laminated composite beams. *AIAA Journal*, 42(6), pp.1219-1226.

Ray, M.C. and Reddy, J.N., 2004b. Optimal control of thin circular cylindrical laminated composite shells using active constrained layer damping treatment. *Smart Materials and Structures*, 13(1), p.64.

Ray, M.C. and Reddy, J.N., 2005. Active control of laminated cylindrical shells using piezoelectric fiber reinforced composites. *Composites Science and Technology*, 65(7-8), pp.1226-1236.

Reddy, J.N., 2003. Mechanics of laminated composite plates and shells: theory and analysis. *CRC press*.

Reddy, J.N. and Phan, N., 1985. Stability and vibration of isotropic, orthotropic and laminated plates according to a higher-order shear deformation theory. *Journal of Sound and Vibration*, 98(2), pp.157-170.

Ro, J. and Baz, A., 2002. Optimum placement and control of active constrained layer damping using modal strain energy approach. *Journal of Vibration and Control*, 8(6), pp.861-876.

Robaldo, A., Carrera, E. and Benjeddou, A., 2006. A unified formulation for finite element analysis of piezoelectric adaptive plates. *Computers & Structures*, 84(22-23), pp.1494-1505.

Robbins Jr, D.H. and Reddy, J.N., 1996. An efficient computational model for the stress analysis of smart plate structures. *Smart Materials and Structures*, 5(3), p.353.

Robertson, D.H., Brenner, D.W. and Mintmire, J.W., 1992. Energetics of nanoscale graphitic tubules. *Physical Review B*, 45(21), p.12592.

Ru, C.Q., 2000. Effective bending stiffness of carbon nanotubes. *Physical Review B*, 62(15), p.9973.

Sadri, R., Ahmadi, G., Togun, H., Dahari, M., Kazi, S.N., Sadeghinezhad, E. and Zubir, N., 2014. An experimental study on thermal conductivity and viscosity of nanofluids containing carbon nanotubes. *Nanoscale Research Letters*, 9(1), pp.1-16.

Sahoo, S.R. and Ray, M.C., 2018. Analysis of smart damping of laminated composite beams using mesh free method. *International Journal of Mechanics and Materials in Design*, 14(3), pp.359-374.

Sahoo, S.R. and Ray, M.C., 2019a. Active control of doubly curved laminated composite shells using elliptical smart constrained layer damping treatment. *Thin-Walled Structures*, 140, pp.373-386.

Sahoo, S.R. and Ray, M.C., 2019b. Active control of laminated composite plates using elliptical smart constrained layer damping treatment. *Composite Structures*, 211, pp.376-389.

Salvetat, J.P., Briggs, G.A.D., Bonard, J.M., Bacsa, R.R., Kulik, A.J., Stöckli, T., Burnham, N.A. and Forró, L., 1999. Elastic and shear moduli of single-walled carbon nanotube ropes. *Physical Review Letters*, 82(5), p.944.

Sarangi, S.K. and Basa, B., 2014. Nonlinear finite element analysis of smart laminated composite sandwich plates. *International Journal of Structural Stability and Dynamics*, 14(03), p.1350075.

Sarangi, S.K. and Ray, M.C., 2010. Smart damping of geometrically nonlinear vibrations of laminated composite beams using vertically reinforced 1–3 piezoelectric composites. *Smart Materials and Structures*, 19(7), p.075020.

Sarangi, S.K. and Ray, M.C., 2013. Smart control of nonlinear vibrations of doubly curved functionally graded laminated composite shells under a thermal environment using 1–3 piezoelectric composites. *International Journal of Mechanics and Materials in Design*, 9(3), pp.253-280.

Sastry, C.V.S., Mahapatra, D.R., Gopalakrishnan, S. and Ramamurthy, T.S., 2004. Distributed sensing of static and dynamic fracture in self-sensing piezoelectric composite: finite element simulation. *Journal of Intelligent Material Systems and Structures*, 15(5), pp.339-354.

Di Sciuva, M., 1985. Development of an anisotropic, multilayered, shear-deformable rectangular plate element. *Computers & Structures*, 21(4), pp.789-796.

Di Sciuva, M. and Sorrenti, M., 2019. Bending, free vibration and buckling of functionally graded carbon nanotube-reinforced sandwich plates, using the extended Refined Zigzag Theory. *Composite Structures*, *227*, p.111324.

Sedira, L., Ayad, R., Sabhi, H., Hecini, M. and Sakami, S., 2012. An enhanced discrete Mindlin finite element model using a zigzag function. *European Journal of Computational Mechanics/Revue Européenne de Mécanique Numérique*, 21(1-2), pp.122-140.

Seidel, G.D. and Lagoudas, D.C., 2006. Micromechanical analysis of the effective elastic properties of carbon nanotube reinforced composites. *Mechanics of Materials*, 38(8-10), pp.884-907.

Shady, E. and Gowayed, Y., 2010. Effect of nanotube geometry on the elastic properties of nanocomposites. *Composites Science and Technology*, 70(10), pp.1476-1481.

Shaffer, M.S. and Windle, A.H., 1999. Fabrication and characterization of carbon nanotube/poly (vinyl alcohol) composites. *Advanced Materials*, 11(11), pp.937-941.

Shao, L.H., Luo, R.Y., Bai, S.L. and Wang, J., 2009. Prediction of effective moduli of carbon nanotube–reinforced composites with waviness and debonding. *Composite Structures*, 87(3), pp.274-281.

Shen, I.Y., 1996. Stability and controllability of Euler-Bernoulli beams with intelligent constrained layer treatments. *Journal of Vibration and Acoustics*, 118(1), pp. 70–77.

Shen, L. and Li, J., 2004. Transversely isotropic elastic properties of single-walled carbon nanotubes. *Physical Review B*, 69(4), p.045414.

Shen, L. and Li, J., 2005. Transversely isotropic elastic properties of multiwalled carbon nanotubes. *Physical Review B*, 71(3), p.035412.

Shi, D.L., Feng, X.Q., Huang, Y.Y., Hwang, K.C. and Gao, H., 2004. The effect of nanotube waviness and agglomeration on the elastic property of carbon nanotube-reinforced composites. *Journal of Engineering Materials and Technology*, 126(3), pp.250-257.

Shin, D.K., 1997. Large amplitude free vibration behavior of doubly curved shallow open shells with simply-supported edges. *Computers & Structures*, 62(1), pp.35-49.

Smith, W.A. and Auld, B.A., 1991. Modeling 1-3 composite piezoelectrics: thickness-mode oscillations. *IEEE Transactions on Ultrasonics, Ferroelectrics, and Ffrequency Control*, 38(1), pp.40-47.

Song, Y.S. and Youn, J.R., 2006. Modeling of effective elastic properties for polymer based carbon nanotube composites. *Polymer*, 47(5), pp.1741-1748.

Sun, D. and Tong, L., 2003. Effect of debonding in active constrained layer damping patches on hybrid control of smart beams. *International Journal of Solids and Structures*, 40(7), pp.1633-1651.

Sun, D., Tong, L. and Wang, D., 2001. Vibration control of plates using discretely distributed piezoelectric quasi-modal actuators/sensors. *AIAA Journal*, 39(9), pp.1766-1772.

Sze, K.Y. and Yao, L.Q., 2000. Modelling smart structures with segmented piezoelectric sensors and actuators. *Journal of Sound and Vibration*, 235(3), pp.495-520.

Tans, S.J., Devoret, M.H., Dai, H., Thess, A., Smalley, R.E., Geerligs, L.J. and Dekker, C., 1997. Individual single-wall carbon nanotubes as quantum wires. *Nature*, 386(6624), pp.474-477.

Tarfaoui, M., Lafdi, K. and El Moumen, A., 2016. Mechanical properties of carbon nanotubes based polymer composites. *Composites Part B: Engineering*, 103, pp.113-121.

Tehrani, M., Safdari, M., Boroujeni, A.Y., Razavi, Z., Case, S.W., Dahmen, K., Garmestani, H. and Al-Haik, M.S., 2013. Hybrid carbon fiber/carbon nanotube composites for structural damping applications. *Nanotechnology*, 24(15), p.155704.

Terrones, M., 2003. Science and technology of the twenty-first century: synthesis, properties, and applications of carbon nanotubes. *Annual Review of Materials Research*, 33(1), pp.419-501.

Tessler, A., Di Sciuva, M. and Gherlone, M., 2009. A refined zigzag beam theory for composite and sandwich beams. *Journal of Composite Materials*, 43(9), pp.1051-1081.

Thai, H.T. and Kim, S.E., 2013. A simple quasi-3D sinusoidal shear deformation theory for functionally graded plates. *Composite Structures*, 99, pp.172-180.

Thostenson, E.T., Li, W.Z., Wang, D.Z., Ren, Z.F. and Chou, T.W., 2002. Carbon nanotube/carbon fiber hybrid multiscale composites. *Journal of Applied Physics*, 91(9), pp.6034-6037.

Thostenson, E.T. and Chou, T.W., 2003. On the elastic properties of carbon nanotube-based composites: modelling and characterization. *Journal of Physics D: Applied Physics*, 36(5), p.573.

Tombler, T.W., Zhou, C., Alexseyev, L., Kong, J., Dai, H., Liu, L., Jayanthi, C.S., Tang, M. and Wu, S.Y., 2000. Reversible electromechanical characteristics of carbon nanotubes underlocal-probe manipulation. *Nature*, 405(6788), pp.769-772.

Treacy, M.J., Ebbesen, T.W. and Gibson, J.M., 1996. Exceptionally high Young's modulus observed for individual carbon nanotubes. *Nature*, 381(6584), pp.678-680.

Trindade, M.A., Benjeddou, A. and Ohayon, R., 2000. Modeling of frequency-dependent viscoelastic materials for active-passive vibration damping. *Journal of Vibration and Acoustics*., 122(2), pp.169-174.

Tsai, C.H., Zhang, C., Jack, D.A., Liang, R. and Wang, B., 2011. The effect of inclusion waviness and waviness distribution on elastic properties of fiber-reinforced composites. *Composites Part B: Engineering*, 42(1), pp.62-70.

Tsai, J.L., Tzeng, S.H. and Chiu, Y.T., 2010. Characterizing elastic properties of carbon nanotubes/polyimide nanocomposites using multi-scale simulation. *Composites Part B: Engineering*, 41(1), pp.106-115.

Tserpes, K.I. and Papanikos, P., 2005. Finite element modeling of single-walled carbon nanotubes. *Composites Part B: Engineering*, 36(5), pp.468-477.

Tzou, H.S. and Gadre, M., 1989. Theoretical analysis of a multi-layered thin shell coupled with piezoelectric shell actuators for distributed vibration controls. *Journal of Sound and Vibration*, 132(3), pp.433-450.

Tzou, H.S. and Gadre, M., 1990. Active vibration isolation and excitation by piezoelectric slab with constant feedback gains. *Journal of Sound and Vibration*, 136(3), pp.477-490.

Valavala, P.K. and Odegard, G.M., 2005. Modeling techniques for determination of mechanical properties of polymer nanocomposites. *Reviews on Advanced Materials Science*, 9(1), pp.34-44.

Varadan, V.V., Kim, J. and Varadan, V.K., 1997. Optimal placement of piezoelectric actuators. *AIAA Journal*, 35(3), pp.526-533.

Varadan, V.V., Lim, Y.H. and Varadan, V.K., 1996. Closed loop finite-element modeling of active/passive damping in structural vibration control. *Smart Materials and Structures*, 5(5), p.685.

Vasques, C.M.A., Mace, B.R., Gardonio, P. and Rodrigues, J.D., 2006. Arbitrary active constrained layer damping treatments on beams: Finite element modelling and experimental validation. *Computers & Structures*, 84(22-23), pp.1384-1401.

Vasques, C.M.A. and Rodrigues, J.D., 2008. Combined feedback/feedforward active control of vibration of beams with ACLD treatments: Numerical simulation. *Computers & Structures*, 86(3-5), pp.292-306.

Vigolo, B., Penicaud, A., Coulon, C., Sauder, C., Pailler, R., Journet, C., Bernier, P. and Poulin, P., 2000. Macroscopic fibers and ribbons of oriented carbon nanotubes. *Science*, 290(5495), pp.1331-1334.

Vinyas, M., 2019. Vibration control of skew magneto-electro-elastic plates using active constrained layer damping. *Composite Structures*, 208, pp.600-617.

Vinyas, M., 2020. Interphase effect on the controlled frequency response of three-phase smart magneto-electro-elastic plates embedded with active constrained layer damping: FE study. *Materials Research Express*, 6(12), p.125707.

Wang, S.Y., Quek, S.T. and Ang, K.K., 2001. Vibration control of smart piezoelectric composite plates. *Smart Materials and Structures*, 10(4), p.637.

Wernik, J.M. and Meguid, S.A., 2010. Recent developments in multifunctional nanocomposites using carbon nanotubes. *Applied Mechanics Reviews*, 63(5).

Wernik, J.M. and Meguid, S.A., 2011. Multiscale modeling of the nonlinear response of nano-reinforced polymers. *Acta Mechanica*, 217(1), pp.1-16.

Wilder, J.W., Venema, L.C., Rinzler, A.G., Smalley, R.E. and Dekker, C., 1998. Electronic structure of atomically resolved carbon nanotubes. *Nature*, 391(6662), pp.59-62.

Xiao, J.R., Gama, B.A. and Gillespie Jr, J.W., 2005. An analytical molecular structural mechanics model for the mechanical properties of carbon nanotubes. *International Journal of Solids and Structures*, 42(11-12), pp.3075-3092.

Xu, F., Wang, X., Zhu, Y. and Zhu, Y., 2012. Wavy ribbons of carbon nanotubes for stretchable conductors. *Advanced Functional Materials*, 22(6), pp.1279-1283.

Yakobson, B.I., Brabec, C.J. and Bernholc, J., 1996. Nanomechanics of carbon tubes: instabilities beyond linear response. *Physical Review Letters*, 76(14), p.2511.

Yanase, K., Moriyama, S. and Ju, J.W., 2013. Effects of CNT waviness on the effective elastic responses of CNT-reinforced polymer composites. *Acta Mechanica*, 224(7), pp.1351-1364.

Yu, B., Jiang, Z., Tang, X.Z., Yue, C.Y. and Yang, J., 2014. Enhanced interphase between epoxy matrix and carbon fiber with carbon nanotube-modified silane coating. *Composites Science and Technology*, 99, pp.131-140.

Yu, M.F., Lourie, O., Dyer, M.J., Moloni, K., Kelly, T.F. and Ruoff, R.S., 2000. Strength and breaking mechanism of multiwalled carbon nanotubes under tensile load. *Science*, 287(5453), pp.637-640.

Yuan, L., Xiang, Y., Huang, Y. and Lu, J., 2010. A semi-analytical method and the circumferential dominant modal control of circular cylindrical shells with active constrained layer damping treatment. *Smart Materials and Structures*, 19(2), p.025010.

Zhang, J. and He, C., 2008. A three-phase cylindrical shear-lag model for carbon nanotube composites. *Acta Mechanica*, 196(1), pp.33-54.

Zhu, S., Su, C.H., Lehoczky, S.L., Muntele, I. and Ila, D., 2003. Carbon nanotube growth on carbon fibers. *Diamond and Related Materials*, 12(10-11), pp.1825-1828.

List of Publications

The following papers are published/ under review from the research work carried out during PhD:

A1. Refereed Journal Publications from Thesis:

1. **Gupta, M.,** Ray, M.C., Patil, N.D. and Kundalwal, S.I., 2021. Dynamic modelling and analysis of smart carbon nanotube-based hybrid composite beams: Analytical and finite element study, *Proc. Inst. Mech. Eng. L. 235(10): 2185-2206. IF: 2.663*
2. **Gupta, M.,** Ray, M.C., Patil, N.D. and Kundalwal, S.I., 2022. Smart damping of a simply supported laminated CNT-based hybrid composite plate using FE approach. *Thin-Walled Struct., 171*, p.108782. *IF: 5.881*
3. **Gupta, M.,** Ray, M.C., Patil, N.D. and Kundalwal, S.I., 2022. Effect of orientation of CNTs and piezoelectric fibers on the damping performance of multiscale composite plate, *J. Intell. Mater. Syst. Struct. IF: 2.774*
4. **Gupta, M.,** Patil, N.D. and Kundalwal, S.I., 2022. Active damping of multiscale composite shells using Sinus theory incorporated with Murakami's zig-zag function, *Thin-Walled Struct.* (revision submitted). *IF: 5.881*

A2. Refereed Journal Publications other than Thesis work:

5. **Gupta, M.,** Meguid, S.A. and Kundalwal, S.I., 2022. Synergistic effect of surface-flexoelectricity on electromechanical response of BN-based nanobeam. *Int. J. Mech. Mater. Des.*, 18, pp. 3–19. *IF: 3.561*
6. Kundalwal, S.I., Shingare, K.B. and **Gupta, M.**, 2020. Flexoelectric effect on electric potential in piezoelectric graphene-based composite nanowire: Analytical and numerical modelling. *Eur J Mech A Solids*, 84, p.104050. *IF: 4.873*
7. Kundalwal, S.I. and **Gupta, M.**, 2022. Interdependent effects of surface and flexoelectricity on the electromechanical behavior of BNRC nanoplate. *Mech. Mater.* 175, p.104483. *IF: 4.137*
8. Nevhal, S.K., **Gupta, M.** and Kundalwal, S.I., 2022. Influence of flexoelectric effect on the bending regidity of a Timoshenko graphene-reinforced nanorod. Actuators. *IF: 2.523* (To be submitted)

9. Nevhal, S.K., **<u>Gupta, M.</u>** and Kundalwal, S.I., 2022. Polarization of graphene/HBN wandervalls hetero-structures with triangular defects. Actuators. *IF: 2.523* (To be submitted)
10. Bansod, P.V., **<u>Gupta, M</u>.** and Kundalwal, S.I., 2022. A Finite element based study on the electromechanical response of boron nitride reinforced nanocomposite beam incorporating the effects of flexoelectricity and surface. (Manuscript with Supervisor)
11. Bansod, P.V., **<u>Gupta, M.</u>** and Kundalwal, S.I., 2022. Influence of surface and flexoelectric effects on the electromechanical response of BNRC nanoplate. (Manuscript with Supervisor)

A3. Refereed Conference Proceedings during PhD:

1. K. B. Shingare, **<u>Gupta. M.</u>** and S. I. Kundalwal, "Effect of size-dependent properties on static and dynamic behavior of the graphene nanocomposite plate: Analytical approach", International Conference on Precision, Meso, Micro and Nano Engineering (COPEN 2019), IIT Indore.
2. K. B. Shingare, **<u>Gupta. M.</u>** and S. I. Kundalwal, "Evaluation of effective properties for smart graphene reinforced nanocomposite materials", *Materials Today Proceedings*, vol. 23, pp. 523–527, 2020.
3. **<u>Gupta, M.,</u>** Ray, M.C., Patil, N.D. and Kundalwal, S.I., "Influence of CNT waviness on the effective elastic properties of multiscale hybrid composite", International conference on Applied Mechanics, Machine Learning and Advance Computation (AMMLAC-2022), NIT Raipur.
4. **<u>Gupta, M.,</u>** Ray, M.C., Patil, N.D. and Kundalwal, S.I., "Active damping of high performance multiscale composite plates treated with straight and wavy CNTs", National Conference in Mechanical Engineering: Advances in Materials and Design (NCMEAMD-2022), VIT Pune.
5. Dubey. P., **<u>Gupta. M.</u>** and Kundalwal, S.I., "Numerical investigation of shielding effectiveness of multiwalled carbon nanotube reinforced polypyrrole nanocomposite", International Conference on Nanotechnology: Opportunities & Challenges (ICNOC-2022), Jamia Millia Islamia, New Delhi. (Accepted)

Curriculum Vitae

MADHUR GUPTA

Ph.D. Scholar
Indian Institute of Technology, Indore | Pin Code: 453552

+91-8770322689 madhur.gupta03@gmail.com

Google Scholar | ResearchGate |

LinkedIn | ORCID |

ACADEMIC BACKGROUND

Ph.D. in Mechanical Engineering Department Thesis Submitted:
Indian Institute of Technology, Indore 17th May 2022

Dissertation title: "Active Vibration Control of Smart Multiscale Composite Beams, Plates and Shells"
Supervisor: Dr. Shailesh. I. Kundalwal
Co-supervisor: Dr. Nagesh D. Patil

M-Tech. in CAD/CAM/CAE Department June 2018
SGSITS, Indore (RGPV University)

B.E. in Mechanical Engineering Department June 2014
SDITS, Khandwa (RGPV University)

PRINCIPAL AREAS OF INTEREST

To design and develop advanced nanocomposite materials for the application of energy harvesting, energy storage, and vibration attenuation through simulations and experiments using various visualization and characterization techniques.

Key Research Areas*:* Atomistic Modeling of Nanomaterials and Nanostructures, Nanotechnology in Engineering, Micro and Nanomechanics, Flexoelectricity and Piezoelectricity, Smart Materials and Structures, EMI Shielding and Electrical Conductivity.

RESEARCH EXPERIENCE

- Investigation of effective elastic properties of two-/three-phase multiscale composites incorporated with carbon nanotubes (CNTs) nanofiller.
  (Analytical and Finite element study)
- Developed finite element (FE) models using in-house MATLAB codes to investigate the active damping response of CNT reinforced multiscale composite

structures integrated with the patches of the ACLD treatment layer.
(Dynamic study using Finite element model)

- Studied the effects of surface and flexoelectricity on the electromechanical behavior of piezoelectric nanocomposites reinforced with Graphene and Boron-Nitride nanosheets.
(Static and Dynamic study using Analytical and Finite element models, CSIR, SERB sponsored project)
- Design and development of CNT reinforced polymer nanocomposite to improve the EMI shielding effectiveness in C-band.
(Experimental and Analytical Investigation, ISRO sponsored project)
- Prospectives, progress, and challenges of 1D/2D carbon-based nanomaterials in the application of Hydrogen storage.
(Experimental and Molecular dynamics study, DST sponsored project)
- Synthesis of Graphene using chemical vapor deposition (CVD) approach.
(Experimental investigation, DST sponsored project)

ACADEMIC EXPERIENCE

Teaching Assistant, *Department of Mechanical Engineering*
Indian Institute of Technology, Indore

• Kinematics and Dynamics (computational lab)	Autumn 2019, 2020 and 2021
• Engineering Graphics (tutorials)	Spring 2020
• Composite materials (tutorials)	Autumn 2020
• Kinematics and Dynamics (tutorials)	Autumn 2021
• Vehicle Dynamics (tutorials)	Spring 2021

This includes:
Preparing lectures and class activities, conducting exams, and focusing on class and individuals.
Creating and grading course assessments to ensure students understood the material and stayed on track.

Undergraduate Mentor, *A.T.O.M. Lab., Department of Mechanical Engineering*
Indian Institute of Technology, Indore

• Mentored one undergraduate student in Experimental/Simulation work, Data plotting, and Data visualization	Academic Year: 2019-20
• Mentored two undergraduate students in Ansys APDL and WORKBENCH simulations, Data plotting, and Data visualization	Academic Year: 2020-21

- Guided the students in the preparation and presentation of research findings

Postgraduate Mentor, *A.T.O.M. Lab., Department of Mechanical Engineering Indian Institute of Technology, Indore*

- Mentored one postgraduate student in MATLAB coding, COMSOL simulations, and Data plotting — Academic Year: 2019-20
- Mentoring one postgraduate student in handling CVD, various Characterization techniques, and Data visualization — Academic Year: 2021-22
- Guided the students in the preparation and presentation of research findings

Academic Internship, *A.T.O.M. Lab., Department of Mechanical Engineering Indian Institute of Technology, Indore*

- Topic: "Effects of flexoelectricity on the electromechanical behavior of nanocomposite plates" — Sept. 2018 – June 2019
- *Supervisor:* Dr. S. I. Kundalwal;
- *Mentor:* Dr. K. B. Shingare

JOURNALS, CONFERENCES AND WORKSHOPS

- Extracted 4 international journal publications from Ph.D. research work.
- Extracted 3 international journal publications apart from Ph.D. research work.
- Presented/participated in 4 international/national conferences.
- Participated/attended 7 online/offline workshops organized by prestigious institutes and research facilities like IITs, NITs, DRDO and ISRO.
- In addition to this several manuscripts are either with supervisor or under preparation.

SHORT TERM ACADEMIC COURSES AND INDUSTRIAL TRAINING

- Atomistic modelling of solids: Theory and Application — Dec 21 to 25, 2020
  Organized by Indian Institute of Technology, Indore
- Micro- and Nano-Mechanics of solids: Fundamental and Applications — Dec 14 to 19, 2020

Organized by Indian Institute of Technology, Indore

- Industrial training at Bhilai Steel Plant | SAIL — June 17 to July 07, 2013
- PRO-E (summer training) — July 02-21, 2012
  Indo-German Tool Room, Indore
- AutoCAD (summer training) — Feb 02-18, 2012
  Indo-German Tool Room, Indore

HONORS, AWARDS AND ACHIEVEMENTS

- Institute/MHRD sponsored fellowship to pursue Ph.D. — 2019-2022
- AICTE sponsored fellowship to pursue Master's Degree — 2016-2018
- Qualified Graduate Aptitude Test in Engineering (GATE) — 2016
- Recognized as an active reviewer for Material Today: Proceedings — 2020-till date
- A.T.O.M Lab. Representative — 2021 and 2022
- Won 1st prize in intraIIT Chess competition — 2021
- Elected as a Class Representative 3 times during B.E. — 2012, 2013 and 2014

ACADEMIC ACTIVITIES

- **Organized: Short term online** TEQIP course on "Atomistic Modelling of Solids", (Avg. feedback 4.68/5, Participant-65) — Dec 21-25, 2020
  Organized by Indian Institute of Technology, Indore
- **Organized: Short term** Six Days' online QIP-STC program on "Micro- & Nano-Mechanics of Solids: Fundamentals &Applications". (Avg. feedback 4.4/5, Participant-61) — Dec 14 to 19, 2020
  Organized by Indian Institute of Technology, Indore
- **Volunteer:** International Conference on Precision, Meso, Micro and Nano Engineering (COPEN 2019), IIT Indore. — 2019
  Organized by Indian Institute of Technology, Indore

- Assist Dr. Kundalwal to stabilize the high computing facility in *A.T.O.M. Lab., Department of Mechanical Engineering, Indian Institute of Technology, Indore* — 2019-present
- Collaborated with other Ph.D., Postgraduate and Undergraduate students at *A.T.O.M. Lab., Department of Mechanical Engineering, Indian Institute of Technology, Indore* — 2019-present

IT PROFICIENCY

- Well viewed in MATLAB, Origin, Ansys APDL, Ansys WORKBENCH, LAMMPS, COMSOL, Creo
- Skilled in Microsoft Office, LaTeX, MathType, Mendeley, VMD, OVITO
- Familiarity with computer language: Python, C++, Java, DBMS, SQL, .NET

OTHER SKILLS

- Very good Logical and Analytical Skills
- Ability to build Relationship, Tactfulness and Set up Trust
- Excellent Interpersonal and Decision-making Ability
- Confident and Determinant

PERSONAL DETAILS

Name	:	Madhur Gupta
Father's Name	:	Mahesh Kumar Gupta
Date of Birth	:	03rd Feb 1992
Hobbies	:	Reading Books, Playing Chess, Playing Tennis
Language	:	Hindi (Fluent) and English (Proficient)
Strength	:	Positive Attitude, Effective Presentation, Smart Working, Tactfulness

DECLARATION

I do hereby declare that the above information is true to the best of my knowledge.

Place : Indore **Madhur Gupta**

Date :